Development of Cellulose-Based Composite Separator Membranes for Energy Storage Devices

Thesis submitted for the Degree of

Doctor of Philosophy (Science)

of

Department of Chemistry

Jadavpur University, Kolkata

By

Mononita Das

Index No. 205/22/Chem./28

Registration No. SCHEM1120522

Energy Materials and Devices Division
CSIR-Central Glass and Ceramic Research Institute
196 Raja S C Mullick Road
Kolkata 700 032, India

September 2025

CERTIFICATE FROM THE SUPERVISOR

This is to certify that the thesis entitled **"Development of Cellulose-Based Composite Separator Membranes for Energy Storage Devices"** submitted by Ms. Mononita Das **(Registration No. SCHEM1120522** and **Index No. 205/22/Chem./28)**, who got his name registered on **04.07.2022** for the award of Ph.D. (Science) degree of Jadavpur University, is absolutely based upon her own work under the supervision of Dr. Mir Wasim Raja, Principal Scientist and that neither this thesis nor any part of it has been submitted for either any degree/diploma or any other academic award anywhere before.

15.09.2025

(Dr. Mir Wasim Raja)
Supervisor
Principal Scientist
Energy Materials and Devices Division
CSIR-Central Glass and Ceramic Research Institute
Kolkata

डॉ. मीर वसीम राजा / Dr. Mir Wasim Raja
प्रमुख वैज्ञानिक / Principal Scientist
ऊर्जा सामग्री और उपकरण विभाग / Energy Materials & Devices Division
सीएसआईआर-केन्द्रीय काँच एवं सिरामिक अनुसंधान संस्थान
CSIR-Central Glass & Ceramic Research Institute
विज्ञान एवं प्रौद्योगिकी मंत्रालय, भारत सरकार
Ministry of Science & Technology, Govt. of India
196, राजा एस. सी. मल्लिक रोड / 196, Raja S.C. Mullick Road
कोलकाता / Kolkata-700 032

DECLARATION

I hereby declare that the matter embodied in this thesis entitled **"Development of Cellulose-Based Composite Separator Membranes for Energy Storage Devices"** is the result of investigations carried out by me in Energy Materials and Devices Division, CSIR-Central Glass and Ceramic Research Institute, Kolkata under the supervision of Dr. Mir Wasim Raja and it or its any part has not been submitted for any degree or diploma or any other academic award elsewhere.

Mononita Das 15.09.2025.

.....

(MONONITA DAS)

Date: 15.09.2025.

Place: Jadavpur, Kolkata 700032

"Nothing in life is to be feared, it is only to be understood. Now is the time to understand more, so that we may fear less."

- Maria Salomea Skłodowska-Curie

Dedicated to

My Mother, Mrs. Aloka Das

Acknowledgements

The journey of me as a researcher, especially as a battery researcher started in January 2021. Before that, I hardly knew any details about Lithium-ion battery. I was not aware of anything about separator or its functions in battery, as well. But, after joining the project entitled “Energy Storage Platform on Batteries” as a Junior Research Fellow, I started to learn about the numerous interesting phenomena that are continuously taking place inside the batteries of our cell phones, laptops and other everyday electronic devices. It simply fascinated me. The post-graduate electrochemistry started making sense and a whole new world of charge-discharge, SEI, plating and stripping started uncovering in front of me. I want to thank the then Director and current Director of CSIR-CGCRI for giving me the opportunity to conduct my research in the institute.

The term ‘PhD’ entered into my life one year later. Before being my PhD supervisor, Dr Mir Wasim Raja was my Project Investigator and guide, and he still is. All the things about battery which I learnt in my preliminary research days, I learnt from him and his guidance. He always appreciated whatever hard work I did for the project work as well as for my PhD research. Thus, I want to thank my supervisor for his guidance, knowledge and enthusiasm that enlightened my research journey. I also want to thank my research advisory committee (RAC) members: Firstly, Dr Nimai Chand Pramanik, Senior Principal Scientist of Specialty Glass Division, who has always guided in a positive way during the RAC evaluations and all the other times. And Dr Kajal Krishna Rajak, the head of Department of Chemistry, Jadavpur University; who has always supported and guided in every way possible.

I express my gratitude towards my teachers of Chemistry Department in Jadavpur University, who taught and guided me immensely during the coursework. My other teachers from childhood to MSc, especially Kabita di, Dipankar sir, Gautam sir, Amrit sir, Pinaki sir, Swapan sir, Nikhil sir have inspired me a lot and shaped my life in a better way. I convey my heartfelt respect and thanks to them.

During my initial days at CSIR-CGCRI, our departmental head was Dr Abhijit Das Sharma, who has now superannuated. And currently the divisional chair of Energy Materials and Devices Division is Dr Jayanta Mukhopadhyay. I want to convey my gratitude towards both of them for

the support and faith that they have always shown not only in me, but in all the students of the division. I have not collaborated with any other scientist in our division, yet I am aware of their nature and works. I want to thank all of them, especially Dr Srabanti Ghosh, whose procurement of the ZIVE SP1 instrument has helped a lot in my research, the electrochemical results obtained from the instrument have added new dimension to the research works. There are few persons, whom I have hardly met, but they hold a profound influence on my research journey. The most important among them is Dr Sourindra Mahanty, whose contribution towards the development of battery research infrastructure in our institute is unmatchable. I want to thank Mahanty sir for all his efforts and knowledge, which are benefitting today's researchers as well. I want to express my heartfelt gratitude to the technical and contractual persons, like Sudip da, Pradip da, Nabanita di, Ashok da, Nitai da, Dalui da, Pushpam, Mousumi di, Mahadeb da, Hirak, Bimal da, Ratikanta da, Sunil da, Goutam da and every other member of CSIR-CGCRI who have become part of my ~4.5 years journey. ChatGPT, although it is an AI and not a person, still I want to thank this tool for helping me in gaining knowledge and improving research writing in every way possible.

My research journey is incomplete without the fights and supports I have received from Kuntal Ghosh, my one and only senior in the battery lab and my friend, philosopher and guide at the same time. I have seen very less number of researchers who are as dedicated towards research as him. The guidance and insights from him have always motivated me to do something new and something better in my PhD.

Although I am an introvert person, there are some friends whom I want to thank. Ria, Arkapravo and Shreyoshi are very close to my heart and they have always remained my cheerleaders whenever I achieve anything. I want to convey my gratitude to all of them. Aishwarya was there when I started PhD, but in this concluding time, she is not in this world. She was a dear friend of mine and a very bright student from Rajabazar Science College, who passed away in 2022 in blood cancer. I have learnt many things from her, especially resilience and positive attitude towards life; I want to convey my gratitude and love towards her. I want to thank Vijaya, whom I came to know from LinkedIN and later we collaborated in a research work. I have learnt a lot from her positive attitude and forever helping nature.

Whatever I am today, my entire existence is because of only one person and that is my mother. From my childhood to till date, Maa has protected me from all odds, guided me towards right

direction and helped me whenever I needed. If I receive this highest academic honour, i.e., the doctorate degree, it will be only be possible because of her hard work, dedication and believe in the imperfect me. I want to thank Baba as well, who is not with me and I do not remember him well but I always feel his presence inside me.

My Chhoto Mama played a pivotal role in my upbringing. After the leaving of my father, he has always remained my comfort zone, my pampering person. I want to thank him from the core of my heart. When Dida was alive, she always wanted me to pursue higher study. I want to convey my love and regards to her and Dadu, whom I respect a lot but could never meet. I thank all the other members of my family for their support and love I always receive from them.

And last but not the least, I want to thank my pets who are not just animals, but they are like my own children. I want to express my love and gratitude to Michhri, Naru, Gopal, Baghini, Nonte, Fonte, Mishtu, Jamu, Sonte, Chotu, Mishtu, Simba, Sundori, Lalu, Kalu, Kali, Barfi, Kulfi, Sandesh and many more. They have always supported and loved me like no other else. I have learnt so many things from them, which I could never learn from any human being. Their loyalty, resilience and kindness have always inspired me to become a better person. Dustu and Moti are not in this world anymore, I thank them and miss them a lot.

Finally, I thank God and the Universe for everything that I have achieved and not achieved, for every success and failure, for every triumph and disaster. All these have been very important lessons in my 28 years of life journey. Thank You.

CONTENTS

Acknowledgements *V*
Contents *VIII*
List of Figures *XV*
List of Tables *XXIV*
Abbreviations *XXVI*
Highlights of the Thesis *XXVIII*

Chapter 1 1-34
Introduction

Highlights, Summary and Graphical Abstract 1
1.1 Motivation 2
1.2 Electric Mobility 3
1.2.1 Global Scenario 4
1.2.2 Indian Perspective 5
1.3 Background: Battery Landscape 6
1.4 Lithium Storage: Intercalation Chemistry and Beyond 8
1.5 Critical LIB Components 10
1.5.1 Cathode 11
1.5.2 Anode 11
1.5.3 Electrolyte 11
1.5.4 Separator 12
1.6 Evolution of Separator Materials 13
1.7 Critical Technical Parameters: Workable Separator in LIBs 15
1.8 Types of Separators 18
1.8.1 Microporous Membranes 19
1.8.2 Nonwoven Membranes 19
1.8.3 Electrospun Membranes 19
1.8.4 Membranes with External Surface Modification 20
1.6.5 Composite Membranes 20
1.8.6 Polymer Blends 20
1.9 Commercial Separator (PP/PE) & Drawbacks 21
1.10 Cellulose: A Potential Alternative 23
1.11 Paper Chemistry and Functional Paper 24
1.12 Next Generation Separators: Cost & Sustainability 26
1.13 Research on Separator-cum-electrolyte Membranes 27
1.14 Research Gap and Opportunities 28

1.15 Objectives and Scope of the Thesis 29
References 31

Chapter 2 35-60
Research Methodology

Highlights, Summary and Graphical Abstract 35
2.1 Overview 36
2.2 Materials and Chemicals 36
2.3 Development of Paper Separators 38
2.3.1 Paper Separator with Higher Thickness 39
2.3.2 Paper Separator with the Thickness of Commercial Standard 40
2.3.2.1 Monolayer Separator 41
2.3.2.2 Bilayer Separator 41
2.3.2.3 Trilayer Separator 42
2.4 Development of Polymer Electrolytes 42
2.4.1 Composite Solid Polymer Electrolytes (CSPEs) 42
2.4.2 Paper-based CSPEs 43
2.5 Characterization Techniques and Instruments 43
2.5.1 Physical Characterizations 44
2.5.1.1 Thickness 44
2.5.1.2 Air Permeability 44
2.5.1.3 Electrolyte Uptake and Wettability 44
2.5.1.4 Pore Characteristics 45
2.5.1.5 Tensile Properties 45
2.5.1.6 Zeta Potential 46
2.5.2 Structure and Microstructure 46
2.5.2.1 Digital Images 46
2.5.2.1 X-ray Diffraction (XRD) Pattern 46
2.5.2.3 Microstructure by SEM and FESEM 47
2.5.3 Spectral Characteristics 48
2.5.3.1 Fourier Transformed Infrared (FTIR) Spectroscopy 48
2.5.3.2 Raman Spectroscopy 49
2.5.4 Cell Fabrication 49
2.5.4.1 Battery 49
2.5.4.2 Supercapacitor 51
2.5.5 Electrical and Electrochemical Tests 52
2.5.5.1 Electrochemical Impedance Spectroscopy (EIS) 52
2.5.5.2 Distribution of Relaxation Time (DRT) Analysis 53

2.5.5.3 Linear Sweep Voltammetry (LSV) 54
2.5.5.4 DC Polarization 54
2.5.5.5 Galvanostatic Charge-Discharge of Full Cells 55
2.5.5.5 Symmetric Cell Cycling 55
2.5.5.7 Electrochemical Ageing Test 56
2.5.6 Thermal and Safety Studies 56
2.5.6.1 Thermogravimetric and Differential Thermal Analysis 56
2.5.6.2 Thermal Shrinkage 57
2.5.6.3 Flame Test 57
2.5.6.4 Self-extinguishing Time (SET) Measurement 57
2.5.6.5 Thermal Shutdown Property 58
2.5.6.6 Thermal Shock Treatment 58
2.5.7 Data Analysis and Validation 58
2.6 Flow of Work 59
References 59

Chapter 3 61-101
Conversion of Paper into Paper Separator

Highlights, Summary and Graphical Abstract 61
3.1 Background and Overview 62
3.2 Fabrication of Paper Separators 63
3.3 Results and Discussion 65
3.3.1 $BaTiO_3$ Impregnated Paper Separator 65
3.3.1.1 Microstructural Details 65
3.3.1.2 Porosity and Electrolyte Wettability 68
3.3.1.3 Mechanical Properties 72
3.3.1.4 Ionic Conductivity 73
3.3.1.5 Electrochemical Tests 74
3.3.1.5.1 In Lithium-ion Battery 74
3.3.1.5.2 In Supercapacitor 79
3.3.1.6 Thermal Properties and Safety Studies 80
3.3.2 SiO_2 Impregnated Paper Separator 84
3.3.2.1 Microstructural Features 84
3.3.2.2 Porosity and Electrolyte Wettability 85
3.3.2.3 Mechanical Properties 88
3.3.2.4 Electrochemical Potential Window and Ionic Conductivity 89
3.3.2.5 Electrochemical Tests 91
3.3.2.6 Thermal Study and Safety Tests 94

3.4 Conclusion 98
References 99

Chapter 4 101-127
Tri-layer Paper Separator: Reduction of Thickness and Performance Enhancement

Highlights, Summary and Graphical Abstract 101
4.1 Background and Overview 102
4.2 Separator Fabrication Process 103
4.3 Results and Discussion 105
4.3.1 Microstructural Features 105
4.3.2 Air permeability, Porosity and Electrolyte Wettability 106
4.3.3 Mechanical Properties and Thermal Shrinkage Test 109
4.3.4 Electrical Properties 112
4.3.4.1 Ionic Conductivity 112
4.3.4.2 Electrochemical Potential Window 113
4.3.5 Electrochemical Tests 113
4.3.5.1 Full Cell Performance 113
4.3.5.2 Multi-cathode Compatibility of the Separators 116
4.3.5.3 Electrochemical Performance in Supercapacitors 117
4.3.6 Calendar Ageing Test 118
4.3.7 Thermal Safety 122
4.3.6.1 Thermogravimetric Analysis 122
4.3.6.2 Flame Safety Test 123
4.3.6.3 Electrochemical Cycling at Elevated Temperatures 123
4.4 Conclusion 124
References 126

Chapter 5 128-149
Surface Charge-Directed Ceramic Impregnation in Cellulose Paper Separators

Objectives, Summery and Graphical Abstract 128
5.1Background and Overview 129
5.2 Separator Fabrication Process 130

5.3 Results and Discussion 131
5.3.1 Microstructural Features 131
5.3.2 Air permeability, Pore Characteristics and Electrolyte Uptake 134
5.3.3 Mechanical Properties and Flexibility 136
5.3.4 Electrical Properties 138
5.3.5 Electrochemical Tests 140
5.3.5.1 Full Cell Performance 140
5.3.5.2 Pre- and Post-electrochemical EIS Study 142
5.3.5.3 Multi-electrode Compatibility of the Separators 144
5.3.6 Thermal Safety Tests 145
5.4 Conclusion 147
References 148

Chapter 6 150-168
Effect of Chelated ZrO_2 in Paper Separator

Highlights, Summary and Graphical Abstract 150
6.1 Background and Overview 151
6.2 Experimental Details 152
6.2.1 Preparation of Chelated Zirconia Precursor 152
6.2.2 Fabrication of Paper Separators 153
6.3 Results and Discussion 154
6.3.1 Properties of the Zirconia Sol 154
6.3.2 Structural and Microstructural Properties of the Fabricated Separators 155
6.3.3 Porosity, Wettability and Mechanical Properties of the Separators 159
6.3.4 Ionic Conductivity and Electrochemical Potential Window 161
6.3.4 Electrochemical Performance 164
6.4 Conclusion 167
References 167

Chapter 7 169-187
Montmorillonite Clay Impregnated Sustainable Paper Separator

Highlights, Summary and Graphical Abstract 169
7.1 Background and Overview 170
7.2 Experimental Details 171

7.2.1 Preparation of MMT Clay 171
7.2.2 Fabrication of Paper Separator 171
7.3 Results and Discussion 172
7.3.1 Structural and Microstructural Features 172
7.3.1.1 MMT Clay 172
7.3.1.2 MMT-incorporated Paper Separators 174
7.3.2 Pore Characteristics and Electrolyte Wettability 176
7.3.3 Separator Flexibility and Mechanical Properties 178
7.3.4 Ionic Conductivity and Electrochemical Stability Window 179
7.3.5 Electrochemical Performance 181
7.3.6 Thermal Safety Tests 182
7.4 Conclusion 185
References 186

Chapter 8 188-217
Active Ceramic Impregnated Paper Separators for High-Performance LIBs

Objectives, Summary and Graphical Abstract 188
8.1 Background and Overview 189
8.2 Experimental Details 190
8.2.1 Preparation of Cubic LLZO 190
8.2.2 Fabrication of Paper Separators 190
8.3 Results and Discussion 191
8.3.1 Structural, Microstructural and Surface Properties of LLZO Powder 191
8.3.2 Microstructural Features of the Developed Separators 193
8.3.3 Air permeability, Electrolyte Wettability and Mechanical Properties 195
8.3.4 Electrical Properties 198
8.3.5 Electrochemical Performance 200
8.3.6 Multielectrode Compatibility 203
8.3.7 Thermal, Flame-Retardant, and Shock-Resistant Properties 208
8.4 Conclusion 215
References 215

Chapter 9 218-247
Composite Solid Polymer Electrolytes for Paper-Supported Solid-State Li-metal Batteries

Objectives, Summery and Graphical Abstract 218
9.1 Background and Overview 219
9.2 Fabrication Process 220
9.2.1 Development of CSPEs 221
9.2.2 Development of Paper-based CSPEs (p-CSPEs) 222
9.3 Results and Discussion 222
9.3.1 Structural, Microstructural and Mechanical Features 222
9.3.2 Electrical Properties 229
9.3.3 Electrochemical Tests 234
9.3.4 Thermal Properties 241
9.4 Conclusion 244
References 244

Chapter 10 248-258
Conclusion and Future Perspectives

Graphical Overview and Summary 248
10.1 Conclusions 249
10.2 Key Insights 255
10.3 Future Perspectives 256
10.4 Technical Specifications of Paper-based Ceramic Separator 259

Appendix-I (List of Publications, conference papers and awards) 260

Reprints of Published Works

List of Figures

Figure 1.0 Graphical representation of broader motivation of the thesis

Figure 1.1 Transition from IC engine vehicles to electric vehicles

Figure 1.2 (a) Intercalation mechanism of a typical lithium-ion cell [adapted from the idea 61], (b) chemical processes taking place during charge and discharge

Figure 1.3 Schematic representation of evolution of separator technology

Figure 1.4 Various complex processes that a separator undergoes inside an electrochemical cell [reproduced with permission from 40]

Figure 1.5 The different properties of a separator membrane that need to be tuned for its successful functioning [reproduced with permission from 41]

Figure 1.6 Ionic conductivity vs discharge capacity for various polymer membranes, mostly used as battery separators [reproduced with permission from 43]

Figure 1.7 Thermal shutdown of a battery shown schematically, where separator play a critical role [reproduced with permission from 50]

Figure 1.8 Cost comparison of LIB components and manufacturing process parameters

Figure 1.9 A schematic diagram showing different cellulosic materials having potential to be functionalized as battery separator, along with cellulose structure and its advantages55

Figure 1.10 Summary of various scientific and technological applications of paper

Figure 1.11 Current separator market in India for electric vehicles, along with the key market leaders [source: report by Mordor Intelligence]

Figure 1.12 Trend of the research in separator for last 10 years (source: web of science)

Figure 1.13 Visual summary of the roadmap of the thesis

Figure 2.0 Flow of the experimental works done under the scope of this research

Figure 2.1 Digital image of the in-house designed separator fabricating semi-automated double-decker machine; (A) feeding zone for cellulose based locally outsourced commercial paper roll, (B) coating chamber, (C) Infrared thermal zone for drying at upper cabinet, (D) Infrared thermal zone for drying at lower cabinet and (E) final separator product in roll form

Figure 2.2 Process flow chart along with schematic representation of paper separator fabrication process

Figure 2.3 Schematic representation of the fabrication process of CSPEs

Figure 3.0 Sustainable and eco-friendly components used for fabrication of paper separator

Figure 3.1 Micrographs of (a) Commercial PPCom separator, (b) Untreated paper substrate, (c) EDX spectrum of untreated paper along with corresponding micrograph in the inset

Figure 3.2 FESEM micrographs of (a) C25PV1BT01 (b) C25PV2BT01 (c) C25PV4BT01 and (d) C25PV6BT01 showing lamination effect on increasing concentration of PVA

Figure 3.3 (a) & (b) FESEM micrographs of C25PV1BT01 separator and (c) & (d) FESEM micrographs of C25PV1BT15 separator

Figure 3.4 Typical EDX spectrum and its corresponding elemental map showing the presence of Ba, Ti and O in fabricated separator C25PV2BT01

Figure 3.5 Time dependent liquid uptake capability of fabricated paperators and commercial separator

Figure 3.6 Digital pictures of fabricated paperators ((a) C25PV1BT01, (b) C25PV1BT05, (c) C25PV1BT10 and (d) C25PV1BT15) showing electrolyte soaking ability at different time interval along with PPCom

Figure 3.7 Digital images of contact angle of the separators (PPCom, C25PV1BT01, C25PV1BT05, C25PV1BT10, C25PV1BT15 and untreated paper substrate) with liquid electrolyte along with their values of commercial separator

Figure 3.8 Plots of load vs extension of paperators, untreated paper, commercial separator (PPCom); The inset shows the expanded view of load vs extension plots of untreated paper and fabricated paper separators

Figure 3.9 Nyquist plots of developed paperators along with PPCom; Inset shows the enlarged view of the plots

Figure 3.10 Initial charge-discharge profiles of fabricated separators by varying concentration of (a) BTO (0.1-1.5 w/v %), (b) PVA (1.0-6.0 w/v %) and (c) Chitosan (0.25-1.0 w/v %)

Figure 3.11 Charge-discharge capacities against cycle number plot of C25PV1BT01, C25PV1BT05, C25PV1BT10 and C25PV1BT15; the corresponding coulombic efficiencies are also plotted w.r.t right Y-axis

Figure 3.12 Capacity vs cycle number plots for paperator (C25PV1BT01), commercial membrane (PPCom) and untreated paper substrate at different current densities (0.1-0.4 mA.cm-2)

Figure 3.13 Electrochemical charge-discharge performance of paperators C25PV1BT01, C25PV1BT15 along with Commercial PPCom against (a) $LiMn_2O_4$ and (b) $LiCoO_2$ cathodes and MCMB anode

Figure 3.14 Typical constant current charge-discharge (CDC, @200 mA) patterns of selected supercapacitors, fabricated by using (a) paperator and (b) commercial cellulose-based paper (NKK, Japan)

Figure 3.15 TGA curves of (a) untreated paper, (b) commercial separator and (c) C25PV1BT01

Figure 3.16 (a)-(h) Image showing thermal stability and dimensional shrinkage from RT-200ºC at every 25ºC interval and holding time 10 minutes at each temperature for Paperators (above the scale) and Commercial Separator (below the scale); the paper separator samples were placed above the scale based on increasing ceramic loading (from left to right) i.e., C25PV1BT01, C25PV1BT05, C25PV1BT10 and C25PV1BT15

Figure 3.17 Digital images of Paperator (C25PV1BT01) and Commercial separator (PPCom), taken during Flame Test (Combustion) as well as before and after ignition

Figure 3.18 FESEM images of fabricated paper separators; (a1-a3) CPS01 and (b1-b3) CPS15 taken in different magnifications

Figure 3.19 (a) Variation of contact angle with increasing ceramic load, (b) Comparison of contact angle of CPS01 and CPS15 with respect to PP, (c) Electrolyte volume uptake capability of different ceramic loaded paper separators (CPS01, CPS05, CPS10 and CPS15), (d)

Time dependent liquid retention plot of developed paper separator along with commercial PP separator

Figure 3.20 Time dependent electrolyte soaking ability of paper separators with varying ceramic loading (a) CPS01, (b) CPS05, (c) CPS10 and (d) CPS15 along with PP

Figure 3.21 Load vs Extension plot of fabricated Separators, untreated paper (UP) and commercial separator (PP) at machine direction (MD)

Figure 3.22 (a) Current vs Potential plot of Li/Separator/SS asymmetric cells using electrolyte soaked UP, PP and paper separators (b) Impedance plot of symmetric cell with configuration of SS/Separator/SS using developed paper separators, UP and PP soaked in $LiPF_6$ in EC:DMC (1:2)

Figure 3.23 Electrochemical performance of developed paper separators; (a) Initial charge- discharge profiles, (b) Cycle number vs step current density plot of CPS01, CPS05, CPS10 and CPS15, (c) Cycling profiles at a current density of 0.2 mA/cm^2 along with their corresponding coulombic efficiencies of developed paper separators: CPS01, CPS05, CPS10 and CPS15, (d) Comparison of capacity vs cycle no. plot between fabricated paper separator (CPS15) and commercial PP separator, and (e) Average capacity vs current density plot of CPS15 and Commercial separator (PP)

Figure 3.24 Typical charge-discharge profiles of 2032 cells made with commercial cathodes ($LiFePO_4$, $LiCoO_2$ and $LiMn_2O_4$) and MCMB anode. Separators used are commercial polymer (PP) and paper separators CPS01, CPS05, CPS10 and CPS15 as developed in this investigation

Figure 3.25 TGA/DTA plot of paper separator, untreated paper (UP) and Commercial Separator (PP), (b) Intra and inter H-bonding network in cellulose-chitosan and PVA and (c) comparative study of thermal shrinkage with commercial PP separator and fabricated paper separators (CPS01, CPS05, CPS10 and CPS15) at different temperatures (Room Temperature to 200ºC)

Figure 3.26 DSC thermogram of fabricated separators (CPS01 and CPS15), untreated paper and commercial PP based separator from RT to 400ºC at heating ramp of 10ºC/min in inert atmosphere

Figure 3.27 Digital images taken during flame test at different time intervals for PP and developed paper separator, CPS15; the source of continuous flame is a gas lighter

Figure 4.0 Schematic representation of the tri-layer paper separator matrix

Figure 4.1 FESEM micrographs of (a) untreated paper (UP), (b) P35 separator obtained after sizing, (c) P35SB7BT20 separator after ceramic impregnation, (d) P35SB7BT20SB2 separator after laminating with 2 w/v% SBR, (e) selected area elemental mapping by EDX of separator P35SB7BT20, (f) & (g) A schematic representation of cellulosic fiber and its elementary microfibrils is displayed along with FESEM images taken on P35 sized separator

Figure 4.2 (a) Air permeability values in terms of Gurley seconds (per 100 cc air) of untreated paper and fabricated paper separators, (b) comparison of electrolyte wettability of untreated paper and fabricated separators with commercial PP (red dotted line)

Figure 4.3 Contact angles measured using standard electrolyte solution for (i) PP, (ii) P35SB7BT20SB1, (iii) P35SB7BT20SB2 and (iv) P35SB7BT20SB3 with respect to time

Figure 4.4 Load vs extension curve (a) in machine direction (MD) and (b) in transverse direction (TD). (c) Digital images of thermal shrinkage up to 200oC for the separator specimen

with code (a) P35, (b) P35SB7BT20, (c) P35SB7BT20SB1, (d) P35SB7BT20SB2, (e) P35SB7BT20SB3, (f) UP and (g) commercial PP based separator

Figure 4.5 Comparison Plots of Tensile Properties

Figure 4.6 (a) Nyquist plot of fabricated paper separators, (b) electrochemical stability window of fabricated paper separators at scan rate 2.44 mV/s; Electrochemical cell performance in 2032 coin type cell fabricated with MCMB anode, $LiPF_6$ (EC/DMC) liquid electrolyte soaked separators and $LiFePO_4$ cathode (c) initial charge-discharge profiles of UP, commercial PP along with fabricated separators (d) cycleability plot at current density of 0.2 mA/cm^2 and (e) cycling performance of UP, P35 and fabricated separators at current densities in the range of 0.1-0.8 mA/cm^2

Figure 4.7 Capacity vs cycle number plot of fabricated separator- P35SB7BT20SB2 up to 300 cycles. The Y axis represents the columbic efficiency values in each charge-discharge cycle. Each plot from left to right represents the cycle numbers ranging from (a) 1-100th, (b) 101-200th and (c) 201-300th

Figure 4.8 Multi-cathode Compatibility: typical charge-discharge profiles of paper separator (P35SB7BT20SB2) against (a) $LiMn_2O_4$, (b) $LiFePO_4$ and (c) NCM111

Figure 4.9 Multi-cathode Compatibility: Capacity vs cycle number profiles of paper separator (P35SB7BT20SB2) against $LiMn_2O_4$ and NCM111 with step current density

Figure 4.10 Typical constant current charge-discharge (CDC @260 mA) patterns of SCs, made with (a) developed paper separator (N1-SC-UTPS & N2-SC-UTPS) and NKK branded commercial paper separator (N3-SC-NKK & N4-SC-NKK), carried out as per IEC 62391-1 (Class-II) by using the supercapacitor testing system. Inset represents the enlarged portion of CDC patterns during the constant current pulsing stage for measuring cell ESR of SCs

Figure 4.11 (a) Nyquist plot of full cell (Configuration: MCMB/Sep/LFP) fabricated with paper separator P35SB7BT20SB2 during calendar aging (0-8 weeks), (b) Time dependent plot of electrolyte resistance (Re) and charge transfer resistance (R_{ct}) of symmetrical cell fabricated with the developed separator and (c) Nyquist plot taken at regular interval reflecting changes in bulk impedance of paper separator P35SB7BT20SB2 during calendar aging

Figure 4.12 FESEM micrographs of anode facing surface of (a)-(a1) as fabricated and (b)-(b1) aged cell dismantled after 8 weeks; FESEM micrographs of cathode facing surface of [(c)-(c1)] as fabricated and (d)-(d1) aged separator after 8 weeks, Corresponding selected area EDX profile of anode facing (a2-b2) and cathode facing surfaces (c2-d2) for both as-fabricated and aged separators, (e) A schematic illustration of phosphorous containing material deposition on separator surfaces after aging

Figure 4.13 TGA plot of paper separators samples; inset showing the differential weight loss from room temperature to 600°C

Figure 4.14 Digital images taken during vertical flame test for both untreated (above) and functionalized paper separator (below)

Figure 4.15 A comparison of electrochemical performance of composite separator (P35SB7BT20SB2) with that of Commercial PP/PE based separator membrane at elevated temperatures RT-80°C

Figure 5.1 (a)-(b) FESEM images of bare cellulose paper (CP) and (c)-(d) FESEM images of commercial separator (PP)

Figure 5.2 (a)-(b) FESEM images of Al_2O_3 impregnated paper separator (P3S7A2) in low and high magnification respectively; (c)-(d) FESEM images of $BaTiO_3$ impregnated paper separator (P3S7B2) in low and high magnification respectively; (e)-(f) FESEM images of ZrO_2 impregnated paper separator (P3S7Z2) in low and high magnification respectively

Figure 5.3 EDX profiles of (a) P3S7A2, (b) P3S7B2 and (c) P3S7Z2 separators

Figure 5.4 (a) Gurley values and electrolyte uptake capabilities; (b) time dependent contact angles measured for developed paper separators (P3S7A2, P3S7B2 and P3S7Z2); (c) Variation of pore diameter with respect to separator compositions (BJH method)

Figure 5.5 The flexibility and mechanical properties of the developed paper separators: (a)-(c) a strand of paper separator showing utmost flexibility; (d)-(e) load vs extension curves of paper separators (P3S7A2, P3S7B2 and P3S7Z2) along with the untreated cellulose paper (CP) both in machine and transverse directions respectively

Figure 5.6 Electrical properties of the developed paper separators along with the commercial separator: (a) ionic conductivity, (b)electrochemical potential window, (c) Li-ion transference number for PP, (d) Li-ion transference number for P3S7A2, (e) Li-ion transference number for P3S7B2, (f) Li-ion transference number for P3S7Z2

Figure 5.7 Electrochemical properties of the developed paper separators in 2032coin cell with the configuration of NMC111/Separator/MCMB: (a) typical charge-discharge profiles at a low current density i.e., 0.05 $mAcm^{-2}$, (b) cycling performance at different current densities i.e., 0.1-1.2 $mAcm^{-2}$, (c) long cycling test at 0.2 $mAcm^{-2}$, (d) analysis of the long cycling plot for PP, P3S7A2, P3S7B2 and P3S7Z2 separators

Figure 5.8 Pre- and post-electrochemical impedance spectra of (a) P3S7A2, (b) P3S7B2 and (c) P3S7Z2 along with their equivalent circuit and enlarged view of profiles in the inset; The variation of different impedance components is displayed against paper separator compositions:(d) electrolyte resistance, (e) SEI resistance and (f) charge transfer resistances

Figure 5.9 Multielectrode compatibility of commercial and developed paper separators showing (a)-(c) typical charge-discharge profiles and (d)-(f) cycling performances with respect to different electrodes ($LiMn_2O_4$/Separator/MCMB, $LiFePO_4$/Separator/MCMB and $LiFePO_4$/Separator/$Li_4Ti_5O_{12}$)

Figure 5.10 Thermal behaviour of the developed paper separators: qualitative thermal shrinkage measurement (a) at room temperature and (b) at 200ºC; (c) & (d) flame safety test of the developed separators along with the commercial one; (e) thermogravimetric analysis (TGA) plot and differential thermal analysis (DTA) plot (inset of e); (f) Thermal shutdown properties via EIS method

Figure 6.0 Graphical representation of the chapter content

Figure 6.1 Proposed reaction mechanism of ZIP during preparation of zirconia sol

Figure 6.2 ATR-FTIR spectra of zirconia sol

Figure 6.3 X-ray Diffraction (XRD) patterns of all the developed paper separators (HY00, HY05, HY10, HY15, HY20 and HY25), along with pristine cellulose paper (CP)

Figure 6.4 Fourier Transformed Infrared (FTIR) Spectra in ATR mode for HY00, HY05, HY10, HY15, HY20, HY25 and CP

Figure 6.5 FESEM micrographs (a)-(b) HY05 and (d)-(e) HY25; EDX profiles of (c) HY05 and (f) HY25, respectively

Figure 6.6 (a) Contact angle in LIB liquid electrolyte (1M $LiPF_6$ in EC:DMC (1:2)), (b) Air permeability in terms of Gurley value and electrolyte uptake percentage, (c) flexibility of the developed paper separators demonstrated via stretching and bending activities, (d) demonstration of separator flexibility; Tensile stress vs tensile strain plots at (e) machine direction (MD) and (f) transverse direction (TD) for CP, HY00, HY05, HY10, HY15, HY20 and HY25, respectively

Figure 6.7 Nyquist plots for all the developed paper separators along with CP

Figure 6.8 Linear Sweep Voltammetry plots for HY00 and HY15, for determining electrochemical potential window

Figure 6.9 Galvanostatic charge-discharge cycling of HY00 and HY15 in MCMB/LFP full cell configuration; (a) long term cycling at 0.2 $mA.cm^{-2}$, (b) cycling at varying current densities for HY00 and (c) cycling at varying current densities for HY15

Figure 7.0 A graphical demonstration of paper-clay separator

Figure 7.1 Structural and microstructural features of Na-MMT powder; (a) X-ray diffraction pattern, (b) FTIR spectrum, (c) FESEM image and (d) EDX spectrum

Figure 7.2 Structure of Na-MMT clay, as obtained using the standard JCPDS file

Figure 7.3 X-ray diffractogram of CP, M05 and M20

Figure 7.4 FESEM micrographs of (a) & (b) M05, (d) & (e) M20; EDX profiles of (c) M05, (f) M20

Figure 7.5 (a) Air permeability in terms of Gurley value and electrolyte uptake, (b) BET adsorption isotherm for M05, M10, M15 and M20

Figure 7.6 Mechanical integrity of the developed separators: (a) bending and twisting experiments showing good flexibility; Tensile stress vs tensile strain curves along (b) machine direction and (c) transverse direction for M05, M10, M15, M20 and CP

Figure 7.7 Electrical properties: (a) Nyquist plots and (b) LSV plots for M05, M10, M15 and M20 along with commercial PP

Figure 7.8 Typical galvanostatic charge-discharge cycles for M05, M10, M15 and M20 along with commercial PP-based separator in NMC111/MCMB cell configuration

Figure 7.9 Long cycling profiles for M05, M10, M15, M20 and PP in NMC111/MCMB cell configuration: charge and discharge capacity with coulombic efficiency

Figure 7.10 Thermogravimetric analysis of the developed separators along with commercial cellulose paper; TGA plots along with the DTA curves in inset

Figure 7.11 Digital images of various stages of the self-extinguishing time measurement for (a)-(c) M15 and (d)-(f) PP

Figure 7.12 Typical galvanostatic charge-discharge cycles for (a) PP and (b) M15 before and after SET test

Figure 8.0 Graphical abstract illustrating effect of LLZO impregnation in the cellulose matrix

Figure 8.1 (a)-(c) describes X-ray diffractogram, FTIR spectra and Raman spectra of LLZO powder calcined at 900°C respectively; (d) FESEM image of LLZO calcined powder; (e) Particle size distribution of LLZO powder calculated from the micrograph; (f) particle size

distribution pattern of LLZO powder; Measured Zeta potential of (g) commercial cellulose paper and (h) LLZO powder

Figure 8.2 FESEM micrographs of (a) P5L01, (b) P5L03, (c) P5L05, (d) P5L07, (e) P5A03 and (f) PP with their higher magnification images in the insets and EDX profiles of (g) P5L03 and (h) P5A03

Figure 8.3 (a) Gurley values and electrolyte uptake capabilities of our developed separators and the corresponding contact angle measurement was provided in the inset for each separator; Tensile stress vs tensile strain plot of developed paper-based separator in (b) machine direction (MD) and (c) transverse direction (TD)

Figure 8.4 Electrical properties of developed paper separator along with the commercial separator, (a) EIS spectra along with the corresponding equivalent circuit of SS/Separator/SS cell for measurement of ionic conductivity, (b) Current vs Potential sweep voltammetry (LSV) for measurement of electrochemical potential window, (c) Lithium-ion transference number (t_{Li^+}) calculated using Bruce-Vincent-Evans equation, DC polarization with the EIS spectra before and after polarization along with its corresponding equivalent circuit in the inset for (d) P5L03, (e) P5A03 and (f) PP respectively

Figure 8.5 Electrochemical characterizations of all the developed paper separators (P5L01, P5L03, P5L05, P5L07 and P5A03) as well as of the commercial separator (PP): (a) typical charge-discharge profiles, (b) capacity vs cycle number plots with varying current densities from 0.1 $mA.cm^{-2}$ to 0.8 $mA.cm^{-2}$ in (b1) forward and (b2) reverse directions, (c) summary of average capacity loss or gain in different current densities, (d) long cycling profiles and (e) their summary for the different separators, (f) EIS spectra of MCMB/P5L03/LFP cell before cycling (BC) and after cycling (AC), (g) EIS spectra of MCMB/P5A03/LFP cell before cycling and after cycling, (h) summary plot of change in different type of resistance values before and after cycling

Figure 8.6 Electrochemical compatibility of developed paper separators (P5L03, P5A03) and commercial separator (PP) with LTO anode and different cathodes; showing typical charge discharge profile and long cycling behavior against (a) & (b) LCO, (c) & (d) LMO, (e) & (f) LFP and (g) & (h) NCM respectively

Figure 8.7 Electrochemical compatibility of developed paper separators (P5L03, P5A03) and commercial separator (PP) with MCMB anode and different cathodes; showing typical charge discharge profile and long cycling behavior against (a) & (b) LCO, (c) & (d) LMO, (e) & (f) LFP and (g) & (h) NCM respectively.

Figure 8.8 (a) Thermogravimetric Analysis (TGA) plots of the developed paper separators (P5L01, P5L03, P5L05, P5L07 and P5A03) with their Differential Thermal Analysis (DTA) plots in the inset; (b) Qualitative thermal shrinkage analysis of the developed paper separators and commercial PP separator at room temperature (RT) and at 200ºC (30 min at each temperature); (c) Flame test for P5L03, P5A03 and PP

Figure 8.9 (a) Visualization of self-extinguishing time (SET) test for P5L03, P5A03 and PP separators; (b) Electrochemical long cycling of the separators before and after SET in MCMB/separator/LFP configuration; Typical charge-discharge profiles before and after SET for (c) PP, (d) P5L03 and (e) P5A03

Figure 8.10 Investigation of electrochemical and electrical properties of paper based develop separator along with commercial separator under vigorous thermal treatment; (a) & (b) Potential vs time plot after thermal shock treatment at two different temperature and

corresponding changes in EIS spectra after cycling for P5L03 respectively. (c) & (d) Potential vs time plot after thermal shock treatment at two different temperature and corresponding changes in EIS spectra after cycling for P5A03 respectively. (e) & (f) Potential vs time plot after thermal shock treatment at two different temperature and corresponding changes in EIS spectra after cycling for P5L03 respectively. (g) Cycling behavior of developed separator and commercial PP separator after thermal shock treatment. (h) Thermal shutdown measurement by EIS method with temperature variation for P5L03, P5A03 and PP.

Figure 9.0 Graphical abstract

Figure 9.1 (a) Digital images of the four developed membranes; (b) Schematic representation of the orientation of polymer, Li-salt, and ceramic nanoparticles inside the CSPEs

Figure 9.2 Microstructural features of the developed CSPEs: Low and high magnification FESEM images of (a) & (b) PL, (d) & (e) PLA, (g) & (h) PLB (j) & (k) PLZ; EDX profile of (c) PL, (f) PLA, (i) PLB, (l) PLZ

Figure 9.3 Elemental mapping from EDX for (a) PLA, (b) PLB, and (c) PLZ: (a1), (b1) and (c1) are the selected area from SEM for EDX analysis, (a2) and (a3) mapping for Al and O, (b2) and (b3) mapping for Ba and Ti, (c2) and (c3) mapping for Zr and O, respectively

Figure 9.4 X-ray diffraction patterns, (b) XRD peak corresponding to PVDF-HFP, (c) FTIR spectra, (d) Tensile stress vs tensile strain curves, (e) Summary of tensile strength for PL, PLA, PLB and PLZ; (f) Tensile stress vs tensile strain profiles for PLZ05, PLZ10 and PLZ15, (g) Summary of tensile strength values for PLZ05, PLZ10 and PLZ15

Figure 9.5 (a) X-ray diffractograms of PELZ and paper-based PELZ (p-PELZ), (b) & (c) FESEM micrographs of p-PELZ at lower and higher magnifications, respectively

Figure 9.6 Variation of electrical properties with respect to ZrO_2 variation in the CSPEs named as PLZ05, PLZ10 and PLZ15; (a) Nyquist plots at 303K, (b) Arrhenius plots, (c) Summary plot consisting of ionic conductivity for the three CSPEs at 303K along with their activation energy; Nyquist plots at temperatures ranging from 303 K to 363 K for (d) PLZ05, (e) PLZ10, and (f) PLZ15

Figure 9.7 Electrical properties of PL, PLA, PLB, and PLZ: (a) Nyquist plots at 30ºC, (b) Arrhenius plots, (c) Summary plot of ionic conductivity and activation energy, (d) - (f) Nyquist plots in the temperature range of 30-90°C for PL, PLA and PLB, respectively, (g) Linear Sweep Voltammetry (LSV) plots, for PL, PLA, PLB, and PLZ, (h) DC polarization of Li/PLZ/Li cell, (i) Summary of Li-ion transference numbers for all the four developed CSPEs

Figure 9.8 (a) Nyquist plots and (b) Arrhenius plots for PELZ and p-PELZ

Figure 9.9 (a) Voltage vs time profiles for Li/Li symmetric cells of PL, PLA, PLB, and PLZ at 60ºC, (b) Nyquist plot of all the developed CSPEs in Li/Li symmetric cells for the variation of electrolyte-metal interface resistance, EIS spectra before and after long-term cycling for (c) PL, (d) PLA, (e) PLB, and (f) PLZ, (g) Variation of interfacial resistance for developed CSPEs before and after a long cycling test

Figure 9.10 (a), (b) Nyquist plots of Li/PLZ/Li and Li/PL/Li symmetric cells during cycling up to 60 h. (c), (d) Corresponding DRT spectra at various cycling times, decoupling the contributions from electrolyte resistance, SEI resistance, charge transfer, and diffusion processes. (e), (f) 2D contour plots of DRT intensity vs. time show the stable interfacial kinetics for PLZL composite and unstable SEI for bare PL electrolyte

Figure 9.10 (a), (b) and (c) Typical charge-discharge profiles of Li/LFP cells of PL, PLA, PLB, and PLZ at 0.05, 0.10 and 0.20 $mA.cm^{-2}$ current densities respectively; (d) Comparison among specific discharge capacities of the different CSPEs in the three current densities; (e) Specific capacity vs cycle number plot of Li/PLZ/LFP cell along with coulombic efficiency; (f) Comparison of Nyquist plots for as fabricated Li/LFP cells of PL, PLA, PLB and PLZ

Figure 9.11 Thermal studies of the developed CSPEs: (a) Thermogravimetric Analysis (TGA) plots; (b) Differential Thermal Analysis (DTA) plots; Flame safety tests for (c) PL, (d) PLA, (e) PLB, and (f) PLZ at 0 and 30 seconds

Figure 9.12 Full cell performance in paper-based LFP/p-CSPE/paper-based MCMB configuration

Figure 9.13 Stable Li plating-stripping for 1200h without any short-circuit

Figure 9.14 Thermal studies of the developed CSPEs: (a) Thermogravimetric Analysis (TGA) plots; (b) Differential Thermal Analysis (DTA) plots; Flame safety tests for (c) PL, (d) PLA, (e) PLB, and (f) PLZ at 0 and 30 seconds

Figure 10.0 Graphical overview of the research works conducted under this thesis and their major outcomes

List of Tables

Table 1.1 Ideal values of the main parameters of lithium-ion battery separators, their relevance in battery performance and the typical experimental techniques for their determination

Table 2.1 Details of the materials and chemicals used in the research

Table 3.1 Compositions of the separators and their corresponding codes

Table 3.2 Thickness, Gurley value air permeability and tensile properties of developed paper separators, untreated paper and commercial separator

Table 3.3 Discharge capacities of fabricated paperators along with their compositions

Table 3.4 Comparison of mechanical performance properties of fabricated paper separators with respect to commercial PP and UP, measured along machine direction

Table 3.5 Summary of specific discharge capacities (mAh/g) of different commercial cathodes achieved with separator PP and paper separators (CPS01, CPS05, CPS10 and CPS15)

Table 4.1 Summary of mechanical properties of the developed paper separators

Table 4.2 Literature study and comparison of other relevant research work with this chapter work

Table 5.1 Average specific capacity of 20 cycles for PP, P3S7A2, P3S7B2 and P3S7Z2 at various current densities ranging from 0.1-1.2 $mA.cm^{-2}$

Table 5.2 Values of electrolyte resistance, SEI resistance and charge-transfer resistance before and after electrochemical cycling for the NMC111/Separator/MCMB cells comprising the three developed paper separators i.e., P3S7A2, P3S7B2 and P3S7Z2

Table 5.3 3 Comparison chart of different properties of the developed paper separators (P3S7A2, P3S7B2 and P3S7Z2)

Table 6.1 Composition and codes for different paper separators developed under this study

Table 6.2 Comparison of different properties of the chelated zirconia embedded paper separators with those of commercial cellulose paper

Table 6.3 Literature review of Lewis acid-base interaction-driven performance modulation of electrochemical systems by various strategies

Table 7.1 Codes and compositions of the developed paper-clay separators

Table 8.1 Nomenclature of various composite paper separator developed in this study

Table 8.2 A summary of different physical parameters of our developed paper separators

Table 8.3 A summary of different electrical and electrochemical parameters of P5L01, P5L03, P5L05, P5L07, P5A03 and commercial PP separators

Table 8.4 A summary of electrochemical performances of three different separator (P5L03, P5A03 and PP) during multi electrodes compatibility test

Table 8.5 An overview of different behavior observed for P5L03, P5A03 and PP separator during thermal stability test

Table 8.6 Comparison of Li-ion active ceramic-coated separators and their key properties

Table 9.1 Composition of the developed CSPEs along with the codes assigned to them

Table 9.2 Li-ion transference number and corresponding EIS test results of the CSPEs

Table 9.3 Comparison among various properties of passive ceramic filler-based composite solid polymer electrolytes for solid-state lithium batteries

ABBREVIATIONS

Abbreviation and Symbol	Full Form
LIB	Lithium-Ion Battery
SIB	Sodium-Ion Battery
SC	Supercapacitor
HESS	Hybrid Energy Storage System
PHS	Pumped Hydro Storage
TES	Thermal Energy Storage
SDGs	Sustainable Development Goals
LCO	Lithium Cobalt Oxide
LFP	Lithium Iron Phosphate
NMC	Lithium Nickel Manganese Cobalt Oxide
NCA	Lithium Nickel Cobalt Aluminum Oxide
LMO	Lithium Manganese Oxide
LTO	Lithium Titanate
MCMB	Mesocarbon Microbeads
SEI	Solid Electrolyte Interphase
EC	Ethylene Carbonate
DMC	Dimethyl Carbonate
DEC	Diethyl Carbonate
PC	Propylene Carbonate
$LiPF_6$	Lithium Hexafluorophosphate
LiTFSI	Lithium bis(trifluoromethanesulfonyl)imide
PVDF	Polyvinylidene Fluoride
PVDF-HFP	Poly(vinylidene fluoride-co-hexafluoropropylene)
PEO	Polyethylene Oxide
PVA	Polyvinyl Alcohol
SBR	Styrene–Butadiene Rubber
NMP	N-Methyl-2-pyrrolidone
DMF	N,N-Dimethylformamide
FESEM	Field Emission Scanning Electron Microscopy
SEM	Scanning Electron Microscopy

EDX	Energy Dispersive X-ray Spectroscopy
FTIR	Fourier Transform Infrared Spectroscopy
XRD	X-ray Diffraction
TGA	Thermogravimetric Analysis
DTA	Differential Thermal Analysis
LSV	Linear Sweep Voltammetry
EIS	Electrochemical Impedance Spectroscopy
CCD	Critical Current Density
CE	Coulombic Efficiency
CI	Crystallinity Index
ESR	Equivalent Series Resistance
C_{eff}	Effective Capacitance
PP	Polypropylene
PE	Polyethylene
CP	Cellulose Paper
MMT	Montmorillonite
LLZO	Lithium Lanthanum Zirconium Oxide
Al_2O_3	Aluminum Oxide
$BaTiO_3$	Barium Titanate
ZrO_2	Zirconium Dioxide
SiO_2	Silicon Dioxide
ZIP	Zirconium Isopropoxide
acac	Acetylacetone
RT	Room Temperature
SET	Self-Extinguishing Time
R_e	Electrolyte Resistance
R_{ct}	Charge Transfer Resistance
R_b	Bulk Resistance
R_{SEI}	SEI resistance

Highlights of the Thesis

The present thesis addresses the pressing challenge of developing sustainable, cost-effective, and safe alternatives to conventional polyolefin-based separators in lithium-ion batteries (LIBs). Commercial separators made of polypropylene (PP) or polyethylene (PE) suffer from low thermal stability, limited electrolyte wettability, and originate from non-renewable resources, which collectively limit their performance and raise safety concerns. In contrast, natural cellulose paper, with its fibrous network, abundant availability, and eco-friendly origin, provides a compelling base material for constructing next-generation battery separators. This work systematically investigates cellulose paper and its functional modification with ceramic fillers, hybrid systems, and natural clays to achieve a new class of paper-based composite separators with enhanced thermal safety, ionic transport, and electrochemical stability.

Throughout the thesis, multiple strategies were explored to modify cellulose paper through scalable impregnation and coating processes. Inorganic fillers such as alumina (Al_2O_3), silica (SiO_2), and lithium-ion conducting garnets (LLZO) were incorporated to enhance structural reinforcement, electrolyte affinity, and interfacial stability. Organo–inorgano hybrid systems, derived from chelation of zirconium isopropoxide, were introduced to regulate lithium salt dissociation and optimize ionic conductivity. In parallel, montmorillonite (MMT) clay, a naturally abundant mineral with high ion-exchange capacity and strong flame-retardant properties, was employed to fabricate sustainable paper–clay separators. The combination of cellulose fibers with inorganic and hybrid domains gave rise to unique separators that demonstrated tunable porosity, controllable wettability, and robust thermal resistance.

The structural and morphological studies confirmed that the fillers were uniformly distributed within the paper matrix, creating a hierarchical network that maintained flexibility while enhancing dimensional stability. Electrochemical investigations revealed that these modifications improved ionic conductivity, broadened the electrochemical stability window beyond 5.0 V versus Li/Li^+, and reduced interfacial resistance compared to pristine paper and commercial PP separators. Full-cell evaluations, particularly with NMC111 cathodes and MCMB anodes, validated the superior performance of optimized paper composites, which delivered higher discharge capacities, stable long-term cycling, and excellent coulombic efficiency. Notably, separators impregnated with

MMT and LLZO outperformed the commercial PP membrane in both performance and safety metrics.

A crucial highlight of this work is the significant improvement in thermal safety. Thermogravimetric analysis demonstrated higher char yields and delayed decomposition for the composite separators, while flame-resistance tests established their rapid self-extinguishing ability. Unlike PP membranes, which undergo severe shrinkage and sustained combustion, the paper-based composites retained their morphology and functionality even after flame exposure. This was further corroborated by post-flame charge–discharge testing, where the clay-loaded paper separator maintained stable electrochemical behavior, demonstrating its reliability under extreme thermal stress.

Beyond performance, this thesis emphasizes sustainability and scalability. The use of cellulose and montmorillonite clay, both low-cost and abundantly available, ensures that the developed separators can be manufactured on an industrial scale using aqueous processing routes without compromising environmental responsibility. By aligning material innovation with global energy and environmental needs, the research establishes paper–clay and paper–ceramic separators as strong contenders for next-generation LIBs, offering a safer, greener, and more economically viable alternative to existing synthetic plastic membranes.

In summary, this thesis makes a comprehensive contribution to the design and development of cellulose-based composite separators for lithium-ion batteries. It demonstrates how the integration of natural polymers with functional inorganic fillers can overcome the limitations of current separators, achieving a synergistic balance between ionic transport, mechanical integrity, thermal stability, and cost-effectiveness. The findings not only enrich the scientific understanding of paper-based hybrid separators but also pave the way for their practical application in sustainable and high-performance energy storage systems.

Chapter 1

Introduction

Highlights

- Green Earth, E-Mobility, Sustainable Energy Storage - Global and Indian Perspectives
- Better Lithium Storage technologies, Cost and Sustainability
- Lithium Battery Components - Impact on Safety and Performance
- Focus on Separators - Background and Choice of Materials
- Cellulosic Materials as Separator
- Motivation and Pathways of Present Research

Figure 1.0 *Graphical representation of broader motivation of the thesis*

Sustainable energy storage devices have garnered recent research attention to meet both global sustainability goals and increasing demands for energy. Rechargeable batteries can balance these two quite well in terms of their high energy and power density, long cycle life and potential for using eco-friendly materials. Among the components critical to the performance, safety, and longevity of metal-ion and metal batteries as well as supercapacitors, separator plays a key but often underrepresented role. This thesis focuses on the development of cellulose paper-based composite separator and electrolyte membranes, which offer a unique combination of sustainability, mechanical integrity, and electrochemical stability. From industry-friendly process development to rigorous performance optimization at core level, the study provides an end-to-end approach of development of novel flexible membranes that show high potential for use in various energy storage systems. Through a systematic evolution from passive ceramic-impregnated systems to active composite polymer electrolytes, this research bridges materials chemistry, electrochemical engineering, and green energy solutions.

1.1 Motivation

The accelerated growth of global energy demand has intensified dependence on fossil fuels, which are not only finite in reserves but also major contributors to harmful greenhouse gas emissions and air pollution. The combustion of coal, oil, and natural gas accounts for nearly 75% of global CO_2 emissions and about 90% of all greenhouse gas emissions from human activities, directly driving climate change and worsening public health due to particulate matter and toxic pollutants[1]. Moreover, the uneven geographical distribution of fossil fuel resources raises concerns of energy security and long-term affordability. These pressing challenges highlight the urgent necessity of switching to renewable and low-carbon energy systems. The transition toward carbon neutrality requires profound integration among energy generation, storage, utilization and sustainability. With the focus on achieving the United Nations Sustainable Development Goals (SDGs), the adaptation of green energy solutions helps to attain technological advancement and economic diversification in line with the environmental objectives[2]. SDG 7 (Affordable and Clean Energy) and SDG 13 (Climate Action) influence the global scientific community to put efforts of finding sustainable materials for efficient energy storage and conversion, whereas SDG 9 (Industry, Innovation, and Infrastructure) and SDG 12 (Responsible Consumption and Production) promote the industrial adaptation and required production of those materials.

Among various strategies, sustainable solutions for energy conversion and storage, such as advanced rechargeable batteries, are pivotal to support clean power generation, stabilize grids, and enable large-scale electrification of transport and industry. Lithium-ion batteries (LIBs), with their light weight, high energy density and affordability, dominate the rechargeable battery market, especially in consumer electronics and medical devices[3]. However, despite their widespread adoption and immense application potential, reports of fire and thermal runaway incidents in mobile phones and laptops have raised critical concerns regarding the intrinsic safety of LIBs. Such incidents are generally caused by two of the major LIB components - organic liquid electrolyte and plastic-based separators, which are highly combustible and flammable in nature. The replacement of these components with some robust, sustainable and and eco-friendly alternatives, thus become mandatory, especially for high energy applications like electric vehicles (EVs). Apart from that, majority of the constituents of lithium-ion batteries are exported from other countries to India, which enhances the cost and reliability of the systems. With its Atmanirbhar Bharat and electric mobility mission, the Government of

India pushes the industries as well as researchers to focus more on R&D and develop our own battery components domestically.

This thesis is motivated by that imperative. We have tried to develop cellulose paper-based composite separators and paper-based electrolyte-cum-separator membranes that are (a) fabricated via industry-friendly routes, (b) validated in full cells under application-relevant cycling and temperature, and (c) assessed for sustainability, reproducibility and manufacturability, thereby helping bridge the gap between sustainable policy timelines and Make in India objectives.

1.2 Electric Mobility

The transport sector is one of the largest contributors to global carbon emissions, primarily due to its heavy reliance on fossil fuels. Decarbonizing mobility has therefore become a central pillar of climate action, with electric mobility emerging as a transformative solution. Unlike conventional internal combustion (IC) engine vehicles, electric vehicles eliminate tailpipe emissions and can integrate seamlessly with renewable power sources, thereby reducing lifecycle greenhouse gas emissions, as shown in ***Figure 1.1***. Beyond environmental benefits, EVs also offer higher energy efficiency, lower operating costs, and reduced dependence on imported crude oil, which is particularly relevant for energy-insecure economies such as India. As nations commit to ambitious net-zero timelines, the electrification of mobility represents not only a technological shift but also a socioeconomic necessity. The global electrification surge is no longer speculative, rather it has clear timelines and scale. NITI Aayog has reported that global electric vehicle sales rose from under 1 million in 2016 to nearly 18.8 million in 2024, and global EV stock reached ~61.2

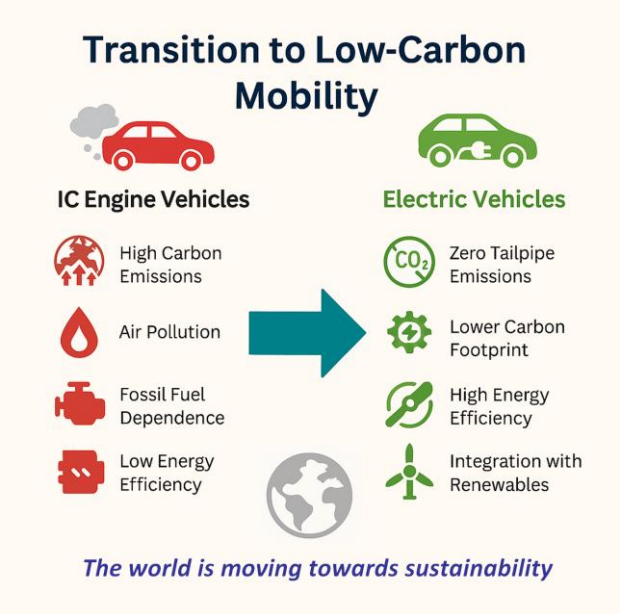

Figure 1.1 *Transition from IC engine vehicles to electric vehicles*

million vehicles in 2024, driving urgent demand for cell capacity, supply chains and safety system[4,5].

Rechargeable lithium ion-batteries (LIBs) are the cornerstone of EV technology. Among the four major components of a commercial LIB, separator is made up of fully plastic-based material and it is also costly. This inert yet safety critical component directly influences thermal response, electrolyte retention, dendrite suppression and pack-level reliability. While commercial polyolefin membranes are serving the markets quite well, the combined push for (i) high-rate/fast-charging EVs, (ii) tropical-climate robustness, (iii) domestic manufacturing and (iv) lifecycle sustainability demands separators that are technically superior, pollution-free and manufacturable at large scale.

1.2.1 Global Scenario

Globally, electric mobility has entered a phase of accelerated growth, driven by policy mandates, consumer adoption, and declining battery costs. In terms of sales and manufacturing of EVs, China remains the largest market, accounting for nearly 66% of global sales. It holds a dominant position cell manufacturing, raw material refining, and supply chain integration, with global EV production of more than 70% as well[6]. The European Union has also demonstrated strong momentum, supported by stringent CO_2 emission regulations for passenger cars and its 2035 deadline to phase out IC engine vehicle sales. In the United States, federal tax incentives, infrastructure investments, and state-level ZEV (Zero Emission Vehicle) mandates have accelerated market penetration, with a national target of 50% new EV sales by 2030[5].

Battery technology has been a central enabler of this transition. The average cost of LIB packs has fallen from more than US$1,200 kWh^{-1} in 2010 to nearly US$140 kWh^{-1} in 2024, moving steadily toward the US$100 kWh^{-1} threshold[5]. Such increasing cost-effectiveness of LIBs is critical for mass-market affordability. In parallel, charging infrastructure deployment has expanded rapidly, with more than 5 million public charging points and ~50% growth in ultra-fast chargers (>150 kW) installed worldwide by 2024[6,7]. EVs successfully displaced more than 1 million barrels of oil per day in 2024, projected to exceed 5 million barrels/day by 2030 under current policies.

Nevertheless, challenges remain, such as supply chain bottlenecks for lithium, cobalt, and nickel; regional disparities and uneven distribution among developed and developing economies; and the urgent need for large-scale recycling to mitigate environmental impacts. Consequently, global R&D efforts are increasingly focused on solid-state batteries, sodium-ion systems, and sustainable component designs, especially separators and electrolytes, that can deliver higher safety margins and sustainability. According to the International Energy Agency (IEA), achieving a net-zero pathway by 2050 will require global EV sales to exceed 200 million units by 2030, alongside significant investments in battery recycling, renewable-powered charging, and sustainable supply chains[5]. These trends underscore the dual challenge faced by the global EV ecosystem: scaling rapidly to meet climate timelines while ensuring that the underlying technologies are affordable, safe, and environmentally sustainable.

1.2.2 Indian Perspective

India's transition toward electric mobility has accelerated in recent years, though it remains at an early stage compared with global leaders. EV sales in the country increased from only ~50,000 units in 2016 to nearly 2.08 million units in 2024, raising the national penetration rate to 7.6% of new vehicle sales. Despite this growth, India is still some distance from its ambitious goal of achieving 30% EV sales by 2030, and the pace of adoption must therefore increase dramatically in the coming decade[4].

India's policy targets and programmes set precise near-term and mid-term deadlines. Various policy instruments have been developed, which are focused on these timelines. At the national level, the Faster Adoption and Manufacturing of Hybrid and Electric Vehicles (FAME-I and II) schemes offered purchase incentives and charging infrastructure support with ~₹10,000 crore outlay, while the recently launched PM e-Drive program (2024-2026) aims to sustain demand through continued subsidies and ecosystem development[4]. Parallel initiatives such as the Production Linked Incentive (PLI) scheme are fostering domestic manufacturing of batteries and EV components, reducing reliance on imports. Importantly, nearly 27 states and union territories have introduced their own EV policies, creating a diverse but sometimes fragmented policy landscape[8,9]. India has pledged net-zero by 2070 at COP26, with intermediate commitments (e.g., carbon-intensity reductions by 2030). These schedules create both global and India-specific pressure to deliver safe, affordable, and circular energy storage technologies at scale[5,10].

India's EV transition is shaped by several unique contextual drivers. The country imports over 85% of its crude oil requirements, making electrification a strategic necessity for energy security. Air pollution is another critical factor: 35 of the 50 most polluted cities globally are in India, and road transport accounts for 20–30% of urban particulate emission[11]. For a rapidly urbanizing economy, EVs thus offer not only climate benefits but also significant co-benefits in terms of public health, reduced import dependency, and improved grid efficiency through managed charging and vehicle-to-grid integration.

Despite strong policy support, India's EV transition faces persistent barriers. Financing remains a key hurdle for capital-intensive segments like buses and trucks, highlighting the need for innovative models such as battery leasing, vehicle leasing, and service-based procurement. Charging infrastructure is unevenly deployed, with urban centers better served than highways, prompting experts to recommend a "saturation approach" that prioritizes full electrification in select cities and corridors[4]. Supply chain constraints are equally pressing, as India has limited reserves of lithium, cobalt, and nickel, underscoring the importance of indigenous innovation and the R&D Roadmap on Tropical EV Batteries, which emphasizes chemistries such as NMC, LFP, and LMFP in the near term, and sodium-ion or solid-state systems in the longer run[11]. Strengthening battery management systems, diagnostics, and recycling frameworks, including digital battery passports, is also essential for safety and circularity. Looking forward, the IEA estimates that ambitious EV adoption and efficiency policies could cut India's transport energy demand by 30% and avoid up to 60% of projected CO_2 emissions by 2050, provided annual investments of USD 20-30 billion and rapid infrastructure expansion are sustained

1.3 Background: Battery Landscape

The history of batteries reflects the broader trajectory of energy use and technological progress. The concept of storing electricity in chemical form dates back to Alessandro Volta's pile in 1800, which demonstrated a continuous source of current for the first time. Over the nineteenth century, the Daniell cell and the lead-acid battery laid the foundation for practical electrochemical storage. Lead-acid cells are widely used in automotive and backup applications till today, due to low cost and robustness. The twentieth century witnessed the rise of nickel-cadmium and nickel-metal hydride batteries, which provided higher energy densities and dominated portable electronics before the advent of lithium-based systems. The commercialization of lithium-ion batteries in the early 1990s marked a turning point in the

energy world: their combination of high energy density, long cycle life, light weight and decreasing cost enabled the rapid growth of laptops, smartphones, and eventually today's electric vehicles. The invention of LIBs brought the 2019 Nobel Prize in Chemistry to its inventors - John B. Goodenough, M. Stanley Whittingham, and Akira Yoshino for their pioneering work on LIB electrodes and electrolytes.

The rising penetration of renewable energy sources such as solar and wind, while environmentally favourable, produces significant challenges that necessitate reliable and scalable energy storage systems (ESS). Among the various technologies, rechargeable batteries, especially lithium-ion batteries (LIBs) have emerged as the most widely deployed storage solution due to their high energy density, long cycle life, and adaptability across multiple scales - from consumer electronics and electric vehicles to grid-scale storage[12]. However, environmental concerns regarding lithium, cobalt, and nickel supply, as well as issues of recyclability and environmental footprint, are fuelling the exploration of alternative battery chemistries. Sodium-ion batteries (SIBs), owing to the abundance and low cost of sodium, have recently gained traction as a competitive alternative, particularly for stationary storage[13]. Also, solid-state batteries, which replace flammable liquid electrolytes with inorganic or polymeric solid electrolytes, are being intensively investigated for their promise of higher energy density and enhanced safety[14].

Beyond rechargeable batteries, a diverse array of non-battery storage technologies plays an equally critical role in the rechargeable world. Supercapacitors (SCs) play a pivotal role in bridging the gaps persistent in renewable energy technologies. These charge storage devices help in smoothing intermittent energy generation in solar and wind power systems, enhancing the efficiency of electric vehicles etc[15]. hybrid energy storage systems (HESS) combine supercapacitors or flywheels with batteries to balance energy and power requirements[16,17]. Large-scale methods such as pumped hydro storage (PHS), thermal energy storage (TES), and green hydrogen remain central to global capacity portfolios.[18–20]. However, for India's fast-growing renewable sector and electrification goals, rechargeable batteries, particularly LIBs, are emerging as the most viable near- to mid-term solution.

With the transition from internal combustion engines to electric vehicles, the battery pack has become the core determinant of efficiency, lifetime, cost, and safety. While cathode and anode chemistries often dominate discussions, sustainability goals demand equal attention to supporting components. Life-cycle assessments highlight that beyond electrodes and

electrolytes, the separator is a critical enabler of ionic transport, thermal stability, and mechanical integrity, yet it has historically been underemphasized. As global and national priorities converge on decarbonization and circularity, innovations in separator design—particularly with renewable, functionalized materials such as cellulose—are central to advancing both performance and sustainability. This recognition motivates the focus of the present thesis.

1.4 Lithium Storage: Intercalation Chemistry and Beyond

The dominance of lithium in modern electrochemical energy storage originates from its unique electrochemical properties; it is the lightest metal with the smallest ionic radius, and it resides at the top of the electrochemical series with the most negative standard reduction potential (–3.04 V vs SHE)[21]. This combination yields the highest possible cell voltage and gravimetric energy density, while the small Li^+ ion enables fast intercalation into host electrode lattices with minimal structural strain. As a result, lithium-based systems deliver superior energy and power performance compared with other alkali or multivalent ion chemistries. These attributes explain why lithium-ion batteries (LIBs) have become the backbone of today's energy storage technologies, spanning portable electronics, electric mobility, and stationary renewable energy storage systems[22,23]. In practical scenario, LIBs typically deliver specific energies of 150-250 $Wh.kg^{-1}$ with power densities exceeding 1,000 $W.kg^{-1}$, outperforming conventional systems such as nickel-metal hydride or lead-acid batteries[24]. Their success lies in the highly reversible intercalation/deintercalation of Li^+ ions within host electrode structures, which allows for long cycle life while maintaining structural integrity.

The lithium-ion intercalation mechanism is the heart of LIBs, which enables Li^+ ions to reversibly insert into and extract from host electrode materials with minimal structural disruption. The layered frameworks of cathode materials consist of alternating transition-metal oxide sheets and Li layers, that facilitate suitable interlayer Li^+ diffusion[25]. On the other hand, graphitic carbon-based anodes remain the industry standard due to its ordered layered structure capable of forming staged Li-C intercalation compounds. These layers accommodate Li^+ with minimal lattice distortion, vital for enduring extensive cycling, high efficiency and low potential[26]. The intercalation process is schematically shown in ***Figure 1.2(a)***, along with their corresponding chemical reactions in ***Figure 1.2(b)***. The layered matrix concept, both at cathode and anode, offers several advantages. Firstly, the planar diffusion pathways facilitate low-voltage hysteresis and long-term cycling retention. Secondly, layered structures permit one-

dimensional or two-dimensional Li diffusion that helps to achieve high ionic conductivity and high-rate charge/discharge. Also, substituting Ni, Mn, and Co tailors voltage, capacity, and thermal behavior, while doping with Al, Ti etc further stabilizes the lattice against oxygen release and structural phase transitions under long cycling. Understanding how Li^+ migrates through these layered architectures and how lattice stability, transition-metal migration, and interlayer chemistry evolve during cycling, provides foundational insight for the separator and electrolyte design and their chemistry integrated approaches.

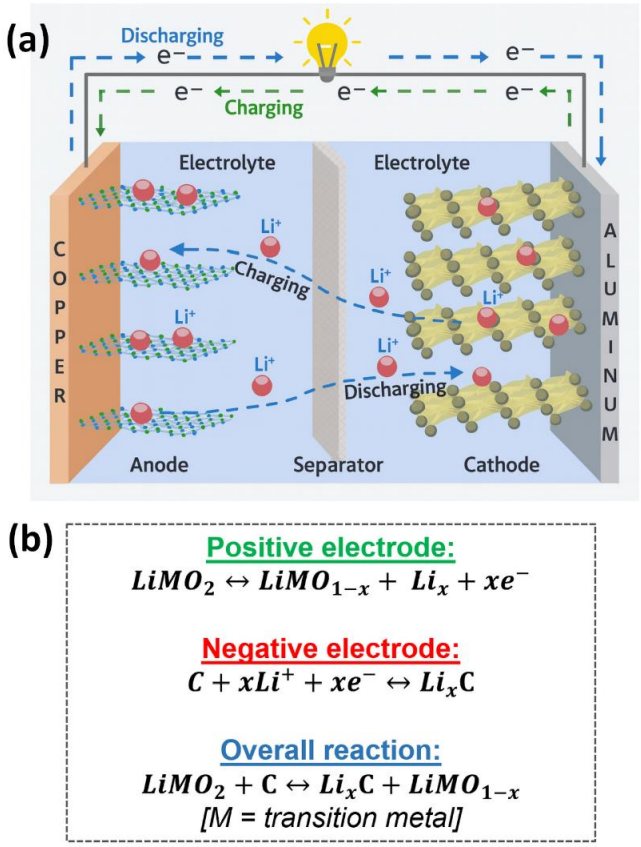

Figure 1.2 *(a) Intercalation mechanism of a typical lithium-ion cell [adapted the idea from 65], (b) chemical processes taking place during charge and discharge*

While intercalation chemistry has backboned the unparalleled success of commercial lithium-ion batteries since 1991, its intrinsic capacity limits, approximately 372 $mAh.g^{-1}$ for graphite anodes and 140-200 $mAh.g^{-1}$ for layered transition-metal oxide cathodes, have attracted researchers to dig into alternative electrochemical reactions capable of delivering higher energy densities. Also, fast charging in LIBs often triggers localized lithium plating, capacity fade, or safety hazards, while elevated C-rates require electrodes and electrolytes capable of supporting uniform ion transport and heat dissipation. In parallel, concerns regarding the availability and cost of lithium, cobalt, and nickel have heightened the need to optimize lithium utilization and extend battery lifetime through improved electrode chemistries and recycling strategies[27]. Although alternative chemistries such as sodium-ion and multivalent systems are being investigated, lithium remains the benchmark for electrochemical energy storage. Its superior energy and power efficiency

serve as both a practical foundation for current technologies and a reference point for next-generation systems. Due to this, three major classes of Li-based reactions have been actively pursued: conversion-type, alloy-type, and lithium-metal-based systems. Conversion-type reactions involve the full reduction of transition-metal compounds (oxides, sulfides, fluorides etc) into metallic nanoparticles dispersed in a Li_2X (X = O, S, F) matrix. For instance, transition-metal fluorides (e.g., FeF_3) provide theoretical capacities above 700 $mAh.g^{-1}$[28]. However, large volume changes and voltage hysteresis hinder their commercial use. Alloy-type anodes, such as silicon, tin, and phosphorus, exploit Li-metal alloy formation to achieve capacities far beyond graphite (e.g., 3579 $mAh.g^{-1}$ for $Li_{15}Si_4$)[29]. Silicon, in particular, has emerged as a strong candidate for next-generation anodes due to its abundance and high gravimetric and volumetric capacities. Yet, repeated lithiation/delithiation induces ~300% volume expansion, leading to electrode pulverization and unstable solid electrolyte interphase (SEI) formation[30,31]. Strategies such as nanostructure engineering, binder modification, and composite design are being developed to mitigate these issues. Lithium-metal anodes represent the ultimate energy-dense option, with a theoretical capacity of 3860 $mAh.g^{-1}$ and the lowest possible electrochemical potential (–3.04 V vs SHE). Lithium-metal cells enable the realization of high-energy chemistries such as lithium-sulfur (Li-S) and lithium-oxygen (Li-O_2) batteries. Li-S batteries promise specific energies up to 2600 $Wh.kg^{-1}$, while Li-O_2 cells can theoretically reach 3500 $Wh.kg^{-1}$[32]. However, both face critical challenges, including lithium dendrite growth, polysulfide shuttling in Li-S batteries, and parasitic reactions in Li-air systems.

1.5 Critical LIB Components

The performance and safety of rechargeable batteries depend on the conjugal function of four key components—cathode, anode, electrolyte, and separator, each contributing unique physicochemical properties that govern capacity, cycling stability, ionic conductivity, and thermal resilience. While cathodes largely determine energy density, anodes control specific capacity and rate performance. Electrolytes, mainly in liquid form, provide the ionic medium but introduce safety challenges due to volatility and flammability. Separators act as physical and electrochemical safeguards, that basically prevents the handshaking of the two electrodes by separating them. The synergy between these materials has been shaped by decades of innovation, culminating in the 2019 Nobel Prize in Chemistry awarded to John B. Goodenough, M. Stanley Whittingham, and Akira Yoshino for their pioneering work on LIB electrodes and electrolytes[33].

1.5.1 Cathode

The cathode is the energy-defining component of rechargeable batteries. The earliest breakthrough in battery cathodes was by M. Stanley Whittingham, who in the 1970s employed titanium disulfide (TiS_2) as a host for lithium intercalation, laying the foundation for rechargeable LIBs[34]. Later, John B. Goodenough introduced lithium cobalt oxide ($LiCoO_2$ or LCO) in 1980, a layered oxide cathode with high operating voltage (~4 V), which remains a cornerstone in commercial batteries till date[35]. Today, layered oxides such as NMC and NCA dominate EV applications due to their high energy densities, while $LiFePO_4$ (LFP), discovered by Padhi et al. in 1997, offers enhanced safety and cycle stability that are essential for portable electronics[36]. Cathode optimization now focuses on Ni-rich systems, doping, and structural stabilization for longer lifetimes, safer operation and cost effectiveness.

1.5.2 Anode

The anode critically influences specific capacity and cycling efficiency of a battery. Akira Yoshino's pioneering work in the 1980s demonstrated a carbonaceous anode derived from petroleum coke which enabled safe and reversible lithium-ion shuttling, eliminating dendritic lithium deposition observed in earlier prototypes[37]. This breakthrough, combined with Goodenough's cathode and stable organic electrolytes, formed the first commercial LIBs released by Sony in 1991. Graphite soon replaced coke, offering a well-defined layered structure with reversible intercalation up to LiC_6 (theoretical capacity ~372 $mAh.g^{-1}$). Beyond graphite, alloy-type anodes such as silicon (3579 $mAh.g^{-1}$) and tin are under active development for higher energy density, though they face challenges of large volume expansion and unstable SEI formation[38]. Lithium-metal anodes, with their ultrahigh capacity (3860 $mAh.g^{-1}$), remain the ultimate target, but dendrite formation and safety issues necessitate innovative separators and electrolytes, linking directly to the theme of this thesis.

1.5.3 Electrolyte

Electrolytes, typically comprising a lithium salt ($LiPF_6$) dissolved in carbonate-based organic solvents, provide the ionic conduction medium. This formulation, introduced in the late 1980s, enabled stable cycling of LIBs by forming a solid electrolyte interphase (SEI) on graphite anodes[39]. However, the flammability and volatility of organic solvents remain significant safety concerns. High-voltage cathodes accelerate electrolyte decomposition, generating gas and impedance rise. Additives such as fluoroethylene carbonate (FEC) and lithium

bis(fluorosulfonyl)imide (LiFSI) salts have been developed to stabilize interfaces and extend voltage windows[40]. Current research emphasizes solid-state electrolytes (polymer, sulfide, and garnet-type ceramics), which can eliminate leakage and reduce flammability risks while enabling the use of lithium-metal anodes. Electrode-electrolyte compatibility remains critical to overall battery stability.

1.5.4 Separator

The separator, though electrochemically inert, is a vital safety and reliability component. Its primary role is to prevent short-circuiting by physically isolating the two electrodes while allowing ionic conduction. Conventional separators are made of polyolefin-based polymers like polypropylene (PP), polyethylene (PE) etc. Introduced in the 1980s, battery separator's multilayer variants (e.g., PP/PE/PP) provide mechanical strength and "shutdown" functionality upon collapsing of pores at elevated temperatures[41].

From systems perspective, EV duty cycles demand wide temperature operation, frequent partial-state-of-charge cycling, high C-rate charge/discharge events or fast charging, and stringent lifetime targets. These conditions amplify the functional requirements of separators beyond their basic role of physical isolation. High porosity with optimized pore-size distribution and low tortuosity are needed to sustain uniform ion flux at high rates without local concentration polarization. At the same time, adequate mechanical integrity must be preserved, particularly when wetted with low-viscosity electrolytes. Also, mechanical robustness and puncture resistance, stack pressure, particle asperities, gas evolution, and manufacturing defects can impose localized stresses; separators must resist tearing and maintain dimensional stability to avoid internal shorts during cycling and vibration typical of automotive use. Elevated temperature events originating from exothermic reactions or external abuse can lead to shrinkage and pore collapse in conventional polyolefin membranes. Engineered separators must delay thermal runaway by maintaining structure at higher temperatures and, where applicable, enabling controlled shutdown. The limited thermal stability and poor electrolyte wettability of plastic-based separators present risks in high-energy cells. That is why with the rising demand for safer and more sustainable batteries, advanced separators incorporating ceramic coatings, functional polymers, and bio-derived substrates such as cellulose are being investigated[42]. These developments highlight the separator's evolving role from a passive physical barrier to an active enabler of stability and performance, which forms the central research direction of this thesis.

1.6 Evolution of Separator Materials

The development of battery separators has progressed through distinct stages, each reflecting the growing performance and safety requirements of rechargeable batteries. In the earliest generation, separators were adopted from porous membranes used in alkaline and lead–acid batteries. These films provided only a mechanical barrier to prevent short circuits, with little consideration of ionic conductivity or thermal endurance.

With the commercialization of lithium-ion batteries in 1991, polyolefin-based microporous membranes became the industry standard. Their low cost, mechanical robustness, and ability to be manufactured at large scale made them suitable for the first wave of portable electronics. However, their inherent drawbacks like limited wettability toward polar carbonate electrolytes and shrinkage above 120-140°C, posed safety risks under high-power or high-temperature operation[41]. To overcome these challenges, the next stage of evolution introduced multilayer separators (e.g., PP/PE bilayers and PP/PE/PP trilayers), which enabled the shutdown functionality effectively. The central PE layer in the three-layered matrix melted under abuse conditions to block ionic transport, reducing the risk of thermal runaway. Still, their overall thermal resistance and interfacial compatibility remained limited.

To improve these properties, thin ceramic or porous functional coatings were applied onto PE/PP. The coating materials include Al_2O_3, TiO_2, silica aerogel, porous organic polymer (POP), or hybrid skins such as SiO_2/PVDF-HFP on PP. These coatings helped to increase surface energy and wettability, raised the softening temperature, and hardened the surface against particle asperities, while preserving the microporous scaffold underneath. A complementary route also introduced surface activity directly on PE/PP. Grafting of some functional materials (e.g., poly(ethylene glycol) methacrylate, SiO_2 etc) in the separator matrix add polar and oxophilic moieties that anchor solvated Li^+ and reduce interfacial impedance. Compared with simple coatings, grafting resists delamination, maintains pore interconnectivity, and fine-tunes wetting without excessive mass gain.

In the next stage, polymer blends were developed that perfectly balance thermal stability, pore formation and interfacial compatibility. Ultra-high-molecular-weight PE with poly(4-methyl-1-pentene) (UHMWPE/PMP) and high-density PE with methyl cellulose (HDPE/MC) are representatives of this series. Blending of polymers help to modify crystallinity and glass transition temperature (T_g) to improve puncture resistance and to engineer pore size and

tortuosity for uniform ion flux at higher C-rates. Next phase of separator development consisted high-T_g polymers like polyamide (PA) and polybenzoxazole (PBO) which offer superior thermo-oxidative stability. PVDF-HFP/PI multilayers pair ionic affinity (PVDF-HFP) with high-temperature integrity (PI). Sandwich structures such as SiO_2@PI/m-PE/SiO_2@PI nanofiber combine electrospun ceramic-reinforced membranes with a melt-blown PE core, yielding low shrinkage, improved wetting, and enhanced puncture strength—key for abuse tolerance and fast-charge conditions.

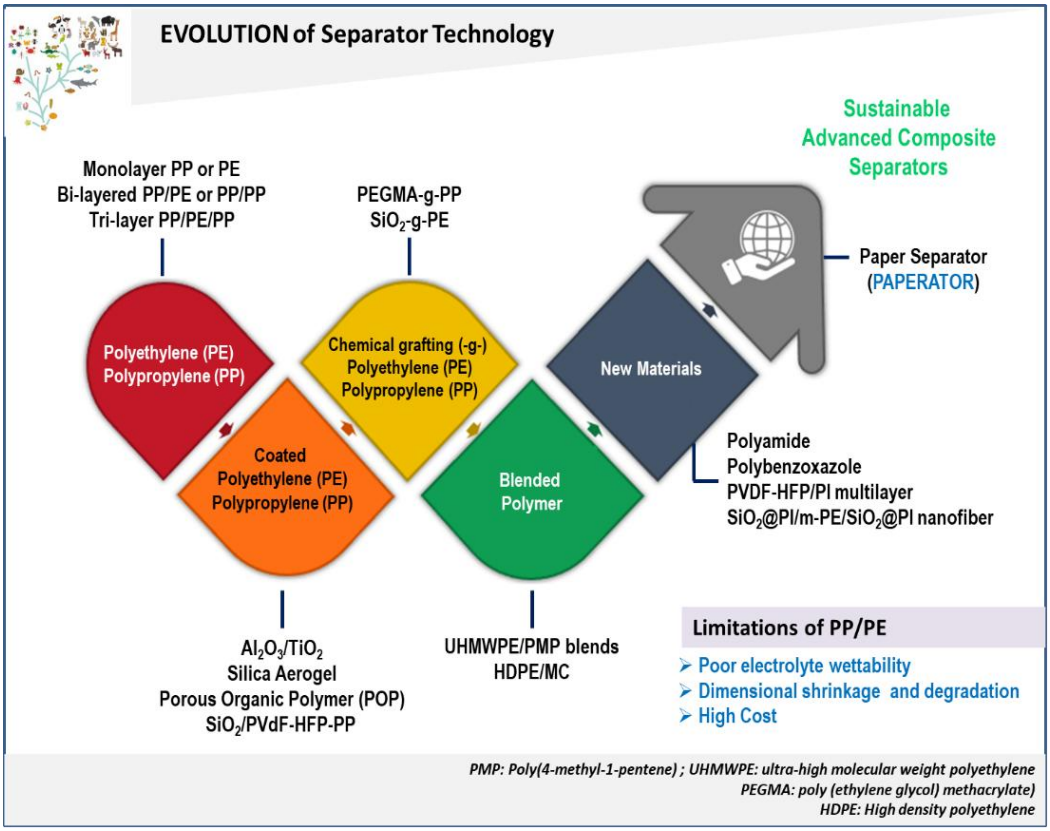

Figure 1.3 *Schematic representation of evolution of separator technology*

Most recently, the focus has been shifted to functionalized and sustainable separators which involve the cellulose-based separators. Cellulose, being the most abundant natural polymer on earth, holds sufficient potential to be functionalized and used as battery separator. It possesses good mechanical robustness and flexibility owing to the intra- and intermolecular hydrogen bonded networks present in its structure. Cellulose structure contains numerous micro- and nano-fibrils that shows immediate swelling upon liquid absorption; this results in excellent electrolyte wettability of the cellulose-based separators. Paper is mostly composed of cellulose, with some amounts of lignin and hemicellulose. With its firm structure, paper consists of all the advantages of cellulose and can potentially be used as separators in different energy storage

systems. Also, if paper can be functionalized to an extent that it becomes able to conduct ions, it can also act as a flexible electrolyte that can be a game changer in research in electronics for the curved surface applications. The journey of separator evolution has been summarized in ***Figure 1.3***. The research on battery separators, thus captures a trajectory where the separator has transformed from a silent component into a critical controller of battery safety, performance, and sustainability.

Globally, the separator market is growing rapidly due to the surge in electric mobility and renewable energy storage systems. Countries like China, South Korea, and Japan dominate the production landscape. In India, while battery manufacturing is rising, the development of advanced separator materials remains relatively underexplored, highlighting a critical research and industrial opportunity. Indian research on battery separators is in its early stages but growing. Academic institutions and public laboratories are focusing on indigenous materials like cellulose and clay, aiming to reduce import dependence and promote Atmanirbhar Bharat in energy storage technology.

1.7 Critical Technical Parameters: Workable Separator in LIBs

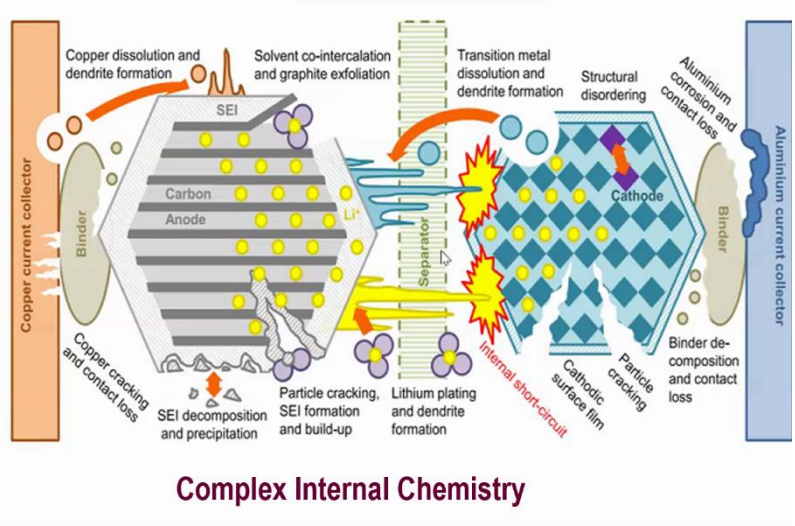

Figure 1.4 *Various complex processes that a separator undergoes inside an electrochemical cell [reproduced with permission from 43]*

A separator inside a battery is not merely an inactive porous membrane, rather it has to endure a lot of physico-chemical processes that take place during electrochemical cycling. These include lithium dendrite growth, binder decomposition, particle cracking, SEI decomposition etc, as illustrated in ***Figure 1.4***. Thus, a practical separator combines a set of engineered

parameters - this so-called inert component must have a suitable and uniform thickness, good mechanical robustness, sufficient porosity, electrolyte wetting ability, thermal stability and it should enable fast, uniform Li^+ transport while surviving mechanical stresses and abuse without compromising safety. The different properties that need to be tuned for a separator are summarized in ***Figure 1.5***.

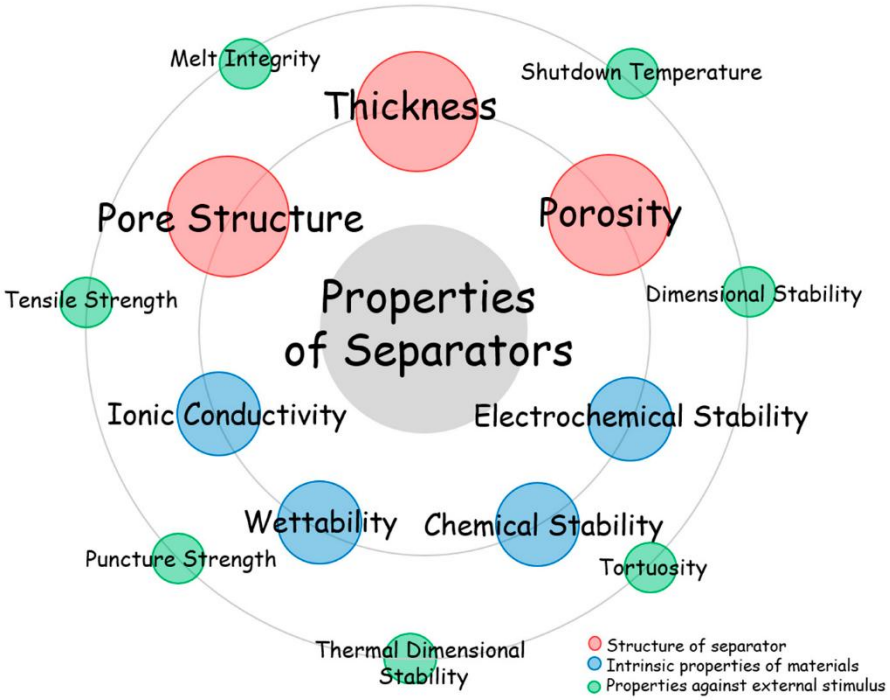

Figure 1.5 *The different properties of a separator membrane that need to be tuned for its successful functioning [reproduced with permission from 44]*

The properties explained below are optimized to design separator materials and to benchmark their performance.

(i) **Thickness & areal resistance:** Thin separators lower cell impedance and boost energy density; commercially useful thickness is typically below 25 µm.

(ii) **Porosity, pore size and electrolyte uptake:** Porosity controls how much electrolyte the membrane can hold and directly impacts ionic conductivity. Ideal porosity of a separator is commonly in the 40–60% range. Sub-micron, uniform pores sized <1 µm, help block unwanted particle penetration and dendrite propagation while enabling sufficient uptake and smooth ion transport. Excessive porosity, however, can weaken mechanical strength and reduce effective ion transport.

(iii) **Tortuosity and connectivity:** Low tortuosity (approaching unity) with well-connected porous network shortens ionic paths, minimizes concentration polarization at high C-rates. Modern topological analyses highlight pore connectivity as a primary determinant of rate performance.

Table 1.1 *Ideal values of the main parameters of lithium-ion battery separators, their relevance in battery performance and the typical experimental techniques for their determination*

Parameter	Ideal Value/Range	Relevance	Measurement Method
Thickness (µm)	<25	Determines the mechanical strength of the separator membrane, help to restrict short-circuit of the battery and affects cell impedance and rate capability	Micrometer
Porosity (%)/ pore size (µm)	40-60/ <1	Affects the swelling process and electrolyte uptake of the separator	Pycnometer and/or mercury intrusion method/scanning electron microscopy (SEM)/BET adsorption
Wettability	High	Controls the amount of electrolyte retained in the separator	Contact angle
Tensile strength (%)	>80 MPa along MD >40 MPa along TD	Determines the mechanical properties: Young modulus, yield strain	Dynamic mechanical analyzer or stress-strain mechanical measurements
Shrinkage (%)	<5% in both MD and TD	Dimensional stability; the separator must not shrink significantly and certainly must not wrinkle when exposed into the electrolyte solution	Thermal analysis
Thermal behavior (ºC)	Stable	Thermal properties strongly affect separator performance	Thermogravimetric Analysis (TGA)/Differential scanning calorimetry (DSC)
Ionic conductivity ($S.cm^{-1}$)	$>10^{-4}$	Influences power and energy of the battery	Electrochemical impedance spectroscopy (EIS)
Chemical/ Electrochemical Stability	0-5V	Separator's stability in reactive and oxidative environment	Cyclic voltammetry (CV)/Linear Sweep Voltammetry (LSV)
Lithium transference number	~1	Charge transport during current flow in lithium-ion cell	A.C. impedance spectroscopy or potentiometric analysis

(iv) **Ionic conductivity & Li^+ transference:** Electrolyte-soaked separator should deliver bulk ionic conductivity $>10^{-4}$ $S \cdot cm^{-1}$ for workable cells. The lithium transference number, when approaches unity, helps to reduce concentration polarization and improve high-rate performance. Separator surface functionalization or tailored chemistries can enhance effective Li^+ transport.

(v) **Mechanical and thermal robustness:** Tensile strength, puncture resistance and low thermal shrinkage (<5% MD/TD) ensure mechanical integrity of a separator under stack pressure and abuse. Thermal shutdown is also essential to delay or arrest thermal runaway.

(vi) **Chemical/electrochemical stability & manufacturability:** Stability across the operational cell voltage window with most of the commercial electrodes (0–5 V), is essential for a separator to ensure its real-world applicability.

In short, a "workable" separator is indeed an optimal combination of thickness, controlled porosity/connectivity, low tortuosity, high wettability and ionic transport, and sufficient mechanical and thermal integrity. The properties along with their required range and measurement technique are summarized in ***Table 1.1***.

1.8 Types of Separators

Conventionally, separator membranes can be of various types. The most important types are based on polymers, and include microporous membranes, nonwoven membranes, electrospun membranes, membranes with external surface modification, composite membranes and polymer blends, or some combination of these types. Among these, microporous membranes, composites and polymer blends are the most widely used separators. Recently, other types of separators (e.g., nonwoven membranes, electrospun membranes and membranes with external surface modification) have become highly relevant due to the many works showing improved specific properties such as wettability or thermal properties. The mostly used polymers as battery separators include polypropylene (PP), polyethylene (PE), polyvinylidene fluoride (PVDF), polyethylene oxide (PEO), polyacrylonitrile (PAN), polyvinyl alcohol (PVA), polyimide (PI), cellulose etc. Among them, PE, PP, and PVDF-based membranes show a promising combination of ionic conductivity and capacity, as displayed in ***Figure 1.6***.

Types of LIB separator along with brief fabrication process and examples are summarized below:

1.8.1 Microporous Membranes

Microporous membranes dominate commercial Li-ion cells. Typically fabricated from polyolefins such as polyethylene (PE) and polypropylene (PP), they are produced by *dry-stretching* (mechanical drawing of extruded films) or *wet processes* (solvent-induced phase separation). The resulting membranes show uniform pore distribution and acceptable mechanical strength, but limited thermal stability and poor electrolyte wettability restrict their use in high-power or next-generation systems[45].

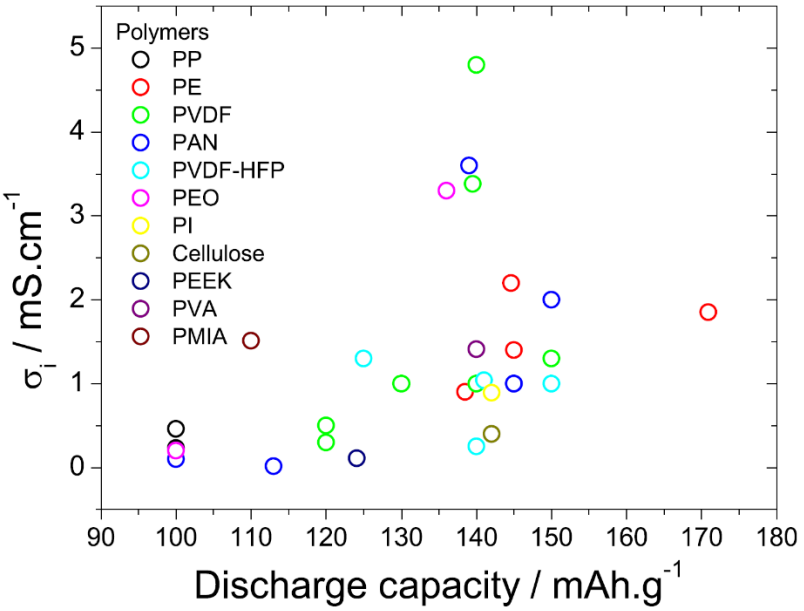

Figure 1.6 *Ionic conductivity vs discharge capacity for various polymer membranes, mostly used as battery separators [reproduced with permission from 46]*

1.8.2 Nonwoven Membranes

Nonwoven separators are obtained from fibrous mats or polymer granules, often produced by melt-blowing, spunbond, air and wet-lay processes. Their open structure provides high porosity and electrolyte retention. However, mechanical weakness necessitates reinforcement or coating[47]. Recently, researchers are working on cellulose-based nonwoven membranes coated with ceramic nanoparticles to achieve improved puncture strength and high-temperature stability.

1.8.3 Electrospun Membranes

Electrospun membranes represent a highly versatile class. Electrospinning creates ultrafine fibers with interconnected pore networks and large surface area, yielding separators with

outstanding electrolyte wettability, rapid ion transport, and thermal tolerance. By adjusting spinning parameters like applied voltage, needle-collector distance, flow rate and needle inner diameter, morphology of the fibers can be precisely tuned[48]. Functional additives (e.g., ceramic nanoparticles or ionic liquids) can also be co-electrospun for enhanced safety and conductivity.

1.8.4 Membranes with External Surface Modification

Surface-modified membranes involve post-treatment of commercial polyolefin separators with coatings or grafted layers. In recent years, conventional PP, PE and PVDF separators have been surface modified in order to improve wettability, thermal stability and mechanical properties. Surface modification has been accomplished externally by several strategies, which include dip-coating with ceramic/polymer slurries, plasma treatment, polymer grafting and chemical modification. These processes help to extend the usable lifetime of conventional membranes without altering their bulk microstructure[46].

1.8.5 Composite Membranes

Composite separator membranes are developed by dispersing various fillers into polymer matrix, followed by solvent casting. The fillers generally include inert ceramic oxides (Al_2O_3, SiO_2, TiO_2, ZrO_2), ferroelectric materials ($BaTiO_3$), super acid oxides ($CaCO_3$, $AlPO_4$, Fe_2O_3, Zr–O–SO_4, BN, SN, NiO, CuO, nano-ZnO), natural clays (montmorillonite), carbonaceous materials (CNT), molecular sieves, zeolites and metal-organic frameworks (ZSM, NaY, MCM-41, MOF-5), as well as lithium-ion conducting fillers ($LiAlO_2$, LATP, LLTO). Such fillers enhance dimensional stability, improve electrolyte uptake, and provide tortuous ion-blocking pathways that suppress lithium dendrites. Fabrication routes include slurry casting, vacuum impregnation, or in-situ nanoparticle growth on the polymer framework[46].

1.8.6 Polymer Blends

Polymer blend membranes combine two or more polymers with complementary characteristics in order to improve the ionic conductivity, electrochemical stability and cycling performances of battery separators. These membranes are produced by different techniques such as phase inversion technique or UV-induced radical photo-polymerization etc[49]. Polymer blends typically used for battery separators are based in polymers such as PVDF, PVDF-HFP, PEO, PAN, PMMA, PE and PVC and the commonly used polymer blends are PVDF-HFP/PAN, PVDF/PMMA and PVDF-HFP/PMMA etc. Some novel polymer bland separators also include

cellulose derivatives such as ethyl cellulose (EC), carboxymethyl cellulose (CMC) etc blended in PVDF or PE.

Apart from the conventional types of separators, there are two other broad categories, especially when we work with cellulose-based separators. They include:

(i) **Passive filler impregnated separators:** While developing cellulose-based, especially paper-based separators, the cellulose paper matrix need to be functionalized with different polymer and ceramic materials, in order to improve wettability, interfacial contact and flame retardancy. Primarily, the passive or non-Li-ion-conducting ceramics can enhance these properties quite well. In our work, we have incorporated nanoceramics like Al_2O_3, $BaTiO_3$, ZrO_2, SiO_2, Montmorillonite (MMT) clay in the paper matrix and discussed their development and performance optimization in Chapters 3-7.

(ii) **Active filler impregnated separators:** Although the passive fillers help in enhancing separator functionalities quite well, they also increase the dead mass inside an electrochemical cell which may be disadvantageous for long term operation. That is why we tried to incorporate ionically conducting ceramics in paper matrix such as garnet-type LLZO to enhance ionic conductivity and extend cycle life. The research has been discussed in detail in Chapter 8.

It is well-known that the flammable organic liquid electrolyte used in commercial cells causes several safety concerns, which is why the global research is moving towards the development of much safer solid-state electrolytes (SSEs). Solid electrolytes can be either inorganic solid electrolytes (ISEs) or solid polymer electrolytes (SPEs). When solid electrolytes are used in a cell, there is no requirement to use a separator since the electrolyte pellet or membrane itself separates the electrodes. We have developed different ceramic-incorporated composite solid polymer electrolytes (CSPEs) and finally paper-supported composite solid polymer electrolytes (p-CSPEs). Their fabrication, performance and application potential in future Paper Cell Technologies have been discussed in detail in Chapter 9.

1.9 Commercial Separator (PP/PE) & Drawbacks

Commercial separators used in lithium-ion batteries are predominantly made from polyolefin polymers, such as polypropylene (PP) and polyethylene (PE). These commercial membranes are typically fabricated through dry stretching (mechanical drawing of extruded films) or wet

phase-separation processes, which yield microporous structures with controlled thickness and porosity[50]. The success of polyolefin in terms of commercial standards arises from a balance of mechanical robustness, light weight, ductility, chemical inertness, large-scale manufacturability, and shutdown functionality provided by multilayer PP/PE/PP designs[51]. These features have ensured their widespread adoption in commercial LIB cells, used in consumer electronics, medical devices, and electric vehicles as well, despite their well-recognized shortcomings.

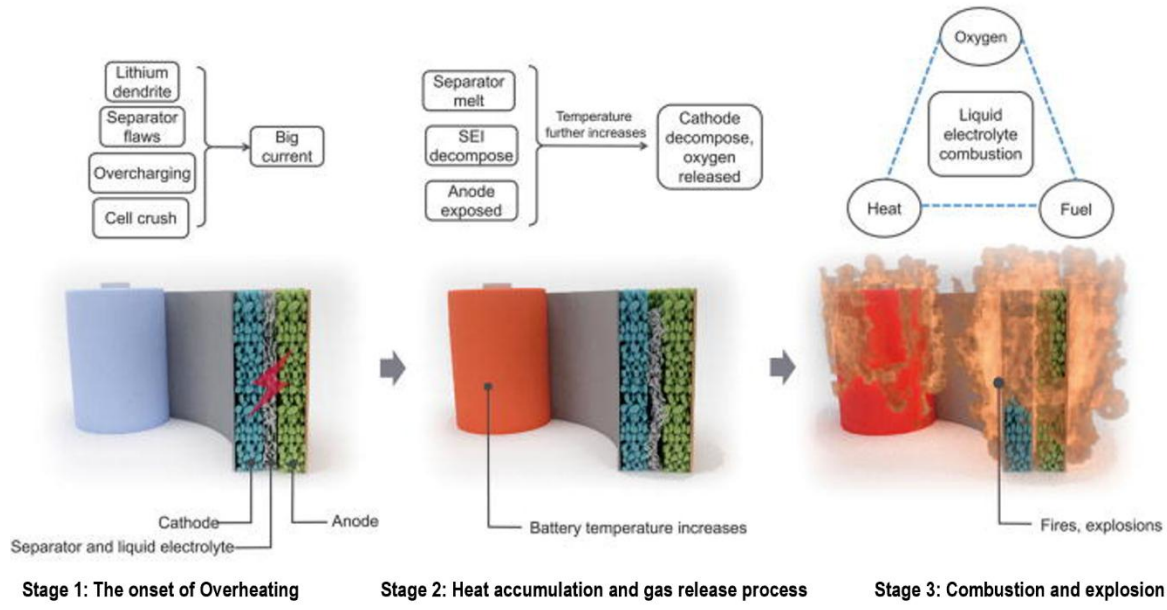

Figure 1.7 *Thermal shutdown of a battery shown schematically, where separator play a critical role [reproduced with permission from 52]*

The major limitations of PP/PE-based membranes that constrain their performance, safety, and long-term reliability, are as follows:

- **Poor Thermal Stability:** Polyolefin separators melt at elevated temperatures (>120 °C), thereby shrinking and leading to internal short-circuits and safety hazards such as thermal runaway. Along with the separators, the flmmable organic liquid electrolyte also has a significant contribution towards the accidents caused by thermal runaway, as schematically represented in ***Figure 1.7***.
- **Limited Electrolyte Wettability:** Non-polar polyolefin surfaces exhibit low affinity for liquid electrolytes, resulting in high interfacial resistance, incomplete pore filling, reduced ionic conductivity and longer battery fabrication time.

- **Limited Electrochemical Stability:** Polyolefin membranes have limited oxidative stability (~4.5–5 V vs Li^+/Li), which constrains compatibility with high-voltage cathodes.
- **Dendrite Growth Vulnerability:** Submicron pores may still allow Li dendrite penetration over prolonged cycling, causing internal short-circuits.
- **Environmental Concerns:** Polyolefin separators are derived from non-renewable petrochemical sources and are not biodegradable, and extremely inert to environmental changes which extends their life a lot. Polyolefins, primarily polyethylene (PE) and polypropylene (PP), are the most produced polymers globally, representing approximately 45.2% of the total plastic production[53]. These issues raise significant concerns of sustainability and recycling.
- **High Cost:** The processing and fabrication of commercial plastic-based separator is quite high. It contributes to around 7% of the total cost of a battery. The contribution of costs from different components and process techniques has been summarized in ***Figure 1.8***.

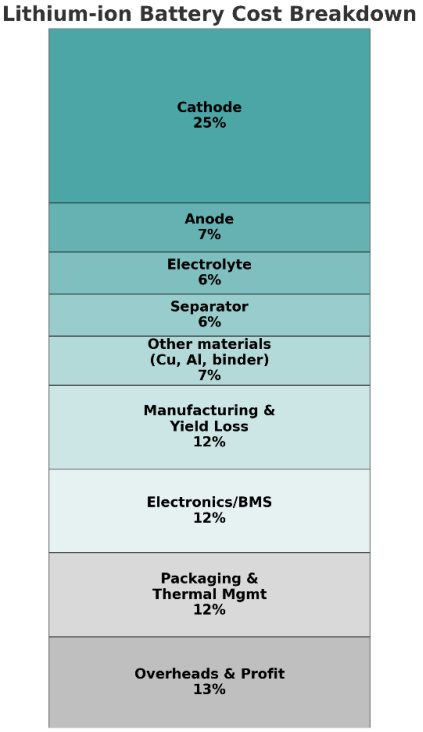

Figure 1.8 *Cost comparison of LIB components and manufacturing process parameters*

The limitations of polyolefin-based commercial separator membranes compel the researchers to search for a sustainable and low cost alternative, that will simultaneously ensure the performance and safety of an energy storage system.

1.10 Cellulose: A Potential Alternative

As already discussed, commercial polyolefin-based separator membranes show severe environmental and safety issues, which garner the quest of sustainable separator materials as suitable alternative. Other than conventional ceramic-coated membranes and non-woven fabrics, cellulose can be considered as a potential alternative to commercial separator membranes. Apart from being the highest abundant natural polymer on earth, cellulose consists of some other suitable phenomena. Biodegradability, high affection towards water and other

liquids and resultant excellent wettability, sufficient porosity, thermal stability, good mechanical strength owing to its inherent hydrogen bonding network and easy processability are some of them. These are the characteristics that make the functionalization of cellulose easy and development of cellulose-based separators feasible.

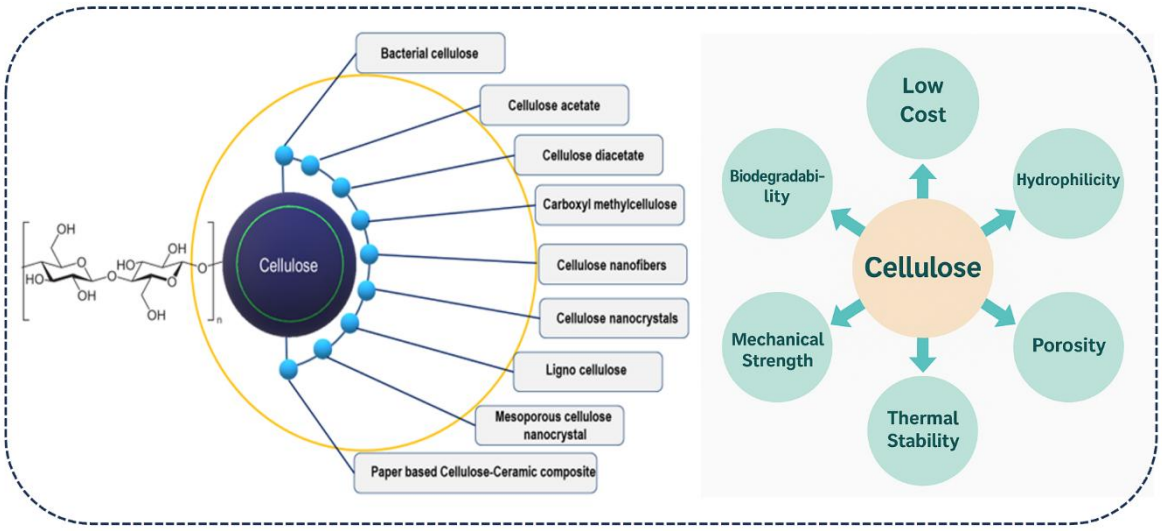

Figure 1.9 *A schematic diagram showing different cellulosic materials having potential to be functionalized as battery separator, along with cellulose structure and its advantages*[54]

In recent past, several research groups attempted to process cellulose or its modified forms as separator for use in lithium-ion batteries. Jiang et al. reported bacterial cellulose derived separator, which showed excellent dimensional stability up to 180ºC with good ionic conductivity[55]. In another approach, Xu et al.[56] explored the preparation of polydopamine-coated cellulose micro-fibrillated membrane and reported to have the superior mechanical strength and electrochemical performance. Pan et al.[57] reported the development of a tri-layer cellulose-based separator, which showed effective thermal shutdown function with improved wettability and thermal stability. Guo et al.[58] has also reported the preparation of green cellulose-based composite separator, which were thermally stable and the mechanical strengthening were done through styrene-coacrylate latex. The structure of cellulose, its various usable forms and advantages are summarized in ***Figure 1.9***.

1.11 Paper Chemistry and Functional Paper

Among various cellulosic materials, the inherent chemistry of Paper is quite interesting. Rooted in the semicrystalline microfibrillar structure of cellulose and its dense network of surface

hydroxyl groups, paper combines both the mechanical integrity and the functional versatility of cellulose

Paper is generally produced by isolating cellulose fibers from renewable sources such as wood, cotton, jute, bamboo, or agricultural residues, followed by pulping to remove lignin and hemicellulose. The purified cellulose fibers are then suspended in water, deposited as a thin mat, and dried, during which hydrogen bonding between fibers gives the sheet its strength and integrity. This simple yet scalable process underpins the wide availability and versatility of paper. During sheet formation, intimate contact between hydrated fibers followed by drying creates extensive inter-fiber hydrogen bonding (often assisted by adsorbed hemicelluloses), which gives paper its surprising tensile strength, anisotropic layering, and recyclability. The same fiber network and processing-controlled web structure set the pore-size distribution and through-plane tortuosity that govern liquid uptake and transport; coupled with cellulose's intrinsic hydrophilicity[59]. These help to yield excellent wettability and rapid electrolyte penetration, making the paper matrix highly desirable for use as battery separators. Crucially for engineering applications, the polysaccharidic chemistry of paper is readily modified: surface sizing, grafting, polymer coatings, and inorganic impregnation can tailor surface energy, thermal behavior, and interfacial chemistry without destroying the fiber scaffold. These combined features - tunable porosity, high wettability, mechanical robustness from hydrogen bonding, and straightforward chemical/physical functionalization, make paper an attractive, low-cost scaffold for next-generation separator and separator-cum-electrolyte membranes in energy-storage systems.

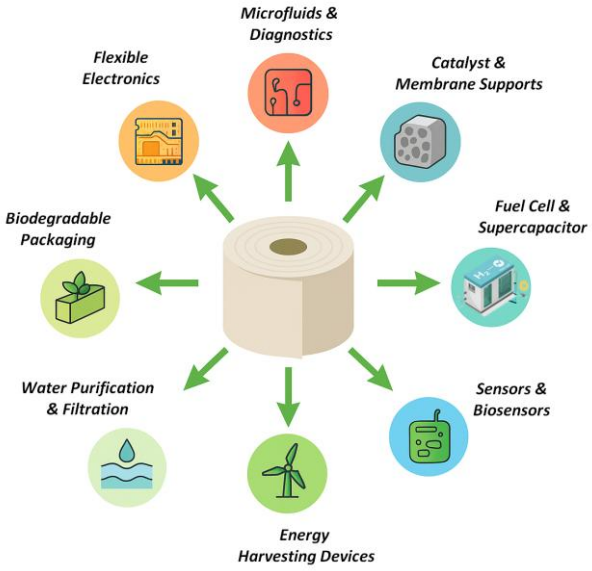

Figure 1.10 *Summary of various scientific and technological applications of paper*

Recently, Zeng et al. has functionalized tissue paper with PVDF-HFP and SiO_2 to obtain a paper separator for LIBs, with high Li-ion transport (t_{Li}^{+} = 0.56), better thermal safety and flame retardancy[60]. In another study by Wang et al., cellulose paper is undergone acetylation reaction followed by a metal-organic framework (MOF) coating, which helped to enhance the

electrolyte wettability, ionic conductivity and capacity retention as an LIB separator[61]. Apart from being used as battery separators, paper is substantially used in flexible electronics, such as printed circuits, RFID tags, sensors, disposable electronics and wearable devices, as recently reviewed by Ying et al[62]. A paper-based microfluidic analytical device is developed by Cai et al. for blood glucose examination. It is named as μPAD, which is able to determine point-of-care blood glucose and hematocrit concentrations accurately[63]. Tanveer et al. has mentioned various paper-based microfluidic fuel cells (PMFCs) and their potential applications in a recent review[64]. Apart from these applications, paper also is diversely used in supercapacitors, biosensors, energy harvesting devices, water purification, filtration and biodegradable packaging purposes. The various possible applications of paper-based matrices are summarized in ***Figure 1.10***.

1.12 Next Generation Separators: Cost & Sustainability

The development of next-generation separators is not only a scientific challenge but also an economic and environmental necessity. Commercial polyolefin membranes, despite their performance in today's cells, contribute substantially to battery cost and are derived from non-renewable petrochemical sources, raising long-term sustainability concerns. The current status of separator production in India's EV market is given in ***Figure 1.11***.

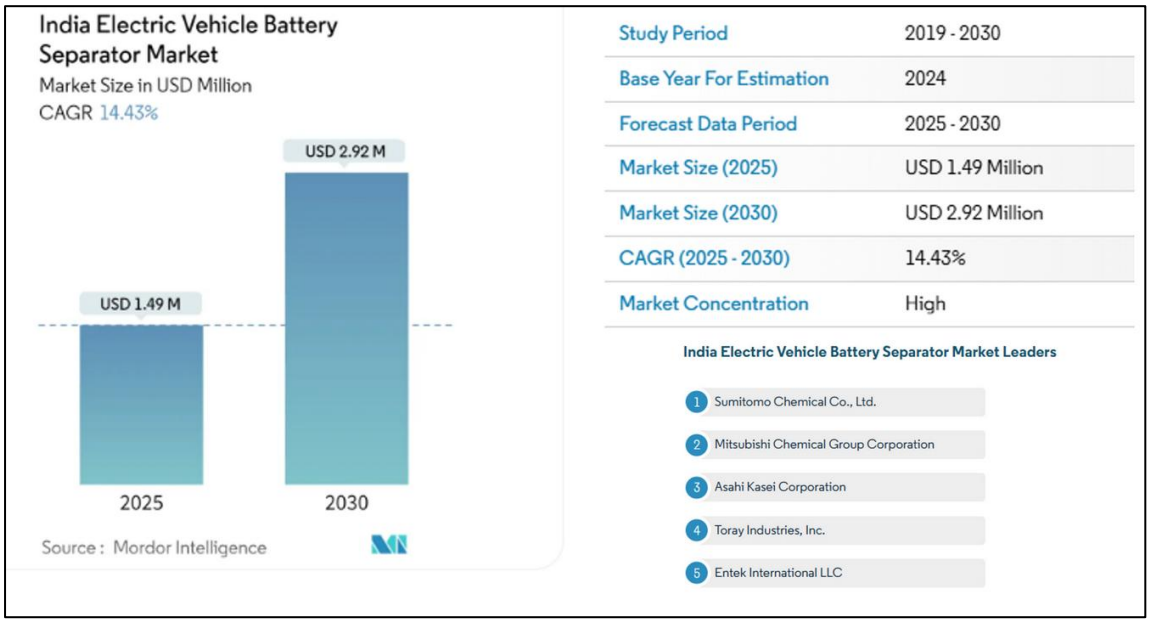

Figure 1.11 *Current separator market in India for electric vehicles, along with the key market leaders [source: report by Mordor Intelligence]*

In India, market leaders like Asahi Kasei, Sumimoto Chemicals etc are also tending towards ceramic-based and sustainable separator options. As electric mobility and grid storage scale globally, the demand for safe, low-cost, and recyclable separators has intensified more. Cost competitiveness will be decisive for large-scale EV adoption, while circular design principles are essential to reduce environmental footprint and resource dependency. Therefore, research has increasingly shifted toward renewable, bio-derived, and functionalized alternatives, such as cellulose paper-based membranes, which offer a compelling balance of affordability, safety, manufacturability, and ecological responsibility.

Such commercial drive is compelling the global research community to intensify the quest for sustainable alternatives, both for polyolefin separator and organic liquid electrolyte. It is a common trend that research on battery separators is quite less in number as compared to cathode, anode and electrolyte. However, the scenario is changing with, as can be observed in Figure 1.12. As per the last ten years' web of science data, research on separators is increasing exponentially and it is expected to see more and more scientific and innovative research in functional separators in the coming years.

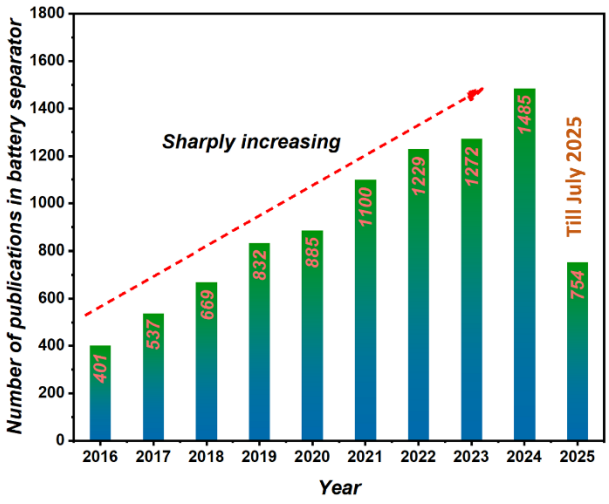

Figure 1.12 *Trend of the research in separator for last 10 years (source: web of science)*

1.13 Research on Separator-cum-electrolyte Membranes

Conventional liquid electrolytes in lithium-ion batteries, typically composed of $LiPF_6$ dissolved in carbonate solvents (e.g., EC, DMC, DEC), provide adequate ionic conductivity but suffer from severe safety, stability, and sustainability issues. Their high volatility and flammability make them prone to leakage, fire, and thermal runaway, while decomposition at elevated temperatures and freezing near 0°C limit their usable temperature range. Moreover, their

electrochemical stability window rarely exceeds 4.3-4.5 V vs Li^+/Li, restricting compatibility with high-voltage cathodes. $LiPF_6$-based electrolytes also form fragile SEI layers that degrade at high temperature, undergo hydrolysis to generate HF in moist conditions, and fail to suppress lithium dendrite growth in Li-metal configurations, leading to internal short-circuits. Beyond these performance limitations, carbonate solvents are petroleum-derived, toxic, and difficult to recycle, raising both environmental and cost concerns.

Replacing flammable liquid electrolytes with solid-state alternatives addresses these limitations at the material level and enables the use of Li-metal anodes with theoretical capacities of 3860 mAh g^{-1}. Solid-state electrolytes (SSEs) include inorganic ceramics (oxides, sulfides) with high ionic conductivities but brittle mechanics, polymer electrolytes (PEO, PVDF-based) with flexibility but low room-temperature conductivity, and composite polymer electrolytes that combine polymer flexibility with ceramic fillers for improved ionic transport and stability. Other variants such as gel polymers, ionic-liquid hybrids, and glassy electrolytes offer intermediate solutions. In this context, paper-based composite polymer electrolytes, as developed in Chapter 9, provide a sustainable, flexible platform that integrates separator and electrolyte functionality, though further optimization of conductivity, interfacial resistance, and large-scale processability remains essential.

1.14 Research Gap and Opportunities

Despite decades of progress in lithium-ion battery technology, separators and electrolytes remain critical bottlenecks for performance, safety, and sustainability. Commercial polyolefin separators (PP/PE) dominate the market, but their poor thermal stability, limited wettability, dendrite vulnerability, and petrochemical origin raise serious concerns for next-generation applications such as fast-charging EVs and high-voltage cells. Similarly, carbonate-based liquid electrolytes, though widely adopted, are volatile, flammable, and chemically unstable, restricting safe operation and complicating recycling. Research has produced partial solutions through ceramic coatings, polymer blends, or inorganic/polymer solid-state electrolytes, yet these approaches face challenges of cost, interfacial resistance, brittleness, and large-scale manufacturability.

In this context, cellulose paper emerges as a sustainable, abundant, and low-cost platform with inherent mechanical strength, porosity, and hydrophilicity, which can be further functionalized with polymers and ceramics. While promising demonstrations exist, systematic optimization

of thickness, filler distribution, ionic conductivity, and interfacial compatibility is still lacking. Opportunities lie in tailoring paper-based matrices not only as separators but also as multifunctional separator-cum-electrolyte membranes, thereby reducing component count and enhancing circularity. Furthermore, integration with advanced chemistries such as lithium metal, sodium-ion, and solid-state batteries offers exciting prospects. To bridge the gap between laboratory feasibility and commercial adoption, future work must address scalability, reproducibility, and cost-competitiveness, ensuring that paper-based technologies can align with global sustainability goals and India's Atmanirbhar Bharat mission.

1.15 Objectives and Scope of the Thesis

This thesis primarily aims to develop a sustainable, low cost and cost-effective alternative to commercial polyolefin-based LIB separator membranes. Cellulose paper, being the most abundant and potential material available, was our first choice in this perspective. The major scopes and related objectives of this thesis are described as follows:

(i) Functionalizing the locally outsourced low cost paper matrix with suitable polymer and ceramic materials along with the process and composition optimization was the first and foremost task that has been completed and covered in ***Chapter 3***. Paper substrate from local market although is the most cost-effective option, its high thickness (80-90 μm) and inherent impurities caused the cell impedance to rise and as a result limited electrochemical performance.

(ii) Reduction of thickness of the paper separator to commercial standard (20 μm) was crucial. Substituting that paper with a pure cellulose paper of low thickness proved to be an effective approach, only with multilayer polymer coating and $BaTiO_3$ ferroelectric impregnation. Variant of this trilayer paper separator not only performed well in lithium-ion batteries, but it showed optimal performance in sodium-ion battery and supercapacitor applications, as described in ***Chapter 4***.

(iii) To improve cycling stability, interface compatibility and safety features of the separator, a wide range of ceramic and clay materials has been explored as fillers in paper matrix. Al_2O_3, $BaTiO_3$ and ZrO_2 impregnation proved to be effective in enhancing thermal stability and electrolyte wettability. However, ZrO_2, for its strongest surface charge-based interaction with cellulose, provided the most stable electrode-separator interface, hence reducing the charge-transfer impedance and facilitating ion transport. In another approach, a natural clay material namely

Montmorillonite (MMT) has been incorporated in paper matrix to develop the most sustainable and cost-effective separator for LIBs. MMT having a beautiful layered structure, high porosity and flame resistance characteristics, helped to induce better wettability, improved ion transport and better safety features into the separator membrane. The effect of different ceramic and clay material impregnation in paper separator on overall battery performance has been elaborated in ***Chapters 5 and 7***.

(iv) So far, ZrO_2-based paper separators performed very well, mostly due to the homogeneous distribution and high surface activity of ZrO_2 as well as the Lewis acid-base interaction of Zr^{4+} with the anions present in Li-salt-based liquid electrolytes. However, Zr^{4+} remain coordinated with O^{2-}, thereby saturating the positive charge and resultant decrease in interaction with anions and effective salt dissociation. The research consisted in ***Chapter 6*** focuses on the coordination unsaturation of Zr^{4+} via complexation with some organic chelating agent. This approach helps in facilitating Li-salt dissociation as well as smooth Li-ion transport through selective zirconia nanodomains. As a result, the chelated zirconia-modified paper separators exhibit extended cycling, better Li transference number and high interfacial stability.

(v) Apart from these passive ceramic and clay-based filler materials, ion-conducting active ceramic such as LLZO has also been incorporated in paper matrix. This provided an alternative lithium migration pathway, thereby enhancing ion conductivity and transport phenomena. Also, LLZO helps in modifying the surface of paper in such a way that the thermal stability and self-extinguishing nature of separator enhanced significantly. This study is described in ***Chapter 8***.

(vi) Finally, with all these optimizations, we moved toward the development of paper-based electrolyte which will successfully replace both polyolefin separator and liquid electrolyte. Development and performance optimization of this ultimate separator-cum-electrolyte membrane have been demonstrated in ***Chapter 9***.

A graphical overview of the research works conducted under this thesis timeline along with their key findings, is provided in the thesis roadmap of ***Figure 1.13***.

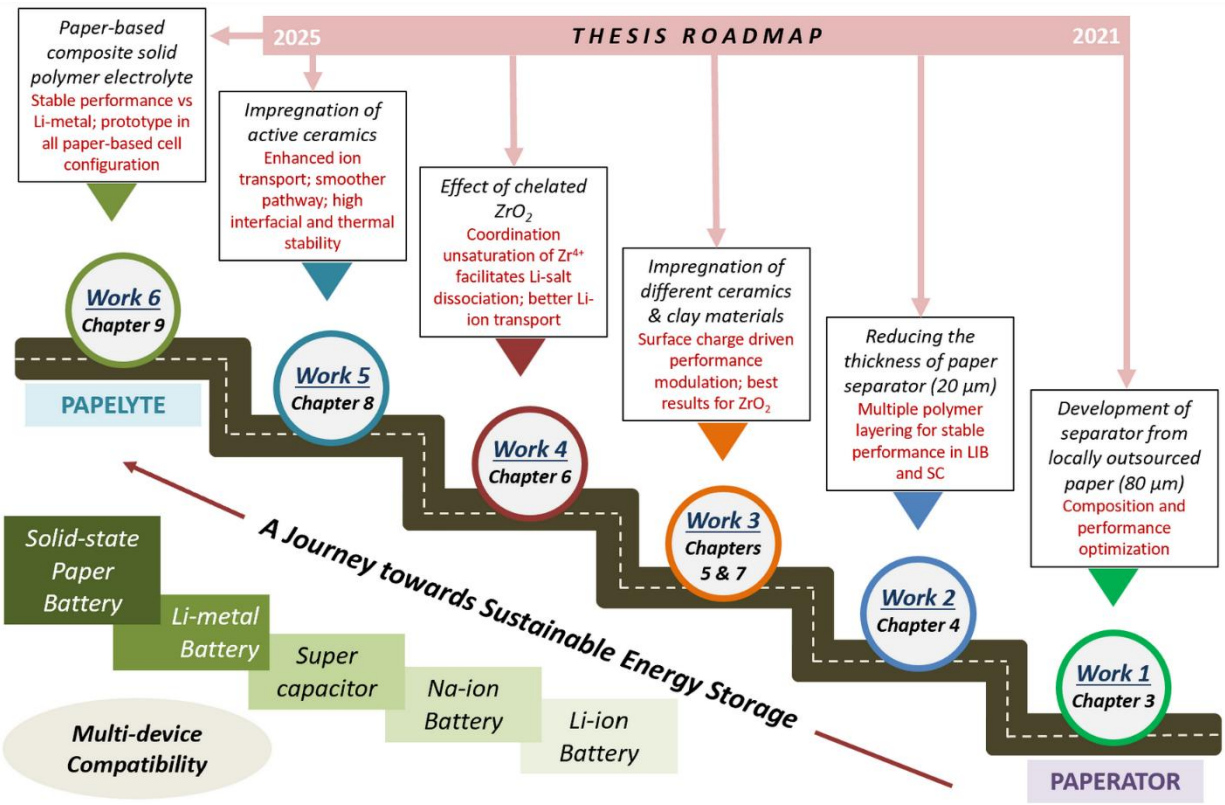

Figure 1.13 *Visual summary of the roadmap of the thesis*

References

1 M. E. Munawer, *Journal of Sustainable Mining*, 2018, **17**, 87–96.

2 Z. Qin, J. Ma, M. Zhu and T. Khan, *Energy Strategy Reviews*, 2025, **59**, 101710.

3 K. R. Ngoy, V. T. Lukong, K. O. Yoro, J. B. Makambo, N. C. Chukwuati, C. Ibegbulam, O. Eterigho-Ikelegbe, K. Ukoba and T.-C. Jen, *Renewable and Sustainable Energy Reviews*, 2025, **223**, 115971.

4 G. of I. NITI Aayog, *Unlocking a $200 Billion Opportunity: Electric Vehicles in India*, 2025.

5 International Energy Agency, *Net Zero by 2050 A Roadmap for the Global Energy Sector*, 2021.

6 International Energy Agency, *Global EV Outlook 2025*, 2025.

7 N. Tilly, T. Yigitcanlar, K. Degirmenci and A. Paz, *Sustain Cities Soc*, 2025, **131**, 106739.

8 G. of I. NITI Aayog, G. of I. Ministry of Power, I. Department of Science and Technology and R. C. WRI India, *HANDBOOK of ELECTRIC VEHICLE CHARGING INFRASTRUCTURE IMPLEMENTATION Version I*, 2021.

9 G. of I. Ministry of Heavy Industries, *PM e-DRIVE AND PLI SCHEMES*, 2025.

10 G. of I. Ministry of External Affairs, *National Statement by Prime Minister Shri Narendra Modi at COP26 Summit in Glasgow*, 2021.

11 International Energy Agency and G. of I. NITI Aayog, *Transitioning India's Road Transport Sector Realising climate and air quality benefits*, 2023.

12 J.-M. Tarascon and M. Armand, *Nature*, 2001, **414**, 359–367.

13 M. D. Slater, D. Kim, E. Lee and C. S. Johnson, *Adv Funct Mater*, 2013, **23**, 947–958.

14 J. Janek and W. G. Zeier, *Nat Energy*, 2016, **1**, 16141.

15 K. Dissanayake and D. Kularatna-Abeywardana, *J Energy Storage*, 2024, **96**, 112563.

16 C. V. M. Gopi and R. Ramesh, *Results in Engineering*, 2024, **24**, 103598.

17 Tanwa M. Iwayemi, Stanley O. Tomomewo, Sudhanshu Choudhary and Daniel Kelly Boakye-Danquah, *International Journal of Latest Technology in Engineering Management & Applied Science*, 2025, **14**, 363–385.

18 C.-J. Yang and R. B. Jackson, *Renewable and Sustainable Energy Reviews*, 2011, **15**, 839–844.

19 H. Zhang, J. Baeyens, G. Cáceres, J. Degrève and Y. Lv, *Prog Energy Combust Sci*, 2016, **53**, 1–40.

20 I. Staffell, D. Scamman, A. Velazquez Abad, P. Balcombe, P. E. Dodds, P. Ekins, N. Shah and K. R. Ward, *Energy Environ Sci*, 2019, **12**, 463–491.

21 Petr Vanýsek, *CRC Handbook of Chemistry and Physics, 91th Edition*.

22 J. B. Goodenough and K.-S. Park, *J Am Chem Soc*, 2013, **135**, 1167–1176.

23 A. Manthiram, *Nat Commun*, 2020, **11**, 1550.

24 N. Nitta, F. Wu, J. T. Lee and G. Yushin, *Materials Today*, 2015, **18**, 252–264.

25 J.-M. Tarascon and M. Armand, *Nature*, 2001, **414**, 359–367.

26 J. Cabana, Z. Stoeva, J. J. Titman, D. H. Gregory and M. R. Palacín, *Chemistry of Materials*, 2008, **20**, 1676–1678.

27 S. Lee and A. Manthiram, *ACS Energy Lett*, 2022, **7**, 3058–3063.

28 P. Poizot, S. Laruelle, S. Grugeon, L. Dupont and J.-M. Tarascon, *Nature*, 2000, **407**, 496–499.

29 W. J. Jeong, C. Wang, S. G. Yoon, Y. Liu, T. Chen and M. T. McDowell, *ACS Energy Lett*, 2024, **9**, 2554–2563.

30 M. Jareer, B. K, S. Safa and S. Shahgaldi, *J Alloys Compd*, 2025, **1010**, 177124.

31 X. Xia, X. Qian, C. Chen, W. Li, D. He, G. He and H. Chen, *J Energy Storage*, 2023, **72**, 108715.

32 P. G. Bruce, S. A. Freunberger, L. J. Hardwick and J.-M. Tarascon, *Nat Mater*, 2012, **11**, 19–29.

33 J.-L. Brédas, J. M. Buriak, F. Caruso, K.-S. Choi, B. A. Korgel, M. R. Palacín, K. Persson, E. Reichmanis, F. Schüth, R. Seshadri and M. D. Ward, *Chemistry of Materials*, 2019, **31**, 8577–8581.

34 M. S. Whittingham, *Science (1979)*, 1976, **192**, 1126–1127.

35 K. Mizushima, P. C. Jones, P. J. Wiseman and J. B. Goodenough, *Mater Res Bull*, 1980, **15**, 783–789.

36 A. K. Padhi, K. S. Nanjundaswamy and J. B. Goodenough, *J Electrochem Soc*, 1997, **144**, 1188–1194.

37 A. Yoshino, *Angewandte Chemie International Edition*, 2012, **51**, 5798–5800.

38 C. Zhu, T. Liu, F. Qian, W. Chen, S. Chandrasekaran, B. Yao, Y. Song, E. B. Duoss, J. D. Kuntz, C. M. Spadaccini, M. A. Worsley and Y. Li, *Nano Today*, 2017, **15**, 107–120.

39 K. Xu, *Chem Rev*, 2004, **104**, 4303–4418.

40 Y. Yamada, K. Usui, K. Sodeyama, S. Ko, Y. Tateyama and A. Yamada, *Nat Energy*, 2016, **1**, 16129.

41 P. Arora and Z. (John) Zhang, *Chem Rev*, 2004, **104**, 4419–4462.

42 Z. Liu, Y. Jiang, Q. Hu, S. Guo, L. Yu, Q. Li, Q. Liu and X. Hu, *ENERGY & ENVIRONMENTAL MATERIALS*, 2021, **4**, 336–362.

43 M. R. Palacín, *Chem Soc Rev*, 2018, **47**, 4924–4933.

44 J. Jang, J. Oh, H. Jeong, W. Kang and C. Jo, *Materials*, 2020, **13**, 4625.

45 G. Venugopal, J. Moore, J. Howard and S. Pendalwar, *J Power Sources*, 1999, **77**, 34–41.

46 C. M. Costa, Y.-H. Lee, J.-H. Kim, S.-Y. Lee and S. Lanceros-Méndez, *Energy Storage Mater*, 2019, **22**, 346–375.

47 Y. Yu, M. Liu, Z. Chen, Z. Zhang, T. Qiu, Z. Hu, H. Xiang, L. Zhu, G. Xu and M. Zhu, *Advanced Fiber Materials*, 2023, **5**, 1827–1851.

48 W. Ding, C. Ru and L. Xu, *J Energy Storage*, 2024, **102**, 114200.

49 V. Gregorio, J. H. Chang, N. García and P. Tiemblo, *J Memb Sci*, 2025, **730**, 124187.

50 S. C. Mun and J. H. Won, *Crystals (Basel)*, 2021, **11**, 1013.

51 L. Carvalho, G. Mattos, N. Sitton, J. Barros, D. Miranda, R. Luciano and J. C. Pinto, *Processes*, 2025, **13**, 2114.

52 J. Sun, C. Liu, X. Song, J. Zhang, Y. Liu, L. Liang, R. Jiang and C. Yuan, *Appl Phys Rev*, DOI:10.1063/5.0086130.

53 Plastics Europe, *Plastics – the fast Facts 2024*, 2024.

54 M. Das, P. S. Das, R. N. Basu and M. W. Raja, *Cellulose*, DOI:10.1007/s10570-022-04873-3.

55 F. Jiang, L. Yin, Q. Yu, C. Zhong and J. Zhang, *J Power Sources*, DOI:10.1016/j.jpowsour.2014.12.090.

56 Q. Xu, Q. Kong, Z. Liu, J. Zhang, X. Wang, R. Liu, L. Yue and G. Cui, *RSC Adv*, DOI:10.1039/c3ra45879b.

57 R. Pan, X. Xu, R. Sun, Z. Wang, J. Lindh, K. Edström, M. Strømme and L. Nyholm, *Small*, DOI:10.1002/smll.201704371.

58 T. Guo, J. Song, Y. Jin, Z. Sun and L. Li, *Carbohydr Polym*, DOI:10.1016/j.carbpol.2018.11.025.

59 J. C. Roberts, *The Chemistry of Paper*, 1996.

60 X. Zeng, Y. Liu, R. He, T. Li, Y. Hu, C. Wang, J. Xu, L. Wang and H. Wang, 2021, preprint, DOI: 10.21203/rs.3.rs-1038574/v1.

61 W. Wang, X. Long, L. Pang, D. Shen and Q. Wang, *Front Chem Sci Eng*, 2024, **18**, 144.

62 W. Ying, C. Zhou, H. Sun and W. Huang, *npj Flexible Electronics*, 2025, **9**, 80.

63 Z.-X. Cai, M.-Z. Jiang, Y.-J. Chuang and J.-N. Kuo, *Sensors*, 2024, **24**, 4792.

64 M. Tanveer, T. Ambreen, H. Khan, G. Man Kim and C. Woo Park, *Energy Convers Manag*, 2022, **264**, 115732.

65 A. M. Divakaran, M. Minakshi, P. A. Bahri, S. Paul, P. Kumari, A. M. Divakaran and K. N. Manjunatha, *Progress in Solid State Chemistry*, 2021, **62**, 100298.

Chapter 2

Research Methodology

Highlights

- Strategies adopted for the preparation and modification of paper-based separators and composite electrolytes
- Experimental techniques used for structural, physicochemical, mechanical, and electrochemical characterizations
- To establish the methodological framework linking material processing with performance evaluation in sustainable energy storage applications

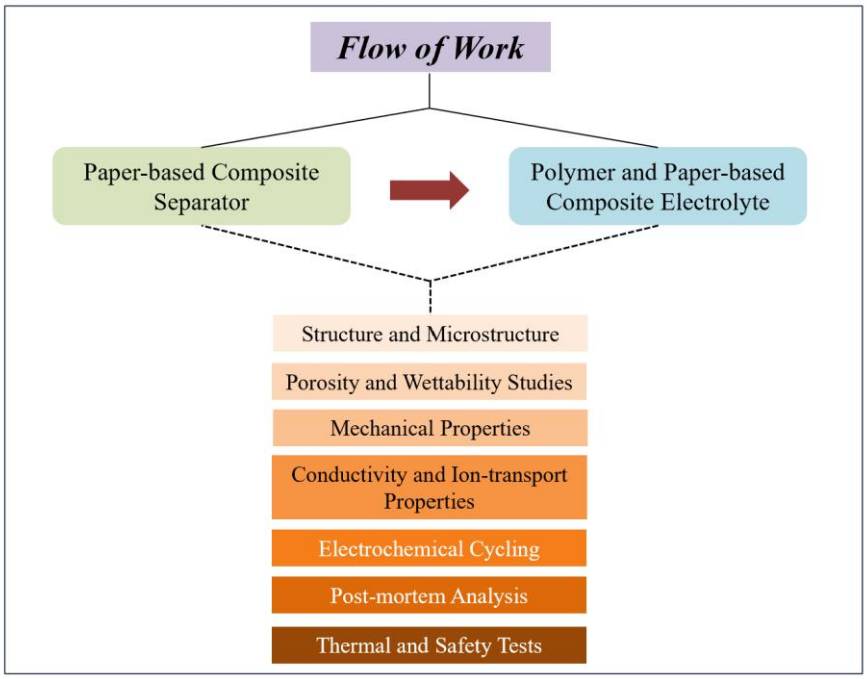

Figure 2.0 *Flow of the experimental works done under the scope of this research*

Every scientific experiment needs a set of materials, instruments and techniques for it to attain success. The present chapter provides the details of the experiments accomplished throughout the timeline of the research summarized in this thesis. The development of paper-based ceramic separators and electrolytes for sustainable energy storage applications went through various stages. During the material development phase, we had to optimize the fabrication process as well as the component compositions extensively. In the later stage, we measured the physical, mechanical and electrochemical phenomena of the developed membranes, and tried to find the science behind the happenings.

2.1 Overview

This chapter outlines the experimental framework established to develop and evaluate cellulose-based paper separators and composite polymer electrolytes for safe, high-performance lithium-ion batteries. It first describes the selection and handling of raw materials and the fabrication strategies - including aqueous and solvent-based sizing, ceramic impregnation, lamination and solution-casting of PVDF-HFP/LiTFSI-based composite films - that were optimised to produce mono-, bi- and tri-layer paper-derived membranes. A hierarchical characterisation pathway is then presented: microstructural and morphological features are examined (FESEM/EDX, XRD) to assess filler distribution and crystallinity; physical properties (thickness, Gurley air permeability, porosity, wettability, tensile behaviour and zeta potential) quantify electrolyte uptake, mechanical integrity and pore architecture; thermal and safety performance is probed through TGA/DTA, shrinkage, flame test/SET, shutdown and thermal-shock tests; and electrochemical functionality is evaluated via EIS (with DRT analysis), LSV, DC polarization, CCD and galvanostatic cycling in symmetric and full-cell configurations. All measurements were performed under controlled atmosphere where required and with statistical replication to ensure reproducibility. The methods are organised to correlate processing → structure → properties → performance, and the detailed procedures and instrumentation are presented in the following sections; results and discussion of specific compositions appear in Chapters 3–9.

2.2 Materials and Chemicals

The present thesis work focuses on the development of composite separator and electrolyte systems for energy storage devices. A set of materials and chemicals was used to carry out the research work. ***Table 2.1*** represents a dedicated list of the chemicals and reagents used in this thesis. All the commercial chemicals have been used without any further purification. Highly moisture-sensitive materials have always been stored and handled inside an argon-filled glove box (MBraun, Germany) (H_2O<0.1 ppm and O_2< 0.1 ppm, make: MBraun, Germany) to avoid any exposure, degradation, or parasitic side reactions during synthesis, storage, and cell fabrication.

Table 2.1 *Details of the materials and chemicals used in the research*

Sl. No.	Material	Make/Source	Purity/Assay
1	Cellulose paper (Thickness ~ 80/90 µm)	Local market	Impurities present
2	Cellulose paper (Thickness ~ 20/25 µm)	Bat-Sol Equipment and Technology, India	100% pure cellulose
3	PP-based commercial separator for LIBs	Maxtiger, China	100% pure PP/PE
4	Chitosan	Sigma-Aldrich	≥99.9%
5	Polyvinyl alcohol (PVA)	Sigma Aldrich	≥99.9%
6	Styrene butadiene rubber (SBR) suspension	MTI Corporation, USA	49.0-51.0%
7	Polyvinylidene fluoride (PVDF)	MTI Corporation, USA	≥99.99%
8	Polyvinylidene fluoride co-hexafluoropropylene (PVDF-HFP)	Sigma Aldrich	≥99.9%
9	Polyethylene oxide	Sigma Aldrich	≥99.8%
10	N-Methyl-2-pyrrolidone (NMP)	Sigma Aldrich	≥99.99%
11	N,N-Dimethylformamide	Sigma Aldrich	≥99.99%
12	Acetic acid	SRL	≥99.0%
13	1-propanol	SRL	≥99.0%
14	Miilipore water	-	Pure
15	Aluminum oxide	Sigma Aldrich	≥99.99%
16	Barium titanium oxide	Sigma Aldrich	≥99.99%
17	Zirconium dioxide	Sigma Aldrich	≥99.99%
18	Silicon dioxide	Sigma Aldrich	≥99.99%
19	Lithium bis(trifluoromethanesulfonyl)imide (LiTFSI) (anhydrous)	Sigma Aldrich	≥99.99%
20	Li-foil	MTI Corporation, USA	100% pure
21	Mesocarbon microbead (MCMB) powder	MTI Corporation, USA	≥99.99%
22	$Li_4Ti_5O_{12}$ anode powder	MTI Corporation, USA	≥99.99%
23	$LiFePO_4$ cathode powder	MTI Corporation, USA	≥99.99%
24	$LiNi_{1/3}Mn_{1/3}Co_{1/3}O_2$ cathode powder	MTI Corporation, USA	≥99.99%
25	$LiMn_2O_4$ cathode powder	MTI Corporation, USA	≥99.99%
26	$LiCoO_2$ cathode powder	MTI Corporation, USA	≥99.99%
27	$LiPF_6$ in EC:DMC (1:2) liquid electrolyte	MTI Corporation, USA	≥99.99%
28	$NaPF_6$ powder	Sigma Aldrich	≥99.9%
29	Active carbon (Super P)	MTI Corporation, USA	≥99.9%
30	Lithium nitrate ($LiNO_3$)	SRL	≥99.5%
31	Lanthanum nitrate hexahydrate ($La(NO_3)_3.6H_2O$)	SRL	≥99.5%
32	Zirconyl nitrate hydrate ($ZrO(NO_3)_2.xH_2O$)	Sigma Aldrich	≥99.9%
33	Alanine ($C_5H_7NO_2$)	Merck	>99%

2.3 Development of Paper Separators

As directed by the introductory chapter, we have tried to develop cellulose paper-based sustainable separators, that have shown comparable physico-chemical and electrochemical performances as compared to commercial LIB separator. Optimized thickness and porosity, high thermal and mechanical stability, good Li-ion conductivity etc are some crucial parameters to develop a workable separator for batteries. With our broader vision of developing EV-ready separators, greater emphasis has been put to enhance the thermal stability as well as cycling performance. Paper consists of mainly cellulose along with some amounts of hemicellulose and lignin. The linear chain structures of cellulose provide mechanical integrity to paper, mainly due to the presence of intra- and intermolecular hydrogen bonds. Cellulose micro and nanofibers create a cross-linked network inside the paper matrix along with some pore spaces. The porosity and mechanical strength of paper are not always up to the standard of a battery separator. That is why the paper substrate should be sized and functionalized with some suitable polymer and ceramic materials prior to be used as a separator or as an electrolyte membrane. The sizing and ceramic impregnation inside the paper matrix are done via a wet-coating process using an in-house designed double-decker fabricator machine, as shown in ***Figure 2.1***.

Figure 2.1 *Digital image of the in-house designed separator fabricating semi-automated double-decker machine; (A) feeding zone for cellulose based locally outsourced commercial paper roll, (B) coating chamber, (C) Infrared thermal zone for drying at upper cabinet, (D) Infrared thermal zone for drying at lower cabinet and (E) final separator product in roll form*

2.3.1 Separator with Higher Thickness

At the initial stage of the research work, a paper substrate was chosen from local market, whose thickness (~80 μm) is much higher than the commercial separator standard. The aim was to first confirm whether paper can truly be used inside an electrochemical environment or not. After buying, we had observed the microstructure of the paper substrate and we had done EDX analysis to see what elements were present inside it. Quite expectedly, the raw paper substrate consisted of several impurities, which needed to be anchored before its implementation as a separator in a battery.

For this purpose, the cellulose paper had been coated with Chitosan, which is the second most abundant natural polymer on earth (first is cellulose itself). Chitosan was dissolved in acetic acid in 0.25, 0.50 and 1.00 w/v% by continuous stirring. Next, an aqueous solution of polyvinyl alcohol (PVA) and was prepared via stirring and mildly heating at 60°C. The concentration of PVA was varied within the range of 0.1-0.6 w/v%. This solution was mixed with the already prepared solution of Chitosan in 3:1 volume ratio. After that, a nanoceramic powder ($BaTiO_3$ or SiO_2) was dispersed in the polymer solution via stirring for 12h. The amount of ceramic powder was also varied with the concentrations of 0.1, 0.5, 1.0 and 1.5 w/v%. The details of the compositions and their respective nomenclature used have been provided in ***Chapter 3***. After the final solution is prepared, it is put in the solution chamber of the separator fabricator machine. The paper substrate was previously dried at 80°C under vacuum for de-moisturization purpose. The ceramic-polymer blend with optimum viscosity was then applied to both the surfaces of the cellulose paper substrate by dip-coating technique as illustrated schematically in ***Figure 2.2***. The coated paper was dried in-situ under two infrared thermal zones located both at upper and lower decks of the fabricator machine and finally winded in roll form. The dried separator roll was then compacted using double roller calendaring machine under varying pressure of 60-300 tons. The thickness of the paper was reduced to 60-70 μm after drying and compaction.

The paper separator was further named as Paperator and it was stored carefully for the physical and electrochemical characterizations. Before each experiment, the paper had been oven-dried at 60°C under vacuum since cellulose is generally very much hydrophilic in nature. Also, before cell fabrication, the paper separators had been kept in the evacuated anti-chamber of the Ar-filled glove box for overnight to remove any traces of surface moisture. The physical and electrochemical experiments proved that paper can be successfully used as LIB separator after effective treatment. While the electrochemical performance of paperator had matched the

benchmark of commercial PP-based separator, the thermal stability and electrolyte wettability had surpassed the commercial standard by a significantly high margin.

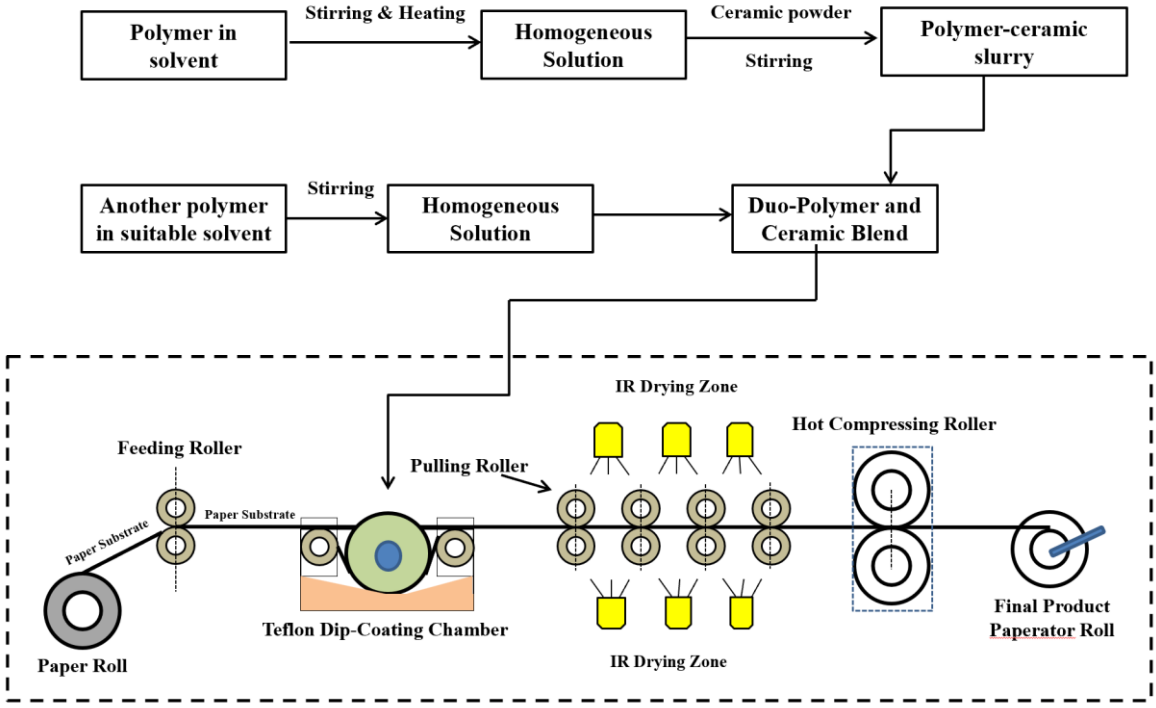

Figure 2.2 *Process flow chart along with schematic representation of paper separator fabrication process*

2.3.2 Paper Separator with the Thickness of Commercial Standard

After successful conversion of the locally available paper into paper separator, we tried to reduce its thickness to the commercial standard. While commercially available separators are 20-25 µm thick, our paper substrate's thickness was nearly 4 times of that. This is the reason we decided to change the paper substrate. NKK paper was already being used as separator in Supercapacitors, whose thickness is 18-22 µm. We had chosen a paper substrate very similar to the NKK paper with no added impurities. With that, the issues with the unwanted substances present inside the paper matrix were faded away. The surface morphology of the paper substrate was observed by FESEM imaging; simultaneous EDX analysis proved the purity of paper. These details are provided in ***Chapters 4, 5*** and ***8***.

Similar to the previous method, this time also the paper substrate was oven-dried for 12h before separator fabrication process. Since the paper substrate purely is made up of cellulose, aqueous coating like previous is not possible. In aqueous medium, cellulose gets dissolved and the structure of the paper is deformed, as paper is originally derived from aqueous cellulose slurry.

Also, the surface of the raw paper is quite rough and uneven. These are the reasons that the paper needs to be sized with a polymeric solution before any aqueous coating. The polymer helps to coat the individual cellulose fibers, strengthen them and maintain their structural integrity throughout further steps of separator fabrication. In the second layer of coating, the ceramic particles are introduced which enhance the electrolyte wettability, thermal stability and interfacial contact of the separator. However, one drawback of this bilayer separator is that ceramics may leach out from the separator surface and contaminate the electrolyte during long-term cycling of the battery. We faced such issues in the previous method also. To mitigate this problem, a lamination layer of very low concentration of polymer solution is given on the top surface of the paper separator. The overall process gives rise to a trilayer paper separator which is elaborately discussed in ***Chapter 4***.

2.3.2.1 Monolayer Separator

With the paper substrate of ~20 μm thickness, monolayer separator can also be developed, where the ceramic particles are introduced in the first sizing layer only. An optimized amount (generally 3-5 w/v%) of polyvinylidene fluoride (PVDF) was dissolved in N-Methyl-2-Pyrrolidone (NMP) solvent, by mild heating and continuous stirring for 6h. After that, the desired ceramic nanopowder was added in the solution in optimal ratios and it was stirred for overnight. On the next day, the solution is put in the solution chamber of the double-decker equipment and the previously dried paper substrate was dip-coated by the solution . The coating and drying were done following the previous processes mentioned in ***Section 2.2.1***. The paper separators in roll form were compacted in a double roller calendaring machine under 20-30 tons of pressure. In Chapter 8, paper separators impregnated with Li-ion active ceramics have been developed by this process.

2.3.2.2 Bilayer Separator

The pure cellulose-based paper was first coated with a 3.5 w/v% PVDF in NMP solution for sizing purpose. After coating and drying, the paper was compacted under a load of 50-60 tons and named as P35. It was again dip-coated with an aqueous ceramic-polymer blend to get the final bilayer paper separator. For this, styrene butadiene rubber is dissolved in deionized water via stirring, in an optimized proportion. Then the ceramic material is added in the solution and stirred for 12h. The oven-dried P35 paper is again dip-coated with this solution in the same double-decker separator fabricator unit. The drying and compaction process are also same as

previous. The final product is a bilayer separator in roll form. Paper separators have been fabricated using this process in ***Chapters 5, 6*** and *7*.

2.3.2.3 Trilayer Separator

After two layers of successive coatings, the paper was further coated with an aqueous solution of SBR withs varying concentration of 1.0-3.0 w/v%. This is lamination step, which provides smooth separator surface, minimized pore spaces and a protective layer to impede the dissolution and/or leaching of ceramic particles in electrolyte under actual cell environment. After lamination step, the in-situ dried paper separator was finally compacted under pressure of 20-30 tons using the calendaring machine. Paper separators in Chapter 4 were fabricated using this trilayer technique.

All the fabricated paper separators obtained at different stages (sizing, ceramic impregnation and lamination) were stored carefully for further characterizations.

2.4 Development of Polymer Electrolytes

After successfully developing paper-based composite separators for metal-ion batteries and supercapacitors, the next aim of this research work is to develop sustainable separator-cum-electrolyte membranes that will potentially replace both the flammable liquid electrolyte and plastic separator. It will also be used against Lithium metal whose capacity and energy density are highest among the available battery electrodes. To develop composite polymer electrolytes, we have used polyvinylidene fluoride co-hexafluoropropylene (PVDF-HFP) as the base polymer. A Li-salt namely lithium bis(trifluoromethanesulfonyl)imide (LiTFSI) was incorporated in the polymer matrix for enhancing Li-ion conductivity of the electrolyte membranes.

2.4.1 Composite Solid Polymer Electrolytes (CSPEs)

The composite solid polymer electrolytes (CSPEs) were fabricated using a simple solution casting method, as described in ***Figure 2.3***. All the reagents were previously vacuum dried for 24h to remove residual moisture. The PVDF-HFP was then dissolved in N,N-dimethylformamide (DMF) via stirring at high temperature. After dissolving, LiTFSI was added, and the solution was stirred for a few more hours. Then, optimized amounts of ceramic nanopowders were added to the solution to obtain the CSPE suspensions. Those were then cast

on a PTFE substrate using a doctor's blade. The free-standing CSPE films were vacuum dried and then collected for further testing. Along with them, the PVDF-HFP and LiTFSI-based CSPE film with no added ceramic was also fabricated for comparison. In ***Chapter 9***, CSPEs were developed using this process; further details and compositions are duly reported in that chapter.

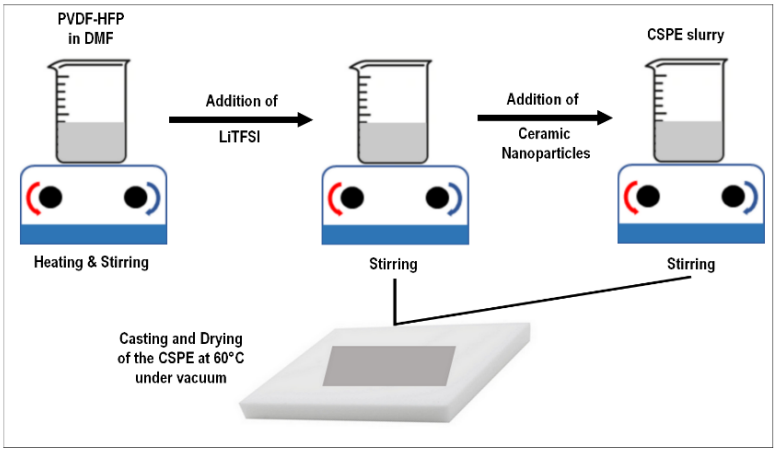

Figure 2.3 *Schematic representation of the fabrication process of CSPEs*

2.4.2 Paper-based CSPEs

Before proceeding with the paper-supported CSPE, a duo-polymer-based CSPE has been developed to enhance the room temperature ionic conductivity to a significant extent. For this purpose, an optimal amount of polyethylene oxide (PEO) of the total polymer was added in the primary polymer solution of PVDF-HFP in DMF. After homogeneous mixing, the optimized amount of nanoceramic powder was added to it and dispersed well via prolonged stirring. Some portion of this solution was cast as it is to get a free-standing CSPE film. The remaining portion is put in the sample chamber of the semi-automated double-decker separator fabricator unit, presented in ***Figure 2.1***. The oven-dried pure cellulose paper roll (thickness ~ 20 µm) is coated by the solution in both sides and air dried in the IR drying zone of the same instrument. After initial drying, the paper-based CSPE membrane is transferred to a vacuum oven. The coated paper is further compacted and collected in roll form with a uniform thickness of ~60±5 µm.

2.5 Characterization Techniques and Instruments

A comprehensive set of structural, physico-chemical, thermal, electrical, and electrochemical experiments was used to investigate the functional properties of the developed separator and electrolyte membranes inside and outside the cell environment. An effort was made to correlate the fabrication processes and strategies with microstructure, thermal properties, ion-transport, interfacial stability, and post-electrochemical studies. In this way, an end-to-end approach is

produced which ranges from sustainable and cost-effective material design to performance modulation.

2.5.1 Physical Characterizations

2.5.1.1 Thickness

A thickness gauge with model no. CD-6" CSX from Mitutoyo Corp., Japan has been used to measure the thickness of all the fabricated as well as commercial membranes.

2.5.1.2 Air Permeability

Air permeability is a critical parameter for evaluating the porosity and tortuosity of separator membranes, as these structural features strongly influence electrolyte uptake and ionic conductivity. It is measured in terms of Gurley value, which can be defined as the time required for a fixed volume of air to pass through a given area of the separator under a constant pressure. The Gurley measurement was carried out using a Gurley precision instrument (Model No. 4110N). A lower Gurley number corresponds to higher air permeability, indicating a more open pore structure, while higher values suggest denser membranes with restricted flow pathways. In the context of battery separators, an optimum balance is essential: excessively high permeability may compromise mechanical strength and safety, whereas very low permeability can hinder electrolyte infusion and ionic transport.

2.5.1.3 Electrolyte Uptake and Wettability

To quantify the electrolyte uptake capability of fabricated separators, circular disks of each sample with diameter of 19 mm have been cut and they are soaked in the standard liquid electrolyte (1M $LiPF_6$ in Ethylene carbonate (EC):Dimethyl carbonate (DMC) (1:2)) for 2h inside glove box. The following equation has been used to measure their electrolyte uptake percentage:

$$\text{Electrolyte uptake} = \frac{W_{wet} - W_{dry}}{W_{dry}} \times 100\% \quad (2.1)$$

where Wdry and Wwet are the respective separator weights before and after the absorption of liquid electrolyte.

Another important parameter for the separators is electrolyte wettability. In our research work, this property is analysed by measuring the contact angle of the separator membranes with the standard liquid electrolyte solution. The contact angle measurement has been carried out using

Data Physics OCA 15PRO, Germany. Consecutive values of contact angle for each separator have been measured in 10-60s time interval.

2.5.1.4 Pore Characteristics

The porosity (%) of the separator membranes is calculated using the following relation[1,2]:

$$Porosity\ (\%) = \frac{(W_{wet} - W_{dry})/\rho_e}{v_{sep}} \tag{2.2}$$

where W_{dry} and W_{wet} are the weights of the separator before and after electrolyte absorption, ρ_e is the density of the liquid electrolyte, and v_{sep} is the geometric volume of the separator. This method correlates the electrolyte uptake with the accessible pore volume, thereby providing an estimation of the effective porosity available for ionic transport.

The Brunauer–Emmett–Teller (BET) adsorption isotherms of the developed separators were obtained using a Surface Area & Pore Size Analyzer (NOVA 4000e, Quantachrome, USA). Prior to analysis, all samples were degassed at 100 °C under vacuum (1×10^{-3} Pa) for 10 h. Nitrogen adsorption–desorption at 77 K was used to evaluate specific surface area from the BET equation,

$$\frac{1}{w[(p_0/p)-1]} = \frac{1}{w_m \times C} + \frac{C-1}{w_m \times C \times (p_0/p)} \tag{2.3}$$

where, p is the equilibrium pressure of the adsorbate**,** p_0 is the saturated equilibrium vapour pressure of the adsorbate, w is the weight of gas adsorbed at a relative pressure, w_m is the weight of adsorbate constituting a monolayer of surface coverage, C is a constant, which is an indication of the magnitude of the adsorbent/adsorbate interactions. Pore volume and size distributions have been determined by the Barrett–Joyner–Halenda (BJH) method[3,4]. The BET model relates the volume of gas adsorbed to the exposed surface area, whereas the BJH approach provides pore size distribution from the isotherm data.

2.5.1.5 Tensile Properties

Mechanical robustness is an indispensable property for separator and electrolyte membranes, as they must withstand stresses during electrode stacking, cell fabrication, and repeated electrochemical cycling without tearing or deformation. Tensile strength, elongation at break, and Young's modulus were measured using a Universal Testing Machine (Model No. 5500R, INSTRON, UK) equipped with a 1 kN load cell, operated at varying crosshead speeds of 5-10

$mm.min^{-1}$. Samples were cut into rectangular strips of desired dimensions, and tensile tests were performed along both the machine direction (MD) and transverse direction (TD) to capture anisotropy in mechanical behavior arising from the fibrous paper matrix. The tensile data provide insights into the reinforcing role of polymer sizing layers and ceramic impregnation, which are expected to enhance fiber bonding and load distribution within the separator. Thus, the tensile property evaluation not only benchmarks the developed paper separators against commercial polypropylene (PP) membranes but also establishes their reliability for practical battery applications.

2.5.1.6 Zeta Potential

Zeta potential measurements were performed by electrophoretic light scattering (ELS) technique, to evaluate the surface charge of aqueous suspension of pure cellulose paper and LLZO particles dispersed in ethanol. Zeta potential is an indicator of suspension stability dominated by surface charge, whose higher absolute values correspond to better electrostatic stabilization and a lower tendency for agglomeration. The zeta potential data were thus used to assess the effective surface charge and dispersion stability of ceramic powders in contact with cellulose paper, which influence subsequent processing and microstructural evolution. All measurements were carried out using a Malvern Zetasizer Nano series instrument after ultrasonication-assisted dispersion of the materials in suitable solvents.

2.5.2 Structure and Microstructure

The structural and microstructural details of the developed membranes are crucial for determining their morphology, pore size and distribution, nature of ceramic impregnation, crystallinity etc.

2.5.2.1 Digital Images

Digital images of separator as well as electrolyte membranes have been captured using a normal mobile camera.

2.5.2.2 X-ray Diffraction (XRD) Pattern

To investigate the crystallographic structure of the separator and CSPE membranes, X-ray diffractograms have been generated using an X'pert Pro MPD XRD system (PANalytical, Netherlands) with nickel-filtered Cu Kα (λ = 1.5406 Å) radiation, irradiated at 40 kV and 40 mA, and a step size of 0.02.

It is noteworthy to mention here that X-ray diffraction is a non-destructive analytical technique used to determine the crystallographic structure, phase composition, and microstructural parameters of materials. The method is based on the interaction of incident X-rays with the periodic arrangement of atoms in a crystalline solid. When a monochromatic X-ray beam impinges on a crystal lattice, the atomic planes act as diffraction gratings and scatter the X-rays coherently. Constructive interference occurs when the path difference between reflected beams from successive lattice planes satisfies Bragg's law[5]:

$$n\lambda = 2dsin\theta \tag{2.4}$$

where n is the order of reflection, λ is the wavelength of the incident X-ray, d is the interplanar spacing, and θ is the diffraction angle.

By recording the diffracted intensity as a function of 2θ, a characteristic diffraction pattern is obtained. Each crystalline phase exhibits a unique set of diffraction peaks, allowing phase identification, crystallite size estimation, and evaluation of lattice strain and preferred orientation.

Crystallinity Index (CI) of a polymer is generally calculated from the XRD pattern using the peak fitting method by using the following equation[6,7]:

$$Crystallinity\ Index\ (CI) = \frac{A_c}{A_c+A_a} \times 100\% \tag{2.5}$$

Where, A_c is the area of the crystalline peaks and A_a is the area of the amorphous peaks. So, (A_c+A_a) in the denominator indicates the area of all the crystalline and amorphous peaks combined. In case of the CSPE films, the XRD peak for the PVDF-HFP polymer at ~20° is amorphous in nature. So, to calculate the change in crystallinity index of the polymer with the incorporation of different ceramic materials, the equation has been modified in the following way:

$$CI = \frac{Area\ of\ the\ targeted\ peak}{Area\ of\ all\ the\ crytalline\ and\ amorphous\ peaks} \tag{2.6}$$

2.5.2.3 Microstructure by SEM and FESEM

The microstructure and morphology of the separators have been studied using a Scanning Electron Microscope (SEM) of Phenom TM series, Model Pro-X, USA and a Field Emission

Scanning Electron Microscope (FESEM, Supra VP35 Carl Zeiss, Germany) followed by elemental compositional analysis by attached EDX setup.

The morphology of the composite solid polymer electrolyte (CSPE) membranes has been analyzed using a field emission scanning electron microscope (FESEM, Zeiss Gemini FE-SEM 500, Germany). EDX and elemental mapping for the samples have been obtained from the same instrument.

It is worthy to mention here that SEM basically works by scanning a focused electron beam over the surface of the given sample. It produces microscopic images from the secondary and backscattered electrons to reveal the overall morphology, surface porosity, and distribution of impregnated particles. FESEM is the advanced version of SEM, which used a field emission source of electron beam. It provides images with much higher resolution and depth. This research focuses on the development of composite separator and electrolyte membranes by incorporating polymer and ceramic in the paper matrix. Energy-dispersive X-ray spectroscopy (EDX) coupled with FESEM was also used for elemental analysis and mapping, which is highly useful for the visualization of any impurity present or distribution of the ceramic nanoparticles.

2.5.3 Spectral Characteristics

Spectroscopic techniques provide valuable insights into the molecular structure and chemical environment of the developed membranes. By probing characteristic bond vibrations and lattice dynamics, these methods help in identifying functional groups, monitoring polymer-ceramic interactions, and confirming structural modifications induced during fabrication.

2.5.3.1 Fourier Transformed Infrared (FTIR) Spectroscopy

Fourier Transform Infrared (FTIR) spectroscopy is a powerful analytical technique used to identify and characterize the functional groups present in polymeric, organic, and composite materials. It works on the principle of absorption of infrared radiation at characteristic frequencies corresponding to the vibrational modes of chemical bonds. The resulting spectra, represented as transmittance or absorbance versus wavenumber, provide information about the chemical structure, molecular interactions, and possible modifications induced during processing. In the present work, FTIR spectra were recorded using a JASCO FTIR-6300 spectrometer in the range of 4000-400 cm^{-1}. The technique was employed to monitor the incorporation of polymers, ceramic fillers, and salts into the cellulose paper matrix, as well as

to detect any changes in bonding environment arising from their interactions. Shifts in characteristic absorption bands and changes in peak intensities were carefully analysed to confirm chemical modification, presence of hydrogen bonding, and uniform distribution of additives in the developed separators and electrolyte membranes.

2.5.3.2 Raman Spectroscopy

Raman spectroscopy is a complementary vibrational technique that provides information about molecular vibrations, lattice modes, and structural order in polymers and composite materials. It is based on the inelastic scattering of monochromatic light, typically from a laser source, where a small fraction of photons undergoes energy shifts corresponding to specific vibrational transitions. The resulting Raman spectra serve as a fingerprint of the material, allowing the identification of crystalline phases, degree of structural disorder, and interactions between polymer chains and ceramic fillers. In the present study, Raman spectra of the developed separator and electrolyte membranes were recorded using a Horiba Jobin Yvon LabRam HR spectrometer with a 633 nm Ar-ion laser. The spectral data were analyzed to confirm the incorporation of ceramic fillers, investigate polymer-filler interactions, and examine changes in local bonding environments. Peak deconvolution was performed using XPSPEAK41 software to resolve overlapping vibrational modes, enabling a more accurate interpretation of structural modifications in the composite membranes.

2.5.4 Cell Fabrication

The developed separators as well as commercial paper and commercial PP-based separator are tested in real electrochemical cell environment. For this purpose, different types of cells have been prepared, especially for different energy storage applications, as described below:

2.5.4.1 Battery

Various types of cells have been prepared to determine the application potential of the separators in Li-ion Li-metal batteries:

(a) Symmetric cell

To investigate the interfacial stability and long-term Li plating/stripping behavior, symmetric cells (Li/Electrolyte/Li) were fabricated with the polymer electrolyte as well as the paper electrolyte membranes of 19 mm diameter. All cells have been assembled inside an Ar-filled glovebox (O_2 and H_2O < 0.1 ppm) to prevent parasitic reactions of Li-metal and electrolyte solvents with ambient air or moisture. Commercial Li foils

(100 μm thickness) were cut into discs (15mm diameter) and carefully stacked on both sides of the electrolyte membrane. The stack was crimped into CR2032-type coin cells with stainless steel spacers and spring components to maintain intimate contact. A moderate pressure of ~800-1200psi was applied during assembly to minimize interfacial voids, ensuring reproducible electrochemical performance. These symmetric cells were used for impedance spectroscopy, DC polarization, and long-term cycling stability tests.

On the other hand, cells with Li-ion blocking electrodes, such as stainless steel (SS), were fabricated for the measurement of ionic conductivity of the separator and electrolyte membranes.

(b) Full cell

To evaluate the practical application of developed separator and electrolyte membranes, full cells have been fabricated with commercial cathode, anode, electrolyte and Li-metal (where applicable). In most cases, mesocarbon microbead (MCMB) anode and commercial $LiFePO_4$ (LFP), $LiMn_2O_4$ (LMO), $LiCoO_2$ (LCO) and $LiNi_{1/3}Mn_{1/3}Co_{1/3}O_2$ (NMC111) cathodes were used along with $LiPF_6$ in EC:DMC (1:2) liquid electrolyte.

Homogeneous cathode slurries were prepared by mixing the active material (80 wt%), Super P carbon (10 wt%), and PVDF binder (10 wt%) in NMP. Then, the slurry was cast onto the aluminum foil using a doctor blade and dried at 100 °C overnight under vacuum. The dried cathode sheets were roll-pressed, punched into discs, and transferred into the glovebox. MCMB anode casting was done in similar manner; the only difference is that the anode slurry is cast onto copper foil itched with HCl solution. Coin cells (CR2032) were assembled, depending on the testing requirements. For NZSP-based separator, commercial NVP as a cathode and Na metal as an anode are used. The NVP cathode was cast in the same ratio (80:10:10), and 1M $NaPF_6$ solution in tetraglyme was used as the wetting medium.

It is very challenging to design all solid-state flexible metal batteries using a hybrid paper-polymer-based composite membrane. Two designs were explored in this study. Firstly, the casted composite cathode consisted of a commercial LFP cathode, composite polymer slurry, and active carbon in the weight ratio of 75:15:10. The casted slurry was coated directly onto the hybrid paper-polymer matrix for good interfacial stability. After drying and compressing, Au gold sputtering was used for coating over the composite cathode to make the electrode connection. The cells were assembled with Li metal and a hybrid paper-polymer electrolyte cum composite cathode inside the

glove box. In the second method, an in-situ polymerization approach has been used to transform the paper from an electronic insulator (>10^6 ohms) matrix to a high electronic conductor (10-20Ω). And then the previous casting step was followed for both cathode and anode. No liquid electrolyte is used in this all soli-state paper cell configuration to understand the role of the solid electrolyte in the electrical and electrochemical process.

2.5.4.2 Supercapacitor

The electrochemical performance of some of the developed separators has been explored in supercapacitors. Cylindrical type supercapacitors (SCs), of cell size 16 mm (ϕ) x 36 mm (H) were fabricated and tested at C-MET (Thrissur, India) by using their state of the art supercapacitor cell fabrication facility. Two wire-leaded carbon aerogel based electrodes (aerogel carbon casted onto thin aluminium foil current collector) were used for this purpose. Two active electrodes and two layers of separator were assembled as per the EDLC configuration and then they were co-axially winded by using semiautomatic capacitor winding machine. After degassing the electrode wounds at 60°C under vacuum, liquid electrolyte (1.0 M Et_4NBF_4, in propylene carbonate) was impregnated within electrode wounds, which then immediately sealed in aluminium cans of size 16 mm (ϕ) x 36 mm (H). Electrochemical characteristics (cell capacitacnce and cell ESR) of the SCs, thus made with the separators were tested as per IEC 62391-1 (Class-I: energy storage and Class-II: power/surge power application). Constant current charge-discharge and constant current pulsing technique were used for evaluating the cell capacitance (C_{eff}) and cell ESR respectively by using supercapacitor testing system. The charge-discharge cyclying for SCs were done between the 0.10-2.50 V DC and C_{eff} of the SCs were calculated from the discharge line of the charge-discharge curves by using the following expanded equation[8],

$$C_{eff}(Farad) = \frac{I_d \times \Delta t}{\Delta V} = \frac{I_d \times (t_2 - t_1)}{(V_1 - V_2)} \quad (2.7)$$

where C_{eff} is cell capacitance in farad, I_d (ampere) = discharge current, V_1 (volt) = 80% of V_R (V_R = upper rated voltage, 2.50 V DC), V_2 (volt) = 20% of V_R, Δt (seconds) = ($t_2 - t_1$) = time taken to discharge a charged SC from V_1 to V_2. Similarly, the cell ESR was measured by applying five consequitive current pulses of 200 mA each sequentially for 10 mS on the SC, charged at V_R (2.50V DC) and the cell ESR of SCs were caluated as[8],

$$ESR_{cell}(Ohm) = \frac{\Delta V_{pulse}}{n \times I_{pulse}} \quad (2.8)$$

where ΔV_{pulse} is the drop of voltage due to applied current pulse (I_{pulse}) and n = no. of consequtive pulses.

2.5.5 Electrical and Electrochemical Tests

The electrical and electrochemical tests carried out under this study are as follows:

2.5.5.1 Electrochemical Impedance Spectroscopy (EIS)

Electrochemical Impedance Spectroscopy (EIS) is a powerful and widely employed technique for probing the electrochemical, interfacial, and transport properties of energy storage and conversion systems. In this method, a small sinusoidal perturbation voltage (typically 5–10 mV) is applied over a broad frequency range (from MHz to mHz), and the resulting current response is measured to obtain the system's impedance as a function of frequency. Unlike steady-state electrochemical techniques, EIS provides information in both the time and frequency domains, thereby enabling the separation of resistive, capacitive, and inductive contributions associated with charge transfer, double-layer formation, diffusion, mass transport, and bulk ionic conduction. The resulting impedance data are generally represented in the form of Nyquist plots (imaginary vs. real impedance) or Bode plots (magnitude and phase vs. frequency). The ionic conductivity is calculated from the impedance recorded as real axis intercept of the Nyquist plots, using the following equation:

$$\sigma = \frac{1}{R_b} \times \frac{l}{a} \quad (2.9)$$

The ionic conductivity (σ) was assessed using the bulk resistance (R_b) of the cell, along with the thickness of the composite membrane (l) and the area of the working electrode (a).

The activation energy is calculated from the Arrhenius equation:

$$\sigma T = Ae^{-E_a/K_bT} \quad (2.10)$$

where A, E_a, and K_b are the pre-exponential factor, activation energy for ionic conduction, and the Boltzmann constant, respectively] from 303 K to 363 K

Equivalent circuit modelling is used to extract physically meaningful parameters such as bulk resistance (R_b), charge transfer resistance (R_{ct}), solid-electrolyte interphase resistance (R_{SEI}),

double-layer capacitance (C_{dl}), and Warburg impedance (W) associated with diffusion-controlled processes.

In the context of this work, EIS has been utilized to evaluate the ionic conductivity of electrolyte-soaked separators as well as of composite solid polymer electrolytes, the interfacial resistance at the electrode-electrolyte interface, and the stability of the separator under prolonged cycling conditions. Measurements were performed in various cell configurations over the frequency range of 1 MHz to 0.1 Hz in Metrohm AutoLab and ZIVE SP1 instruments, with data fitted using equivalent circuit models in ZView software to extract the relevant resistive and capacitive elements.

2.5.5.2 Distribution of Relaxation Time (DRT) Analysis

Electrochemical Impedance Spectroscopy (EIS) is a powerful tool to probe different electrochemical processes occurring during battery operation. However, interpreting EIS spectra with conventional equivalent circuit models (ECMs) can be challenging because overlapping time constants often obscure the contributions of individual processes, leading to possible misinterpretations[9–12]. To overcome this limitation, the Distribution of Relaxation Times (DRT) method has been introduced, which separates electrochemical processes based on their characteristic relaxation times, thereby simplifying EIS analysis.

The impedance response $Z(\omega)$ of an electrochemical system can be expressed as an integration of relaxation processes over a continuous distribution of characteristic times τ,

$$Z(\omega) = R_{\infty} + \int_0^{\infty} \frac{\gamma(\tau)}{1+j\omega\tau} d ln\tau \tag{2.11}$$

Where, R_{∞} is the ohmic resistance (high-frequency intercept), $\gamma(\tau)$ is the distribution function of relaxation times, τ is the relaxation time and ω is the angular frequency is described as,

$$\omega = 2\pi f \tag{2.12}$$

The function $\gamma(\tau)$ reveals the intensity of individual relaxation processes. The sharper peaks correspond to distinct resistive or capacitive processes, while the broader signals typically indicate overlapping processes. In general, the high-frequency signals correspond to bulk ionic transport in the electrolyte, the moderate frequency signals correspond to grain boundary or interphase contribution and the Low-frequency signals correspond to the electrode-electrolyte interface polarization and charge transfer.

In this work, EIS measurements were performed at different states of charge (SOC) and depth of discharge (DOD) using a ZIVE SP1 electrochemical workstation over the frequency range of 0.01 Hz–1 MHz with an applied AC amplitude of 50 mV. The DRT analysis was carried out using the open-source MATLAB-based DRTtools algorithm[13,14]. A Gaussian method with second-order Tikhonov regularization was employed, with the regularization parameter set to 0.0001. Both real and imaginary components of the EIS spectra were fitted, while inductive contributions were excluded. The resulting intensity distributions are further compiled into a two-dimensional map in MATLAB software, where the x-axis represents relaxation time (τ), the y-axis denotes cycling time (h), and the color scale corresponds to normalized DRT intensity. Fitting of DRT is further analyzed in a custom script in MATLAB software. The evolution of resistance was also shown in 2d contour map.

2.5.5.3 Linear Sweep Voltammetry (LSV)

Linear Sweep Voltammetry (LSV) is a widely employed technique to determine the electrochemical stability window of separator and electrolyte membranes, which is a crucial parameter for their safe application in rechargeable batteries. In this method, the current response is measured while the potential is linearly swept at a fixed scan rate, allowing the identification of the voltage range within which the material remains electrochemically inert. In the present work, LSV measurements were performed using 2032-type coin cells in a Li/Separator/SS asymmetric configuration, with the potential swept typically between open circuit voltage (OCV) and 6.5 V at a constant scan rate of 10 $mV.s^{-1}$. All LSV experiments were performed using a ZIVE SP1 electrochemical workstation. The onset of current rise in the LSV curve corresponds to the decomposition voltage, marking the upper stability limit of the separator-electrolyte system. By comparing the electrochemical stability windows of commercial polypropylene separators with the developed paper-based and composite membranes, the influence of polymer sizing, ceramic impregnation, and lamination layers on oxidative stability could be systematically evaluated. This analysis ensured that the fabricated membranes are capable of withstanding the high operating voltages required against mostly used electrodes in next-generation lithium batteries.

2.5.5.4 DC Polarization

DC polarization is an important electrochemical technique employed to evaluate the ionic transference number of lithium ions (t_{Li^+}) in separator and electrolyte membranes. The method involves applying a small constant DC voltage (typically 10 mV) across a symmetric

Li/Separator/Li cell and recording the initial current, steady-state current, and interfacial resistance before and after polarization. In this work, DC polarization measurements were carried out in combination with Electrochemical Impedance Spectroscopy (EIS) to decouple the bulk and interfacial resistances, and the transference number was calculated using the Bruce-Vincent-Evans relation[15], as follows:

$$t_{Li^+} = \frac{I_{SS}(\Delta V - I_0 R_0)}{I_0(\Delta V - I_0 R_0)} \quad (2.13)$$

A higher t_{Li^+} value indicates efficient transport of lithium ions relative to anions, which is desirable for reducing concentration polarization and improving rate capability in rechargeable batteries. By comparing the transference numbers of commercial polypropylene separators with those of the developed paper-based and ceramic-modified membranes, the role of ceramic fillers and polymer coatings in modulating ion transport pathways was systematically analyzed. This study thus provides critical insight into the ion-conduction mechanism of the fabricated membranes under realistic cell conditions.

2.5.5.5 Galvanostatic Charge-Discharge of Full Cells

Galvanostatic charge-discharge cycling of full cells was performed to evaluate the practical electrochemical performance of the developed separators and electrolytes under operating battery conditions. In this method, a constant current is applied during charge and discharge processes within a defined voltage window, and the cell voltage response is recorded as a function of capacity and cycle number. The cycling behavior provides key parameters such as specific capacity, coulombic efficiency, capacity retention, and interfacial stability, thereby serving as a direct assessment of the electrolyte's suitability in full-cell configurations. After performing EIS measurements, all the cells were cycled at various current densities within a potential range that depends on the cathode chemistry. All galvanostatic cycling experiments were carried out using an Arbin automated battery testing system (Arbin Instruments, USA). An isothermal vacuum oven was used to maintain a temperature of 30ºC throughout battery cycling.

2.5.5.5 Symmetric Cell Cycling

Symmetric Li/electrolyte/Li cells were galvanostatically cycled to evaluate the long-term electrochemical stability and interfacial compatibility of the developed composite polymer electrolytes with lithium metal. In this configuration, equal and opposite currents are alternately

applied to the two lithium electrodes, inducing repeated plating and stripping of lithium across the electrolyte. The temporal evolution of overpotential during cycling directly reflects the interfacial stability, dendrite growth resistance, and durability of the separator-electrolyte system. In this study, symmetric cells were operated under continuous plating/stripping cycles at fixed current densities for extended durations, ranging from several hundred to over one thousand hours. The voltage response was monitored throughout cycling, where the absence of abrupt short-circuit events or sharp voltage drops indicated stable Li deposition and effective suppression of dendritic growth. The galvanostatic tests were performed using an Arbin automated battery tester (Arbin Instruments, USA), while Electrochemical Impedance Spectroscopy (EIS) was carried out before and after cycling using a ZIVE SP1 workstation. The impedance data helped decouple bulk and interfacial resistances, providing further insight into the effects of prolonged cycling and potential dendrite penetration. Additionally, the results were correlated with post-mortem analyses to comprehensively assess the reliability of the electrolytes under long-term operation.

2.5.5.7 Electrochemical Ageing Test

The stability inside cell environment during ageing was examined by fabricating 2032 coin cell using paper separators, standard MCMB anode, $LiPF_6$ in EC/DMC electrolyte and $LiFePO_4$ cathode. The cells were aged for eight weeks without cycling at ambient temperature and EIS measurement were carried out in regular interval of one week. To study the topology of composite separator surfaces facing anode and cathode sides, the aged cells were dismantled and FESEM images were taken. The elemental composition of separator surfaces was studied using selected area EDX mapping.

2.5.6 Thermal and Safety Studies

Examining different thermal properties is crucial for separator and electrolyte membranes, since they govern the safety aspects of a cell in large extent.

2.5.6.1 Thermogravimetric and Differential Thermal Analysis

Thermal stability is a key requirement for separator and electrolyte membranes in rechargeable batteries, particularly for electric vehicle applications where safety under high-temperature operating conditions is paramount. Thermogravimetric analysis (TGA) was performed using a STA 449 F3 Jupiter thermal analyzer (NETZSCH, Germany) under air atmosphere, with a constant heating rate of $10^{o}C.min^{-1}$ from room temperature up to $1200^{o}C$. In this technique, the

weight loss of the samples was continuously monitored as a function of temperature, providing information on the decomposition steps of cellulose, polymeric binders, and ceramic fillers. The onset degradation temperature, rate of mass loss, and residual weight were compared among pure cellulose substrates, polymer-coated papers, and ceramic-loaded composites to evaluate improvements in thermal endurance. The incorporation of ceramic nanoparticles and polymer lamination layers is expected to enhance thermal resistance by retarding oxidative degradation and stabilizing the fibrous matrix. Alongside TGA, Differential Thermal Analysis (DTA) data were also recorded in the same instrument, which helped to record the heat flow associated with physical or chemical transitions during heating. The DTA curves provided complementary insights into the endothermic and exothermic events such as polymer softening, decomposition, and char formation. Together, TGA and DTA offer a comprehensive understanding of the degradation behavior, enabling direct correlation between material composition, thermal response, and safety performance of the developed membranes.

2.5.6.2 Thermal Shrinkage

To assess the dimensional integrity of the fabricated paper separators at elevated temperatures (up to 250ºC), circular disks of 19 mm diameter have been placed in a heating oven fitted with a camera, and dimensional changes were photographed at different intervals. From this experiment, thermal shrinkage of the paper separators as well as the commercial paper and commercial separator has been measured qualitatively to determine their thermal stability.

2.5.6.3 Flame Test

Flame test has been done with similar 19 mm disks of paper separators as well as polymer electrolytes, by keeping them near a flame for some time to check their flame retardancy.

Fire retardancy has also been evaluated through a vertical burning test (VBT), classifying the separators under UL 94 V ratings (V-0, V-1, and V-2)[16]. This test involves soaking of the separator samples in an electrolyte ($LiPF_6$ in EC/DMC) for 2 hours before exposing them to a flame from a certain distance, with the changes photographed over time. The photos and videos of these tests have been captured using a mobile phone camera.

2.5.6.4 Self-extinguishing Time (SET) Measurement

Self-extinguishing time is an important safety property for battery electrolytes as well as separators. To check this parameter, 19 mm disks of the membranes were cut and placed on the back side of a coin cell. Around 100 µL of liquid electrolyte was poured on their surfaces and

then they are ignited with flame. The time of ignition of electrolyte on the separator until the flame is totally extinguished was counted. It is always better for a system if the SET is less, because it proves the ability of the separator or electrolyte to self-extinguish any accidental fire occurred inside a cell[17,18]. Digital images and videos of the SET tests were recorded thoroughly with mobile camera.

2.5.6.5 Thermal Shutdown Property

Thermal shutdown is an essential safety feature of battery separators, designed to mitigate the risk of thermal runaway under abusive operating conditions. It refers to the ability of the separator to block ionic transport at elevated temperatures by pore closure or structural collapse, thereby preventing uncontrolled current flow and subsequent overheating of the cell. In the present study, shutdown behavior was investigated by monitoring ionic conductivity of separator membranes using Electrochemical Impedance Spectroscopy (EIS) in SS/Separator/SS symmetric coin cells, as described in detail in section 2.5.6.1. Measurements were first performed at room temperature to obtain baseline conductivity values, and then repeated over a temperature range of 25-160°C in steps of 5°C. The change in ionic conductivity with increasing temperature was analyzed to determine the onset and completion of shutdown.

2.5.6.6 Thermal Shock Treatment

Thermal shock experiment has been carried out to understand the behaviour of separators in a cell environment during challenging conditions, particularly important for EV application. Full cells with a configuration of MCMB/Separator/LFP, fabricated using our developed paper separators as well as the commercial separator, were cycled initially at 0.05 $mA.cm^{-2}$. After that EIS spectra of all the cells were taken and the cells were kept at 120°C for 1h. It was carefully taken out from oven and stored in a fume hood for 24h at room temperature. Then, ten electrochemical charge-discharge cycles were performed and EIS spectra of all the cells were measured after 10 cycles. The same steps were repeated one more time with a preset temperature of 150°C.

2.5.7 Data Analysis and Validation

The experimental data were analyzed with the help of Microsoft Excel and Origin 2018 Software. Every experiment has been carried out with minimum three specimens of each type of separators. The results are found to be similar and reproducible in nature.

2.6 Flow of Work

This thesis primarily focuses on the development of paper-based electrolytes for LIB application. After the fabrication step, microstructural features and morphology of the separators are observed via FESEM. Then the porosity studies and mechanical tests are performed to evaluate the wettability and robustness of the membranes. When the separator passes these tests, different types of Li-ion cells are prepared for the evaluation of ionic conductivity, operating voltage window, specific capacity, coulombic efficiency and other related parameters. When a full cell touches the specific capacity level of 20% DOD, the cycling is typically stopped and the cell is undergone several post-mortem analyses. Sometimes, the cell needs to be dismantled for this purpose. On the other hand, the separator membranes are undergone the thermal studies, which are essential for affirming the safety of a cell. For composite polymer electrolyte and paper-based electrolyte membranes also, a similar order of experiments is followed.

References

1 N. D. Koromilas, C. Anastasopoulos, E. K. Oikonomou and J. K. Kallitsis, *Polymers (Basel)*, 2019, **11**, 59.

2 L. Li and Y. Duan, *Polymers (Basel)*, 2023, **15**, 3690.

3 E. Lizundia, C. M. Costa, R. Alves and S. Lanceros-Méndez, *Carbohydrate Polymer Technologies and Applications*, 2020, **1**, 100001.

4 T. Beuse, M. Fingerle, C. Wagner, M. Winter and M. Börner, *Batteries*, 2021, **7**, 70.

5 *Proceedings of the Royal Society of London. Series A, Containing Papers of a Mathematical and Physical Character*, 1913, **88**, 428–438.

6 E. Tarani, I. Arvanitidis, D. Christofilos, D. N. Bikiaris, K. Chrissafis and G. Vourlias, *J Mater Sci*, DOI:10.1007/s10853-022-08125-4.

7 M. Doumeng, L. Makhlouf, F. Berthet, O. Marsan, K. Delbé, J. Denape and F. Chabert, *Polym Test*, DOI:10.1016/j.polymertesting.2020.106878.

8 B. E. Conway, *Electrochemical Supercapacitors*, Springer US, Boston, MA, 1999.

9 C. Plank, T. Rüther, L. Jahn, M. Schamel, J. P. Schmidt, F. Ciucci and M. A. Danzer, *J Power Sources*, DOI:10.1016/j.jpowsour.2023.233845.

10 R. Soni, J. B. Robinson, P. R. Shearing, D. J. L. Brett, A. J. E. Rettie and T. S. Miller, *Energy Storage Mater*, DOI:10.1016/j.ensm.2022.06.016.

11 A. Subhakumari, T. Thomas and N. P. B. Aetukuri, *ACS Energy Lett*, 2024, **9**, 6109–6116.

12 Y. Lu, C. Z. Zhao, J. Q. Huang and Q. Zhang, 2022, preprint, DOI: 10.1016/j.joule.2022.05.005.

13 F. Ciucci and C. Chen, *Electrochim Acta*, DOI:10.1016/j.electacta.2015.03.123.

14 T. H. Wan, M. Saccoccio, C. Chen and F. Ciucci, *Electrochim Acta*, DOI:10.1016/j.electacta.2015.09.097.

15 J. Evans, C. A. Vincent and P. G. Bruce, *Polymer (Guildf)*, DOI:10.1016/0032-3861(87)90394-6.

16 J. Troitzsch, *Flame Retardants Polymer Blends, Composites and Nanocomposites*, 1999, vol. 89.

17 S. Hess, M. Wohlfahrt-Mehrens and M. Wachtler, *J Electrochem Soc*, DOI:10.1149/2.0121502jes.

18 K. Zhou, Y. Fang, M. Bao, W. Fan, J. Ren, P. He, L. Zhang and T. Liu, *J Power Sources*, 2024, **610**, 234734.

Chapter 3

Conversion of Paper into Paper Separator

Highlights

- Paper – an abundant, low cost and sustainable alternative to polyolefin
- Modification of rough surface of paper by polymer 'sizing'
- Impregnation of ceramics to enhance thermal and electrochemical stability
- Thermal stability and safety of the cell assured
- Multi-system functionality of the separator

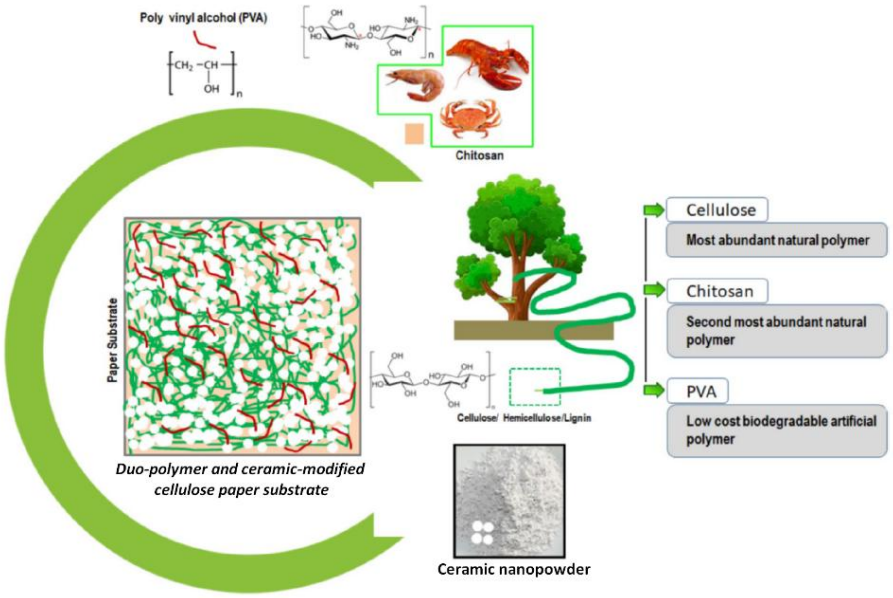

Figure 3.0 *Sustainable and eco-friendly components used for fabrication of paper separator*

This chapter describes the development of paper-based composite separators functionalized with polymer-ceramic blends, as sustainable alternatives to commercial plastic-based separator membranes. The fabrication process and separator composition have been optimized to enhance structural integrity, wettability, thermal stability, and mechanical strength of the separators. Electrochemical evaluations demonstrated their compatibility with different electrodes and comparable performance with commercial separators, while additional tests confirmed their safety and potential for large-scale production.

3.1. Background and Overview

'Separator' is an essential and important component for Li-ion batteries, supercapacitors and other similar electrochemical energy storage devices. The major tasks of separator in energy storage system, LIB & SC in particular, are to prevent physical contact between anode and cathode, to avoid electrical short-circuit, and at the same time it enables transport of ions from one electrode to other across the separator during charge-discharge process. Today's commercial lithium-ion batteries (LIBs) use polyolefin membranes as separator, which remains inert throughout the cell performance without any participation in electrochemical reaction[1–3]. Polyolefin, especially PE/PP based separators have good mechanical and shutdown properties, which can effectively prevent thermal runaway during short-circuits or overcharging of the battery. Apart from tremendous commercial success, polyolefin separators still exhibit poor electrolyte affinity due to their hydrophobic property, low electrolyte absorption rate and severe dimensional shrinkage at elevated temperature[4,5]. Modification of PP/PE surfaces with ceramics proved to be effective to resist thermal shrinkage[6]; however, stripping of ceramic particles from surfaces due to melting of binder in elevated temperature may result in breakdown of ceramic coated layer. To resist such breakdown Peng et al.[7] suggested a reinforcing layer of polypyrrole on top of ceramic coated polyolefin separator which was found to improve thermal properties along with better wettability to the electrolyte. Another approach is to use of inorganic ceramic separator without compromising other physical and electrochemical performance. Although pure inorganic ceramic separator offers several advantages over composite separator, large scale fabrication with optimum mechanical stability and flexibility is still remained a challenge[8].

Apart from these approaches, the separator materials derived from renewable sources are now being considered as sustainable alternatives for application in future energy storage devices[9]. Cellulose being a perfect sustainable material has the ability to replace traditional petroleum-derived synthetic plastics[10–12]. In addition, cellulose can be modified or functionalized to make it suitable as separators due to its several advantageous physico-chemical properties like hydrophilicity, low-density, superior mechanical strength, high porosity, good liquid absorbability, high thermal stability, low cost and natural abundance[13,14]. Therefore, development of novel cellulose-based separator materials with appropriate modification and functionalization would definitely widen the application scope of such materials in energy

storage avenue and will significantly reduce the threats of environmental pollution associated with plastic toxicity.

Various reports on cellulose-based separators, known so far depicted the scope of further improvement of its performance both in terms of physical and electrochemical properties, which would be an environment friendly alternate for use as separator in LIB and other similar electrochemical energy storage devices. In a recent article, Sun et al.[15], suggested that the electrochemical performances of batteries can further be enhanced by incorporating ferroelectric nanoparticles within the polymer-ceramic based electrolytes, where ferroelectric materials facilitate the dissociation of electrolytic salts and also enhance the Li-ion stability at the electrode-electrolyte interface[16]. All the related past literatures showed that embedding ceramic nanoparticles inside any porous membrane for use either as electrolyte or separator has significant effect in increasing ionic conductivity, thermal and mechanical stability.

In this context, the present chapter describes the development of facile low-cost and scalable process for fabrication of 'Paperator', the paper-based cellulose-ceramic composite separator and study of its physical and electrochemical performances, especially use of these paperators in LIB/SC cells. Cellulosic matrix of low-cost commercial papers was modified with $BaTiO_3$ and SiO_2 nanoparticles and dual-polymer for the first time, for which ceramic and aqueous bi-polymer blends of varying proportions were used as ceramic filler and anchoring polymer respectively. In the later section, $BaTiO_3$ was replaced with SiO_2 nanoceramic to see the effect of inert ceramic filler in the paper matrix. The paperators, thus developed showed excellent physico-chemical and electrochemical performances with respect to the commercial polypropylene-based separators. Under the present research, a new process has also been established by using a custom designed semi-automated double-decker type separator fabrication machine, where 'paperator' in roll form of defined sizes (say, width: up to 60 mm & length: up to 50 m) can be fabricated.

3.2 Fabrication of Paper Separators

A paper substrate was chosen from local market with thickness of ~80 μm. From microstructural and EDX analysis, it was observed that the raw paper substrate consisted of several impurities, which needed to be anchored before its implementation as a separator in a battery.

Table 3.1 *Compositions of the separators and their corresponding codes*

Concentration of Chitosan (w/v%)	Concentration of PVA (w/v%)	Name and concentration of ceramic powder	Sample Code
0.25	1.0	$BaTiO_3$ 0.1 w/v%	C25PV1BT01
0.50	1.0	$BaTiO_3$ 0.1 w/v%	C50PV1BT01
1.00	1.0	$BaTiO_3$ 0.1 w/v%	C100PV1BT01
0.25	2.0	$BaTiO_3$ 0.1 w/v%	C25PV2BT01
0.25	4.0	$BaTiO_3$ 0.1 w/v%	C25PV4BT01
0.25	6.0	$BaTiO_3$ 0.1 w/v%	C25PV4BT01
0.25	1.0	$BaTiO_3$ 0.5 w/v%	C25PV1BT05
0.25	1.0	$BaTiO_3$ 1.0 w/v%	C25PV1BT10
0.25	1.0	$BaTiO_3$ 1.5 w/v%	C25PV1BT15
0.25	1.0	SiO_2 0.1 w/v%	C25PV1S01
0.25	1.0	SiO_2 0.5 w/v%	C25PV1S05
0.25	1.0	SiO_2 1.0 w/v%	C25PV1S10
0.25	1.0	SiO_2 1.5 w/v%	C25PV1S15
Commercial cellulose paper	-	-	Untreated paper/UP
Commercial separator	-	-	PP/PPCom

For this purpose, the cellulose paper is coated with a solution of Chitosan in acetic acid. Chitosan was dissolved in the acid in 0.25, 0.50 and 1.00 w/v% by continuous stirring. Next, an aqueous solution of polyvinyl alcohol (PVA) and was prepared via stirring and mildly heating at 60°C. The concentration of PVA was varied within the range of 0.1-0.6 w/v%. This solution was mixed with the already prepared solution of Chitosan in 3:1 volume ratio. After that, a nanoceramic powder ($BaTiO_3$ or SiO_2) was dispersed in the polymer solution via stirring for 12h. The amount of ceramic powder was also varied with the concentrations of 0.1, 0.5, 1.0 and 1.5 w/v%. The details of the compositions and their respective nomenclature used have been provided in ***Table 3.1***. The paper substrate is coated with the polymer-ceramic suspensions following the process described in ***Section 2.3.1*** in ***Chapter 2***. The resultant paper separator

was named as Paperator and it was stored carefully for the physical and electrochemical characterizations.

3.3 Results & Discussion

An array of physico-chemical and electrochemical tests has been performed with the two variants of developed paper separators and the results have duly been compared with those of commercial PP-based separators. The tests include air permeability, electrolyte wettability, contact angle, tensile test, thermal shrinkage test and several electrochemical experiments, which have been performed following their respective methods discussed in previous chapter:

3.3.1 $BaTiO_3$ Impregnated Paper Separator

3.3.1.1 Microstructural Details

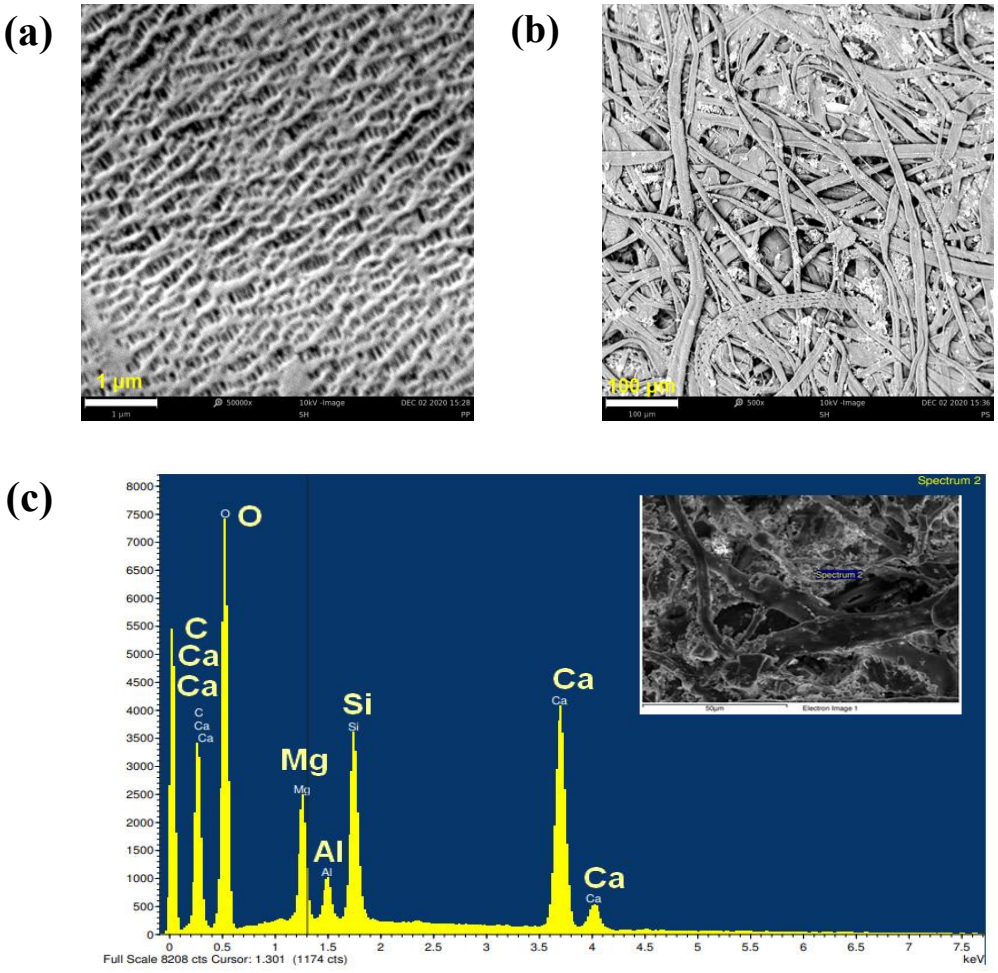

Figure 3.1 *Micrographs of (a) Commercial PPCom separator, (b) Untreated paper substrate, (c) EDX spectrum of untreated paper along with corresponding micrograph in the inset*

Figures 3.1(a) and ***(b)*** show the SEM images of commercial PPCom separator and untreated paper substrate respectively. Since the untreated paper rolls were procured from the local market, these papers require some routine physical characterizations before use. The micrograph of as-received paper shows randomly distributed cross-linked cellulose fibers having diameter of 5-10 µm. Several unknown particles were found to be present on the substrate as observed from the micrograph in ***Figure 3.1(b)***. To identify these unknown impurities, EDX analysis has been carried out and the spectrum is presented along with the FESEM image. The presence of elements such as Mg, Si, Ca, Al etc. can be confirmed as shown in the EDX spectra presented in ***Figure 3.1(c)***. These impurities are probably added by the commercial paper manufacturers as per their targeted applications. On the other hand, the micrograph of commercial PPCom separator showed uniform porous structure with pore diameter of ~0.1 µm as shown in ***Figure 3.1(a)***. The microstructural analysis of as-received (untreated) paper suggested that the surface modification by anchoring the impurities is crucial for converting paper to a functional separator. Such modification of surface is commercially termed as *sizing* of paper. PVA and Chitosan are strategically selected for this purpose due to their intrinsic capability of sizing any paper substrates[17].

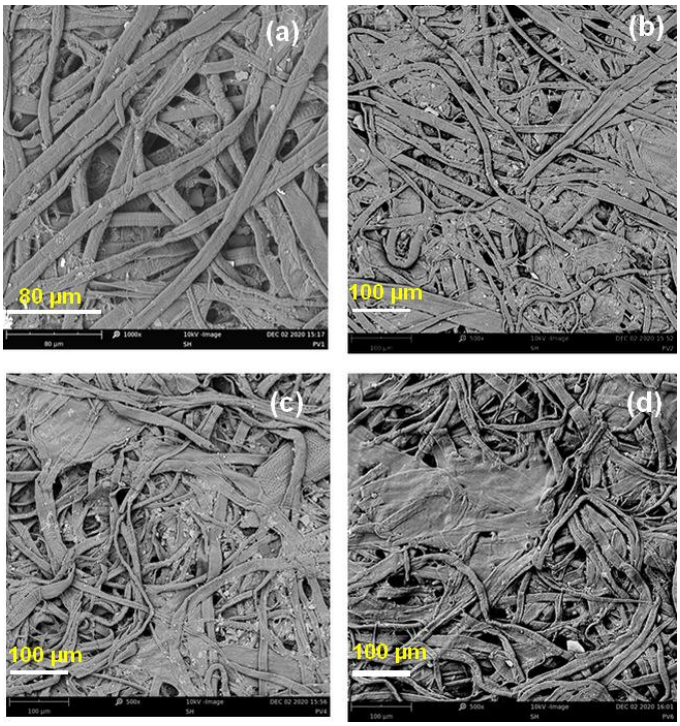

Figure 3.2 *FESEM micrographs of (a) C25PV1BT01 (b) C25PV2BT01 (c) C25PV4BT01 and (d) C25PV6BT01 showing lamination effect on increasing concentration of PVA*

Several compositions for the paperators were prepared by varying Chitosan (0.25-1.00 w/v%) and PVA (1.0-6.0 w/v%) in order to optimize the content of polymer and the ceramic nanoparticles. It is important to mention here that the process of fabrication of paperators by dip-coating technique was found to be heavily affected by the viscosity of precursor solutions. The starting or minimum

concentration of Chitosan, PVA and ceramic were kept in such a level that wet-coating could be performed with double-decker fabricator machine without the possibility of tearing off paper substrate. Thereafter, a gradual variation of polymer and ceramic concentration in paperators was carried out to study the effects of constituent components on physico-chemical performance of separators.

Figures 3.2(a)-(d) show the FESEM micrographs of fabricated paperators with varying PVA concentration. From the FESEM images, it is clear that more and more pore spaces have been found to be blocked when the polymer concentrations are increased and such pore-blocking is common because of lamination effect of the polymer in cellulosic matrix. It is also important to mention here that the lamination effect becomes more prominent when an increased amount of polymer gets incorporated within the predefined porous structure of cellulose-based papers. Further to mention here that such lamination effect is highly undesirable and generally has detrimental impacts on the electrochemical performances, as the same will affect the microporosity, ion permeability and ability to soak liquid electrolyte. Lamination effect is also believed to affect the migration of lithium ion during the charge-discharge cycling and it is discussed in detail later on.

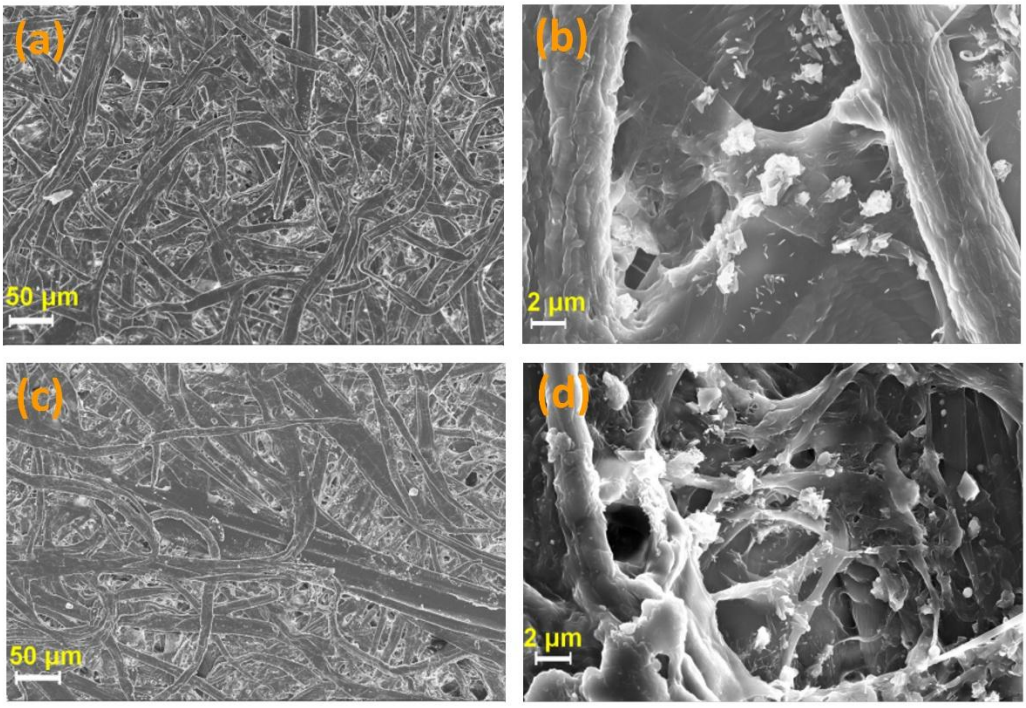

Figure 3.3 *(a) & (b) FESEM micrographs of C25PV1BT01 separator and (c) & (d) FESEM micrographs of C25PV1BT15 separator*

The FESEM micrographs of C25PV1BT01 (with lowest ceramic loading, 0.1 w/v%) and C25PV1BT15 (with highest ceramic loading, 1.5 w/v%) are represented in ***Figure 3.3(a)*** and ***Figure 3.3(c)*** along with their higher magnification images as shown in ***Figure 3.3(b)*** and ***Figure 3.3(d)***. Similar to untreated paper substrate, the morphology of the fabricated paperators shows the cross-linking cellulosic tissues forming tortuous structure with deposition of ceramic particles inside their pore spaces. Such kind of nanostructured ceramic in the substrate matrix facilitates reinforcement of cellulosic substrate. The pore diameters of the separators are estimated to be in the range of 5-10 μm.

EDX results of the paper separators as shown in ***Figure 3.4*** confirmed the presence of BTO nanoparticles within the paperator matrix. The elemental mapping for barium, titanium and oxygen further reconfirmed the presence of BTO, which are clearly visible in the EDX spectrum.

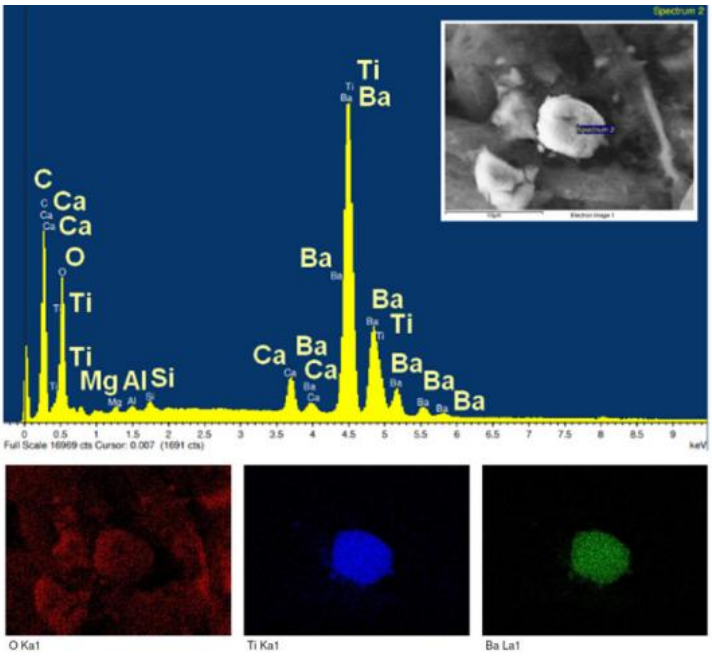

Figure 3.4 *Typical EDX spectrum and its corresponding elemental map showing the presence of Ba, Ti and O in fabricated separator C25PV2BT01*

While working with paper-based substrate, it has been observed that the typical pores are not found on the substrate, rather it is better to define the pores as 'pore spaces' originated due to overlapping and/or crosslinking of cellulose fibers as seen in the SEM image in ***Figure 3.1(b)***. The size of the anisotropic pore spaces is found to be in the range of 10-45 μm for untreated paper substrate which is too high for safe battery application. This is one of the reasons the untreated paper has to be functionalized before its use in batteries.

3.3.1.2 Porosity and Electrolyte Wettability

Air permeability measurement reflects the ability of a separator towards migration of lithium ions, through its pore spaces. The mobility of lithium ions across the separator is affected by

the nature of the materials as well as available pores in the separator matrix. Thus, an efficient separator requires high porosity and uniform distribution of pores[18]. ***Table 3.2*** summarizes the air permeability values and measured thicknesses of commercial PPCom separator, untreated paper substrate and developed paperators. The thickness of the untreated paper substrate was measured to be 80/90 µm with air permeability value of 7.5 seconds suggesting highly porous nature of the cellulose substrate. Typically, a paper substrate comprises of numerous pore spaces which originate from the cross-linked cellulosic fibrous structure.

Table 3.2 *Thickness, Gurley value air permeability and tensile properties of developed paper separators, untreated paper and commercial separator*

Sample Code	Thickness (µm)	Gurley value (s)	Tensile Stress at Max. Load (MPa)	Tensile Strain at Max. Load (%)	Young Modulus (MPa)
PPCom	20	438	183.35	40.70	990.10
Untreated paper	85	7.50	31.65	1.40	4071.19
C25PVA1BT01	70	8.20	41.31	3.11	3275.42
C25PVA1BT05	66	9.16	40.28	2.71	3306.88
C25PVA1BT10	68	11.64	37.49	2.57	2611.66
C25PVA1BT15	66	10.22	45.23	2.89	3543.36

During fabrication process, the duo-polymer-ceramic-coated paperators were dried and compacted under varying load of 60-300 tons, thus, the thickness was found to be reduced to a value of 60/70 µm from its initial thickness of 80/90 µm (i.e., untreated paper). The values of air permeability as presented in ***Table 3.2*** reveal that with increase in ceramic loading (i.e., BTO concentration), the Gurley values of the separators increase marginally suggesting that the ceramics are lying trapped on the surface or inside the pore spaces without blocking the micropores. The particle size of the commercial $BaTiO_3$ ceramic powder is <100 nm, whereas cellulosic pore spaces in paper substrate were found to be much larger (10-45 µm) as confirmed by FESEM. It indicates that ceramic particles can easily move inside the cross-linked pore spaces of the paper matrix. The porosities of fabricated paperators are also calculated using ***Equation 2.2*** of the previous chapter, which have been found to be >40%, and are similar to that of PPCom separator.

The wettability of the developed paper separators was also evaluated, for which the extent of uptake/soaking of xylene into the fabricated paperators were determined and the results were compared with commercial PPCom separator. Paperator of defined size was first dried at 70°C under vacuum for 3h and the dried samples (after noting down the weight) was then immersed into xylene for the period of 20 min in order to equilibrate the xylene soaking within the paperator matrix. Percentage of liquid (xylene) uptake was calculated from difference in two weights (before & after xylene soaking) by using ***Equation 2.1*** given in ***Chapter 2***. ***Figure 3.5*** shows the time dependent liquid retention plot of paperators of different compositions and the same for the commercial separator. It is interesting to note that developed paperators exhibit rapid wetting of organic solvent, while commercial PPCom separator takes prolonged time, which might be due to the non-polar nature of polypropylene. The greater wettability and quicker saturation time of paperators is attributed to the presence of hydrophilic nature of ceramic nanoparticles (BTO) and the fast liquid absorption may be due to passage of liquid formed through the pores of paper by capillary effect. The volume of liquid uptake in paper separators is found to be relatively high (1×10^{-2} mL) in the first instance than that of PPCom separator (2×10^{-3} mL).

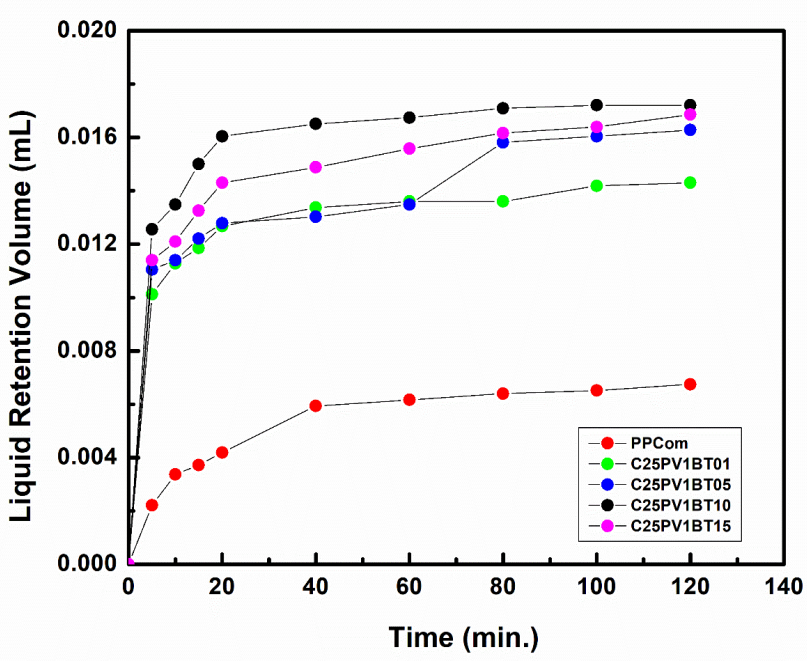

Figure 3.5 *Time dependent liquid uptake capability of fabricated paperators and commercial separator*

Similarly, liquid electrolyte uptake percentage of the developed paperators has been measured by immersing the separators into standard electrolyte solution ($LiPF_6$ in EC/DMC) for 2h inside the Ar-filled glove box. The results are found to be much better (electrolyte uptake values ranging from 99-170% depending on various ceramic loading) with respect to the commercial separator (PPCom, 90%). It is worthy to mention here that the wettability of separator in LIB

greatly influences the cell performance. Therefore, it is expected that greater liquid wettability will also result in better electrolyte soaking performance of the separator membrane. To test the time dependent electrolyte soaking ability of fabricated separators and commercial PPCom, standard $LiPF_6$ solution (EC/DMC, 1:1 w/w%) was drop-casted on the circular disks of separator membranes inside a glove box. The digital images of spreading of electrolyte on membrane surface have been captured at a regular time interval and presented in ***Figure 3.6***. All the fabricated paperators are found to be saturated with electrolyte readily, which successfully solved the problem of sluggish absorption of electrolyte in the case of commercial PP-based separator (PPCom).

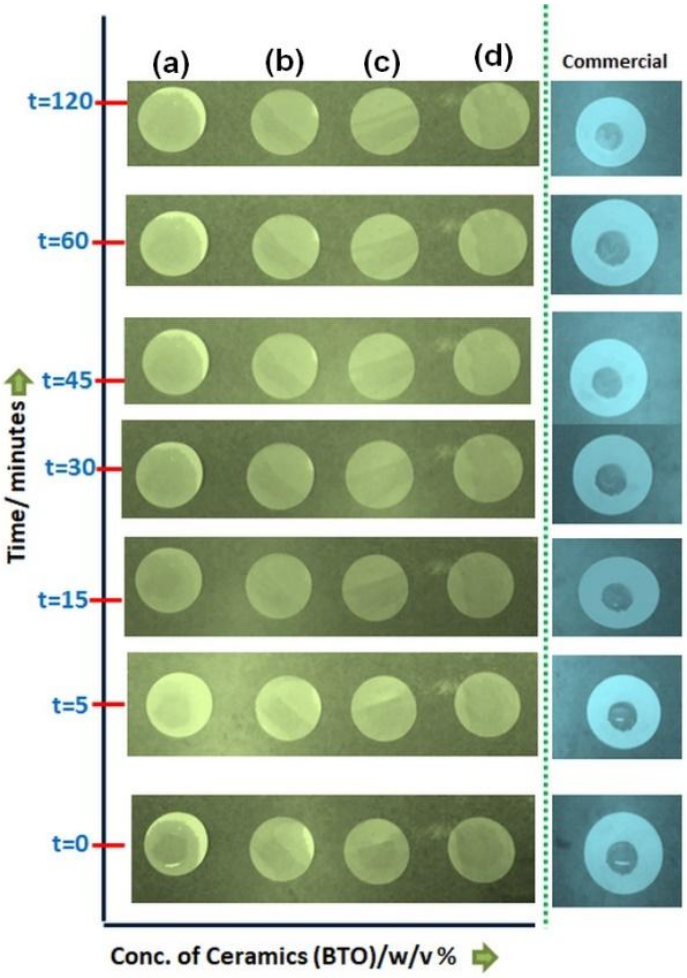

Figure 3.6 *Digital pictures of fabricated paperators ((a) C25PV1BT01, (b) C25PV1BT05, (c) C25PV1BT10 and (d) C25PV1BT15) showing electrolyte soaking ability at different time interval along with PPCom*

The excellent wettability of the separator has also been confirmed by measuring liquid electrolyte contact angle, which is presented in ***Figure 3.7***. In general, lower the contact angle higher is the affinity to the liquid. The measured contact angle of commercial PP separator (PPCom) is almost double (Contact angle left: 79.2°, Contact angle right: 75.3°) to that of fabricated paperators. The contact angle of the developed paper separators are measured to be in the range of 31.0° - 44.6°. This results further corroborate the findings of faster electrolyte saturation and superior electrolyte soaking ability of the fabricated paperators.

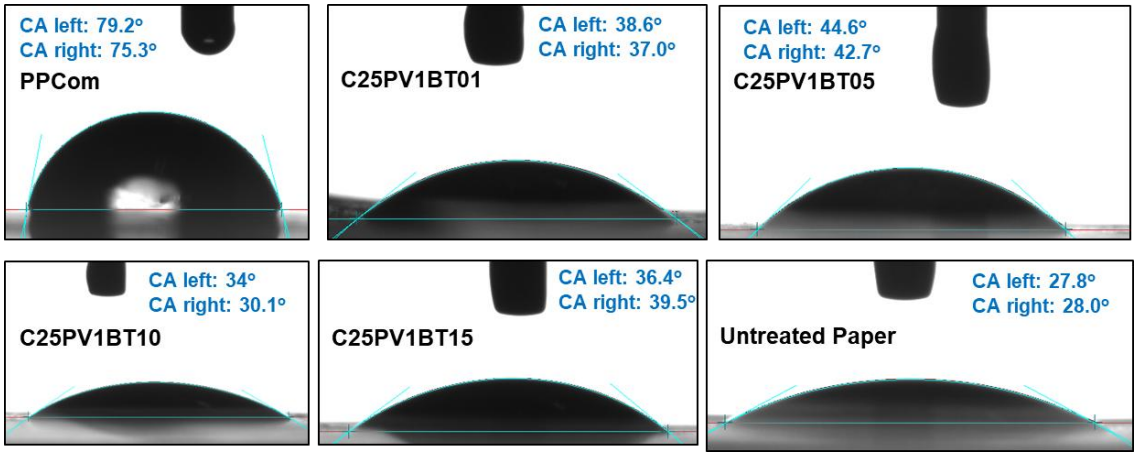

Figure 3.7 *Digital images of contact angle of the separators (PPCom, C25PV1BT01, C25PV1BT05, C25PV1BT10, C25PV1BT15 and untreated paper substrate) with liquid electrolyte along with their values of commercial separator*

3.3.1.3 Mechanical Properties

To understand the mechanical robustness of the fabricated separators, tensile tests were carried out in machine direction (MD) for commercial PPCom, untreated paper and the fabricated separators. The load vs extension plots for all the samples are shown in ***Figure 3.8*** along with larger view in their inset. The mechanical testing data clearly indicates that the commercial polyolefin membrane is much more flexible with higher elongation value than the fabricated paper based separators. The values of tensile strength of different separator compositions along with PPCom and untreated paper have been summarized in ***Table 3.2***. The tensile strength of commercial membrane was found to be 183.35 MPa, whereas fabricated paperators showed values ranging from 37.49-45.23 MPa. It was also observed that ceramic reinforcement and duo-polymer coating in fabricated separator significantly increased the tensile strength when compared with untreated paper (31.65 MPa). It was found to be 42% higher than that of untreated paper substrate. This is may be due to the combined effect of PVA-Chitosan and BTO on cellulose paper, wherein PVA strengthens the crosslinking of cellulose fiber and BTO plays a role as reinforcing agent or filler inside the pore spaces of paper matrix.

In general, ceramic particles in any composite separator function as reinforcement filler. Therefore, while making paper-based cellulose-ceramic composite separator, perfect adhesion between all the constituents has to be assured. Otherwise during mechanical stress, ceramic particles may spill over from the surface or loosen from the substrate. The enhancement of mechanical strength from untreated paper substrate to functionalize paperators is originated

mainly due to good quality adhesion among the polymers (PVA, Chitosan) with cellulose substrate and partly supported by BTO ceramic reinforcement. It is worthy to mention here that the mechanical strength of any paper-based separator directly depends on how much strength the substrate itself can deliver[19]. Thus, with the increase in ceramic loading keeping all other polymers concentration constant showed only marginal increase in mechanical strength. Results obtained also focuses that higher ceramic loading may have effect on wettability and thermal performance of the separator, but has limited effect in enhancing mechanical strength of paper separator after some threshold loading.

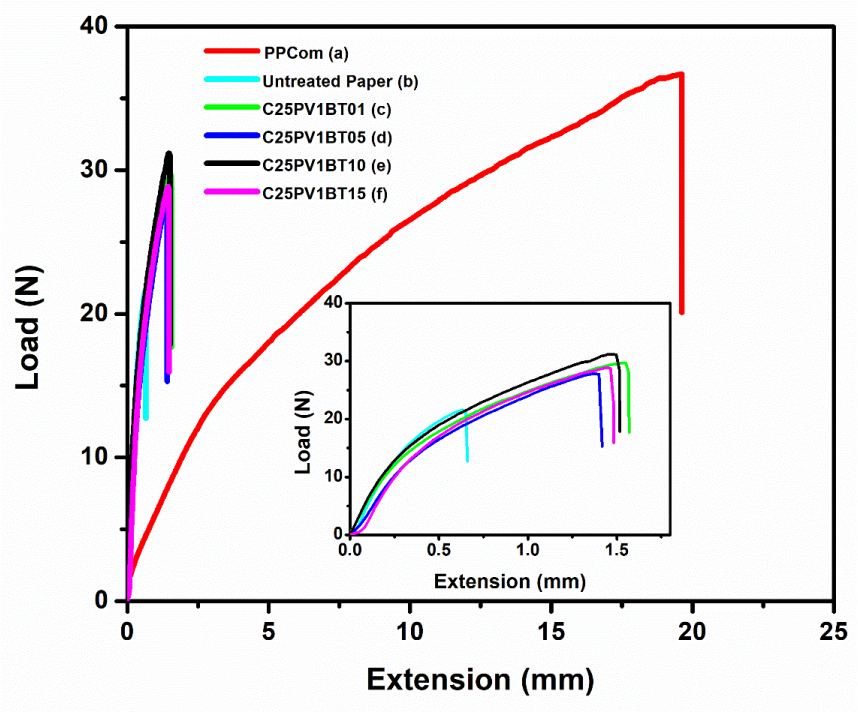

Figure 3.8 *Plots of load vs extension of paperators, untreated paper, commercial separator (PPCom); The inset shows the expanded view of load vs extension plots of untreated paper and fabricated paper separators*

3.3.1.4 Ionic Conductivity

To understand the lamination effect on paper substrate with the increase in polymer concentration, EIS studies were performed using electrolyte-soaked separators and commercial membrane in symmetrical cell configuration (SS/separator/SS). ***Figure 3.9*** shows the Nyquist plots of paperators with different PVA concentrations ranging from 1.0-6.0 w/v%. The frequency dependent impedance plot of the separators showed a linear inclination towards Z' axis representing electrode-electrolyte double layer capacitance behavior. The bulk resistances of the fabricated separators are estimated from the high frequency intercept of the Nyquist plot

on the Z' axis[20]. The value of bulk resistances is shown in the inset of ***Figure 3.9***. It is evident from the figure that with the increase in the concentration of polymer (PVA), the resistance of the separator membrane gradually increases from 6.87 Ω (C25PV1BT01) to 140.53 Ω (C25PV6BT01). However, the bulk resistance of commercial PPCom is found to be lowered than the fabricated paperators. This could be due to the effect of thickness. It is worth mentioning here that while PPCom is around 20 µm thick, the fabricated paperators have thicknesses as high as 60-70 µm.

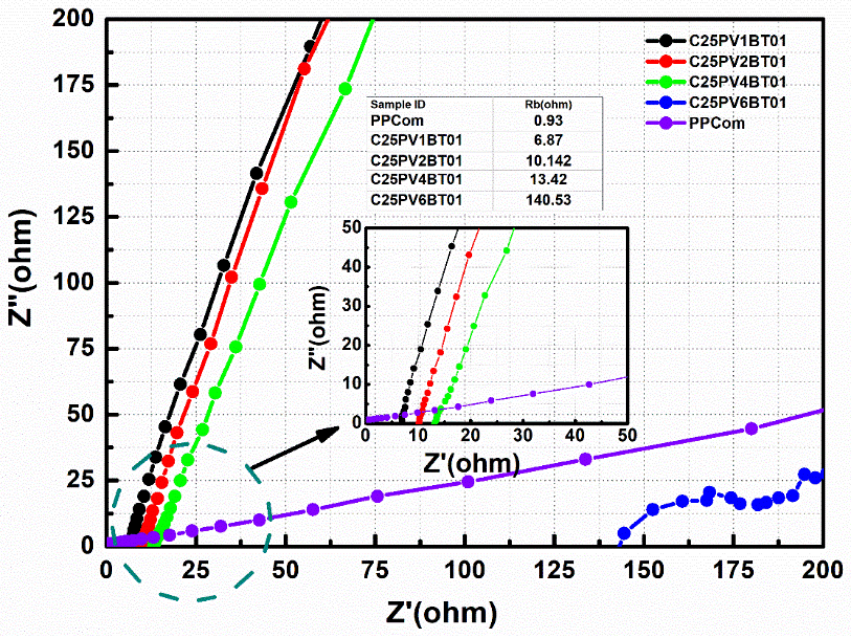

Figure 3.9 *Nyquist plots of developed paperators along with PPCom; Inset shows the enlarged view of the plots*

3.3.1.5 Electrochemical Tests

To understand the ion-transport phenomena across the porous separator membranes, several electrochemical tests have been performed with different electrode systems. The tests have been conducted both in LIBs and SCs;

3.3.1.5.1 In Lithium-ion Battery

Electrochemical cycling performance in 2032 coin type lithium-ion cells ($LiFePO_4$/Separator/MCMB) was evaluated using both fabricated and commercial separators and the results were duly compared. To examine the effect of polymer concentration (Chitosan; 0.25-1.00 w/v% and PVA; 1.0-6.0 w/v%) and ceramic loading (BTO; 0.1-1.5 w/v%) on fabricated separators, a large number of cells were fabricated with different separator

compositions. The initial charge-discharge plots have been given in ***Figures 3.10(a)-(c)*** and their discharge capacities have been summarized in ***Table 3.3***.

The initial discharge profiles as shown in ***Figure 3.10(c)*** reveal that the separator with lowest Chitosan concentration exhibits an initial discharge capacity of 118.69 $mAh.g^{-1}$. As the Chitosan concentration increases, the capacities fall and reach to a minimum value of 94.18 $mAh.g^{-1}$ (C100PV1BT01). A similar trend of decrease in capacity is also observed for increase in concentration of PVA in the composition as shown in ***Figure 3.10(b)***. This may be due to the localized lamination effect i.e., blocking of pore-spaces at higher concentration of polymers which results in decrease in porosity as well as lithium ion mobility. The effect of BTO ceramic loading on separator composition has also been studied by varying the concentration of BTO on paper separator in the range of 0.1-1.5 w/v%. At lower ceramic concentration, the cells delivered a discharge capacity of 118.69 $mAh.g^{-1}$. However, a five fold increase in ceramic loading resulted in the reduction of capacity to a value of 81.5 $mAh.g^{-1}$ as shown in ***Figure 3.10(a)***. The capacities remained constant with futher increase in ceramic concentration in paper separator. The decrease in capacity value may be attributed to the formation of BTO agglomerates at higher concentration, which might have

Table 3.3 *Discharge capacities of fabricated paperators along with their compositions*

Chitosan Variation	**Composition**	**Discharge Capacity (mAh/g)**
	Chitosan conc. (w/v %)	
C25PV1BT01	0.25	118.69
C50PV1BT01	0.50	102.59
C100PV1BT01	1.00	94.18
PVA variation	PVA conc. (w/v %)	
C25PV2BT01	2.00	114.63
C25PV4BT01	4.00	95.79
C25PV6BT01	6.00	47.23
BTO Variation	BTO variation (w/v %)	
C25PV2BT05	0.50	81.50
C25PV4BT10	1.00	82.31
C25PV6BT15	1.50	79.94

created dead pores by blocking the pore spaces, a similar effect of lamination as observed in higher polymer loading.

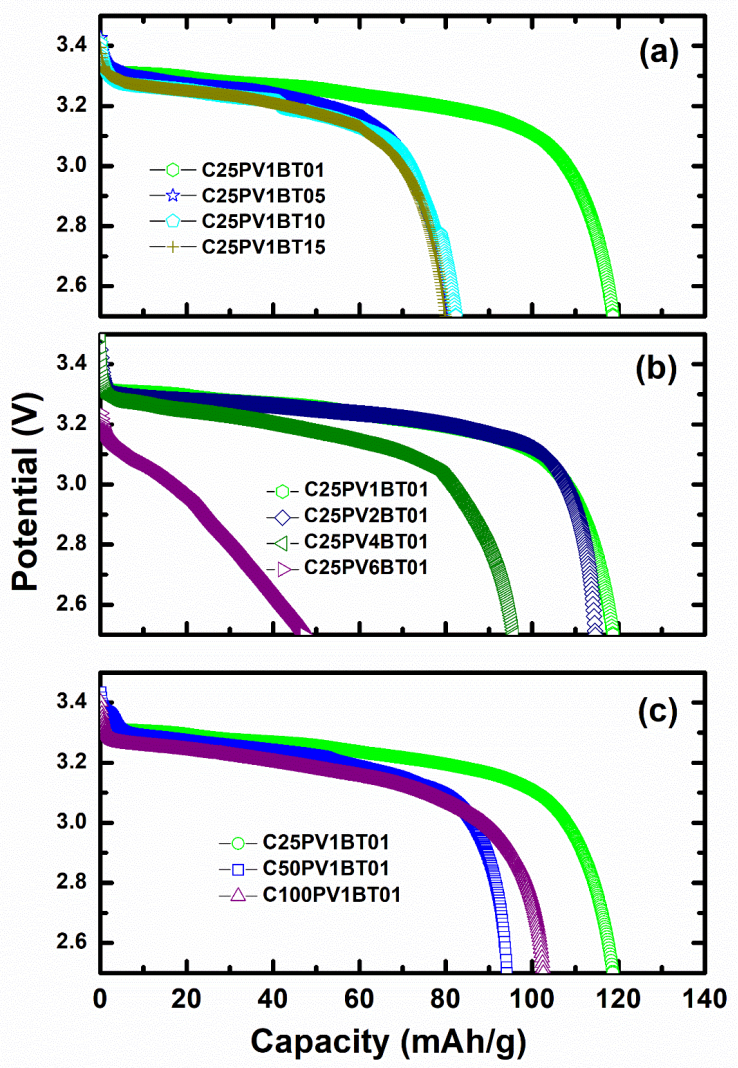

Figure 3.10 *Initial charge-discharge profiles of fabricated separators by varying concentration of (a) BTO (0.1-1.5 w/v %), (b) PVA (1.0-6.0 w/v %) and (c) Chitosan (0.25-1.0 w/v %)*

Figure 3.11 represents the charge-dischage capacities vs cycle number plot for fabricated C25PV1BT01, C25PV1BT05, C25PV1BT10 and C25PV1BT15 paperators. The corresponding coulombic efficiencies are also plotted for each cell. The results revealed that the fabricated separator with the lowest ceramic content initially shows higher discharge capacities than that of higher loading samples but decreases gradually. On the other hand, the separator samples with higher ceramic loading delivered steady but lowered discharge capacities on cycling without fading. The decrease in the discharge capacities for higher ceramic loading samples is mainly due to the pore blocking by BTO agglomerates. However, higher BTO loading may provide interfacial stability with the electrodes, which is reflected in the long term stability. All the cells showed excellent coulombic efficiency in the range of 95-100%.

To study the electrochemical rate performance, the cells were cycled in different current densities ranging between 0.1-0.4 $mA.cm^{-2}$. After being subjected to higher current densities, the cells were once again cycled at lower current density of 0.2 $mA.cm^{-2}$ so that the repeatability in electrochemical performance could be tested. The capacity vs cycle number plot at different

current densities for C25PV1BT01 separator is given in ***Figure 3.12*** along with those of the commercial PPCom membrane and untreated separator.

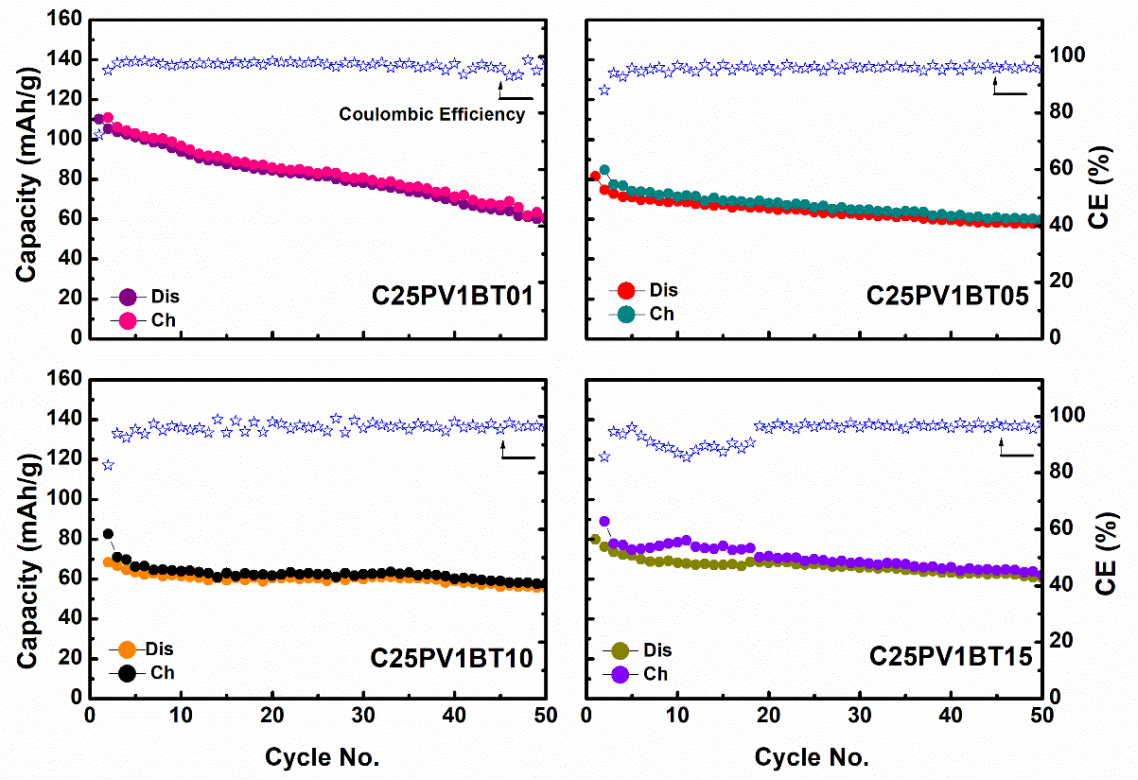

Figure 3.11 *Charge-discharge capacities against cycle number plot of C25PV1BT01, C25PV1BT05, C25PV1BT10 and C25PV1BT15; the corresponding coulombic efficiencies are also plotted w.r.t right Y-axis*

With increase in current densities, a gradual reduction in capacities is observed for all the separators. The commercial PPCom sample shows an average capacity of 114.43 $mAh.g^{-1}$ at 0.1 $mA.cm^{-2}$, 103.30 $mAh.g^{-1}$ at 0.2 $mA.cm^{-2}$ and 83.98 mAh.g at 0.4 $mA.cm^{-2}$, whereas C25PV1BT01 shows average capacity values of 111.48 $mAh.g^{-1}$, 101.74 $mAh.g^{-1}$ and 85.38 $mAh.g^{-1}$ at that current density respectively. A marginal difference in capacity values is due to the effect of thickness of paperator which is about three times higher (60/70 µm) than that of commercial polymer separator membrane (20 µm). The thickness and tortuosity of cellulosic structure in fabricated separator possibly hamper the movement of lithium ion during electrochemical cycling by resulting in decrease in specific capacities. Therefore, it is felt that the minimization of thickness is necessary to make the charge-discharge profiles

superimposable to each other at different curent densities. Further, it was observed from ***Figure 3.12*** that the rate capablity of paperators are found to be much better in comparison with untreated paper, when cycled at different currnt densities, which showed almost zero specific capacity at 0.4 mA.cm^{-2}. This indicated that functionalization of untreated paper with ceramic nanoparticle and duo-polymers has significant role on electrochemical cycling and incorporation of such polymer-ceramic moiety within the cellulosic matrix is very essential to improve its electrochemical performances. Further considering the safety aspects of LIB and/or similar energy storage devices, direct use of such commercial papers are not recommened because of anisotropic large sized 'pore-spaces' in untreated paper substrate might be dangerous to trigger short circuits during cycling and also it may result poor electrochemical performance.

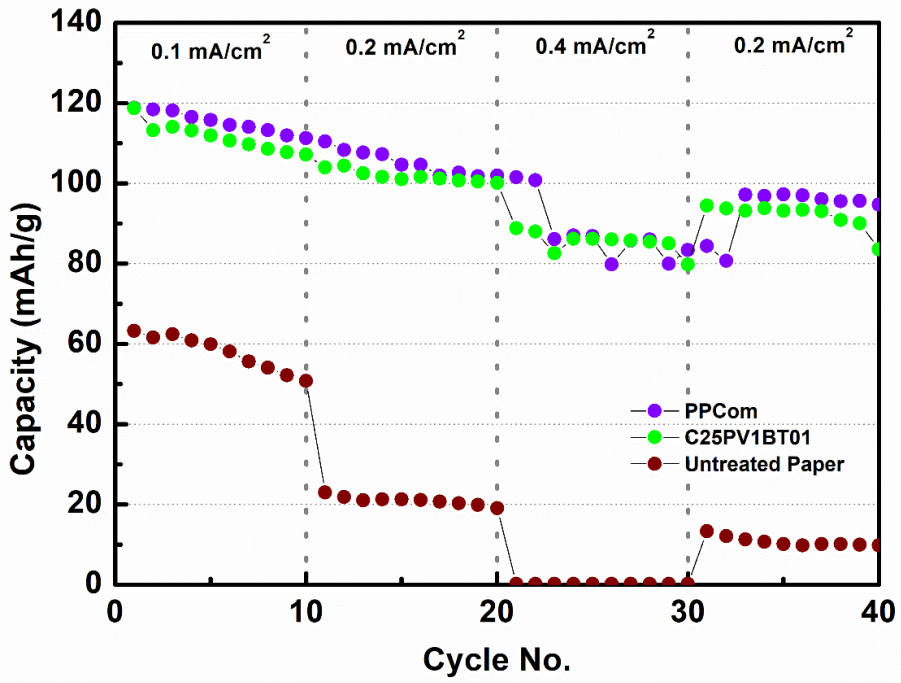

Figure 3.12 *Capacity vs cycle number plots for paperator (C25PV1BT01), commercial membrane (PPCom) and untreated paper substrate at different current densities (0.1-0.4 mA.cm^{-2})*

Compatibility of developed paperators with other cathodes was studied by fabricating 2032 coin cells against commercial $LiMn_2O_4$ (LMO) and $LiCoO_2$ (LCO) cathodes. The cells were tested using highest (C25PV1BT15) and lowest loaded ceramic (C25PV1BT01) samples. The eelectrochemical charge-discharge performance of the developed paperators along with commercial PPCom against (a) $LiMn_2O_4$ and (b) $LiCoO_2$ cathodes and MCMB anode were presented in ***Figure 3.13***. It is observed that the developed 'paperators' delivered the specific capacities, comparable with that of PPCom when cycled against commercial $LiMn_2O_4$ cathode (C25PV1BT01: 47 mAh.g^{-1}, C25PV1BT15: 61 mAh.g^{-1} and PPCom: 51 mAh.g^{-1}). The

performance of 'paperator' was found to be better with respect to the commercial PP separator, when cycled against commercial $LiCoO_2$ cathode (C25PV1BT01: 177 $mAh.g^{-1}$, C25PV1BT15: 176 $mAh.g^{-1}$ and PPCom 118 $mAh.g^{-1}$). These results further corroborate that the paperators thus developed are compatible with major commercially used cathodes.

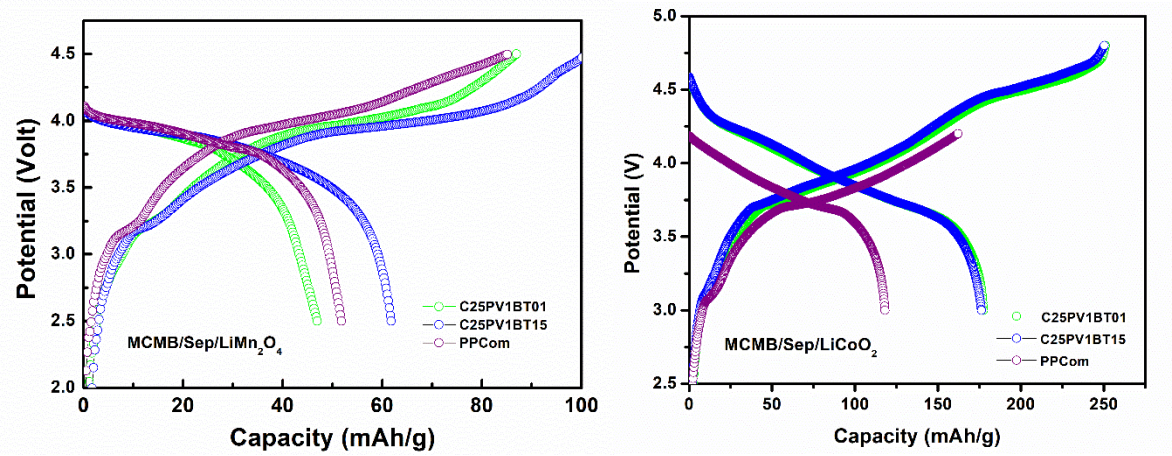

Figure 3.13 *Electrochemical charge-discharge performance of paperators C25PV1BT01, C25PV1BT15 along with Commercial PPCom against (a) $LiMn_2O_4$ and (b) $LiCoO_2$ cathodes and MCMB anode*

3.3.1.5.2 In Supercapacitor

Electrochemical performance of the newly developed 'Paperators' were also studied for extending its applications in supercapacitors. Supercapacitor (SC) cells were fabricated by using the SC cell fabrication facilities of C-MET (Thrissur, India), where two leaded carbon aerogel based electrodes (aerogel carbon coated onto thin aluminium current collector) and the developed paperator of optimized composition were assembled as per electric double layer capacitor configuration. Tetraethyl ammonium tetrafluoroborate (1.0 M) in propylene carbonate (as electrolyte) was vacuum impregnated within electrode assemblies/wounds followed by hermetic sealing of electrode wounds in aluminium cans of size, 16 mm (ϕ) x 36 mm (H). Five such SC cells were fabricated with the developed 'paperator' and their electrochemical performances were evaluated as per IEC 62391-1 by using supercapacitor testing system (SCTS, Arbin Instruments, USA). According to IEC 62391-1, a constant current charge-discharge technique was used in determing the cell capacitance (C_{eff}) of paperator based SCs, while the constant current pulsing technique was used to measure the effective cells ESR. Ten current pulses of each 400 mA with pulse duration of 10 mS were applied on a fully charged SC cells. All the paperater based SC cells showed highly reversible charge-discharge patterns,

which indicated that there is no significant degradation of paperator during charge-discharge cyclying. The cell capacitances and cell ESR of 'paperator' SC cells were found to be in the range of 17.2±0.8 F and 76±3 mΩ. Few numbers of identical SC cells were also fabricated by using commercial cellulose based separator (NKK brand, Japan) in a similar fashion and they were also tested as per IEC 62392-1. The cell capacitances & ESR were found to be 18.0±0.6 F and 22±2 mΩ respectively, which indicated that apart from use of the 'paperator' in LiBs, the newly developed 'paperator' also possess high application potential for use as separator in electrochemical capacitors/supercpacitors or similar devices. A typical charge discharge plot of supercapacitors fabricated by using Paperator and commercial separator (NKK paper) is presented in ***Figure 3.14***.

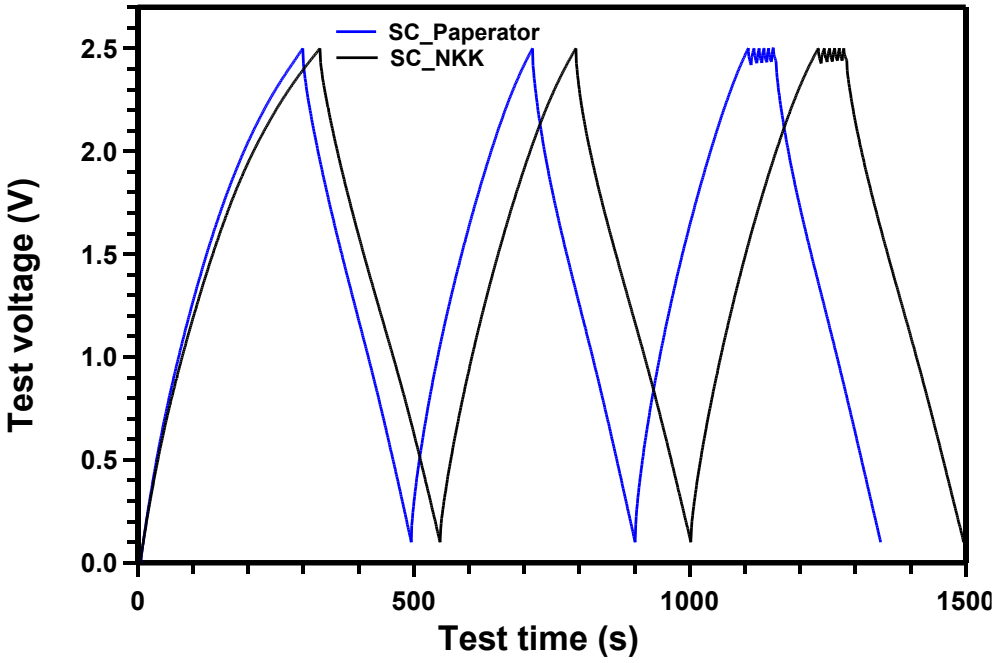

Figure 3.14 *Typical constant current charge-discharge (CDC, @200 mA) patterns of selected supercapacitors, fabricated by using (a) paperator and (b) commercial cellulose-based paper (NKK, Japan)*

3.3.1.6 Thermal Properties and Safety Studies

Figure 3.15 shows the thermal profile of (a) untreated paper, (b) commercial PPCom separator and (c) C25PV1BT01. All the three samples show similar type of weight loss around 100-150°C due to evaporation of moisture from the surfaces. At around 200°C, commercial separator showed three-fold mass loss (9.32%) compared to the untreated paper (3.09%) and

fabricated C25PV1BT01 (3.43%). On further increasing the temperature, the mass of commercial separator continued to degrade. A major degradation peak was observed at around 350ºC followed by complete weight loss till 453ºC which corresponds to complete de-polymerization of commercial PPCom separator under thermal treatment. The thermal profile of Paperator (C25PV1BT01) showed three distinct weight loss steps in three temperature zones – (1) the primary weight loss associated in the temperature range of 50-200ºC is due to the removal of weakly bonded absorbed water molecules on the external or internal surface of the papers, (2) at 200-350ºC, a slight weight loss is observed attributed to the removal of strongly bounded water molecules to the hydroxyl groups present in the polymer matrix (PVA-Chitosan) and (3) above 350ºC, a sharp weight loss is found due to the decomposition of polymers. In case of untreated paper, although the profile looked similar to that of paperator till 200ºC which was primarily due to the removal of weakly bonded surface water molecules, no significant weight loss could be visible above 200ºC up to 350ºC. This is due to the fact that cellulosic paper substrate absorbs only loosely bound water molecules on its surface. After 350ºC, both untreated and paperators follow similar decomposition behaviour. At around 355ºC, untreated paper and C25PV1BT01 showed weight losses of 55.38% and 55.34% respectively. At 453ºC where commercial separator completely degraded, the paperator showed a significantly higher residual mass of 36%.

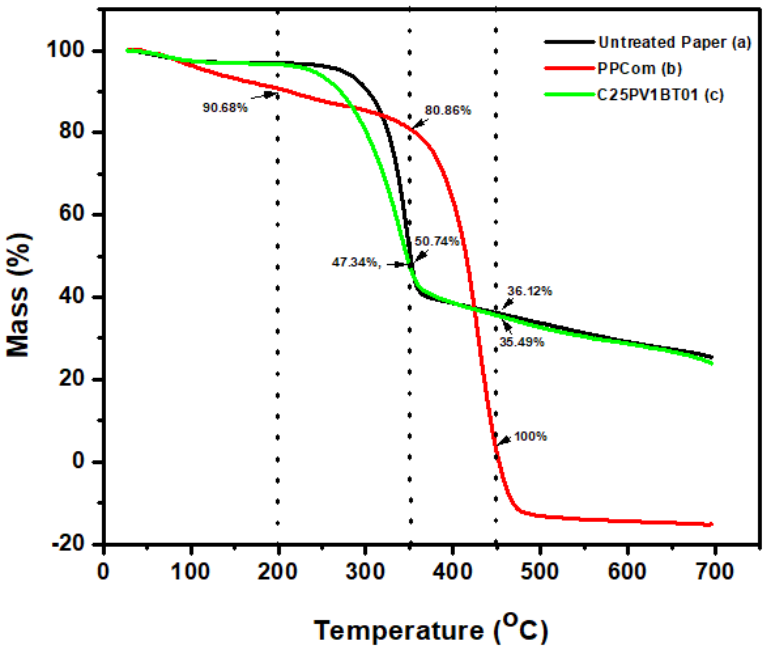

Figure 3.15 *TGA curves of (a) untreated paper, (b) commercial separator and (c) C25PV1BT01*

The results thus obtained from thermal analysis clearly suggest that thermal stability of developed paperator is superior to the commercial PPCom separator.

Further, to understand the dimensional stability at elevated temperature the fabricated paperators were subjected to heat treatment at temperatures ranging from 50°C to 200°C, with an interval of 25°C and equilibrating time of 10 minutes. The photographs of heat-treated separators are shown in ***Figure 3.16***, where no apparent change either in color or in dimension could be observed in the case of paper separators, whereas the commercial separator displays a gradual change in its color with increasing heat-treatment temperature. It is also observed that commercial PPCom separator starts shrinking with its color changing from white to transparent at 150°C onwards and the structure of commercial separator completely collapses at 200°C. No observable change in the case of fabricated paperators is found which indicates that developed paperators are thermally stable without any dimensional shrinkage up to 200°C, which corroborates the similar findings obtained in TGA analysis.

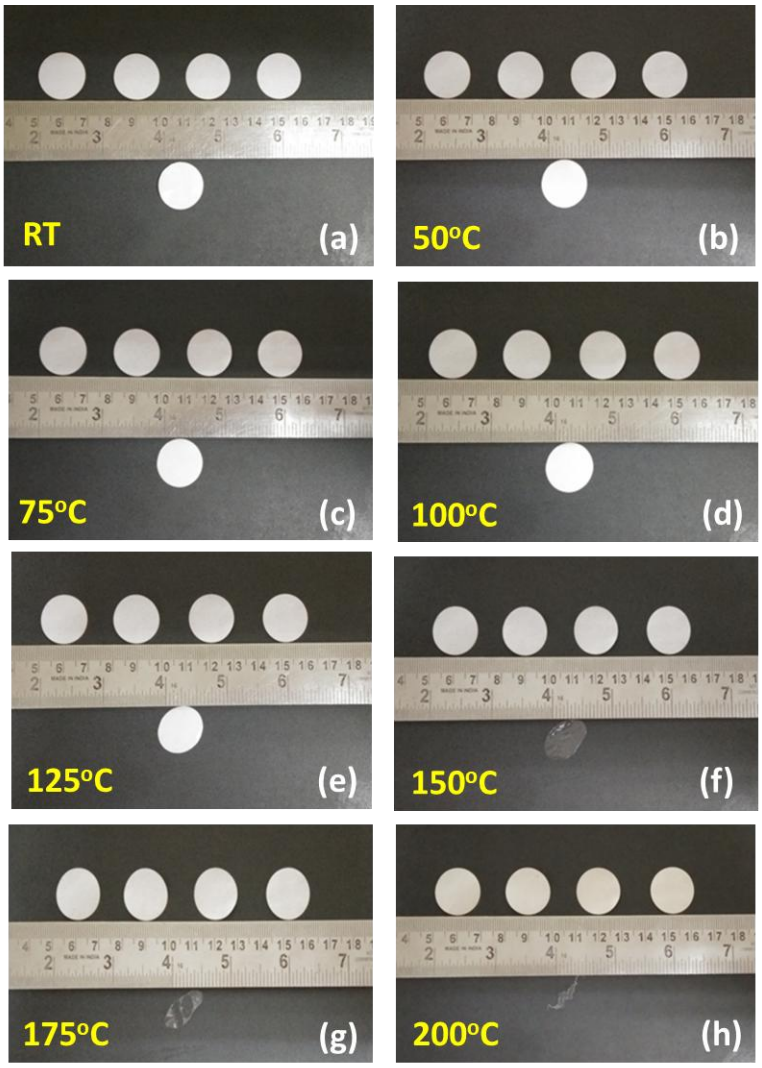

Figure 3.16 *(a)-(h) Image showing thermal stability and dimensional shrinkage from RT-200°C at every 25°C interval and holding time 10 minutes at each temperature for Paperators (above the scale) and Commercial Separator (below the scale); the paper separator samples were placed above the scale based on increasing ceramic loading (from left to right) i.e., C25PV1BT01, C25PV1BT05, C25PV1BT10 and C25PV1BT15*

Safety is always a major concern while dveloping any internal component and/or materails for LIB system, particularly separator because of the fact that during thermal runaway, flame

retardance property of separator plays the vital role in preventing combustion/ explosion of batteries.

It has been reported elsewhere that besides coating with ceramic nanopowder, thermal-resistant polymers used in making separator are also effective in improving the safety of LIBs. In this context, both PVA and chitosan, although not intrinsically flame retardant, are considered to be a very good carbon source that when applied to a polymer substrates, like cellulose, cotton, bulky polymer, textile, foam, wood etc. they can give rise to the formation of stable carbonaceous residue, called 'Char' upon exposure to the flame[21–23]. The formation of char is considered to be one of the most important condensed-phase mechanisms that serves as a protective barrier to heat and mass flow, that prevents conversion of combustible gaseous species further by means of stabilizing carbon[24–26].

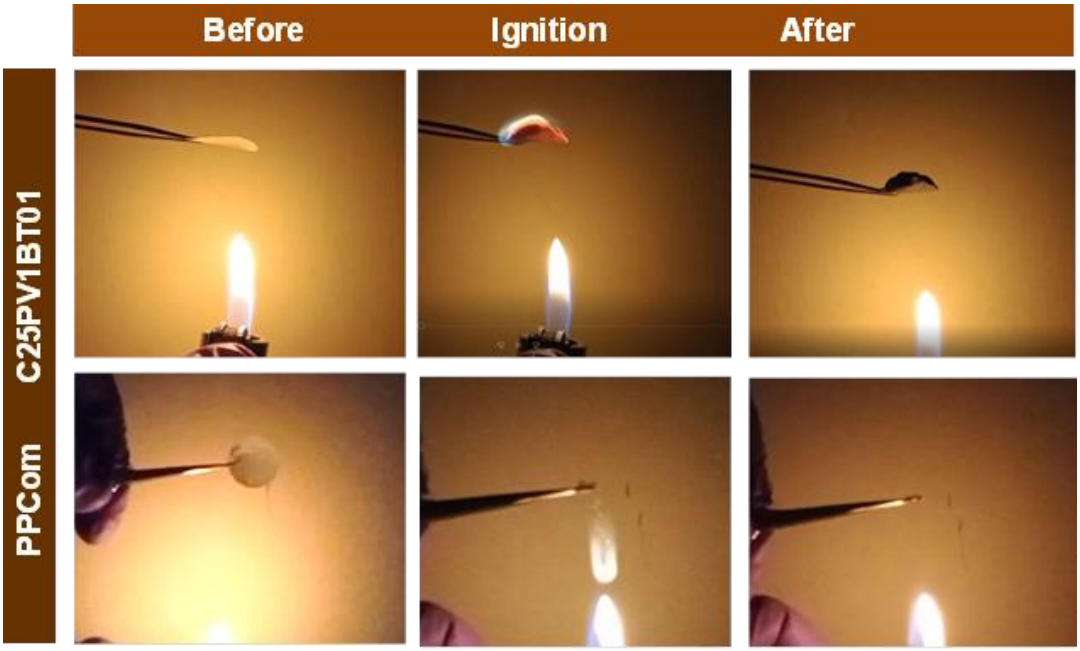

Figure 3.17 *Digital images of Paperator (C25PV1BT01) and Commercial separator (PPCom), taken during Flame Test (Combustion) as well as before and after ignition*

To explore the fire returdant characteritics of developed paperator, a cumbusion test were carried out for the developed paperators. Preparator were soaked with electrolyte ($LiFP_6$ in EC/DMC) for 2h, which then exposed to a flame (from gas lighter) with proper safety precaution. It was observed that on exposure to the flame, paperator (C25PV1BT01) initially ignited due to burning of electrolyte vapour, however flame momentarily self-extinguished and resulted formation of significant amount of char. Observation are shown in ***Figure 3.17***, which

revealed interesting flame retardation properties for developed paperators having the compositions of ceramic (BTO) and duo-polymer (PVA and Chitosan), coated on cellulosic paper substrate. A similar type of findings for HAP-NW based separators was also reported[27]. Recorded flaming time for paperator was measured to be 3s, which can be categorized to V-0 according to IEC 60695-11-10 vertical flame standard test. It was also observed that commercial polypropylene separator (PPCom), comprising aliphatic hydrocarbon backbone burnt itself rapidly without leaving any residual 'char'. This findings clearly indicated that 'paperator' thus developed can offer additional safety feature during thermally abused condition, retarding the propagation of flame that may inhibit further damage to the cell.

3.3.2 SiO_2 Impregnated Paper Separator

Apart from polymeric blend, addition of nanostructured SiO_2 has several advantages as it may decrease the crystallinity of the polymers, can improve electrolyte uptake capability, thus can subsequently increase the ionic conductivity of the separator[28]. Furthermore, the presence of ceramic nanoparticles within the cellulosic matrix is also reported to have improved the heat resistance property of the separator, which in turn enhances the safety features of separator membrane during LIB operation[29,30].

3.3.2.1 Microstructural Features

Figure 3.18 represents the FESEM images of developed paper separators taken in different magnifications; ***Figures 3.18(a1-a3)*** show the image of paper separator CPS01 with lowest ceramic loading and ***Figures 3.18(b1-b3)*** correspond to CPS15 paper separator with highest ceramic loading. The images showed that the SiO_2 ceramic nano particles are homogeneously distributed throughout the paper substrate and embedded with the cross-linked cellulose tissues. It is worthy to mention here that due to smaller size of the SiO_2 particles (<100 nm) than that of pore spaces (10-55 μm) which were created by cellulose crosslinking, particles are predominantly stick to the tissues.

Therefore, the ceramic could not block the micron sized pores spaces of the paper substrate. The diameter of the pore spaces of UP (untreated paper) measured from the micrographs (not shown here) was found to be ranging from 10 μm to 65 μm, which is very large than its acceptable pore dimension required for separator for battery applications. The duo-polymer

coating was applied in this study to create micropores in order to block those large sized pore spaces. With the increase in the ceramic concentration, the distribution of ceramic particles per unit area on paper substrate was found to be increased as expected. However, due to high surface energy of nano particles, they were present in agglomerated form on the separator as confirmed by FESEM [enlarged views of ***Figure 3.18(a3)***-CPS01 and ***Figure 3.18(b3)***-CPS15].

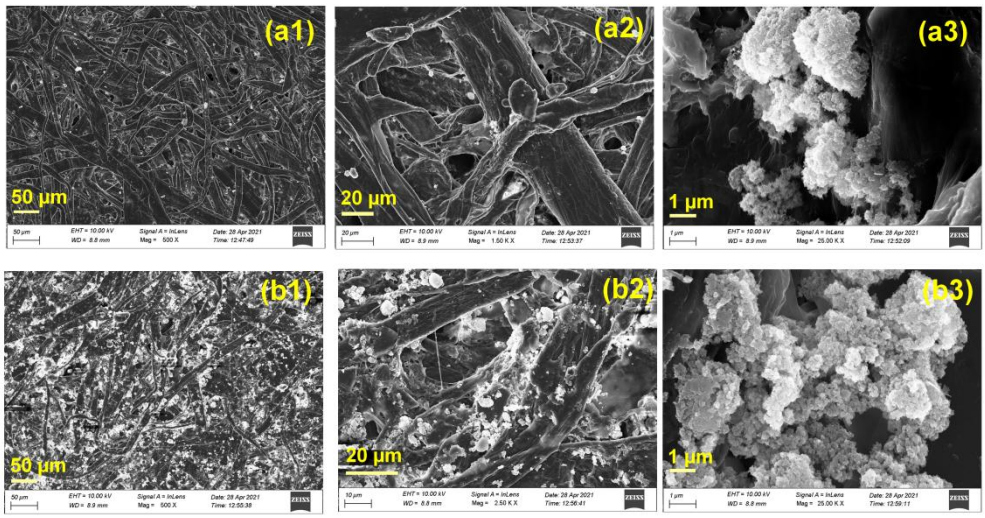

Figure 3.18 *FESEM images of fabricated paper separators; (a1-a3) CPS01 and (b1-b3) CPS15 taken in different magnifications*

3.3.2.2 Porosity and Electrolyte Wettability

Estimation of Gurley value (in seconds) is an indicator of air permeability and considered as one of the most important technical parameters to characterize porous membrane. Lower the Gurley value means higher the air permeability. Here, the highly porous paper substrate has been modified with duo-polymer and ceramic, thus change in Gurley value is expected due to blocking of large pore spaces of paper substrate either by Chitosan-PVA or large sized agglomeration formed due to nano-SiO_2. The Gurley value of commercial untreated paper substrate (UP) was found to be 7.5s, which increased to a value of 15.83s for lowest ceramic loaded composition, CPS01. However, with further increase in ceramic concentrations for CPS05 (25.08s), CPS10 (21.95s) and CPS15 (23.25s), no significant change could be observed in air permeability. This suggests that the blocking of pore spaces in paper substrate might be affected by the polymers, but has little effect on ceramic loading. The porosity of fabricated

paper separators were found to be in the range of 52.62-55.18%, similar to that of commercial PP membrane.

When a liquid comes in contact with a porous material like paper, the liquid in contact with the pores become curved surfaces due to differential surface tension. At equilibrium condition, if the contact angle between solid and liquid is greater than 90º, the liquid will not be able to penetrate by capillary force. However, the capillary suction of fluid into porous matrix like paper is basically a dynamic process of penetration as described by Washburn equation model[31]. In the present study, paper has been critically modified with duo-polymer and ceramic. The film-forming ability of polymers (PVA and chitosan) used along with ceramic filler SiO_2 makes a dense layer of materials on the surfaces of the pristine paper substrate through which the fluid will have to penetrate. Thus, the rate at which the liquid will penetrate through the . On the other hand, commercial PP showed a contact angel of ~78° which almost remain unchanged

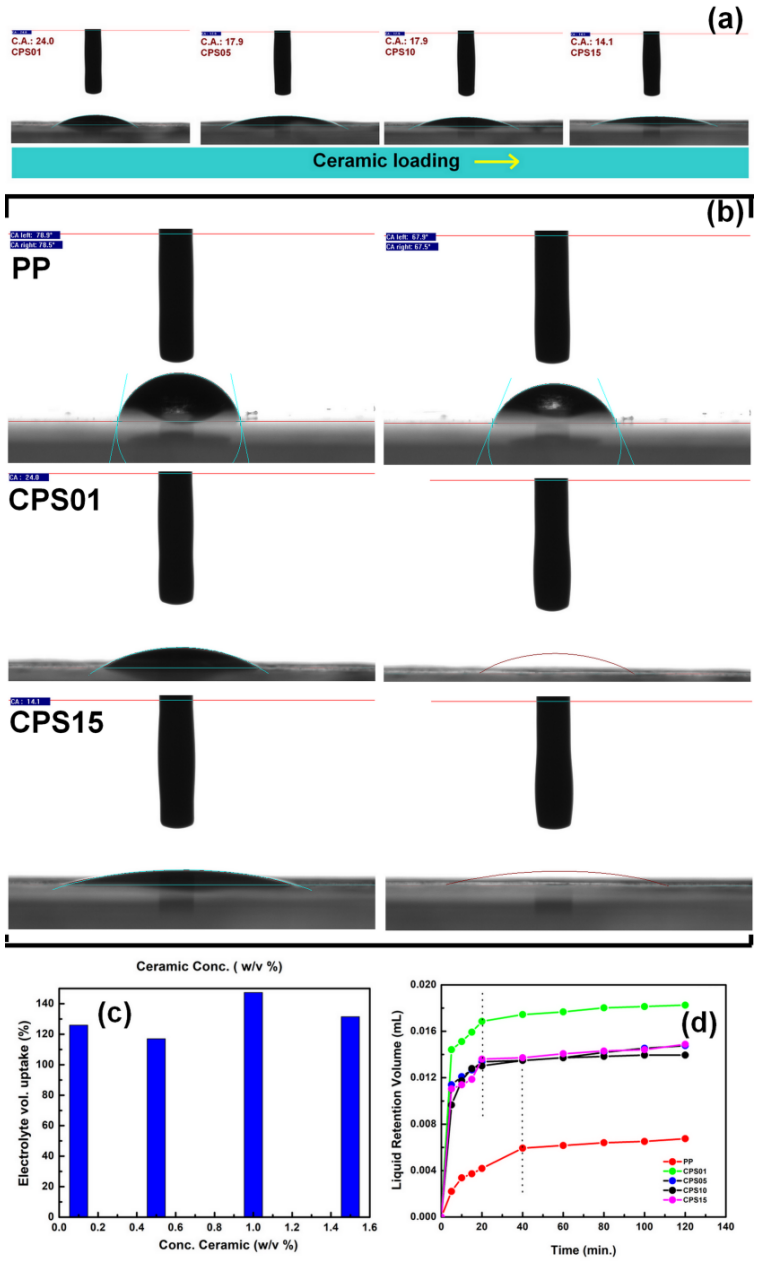

Figure 3.19 *(a) Variation of contact angle with increasing ceramic load, (b) Comparison of contact angle of CPS01 and CPS15 with respect to PP, (c) Electrolyte volume uptake capability of different ceramic loaded paper separators (CPS01, CPS05, CPS10 and CPS15), (d) Time dependent liquid retention plot of developed paper separator along with commercial PP*

over several minutes. This is due to the fact that the presence of ceramic materials accelerates the spreading of polar electrolyte molecules, and provides a path for soaking through the capillary channels originated due to agglomerated ceramic clusters of SiO_2 nano particles and crosslinked-polymeric network of cellulose-PVA-chitosan. The electrolyte soaking ability was also determined and plotted in ***Figure 3.19(c)*** with respect to increasing ceramic loading. It was found that the paper separators showed higher electrolyte soaking ability of 147% and 131% for higher ceramic loaded samples of CPS10 and CPS15 respectively. On the basis of the above, time dependent liquid retention capability in term of volume (ml) of the paper separator was also calculated using xylene as liquid and the results were plotted in ***Figure 3.19(d)***. It was found that the paper separator showed faster liquid saturation capability than that of commercial PP separator.

The time to achieve maximum saturation was found to be two times faster than the commercial PP. The spreading of commercial electrolyte on the surface of paper separators with varying ceramic concentrations along with commercial PP separator with respect to time was further examined inside the glove box and the digital images were presented in ***Figure 3.20***. The images showed that higher the ceramic concentration, the electrolyte quickly spread over the surface, whereas commercial PP separator showed very sluggish type of spreading with respect to time. All the above findings suggest that the developed paper separator showed both superior wettability and electrolyte uptake capability than that of commercial PP based separator membrane. Such

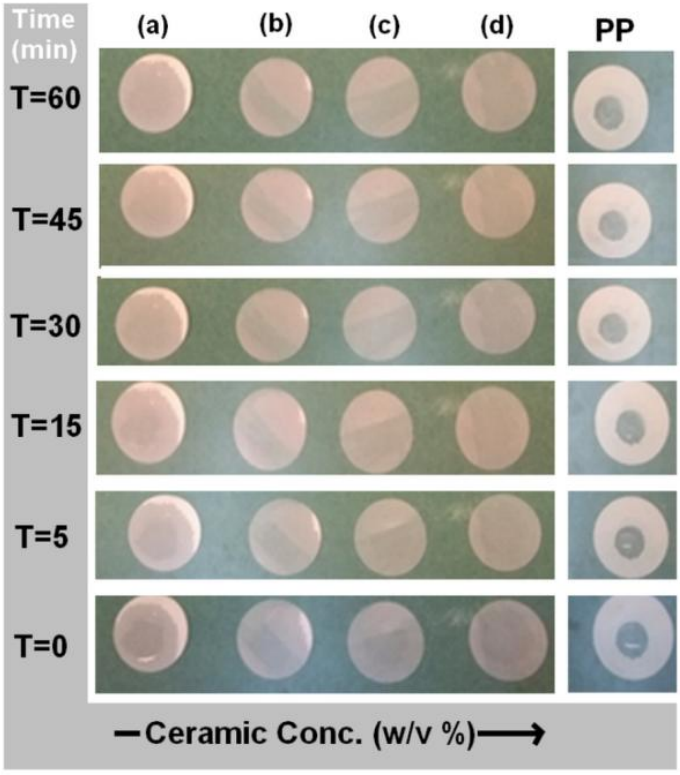

Figure 3.20 *Time dependent electrolyte soaking ability of paper separators with varying ceramic loading (a) CPS01, (b) CPS05, (c) CPS10 and (d) CPS15 along with PP*

properties of the separator are acceptable and plays very important role during electrochemical performance in actual cell environment.

3.3.2.3 Mechanical Properties

Paper is generally considered a sheet material made up of a network of natural cellulosic fibre. The process of manufacturing paper results in a preferential orientation of fibres which gives rise to physical anisotropy and small-scale non-uniformity in the paper matrix[32]. Inside the tortuosity of paper matrix, the contact between the cellulosic fibres is considered to be through hydrogen bonding between polysaccharides. Therefore, the mechanical and other properties not only depend on the nature of the fiber tortuosity or distribution, but also the bonding (H-bonding) between the fibres and its inherent strength. Any modification of paper substrate with other polymers and filler materials can have thus limited effect in enhancing the mechanical properties. However, if the coating polymer creates enough hydrogen bonding with the existing cellulosic fibers of paper substrate, an improvement in its mechanical property can be achieved.

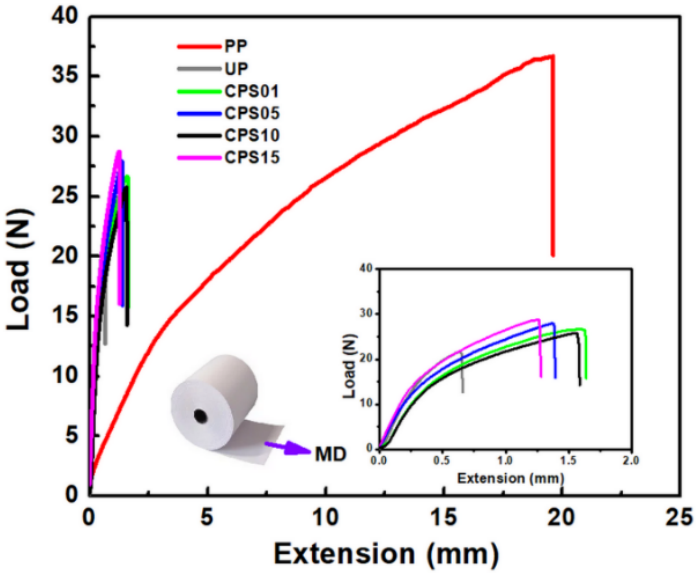

Figure 3.21 *Load vs Extension plot of fabricated Separators, untreated paper (UP) and commercial separator (PP) at machine direction (MD)*

The load vs extension curve of (a) commercial separator PP, (b) untreated paper UP, (c) CPS01, (d) CPS05, (e) CPS10 and (f) CPS15 are shown in ***Figure 3.21*** and the inset shows their enlarged views of (b) to (f). The mechanical properties as evaluated in this study using test specimens of all separators have also been presented in ***Table 3.4*** and their values were compared with untreated paper substrate-UP and PP. As expected, the commercial separator PP showed a maximum tensile strength of 183.35 MPa having 40.7 % elongation due to its inherent plastic nature. The untreated paper substrate revealed a tensile strength of 31.65 MPa

with 1.4 % elongation in machine direction (MD). The tensile strength of fabricated paper separators showed their values ranging from 34.86 MPa to 38.31 MPa with two-fold increase in elongation (tensile strain at max. load: 2.61-2.98%) compared to the untreated paper (1.4%). It is evident from these results that the effect is due to the modification made on the paper substrate using duo-polymer and nano-sized ceramic. This has led to improve the mechanical properties than that of UP, though the value is far less than that of commercial separator (PP). Similar values of mechanical strength have been reported for cellulose-ceramic composite separators[33]. However, a significant enhancement of mechanical properties (increase in elongation and tensile strength) which have been observed could be due to the combined effect of cellulosic network modification and formation of hydrogen bonds with respect to untreated paper. Moreover, the nanostructured SiO_2 used as filler materials within the cellulosic network might be helpful in increasing the packing density to regulate the pore-spaces.

Table 3.4 *Comparison of mechanical performance properties of fabricated paper separators with respect to commercial PP and UP, measured along machine direction*

Sample ID	Thickness (mm)	Max. Load (N)	Tensile stress at Max. Load (MPa)	Tensile strain at Max. Load (%)	Modulus (MPa)
PP	0.020	36.670	183.35	40.70	990.10
UP	0.080	22.153	31.65	1.40	4,071.19
CPS01	0.070	26.278	35.67	2.87	3,010.92
CPS05	0.070	27.978	37.30	2.70	3,166.20
CPS10	0.070	26.146	34.86	2.98	2,855.39
CPS15	0.070	28.735	38.31	2.61	3,143.50

3.3.2.4 Electrochemical Potential Window and Ionic Conductivity

2032 type coin cells were fabricated (configuration: Li/Separator/SS) using electrolyte-soaked paper separators and their working electrochemical potential window was calculated from the Current vs Potential plot (LSV) as given in ***Figure 3.22(a)***. As shown in the LSV curves, small humps are appeared in the LSV plots of all paper separators nearly at 4.0V. This could be

correlated to the formation of passivation layer at the working electrode side[34]. Above 4.5V, a sharp increase in current could be found for the paper separators which were due to the decomposition of the electrolyte. On the other hand, the working potential window of untreated paper and commercial PP were found to be around 5.0V. Therefore, the working potential window as obtained for the paper separators was found to be in the range of 2.5-4.5V, which might be suitable for most of the conventional commercial cathode materials. Apart from electrochemical potential window, the resistivity of separator is also crucial parameters to be analysed.

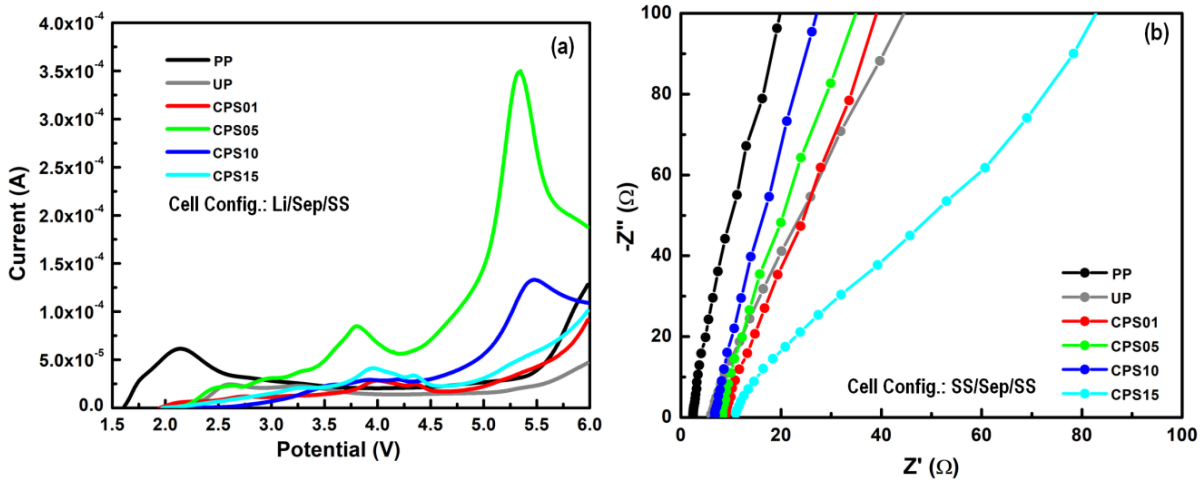

Figure 3.22 *(a) Current vs Potential plot of Li/Separator/SS asymmetric cells using electrolyte soaked UP, PP and paper separators (b) Impedance plot of symmetric cell with configuration of SS/Separator/SS using developed paper separators, UP and PP soaked in $LiPF_6$ in EC/DMC(1:2)*

The electrochemical impedance spectroscopy (EIS) was carried out for untreated paper (UP), commercial polyolefin-based separator (PP) and fabricated paper separators soaked with standard electrolyte using stainless steel plates (15 mm dia) on both sides of the separator specimens (SS/separator/SS) in 2032 coin cell configuration and their corresponding EIS plot was given in ***Figure 3.22(b)***. All the graphs showed capacitance type behaviour and their intercept value along x axis (Z′) provides the bulk resistance values of the fabricated separator samples. The bulk resistance of fabricated separator samples was found to be higher than that of commercial PP. This was due to the higher thickness (60/70 µm) of fabricated paper separators compared to commercial PP membrane (20 µm). The conductivity of electrolyte-soaked fabricated paper was also calculated from their corresponding impedance values and found to be 0.44 mS/cm (CPS01), 0.48 mS/cm (CPS05), 0.58 mS/cm (CPS10) and 0.38 mS/cm (CPS15) respectively. In comparison to the conductivity value obtained from electrolyte-

soaked commercial PP membrane (1.21 mS/cm), the fabricated separators show somewhat lower values which might be also due to the thickness of the fabricated separator.

3.3.2.5 Electrochemical Tests

The electrochemical performances of fabricated separators were studied using 2032 coin cells, against commercial $LiFePO_4$ cathode, MCMB anode and standard $LiPF_6$ liquid electrolyte (1:2 EC/DMC) and the results were presented in ***Figure 3.23***. In ***Figure 3.23(a)***, the initial charge-discharge profiles were displayed within the potential window of 2.5-3.7V for fabricated paper separators. The specific discharge capacities values obtained were 84.71 mAh/g, 115.94 mAh/g, 118.98 mAh/g and 120.94 mAh/g for CPS01, CPS05, CPS10 and CPS15 respectively. A significant difference in specific capacities for lowest and highest ceramic loaded paper separators could be observed. Apart from the enhanced electrolyte wettability for all paper separators, the pore volume also plays a crucial role in determining capacity. To estimate the rate capability and repeatability of fabricated cells comprising different ceramic loaded paper separators (CPS01. CPS05. CPS10 and CPS15), the cells were cycled at step current densities ranging from 0.1-0.4 mA/cm^2 and finally restored to the initial current density of 0.2 mA/cm^2. The results were presented in ***Figure 3.23(b)***, which suggests the increase in ceramic density in paper separator helped in sustaining the high current densities compared to that of low ceramic loaded samples. Even at lower current density of 0.1-0.2 mA/cm^2, the capacity of the cells having CPS01 and CPS05 (with low ceramic loading) gradually decreased and almost reached to <20 mAh/g. At a current density 0.4 mA/cm^2, CPS01 and CPS05 showed lower capacity values. On the other hand, the highest ceramic loaded separator (CPS15) revealed good capacity retention (~60 mAh/g) at current density as high as 0.4 mA/cm^2. The cycle life test along with columbic efficiency of fabricated paper separators were plotted in ***Figure 3.23(c)***, which revealed that all the cells using different ceramic loaded paper separator showed >97% coulombic efficiency when cycled at current density of 0.2 mA/cm^2 and good capacity retention on long term cycling. To compare the cycling performance at different step-current densities, the cells fabricated with paper separator of highest ceramic loading, CPS15 and commercial PP were cycled and the results were presented in ***Figure 3.23(d)***. It showed comparable cycling performance at different current densities. The average capacity obtained for both CPS15 and commercial PP separators at individual current densities ranging from 0.1-0.4 mA/cm^2 were plotted in ***Figure 3.23(e)***, which further confirmed that the electrochemical

performance of paper separator is almost superimposable in nature with that of commercial separator.

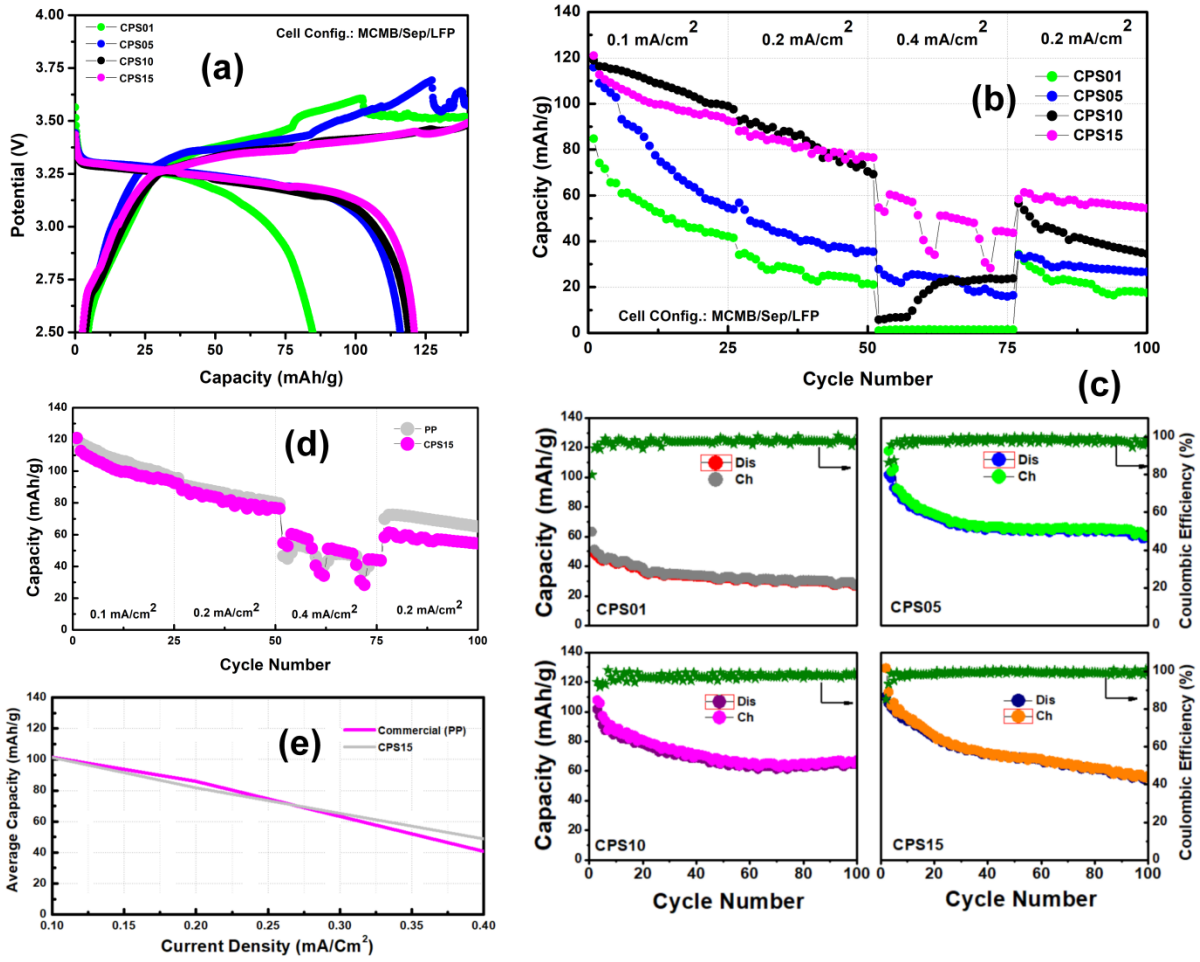

Figure 3.23 *Electrochemical performance of developed paper separators; (a) Initial charge- discharge profiles, (b) Cycle number vs step current density plot of CPS01, CPS05, CPS10 and CPS15, (c) Cycling profiles at a current density of 0.2 mA/cm2 along with their corresponding coulombic efficiencies of developed paper separators: CPS01, CPS05, CPS10 and CPS15, (d) Comparison of capacity vs cycle no. plot between fabricated paper separator (CPS15) and commercial PP separator, and (e) Average capacity vs current density plot of CPS15 and Commercial separator (PP)*

The multi-cathode compatibility study was carried out in 2032 coin type cells using fabricated paper separators (CPS01. CPS05. CPS10 and CPS15) coupling with MCMB anode and commercial cathodes such as $LiFePO_4$, $LiMn_2O_4$ and $LiCoO_2$. To obtain the specific capacities of standard commercial cathode materials against fabricated paper separators and commercial PP, the cells were cycled in CC mode and their charge-discharge profiles are plotted in ***Figure 3.24***. While testing these cells the cathode loading was almost kept same for all the commercial cathodes, preferably 0.02g active materials coated on 15 mm diameter circular aluminium foil

(20 µm) with similar weight ratio of coating composition, cathode:PVDF:conducting carbon: = 80:10:10. The specific discharge capacities were also summarized in ***Table 3.5***.

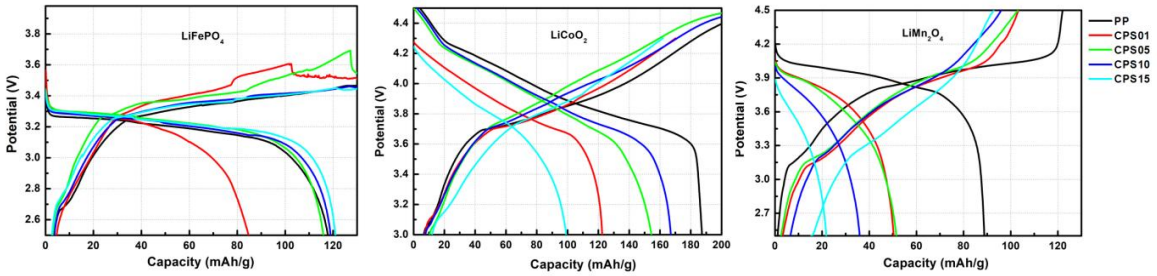

Figure 3.24 *Typical charge-discharge profiles of 2032 cells made with commercial cathodes ($LiFePO_4$, $LiCoO_2$ and $LiMn_2O_4$) and MCMB anode. Separators used are commercial polymer (PP) and paper separators CPS01, CPS05, CPS10 and CPS15 as developed in this investigation*

The electrode compatibility study revealed that the paper separators with relatively higher ceramic loading i.e., CPS05. CPS10 and CPS15, resulted in discharge capacities ranging from 115.93-120.94 mAh/g, similar to that of PP (117.83 mAh/g), when cycled against commercial $LiFePO_4$ cathode material. In case of commercial $LiCoO_2$ cathode, the separator CPS10 was found to deliver a satisfactory specific capacity of 167.08 mAh/g. The developed paper separators when tested against $LiMn_2O_4$ cathode could not perform satisfactorily compare to that of commercial PP. Therefore, the initial electrode compatibility study suggests that the developed separator is well compatible with $LiFePO_4$ and $LiCoO_2$ cathode; however for commercial $LiMn_2O_4$ cathode, further in-depth studies might be necessary to achieve acceptable performance.

Table 3.5 *Summary of specific discharge capacities (mAh/g) of different commercial cathodes achieved with separator PP and paper separators (CPS01, CPS05, CPS10 and CPS15)*

	Cathode specific discharge capacity (mAh/g)		
Separator	**$LiFePO_4$**	**$LiCoO_2$**	**$LiMn_2O_4$**
PP	117.83	187.10	88.78
CPS01	84.70	122.48	50.36
CPS05	115.93	154.44	51.50
CPS10	118.98	167.08	35.95
CPS15	120.94	99.09	21.76

3.3.2.6 Thermal Study and Safety Tests

Thermogravimetric analysis (TGA and DTA) was carried out to perform the thermal stability of separator materials by measuring its degradation behaviour at high temperature and amount of residue left during thermal treatment. The thermal behaviour of developed paper separators (CPS01 and CPS15), untreated paper (UP) and commercial separator (PP) were carried in the temperature range of RT-700ºC and shown in ***Figure 3.25(a)***. The thermal profile of fabricated separators i.e., CPS01 and CPS15 showed similar kind of multi-step weight loss between RT-500ºC. The untreated paper (UP) also followed the similar trend of weight loss up to 250ºC, which was assigned as removal of water from cellulosic paper surfaces. On the other hand, commercial PP separator showed a sluggish weight loss up to 350ºC followed by a sharp weight loss due to decomposition of Polypropylene networks. The PP suffered a complete weight loss at 450ºC as shown in the ***Figure 3.25(a)***. The corresponding DTA plots of the separators were shown in the Y-axis, which revealed three major exothermic peaks. This can be explained considering the thermal degradation profile of cellulosic materials. When heated at temperature above 250ºC, cellulose starts its decomposition process resulting in the formation of products like tar, flammable and inflammable gases, other by-products (such as water, alcohols, organic acids etc), and char (residual mass)[35]. However, in this case the cellulosic fibers of paper substrate have been functionalized using two others types of polymers namely chitosan and PVA. Both these two polymers are highly compatible with that of cellulose fibers in terms of forming intra and inter H-bonding networks as shown schematically in the ***Figure 3.25(b)***. Thus, the decomposition behaviour of paper separators is appeared to be somewhat different than the commercial untreated paper (UP). Any cellulose substrate is intrinsically hydrophilic in nature and naturally moisture (H_2O) is bound on the surfaces of cellulosic substrate. But in case of paper separator, water molecules might be predominantly attached through H-boding with the polymers used for functionalization. Thus, the removal of water molecules from the paper separators takes place in two distinct temperature ranges-(i) below 250ºC, removal of moisture trapped on the both surfaces of the separator and (ii) above 250ºC-300ºC, the release of water molecules which were H-bonded with the -OH groups of the cellulose, chitosan and PVA. Above 300ºC, pyrolysis and exothermic combustion of carbonaceous materials occurred in multi steps as reflected also by the DTA peaks. Around 25% of residual mass could be observed even after heat treatment of 500ºC. This is due to the reason that the commercial paper that are being used as substrate in this study were directly being procured from market, and it was observed that several ceramic particles were

intentionally used by the paper manufacturer for their purpose of application. Again, to functionalize the separator, SiO_2 ceramic particles were also been used. Thus, the residual mass was a cumulative mass of ceramic and char produced after thermal decomposition of paper separators. The residual mass remained unchanged throughout the set experimental temperature up to 700ºC.

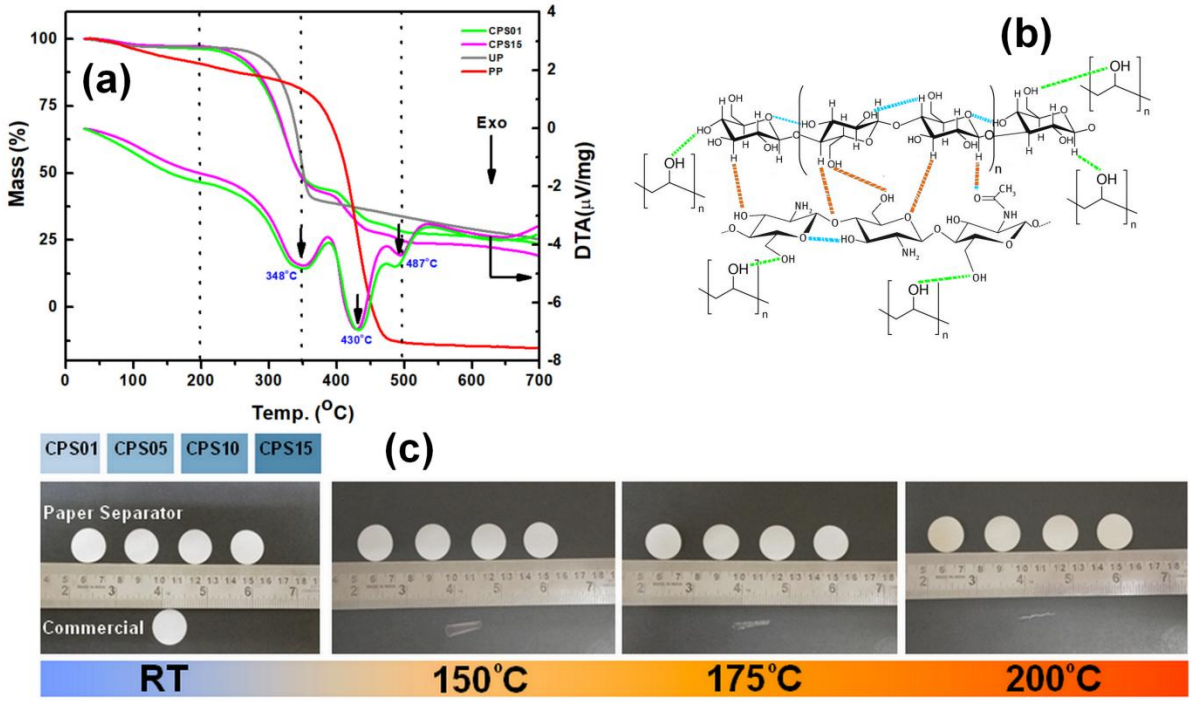

Figure 3.25 *(a) TGA/DTA plot of paper separator, untreated paper (UP) and Commercial Separator (PP), (b) Intra and inter H-bonding network in cellulose-chitosan and PVA and (c) comparative study of thermal shrinkage with commercial PP separator and fabricated paper separators (CPS01, CPS05, CPS10 and CPS15) at different temperatures (Room Temperature to 200ºC)*

The dimensional stability on elevated temperature is one of the crucial properties regarding the safety aspects of batteries. The commercial plastic separator (PP) does not withstand high temperatures (>90ºC) and severe dimensional shrinkage is typically observed for PP beyond 100ºC. In ***Figure 3.25(c)***, the thermal stability of the fabricated paper separators (CPS01, CPS05, CPS10 and CPS15) were compared with commercial PP up to 200ºC and the digital images taken during the experiment were presented. PP was found to be completely collapsed above 150ºC. Unlike PP, no dimensional shrinkage could be observed for the developed paper separators up to 200ºC. It clearly suggests that developed paper separator can offer higher safety than commercial PP during thermally abused condition.

The thermal stability and phase transformation of fabricated separators (CPS01, CPS15), untreated paper (UP) and commercial polyolefin-based separator (PP) was examined by differential scanning calorimeter (DSC) from RT to 400°C @ 10°C /min and presented in ***Figure 3.26***. The thermogram of commercial polyolefin-based separator showed two distinct endothermic peaks at temperatures of 129.4°C, 158.1°C attributed to the melting of the separator membrane. On the other hand, a broad endothermic peak could be detected for the paper separators (CPS01 and CPS15), which might be due to the moisture removal (both surface and H-bonded water molecules) from the cellulose composites. No peaks could be found related to phase transformation or melting of paper separators. Beyond 350°C, exothermic peaks were detected for both untreated paper (UP) and fabricated paper separators (CPS01 and CPS15). The DSC result was found to be corroborating the findings as obtained in TGA/DTA analysis. The change in enthalpy was also calculated by using the software Proteus thermal analysis 8.0.3 by measuring the area under the curve. The ΔH (kJ/mol) values as obtained were found to be 74.5, 47.05 kJ/mol for commercial separator, whereas it showed the value of 164.5 kJ/mol for CSP01 and 107.6 kJ/mol for CPS15 respectively. The DSC results clearly described the better thermal profile of the fabricated paper separators compared to the commercial polyolefin separator membrane.

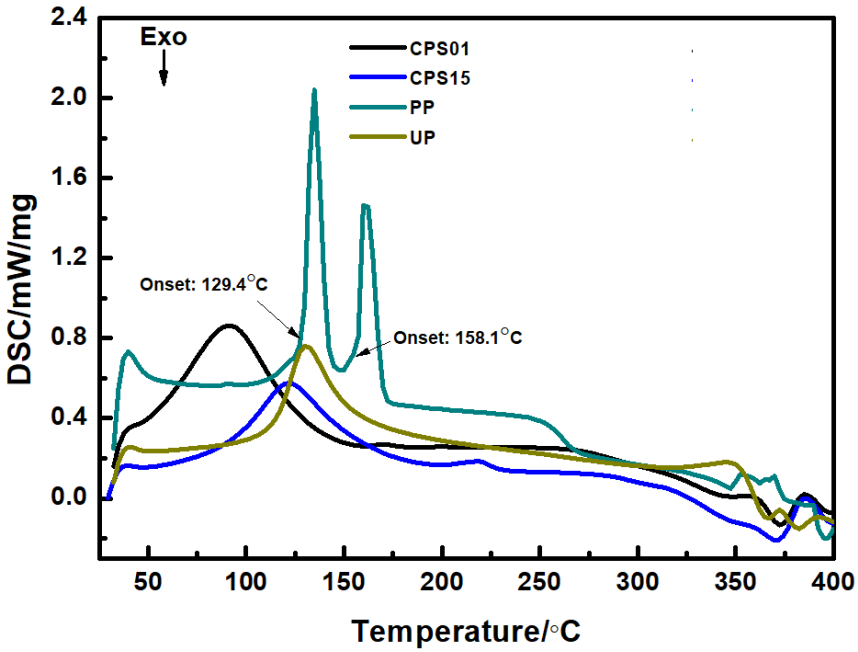

Figure 3.26 *DSC thermogram of fabricated separators (CPS01 and CPS15), untreated paper and commercial PP based separator from RT to 400℃ at heating ramp of 10℃/min in inert atmosphere*

To enhance battery safety features, flame retardant additives (FRAs) are commonly used in the electrolyte composition to reduce its flammability with a view that the FRAs may help in

releasing free radicals with flame-retardant effects during thermal decomposition[36]. Another way is to develop a separator material with flame retardant properties in-built which does not collapse its dimension under thermal runaway preventing handshaking between active electrodes. A commercial plastic separator (PP/PE) has proven to be completely failed due to its easy melting and dimensional collapse. In the present work, in-flame combustion test was carried out for the developed separator-CPS15 along with commercial PP separators. Both the separators were soaked with standard electrolyte solution before conducting the test. ***Figure 3.27*** shows the digital images taken during flame test using two separators; CPS15 and PP. It was observed that due to its aliphatic hydrocarbon structure, commercial PP separator readily shrinked with a relatively smoke-free flame once exposed to flame and burnt out very rapidly without leaving a char residue (as shown in ***Figure 3.27***). It is due to the fact that at initial phase of flame heating, depolymerisation of commercial separator started, followed by volatilization of mass. On the other hand, developed paper separator (CPS15) revealed excellent flame retardant properties in combustion test. An initial flame due to the presence of electrolyte was seen momentarily; however, no further flame or its propagation could be detected on 10 seconds continuous exposure to flame. The flame retardant property of paper separator might be originated due to build-up of char layer which shielded the inner tortuous cellulose fibers against oxygen retarding its combustion or further flame propagation. Duo-polymer and ceramic coating used on paper substrate might have provided a barrier against the heat source creating a carbonaceous surface structure as thermal barrier. The combustion test thus revealed that the developed paper separator can also offer excellent safety features by successfully retarding the propagation of flame. As per UL 94 V ratings, the developed paper separators can be classified as V-0 category in terms of safety.

Figure 3.27 *Digital images taken during flame test at different time intervals for PP and developed paper separator, CPS15; the source of continuous flame is a gas lighter*

3.4 Conclusion

This chapter demonstrated a scalable and eco-friendly route to transform commercial cellulose paper into functional paper-based composite separators, termed "Paperators," by surface modification with polymer–ceramic blends. The incorporation of $BaTiO_3$ and SiO_2 nanoparticles, together with chitosan and PVA as dual binders, enabled effective reinforcement of the fibrous paper matrix, anchoring large pore spaces, and imparting enhanced structural integrity, wettability, and electrochemical stability. The $BaTiO_3$-impregnated separators benefited from the ferroelectric nature of the filler, which improved electrolyte affinity and contributed to interfacial stability during long-term cycling, though excessive loading occasionally led to agglomeration and reduced capacity due to pore blocking. In contrast, SiO_2-based separators offered homogeneous particle distribution, high porosity, and superior electrolyte uptake without adversely affecting pore connectivity, which translated to stable ionic conductivity and favorable electrochemical performance. Both separator types showed significantly faster electrolyte soaking and lower contact angles compared with commercial polypropylene membranes, underlining their strong affinity toward liquid electrolytes. Mechanical testing revealed substantial reinforcement compared to untreated paper, while thermal analysis and dimensional stability tests confirmed resistance to shrinkage and degradation up to elevated temperatures, surpassing commercial PP membranes. Safety tests further highlighted the inherent flame-retardant characteristics of the functionalized papers, with the formation of protective char layers suppressing flame propagation. Electrochemical evaluations in $LiFePO_4$, $LiCoO_2$, and $LiMn_2O_4$ half cells confirmed that the optimized Paperators delivered capacities and cycling stability comparable to commercial separators, with minor limitations arising from higher separator thickness and tortuous ion pathways intrinsic to the cellulose network. Furthermore, demonstration of their application in supercapacitors validated their multifunctional potential beyond lithium-ion batteries. The integration of both $BaTiO_3$ and SiO_2 systems thus establishes that cellulose-based composite paper separators can effectively combine sustainability, safety, and practical performance. Collectively, this work highlights that ceramic selection and optimization of polymer–filler ratios are critical in tailoring performance, while processability using semi-automated roll-to-roll fabrication demonstrates clear pathways for industrial scalability. Overall, the findings confirm that "Paperators" present a promising, sustainable, and safe alternative to conventional polyolefin separators for next-generation rechargeable batteries and related energy storage devices.

References

1 A. A. Heidari and H. Mahdavi, 2020, preprint, DOI: 10.1002/tcr.201900054.

2 M. F. Lagadec, R. Zahn and V. Wood, 2019, preprint, DOI: 10.1038/s41560-018-0295-9.

3 Y. Song, L. Sheng, L. Wang, H. Xu and X. He, 2021, preprint, DOI: 10.1016/j.elecom.2021.106948.

4 W. Luo, S. Cheng, M. Wu, X. Zhang, D. Yang and X. Rui, *J Power Sources*, DOI:10.1016/j.jpowsour.2021.230372.

5 E. Shekarian, M. R. J. Nasr, T. Mohammadi, O. Bakhtiari and M. Javanbakht, *Journal of Nanostructures*, DOI:10.22052/JNS.2019.04.015.

6 X. Jiang, X. Zhu, X. Ai, H. Yang and Y. Cao, *ACS Appl Mater Interfaces*, DOI:10.1021/acsami.7b05535.

7 L. Peng, X. Wang, J. Dai, X. Shen, B. Huang, P. Zhang and J. Zhao, *Mater Chem Front*, DOI:10.1039/d0qm00849d.

8 M. He, X. Zhang, K. Jiang, J. Wang and Y. Wang, *ACS Appl Mater Interfaces*, DOI:10.1021/am507145h.

9 J. Zhang, L. Yue, Q. Kong, Z. Liu, X. Zhou, C. Zhang, Q. Xu, B. Zhang, G. Ding, B. Qin, Y. Duan, Q. Wang, J. Yao, G. Cui and L. Chen, *Sci Rep*, DOI:10.1038/srep03935.

10 Z. Gao, Y. Zhang, N. Song and X. Li, 2017, preprint, DOI: 10.1080/21663831.2016.1250834.

11 T. Guo, J. Song, Y. Jin, Z. Sun and L. Li, *Carbohydr Polym*, DOI:10.1016/j.carbpol.2018.11.025.

12 D. Lv, J. Chai, P. Wang, L. Zhu, C. Liu, S. Nie, B. Li and G. Cui, *Carbohydr Polym*, DOI:10.1016/j.carbpol.2020.116975.

13 E. Lizundia, C. M. Costa, R. Alves and S. Lanceros-Méndez, *Carbohydrate Polymer Technologies and Applications*, 2020, **1**, 100001.

14 R. Shogren, D. Wood, W. Orts and G. Glenn, 2019, preprint, DOI: 10.1016/j.spc.2019.04.007.

15 H. Y. Sun, Y. Takeda, N. Imanishi, O. Yamamoto and H.-J. Sohn, *J Electrochem Soc*, DOI:10.1149/1.1393554.

16 S. Li, W. Zhu, Q. Tang, Z. Huang, P. Yu, X. Gui, S. Lin, J. Hu and Y. Tu, 2021, preprint, DOI: 10.1021/acs.energyfuels.1c02049.

17 S. Bhardwaj and N. K. Bhardwaj, *Nord Pulp Paper Res J*, DOI:10.1515/npprj-2018-0063.

18 A. Gigova, *J Power Sources*, DOI:10.1016/j.jpowsour.2005.11.006.

19 Z. Wang, H. Xiang, L. Wang, R. Xia, S. Nie, C. Chen and H. Wang, *J Memb Sci*, DOI:10.1016/j.memsci.2018.02.040.

20 M. R. Asghar, M. T. Anwar, A. Naveed and J. Zhang, 2019, preprint, DOI: 10.3390/membranes9070078.

21 G. Malucelli, 2020, preprint, DOI: 10.3390/molecules25184046.

22 A. Dasari, Z. Z. Yu, G. P. Cai and Y. W. Mai, 2013, preprint, DOI: 10.1016/j.progpolymsci.2013.06.006.

23 T. N. Rao, I. Hussain and B. H. Koo, in *Materials Today: Proceedings*, 2020, vol. 27.

24 E. V. Gnedin, S. N. Novikov and N. A. Khalturinskij, *Makromolekulare Chemie. Macromolecular Symposia*, DOI:10.1002/masy.19930740145.

25 S. Duquesne and S. Bourbigot, in *Fire Retardancy of Polymeric Materials, Second Edition*, 2009.

26 T. Xu, X. Huang and Y. Zhao, *Fire Saf J*, 2011, **46**, 330–334.

27 H. Li, D. Wu, J. Wu, L. Y. Dong, Y. J. Zhu and X. Hu, *Advanced Materials*, DOI:10.1002/adma.201703548.

28 H. Pingan, J. Mengjun, Z. Yanyan and H. Ling, *RSC Adv*, DOI:10.1039/C6RA25579E.

29 C. J. Orendorff, *Electrochemical Society Interface*, DOI:10.1149/2.F07122if.

30 S. S. Zhang, 2007, preprint, DOI: 10.1016/j.jpowsour.2006.10.065.

31 E. S. Jang, C. W. Kang and S. S. Jang, *Journal of the Korean Wood Science and Technology*, DOI:10.5658/WOOD.2018.46.6.681.

32 J. C. Roberts, *The Chemistry of Paper*, 1996.

33 Z. Zhang, M. Zhou, J. Yu, J. Cai and Z. Yang, *Energy and Environmental Materials*, DOI:10.1002/eem2.12153.

34 Q. Sabrina, C. R. Ratri, A. Hardiansyah, T. Lestariningsih, A. Subhan, A. Rifai, R. Yudianti and H. Uyama, *RSC Adv*, DOI:10.1039/d1ra03480d.

35 J. Alongi, G. Camino and G. Malucelli, *Carbohydr Polym*, DOI:10.1016/j.carbpol.2012.10.029.

36 J. Troitzsch, *Flame Retardants Polymer Blends, Composites and Nanocomposites*, 1999, vol. 89.

Chapter 4

Tri-layer Paper Separator: Reduction of Thickness and Performance Enhancement

Highlights

- Paper separator with multiple functional layers
- Industry-friendly wet-coating process for large scale development
- Comparable physico-chemical, and electrochemical performance with commercial separator; applicability in LIBs and SCs
- Excellent electrolyte wettability, porosity, and safety features

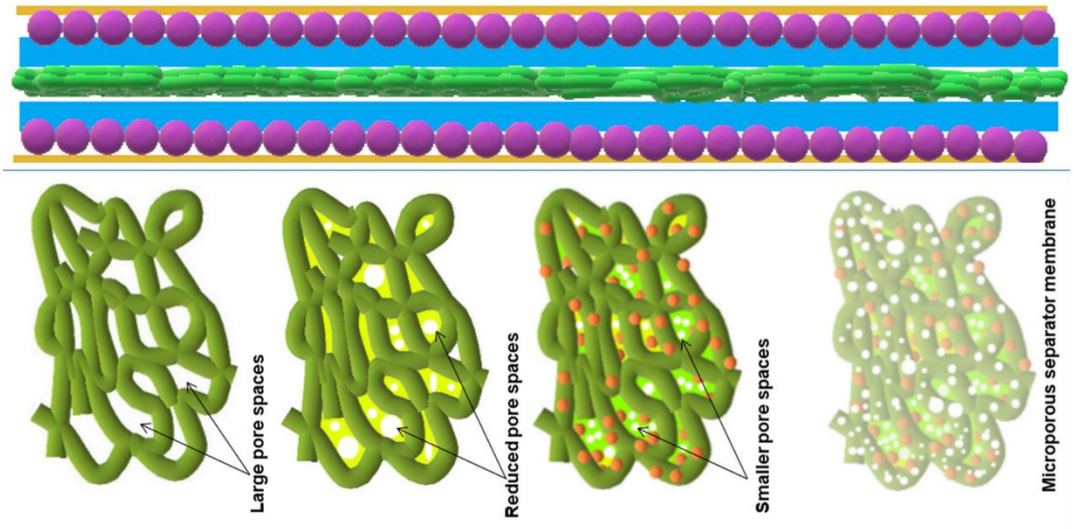

Figure 4.0 *Schematic representation of the tri-layer paper separator matrix*

This chapter describes the development of a tri-layer cellulose paper separator prepared by surface sizing, ceramic impregnation, and lamination. The structural modification improves electrolyte wettability, porosity control, and mechanical robustness while ensuring excellent thermal stability and flame resistance. The in-cell chemical stability as tested via EIS for 8 weeks, revealed nominal change in bulk resistivity with no significant morphological changes. Electrochemical evaluation demonstrates stable cycling, good rate capability, and compatibility with multiple cathodes in lithium-ion batteries, as well as effective performance in supercapacitors. The findings establish ceramic-impregnated cellulose paper as a sustainable and safe alternative to conventional polyolefin separators.

4.1 Background and Overview

Extensive research is being carried out globally on cellulosic papers to convert them into effective separator materials in LIBs[1,2]. However, pristine cellulosic paper with anisotropic pore distribution, large relative pore size and poor mechanical strength has limited its opportunity of being used as separator in LIBs or other energy storage devices because of undesired self-discharge phenomena and vital safety risks caused by lithium dendritic growth[1]. Therefore, paper needs to be functionalized before its use in real cell environment. In the previous work, we have tried to convert locally outsourced paper into paper separator. Although the approach was cost-effective and eco-friendly, the impurities present in the paper matrix hinder the ability of long cycling in an electrochemical cell. The high thickness of the separator contributed significantly in enhancing the bulk resistance and limiting the electrolyte wettability. Also, the issue of ceramic leaching was quite persistent.

To mitigate these problems, an effort has been made here to develop tri-layer ultrathin paper separator (will be henceforth referred as UTPS) using a scalable industry friendly wet-coating method by functionalizing thin paper with polymers and ceramic nanoparticles. It is worthy to mention that the word "ultrathin" is used with respect to the previously developed paper-based separator[17], not in commercial comparison such as PP or PE based separators. During functionalization of paper substrate, porosity and pore size are two major critical parameters which were duly optimized prior to application in cells. This is due to the fact that large number of pores in any separator material is essential, but those need to be uniformly distributed to prevent dendritic growth of lithium during cycling and also to prevent the percolation of active electrode particles across the porous membrane[3]. It is thus argued that the pore size of typical separator materials should be less than 1 μm[4]. In this context, the untreated pure cellulose paper chosen here, does not qualify as separator material to be used directly in the cells. Cellulose-based paper is intrinsically porous in nature, with large anisotropic pore spaces (ranging from 10-45 μm) originated from entangled cross-linked cellulosic fibers. Such high porosity may have adverse impact on electrochemical performance of the cells due to poor mechanical strength and higher internal resistance. Keeping this thought in mind, in this research, the pore spaces present in untreated paper substrate has been systematically manipulated to fabricate paper separator and to do that, the pristine paper has been coated with cellulose compatible polymers namely polyvinylidene difluoride (PVDF) and styrene-butadiene rubber (SBR) via a scalable method. PVDF is a well-known fluoropolymer consisting of valuable properties:

relatively high melting point, high mechanical strength at elevated temperatures, chemical resistance, resistance to hydrolysis, physiological inertness, low thermal conductivity, and exceptional resistance to ignition[5]. Furthermore, PVDF is widely used in paper making industries as sizing agent. On the other hand, ultrafine ferroelectric $BaTiO_3$ (BTO) nano powder was introduced here mainly as a filler to enhance structural integrity and thermal stability of paper matrix. It is reported elsewhere that presence of BTO may also facilitate electrolyte salt dissociation in charged species, can improve ionic conductivity of polymer used by increasing amorphous content and can enhance lithium interface stability[6].

The present chapter thus demonstrates a systematic study towards development of a technologically important low cost sustainable paper based separator component for energy storage devices like lithium-ion batteries (LIBs) and supercapacitors (SCs). A detailed discussion has also been presented here on the strategy of process scaling-up. Separators with varying polymer-ceramic compositions were fabricated and thoroughly characterized in terms of porosity, pore size distribution, microstructure, electrolyte wettability, thermal stability/shrinkage, mechanical behaviour, and electrochemical performances both in lithium-ion cells and supercapacitors. The chemical stability of paper separator inside lithium-ion full cell during calendar ageing (without cycling) for eight weeks was evaluated using impedance spectroscopy (EIS) and surface imageing (FESEM and EDX) continuously. The combustion safety test was also carried out to evaluate the flame retardant properties of composite paper separators. The obtained results were also duly compared with commercial PP based separator. The paper separators thus developed under this study might be considered a step towards achieving sustainability in energy storage domain both for LIBs and supercapacitors. The current research status on cellulose or its derivatives as separator materials for LIBS are duly summarized in ***Table 4.2***.

4.2 Separator Fabrication Process

The process of fabrication of UTPS has been carried out in three major steps- (i) Sizing, (ii) Ceramic impregnation and (iii) Lamination, as described in ***Section 2.3.2.3*** in ***Chapter 2***. The commercial cellulose paper of ~20 μm thickness, as named here untreated paper (UP), is initially coated with 3.5w/v% polyvinylidene fluoride (PVDF) in NMP solution via wet-coating method using an in-house fabricated double-decker (DD) coating machine, as shown in ***Figure 2.1*** of ***Chapter 2***. The dried PVDF coated paper was then compacted using a

calendaring machine under a load of 50-60 tons. This process is called surface 'sizing' which offers certain benefits towards large scale fabrication process improving the tensile strength of the thin paper substrate and extending the scope of further functionalization. Sizing process also consolidates the surface of the paper sheet reducing its tendency to extricate surface fibers and moisture absorption under humid atmosphere[7]. Another most important role of this step is to reduce of pore spaces of untreated bare paper substrate. Such minimization of pore spaces is required to offer directional penetration of electrolyte through the pores rather than fibers. The untreated paper coated with 3.5 w/v% PVDF thus obtained in this step will be henceforth termed as P35.

In next step, the PVDF coated paper was subjected to second coating using an aqueous blend of styrene-butadiene rubber (SBR, 7.0 w/v%) and $BaTiO_3$ nano-ceramic powder (BTO, 2.0 w/v%) using the same wet-coating technique. This step may be termed as 'ceramic impregnation' or internal sizing using ceramic fillers. Through this process of internal sizing, several purposes are served. The surface energy of PVDF coated paper becomes lowered[5]. The ceramic filler BTO sits on the top surface of the fibers giving reinforcement to the entangled cellulosic fibers of paper and further pore spaces are reduced due to SBR coating. Both the above two steps i.e., surface sizing and ceramic impregnation steps have crucial impact on the wettability of separator membrane. The paper separator at this functionalization stage will be henceforth terms as P35SB7BT20.

After two layers of successive coatings in the final step, the paper was further coated with SBR aqueous solution of varying concentration of 1.0-3.0 w/v%. This is called 'lamination' step. It provides smooth separator surface, minimizes pore spaces and also works as protective layer to impede the dissolution and/or leaching of ceramic particles in electrolyte under actual cell environment.

After lamination step, the in-situ dried paper separators were finally compacted under pressure of 20-30 tons using the calendaring machine. Depending on the concentration of SBR solution used for lamination layer, the separator will be henceforth referred as - P35SB7BT20SB1 (coated with 1.0 w/v% SBR), P35SB7BT20SB2 (coated with 2.0 w/v% SBR) and P35SB7BT20SB3 (coated with 3.0 w/v% SBR).

4.3 Results and Discussion

The structural, physical and electrochemical properties of the developed paper separators have been described below, along with proper comparison with commercial PP-based separator, where necessary:

4.3.1 Microstructural Features

Microstructural imageing was carried out in every step of fabrication process starting from untreated paper (UP) to lamination step and shown in ***Figures 4.1 (a)-(d)***.

The untreated paper showed entangled cellulose fibers with heterogeneous porosity or pore spaces measuring 5-20 μm in length as shown in ***Figure 4.1(a)***. Thereafter, the surface sizing as done with PVDF polymer resulted in reduced number of pore spaces as well as pore dimension in separator P35, as reflected in ***Figure 4.1(b)***. From the micrograph of P35, it was also observed that the sized surface of paper was found more compact (in terms of fiber density per unit volume) compared to the untreated paper (UP). In the step of ceramic impregnation, the porosity and pore diameter were found to further reduce due to the introduction of SBR and BTO nano powder as seen in the micrograph presented in ***Figure 4.1(c)***. A typical micrograph of laminated paper separator- P35SB7BT20SB2 as given in ***Figure 4.1(d)*** describes a significant reduction of pore spaces and increase in fiber compact-density due to application of lamination coating with SBR. EDX spectrum presented in ***Figure 4.1(e)*** taken after ceramic impregnation step for the fabricated separator P35SB7BT20 clearly indicates the presence of Ba, Ti and O.

It is interesting to observe that the untreated paper substrate is composed of several cellulosic fibers of different length and width as shown in ***Figure 4.1(g)***. However, such fibers are not elementary in nature, rather composed of large number of microfibrillar bundles. FESEM image taken at the torn edge of fabricated P35SB7BT20 separator as shown in ***Figure 4.1(f)*** revealed the presence of cellulose microfibrils. It was further observed that the ceramic nanoparticles are also present on the surface of the microfibrils. Thus, it can be stated that the ceramic impregnation step not only changed the surface properties but also modified the surface of the elementary fibers, which might be helpful in strengthening mechanical properties of composite paper separator.

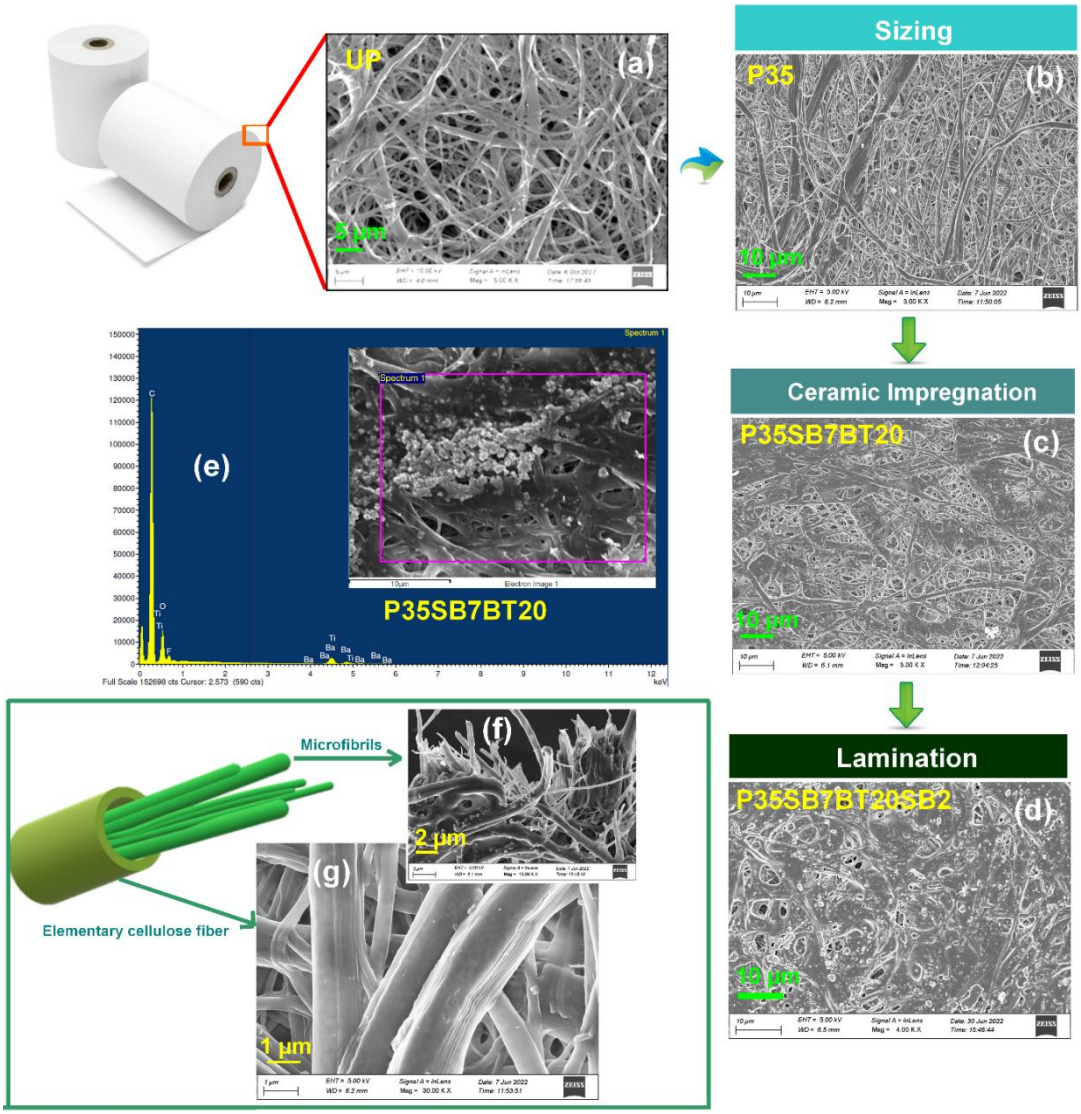

Figure 4.1 *FESEM micrographs of (a) untreated paper (UP), (b) P35 separator obtained after sizing, (c) P35SB7BT20 separator after ceramic impregnation, (d) P35SB7BT20SB2 separator after laminating with 2 w/v% SBR, (e) selected area elemental mapping by EDX of separator P35SB7BT20, (f) & (g) A schematic representation of cellulosic fiber and its elementary microfibrils is displayed along with FESEM images taken on P35 sized separator*

4.3.2 Air permeability, Porosity and Electrolyte Wettability

Figure 4.2(a) shows the air permeability values of UP, P35, P35SB7BT20 and other fabricated paper separators (P35SB7BT20SB1, P35SB7BT20SB2 and P35SB7BT20SB3). Estimation of air permeability of separator membrane in terms of Gurley values (in seconds) is considered to be one of the critical characterization tools which helps to evaluate the nature of porosity and the homogeneous distribution of pores in separator matrix. To perform this test, separator

samples were cut into circular disks from different portions of fabricated separators, particularly front, middle and rear segments of separator roll. The time required for permeation of 100 cc air through those samples is estimated in this test. As shown in ***Figure 4.2(a)***, the untreated paper (UP) show very low Gurley value of 5s due to the presence of large sized pore spaces. However, after completion of first layer coating (sizing) with PVDF 3.5 w/v%, the P35 separator shows a fourfold increase in Gurley value (20s). Thereafter, with the introduction of SBR-BTO ceramic blend over P35, the Gurley value further increases to 28s for P35SB7BT20. The final coating with SBR (in the lamination step) with increased concentrations of 1-3 w/v%, Gurley values increased to 85s (P35SB7BT20SB1), 120s (P35SB7BT20SB2) and 140s (P35SB7BT20SB3), respectively. The sharp decrease in air permeation ability of the separator membranes reveal that the addition of polymeric layers (PVDF and SBR) during sizing, ceramic impregnation and lamination processes has significant effect in reducing number of pore spaces as well as their dimensions in separator matrix.

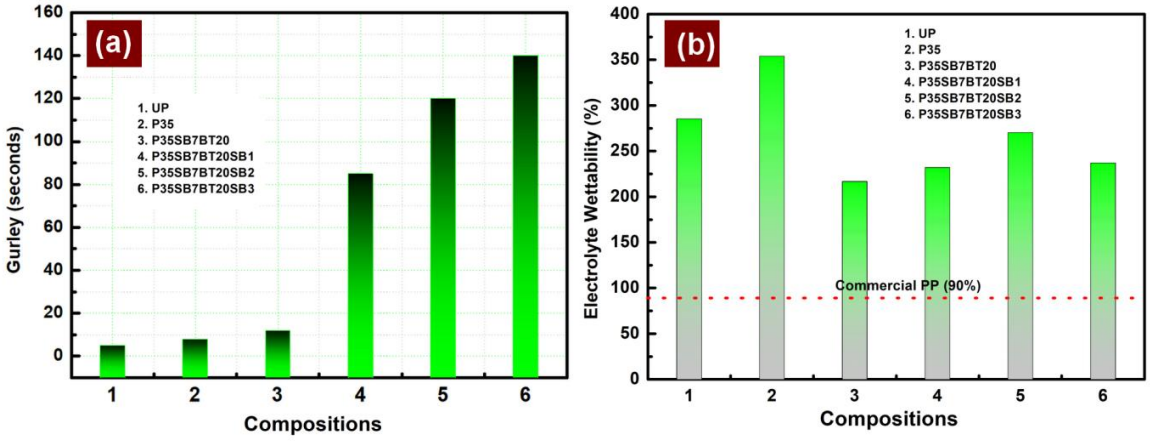

Figure 4.2 *(a) Air permeability values in terms of Gurley seconds (per 100 cc air) of untreated paper and fabricated paper separators, (b) comparison of electrolyte wettability of untreated paper and fabricated separators with commercial PP (red dotted line)*

Figure 4.2(b) shows the variation of electrolyte ($LiPF_6$ in EC/DMC) wettability values of untreated paper and fabricated composite paper separators calculated using ***Equation 2.1***. The estimated values are duly compared with the electrolyte wettability value of commercial PP based separator. The untreated cellulosic paper showed wettability values of 285.29%, three times higher than commercial PP (electrolyte wettability ~ 90%) due to its large number of pore spaces and also high volumetric dimension. In P35 separator, it was observed that PVDF coating significantly increased the hydrophobicity of untreated paper substrate, which further

enabled the cellulosic surface of wide spreading of organic liquid electrolyte and its faster adsorption process resulting in higher wettability value of 353.84%. In the next step i.e., ceramic impregnation process, further coating with SBR and BTO ceramic blend reduces the number of pore spaces that existed in P35 surface and also it reduced its dimension which was reflected in decreased wettability value of 216.67% for P35SB7BT20 separator. In the final lamination step, the P35SB7BT20 separator when coated with 1 w/v% SBR solution (P35SB7BT20SB1), wettability value was found to increase marginally, and reached to maximum value of 270.21% for the laminated separator using 2 w/v% SBR solution (P35SB7BT20SB2) and finally dropped to 236.95% for P35SB7BT20SB3 separator laminated with 3 w/v% SBR. Although lamination process was found to reduce pore volume and pore dimension after ceramic impregnation process, still electrolyte wettability values are significantly higher than the commercial PP separator membrane. It clearly suggests that the three-layer multi-step coating process as executed on untreated paper substrate had intrinsically increased the electrolyte soaking ability of the developed composite paper separators.

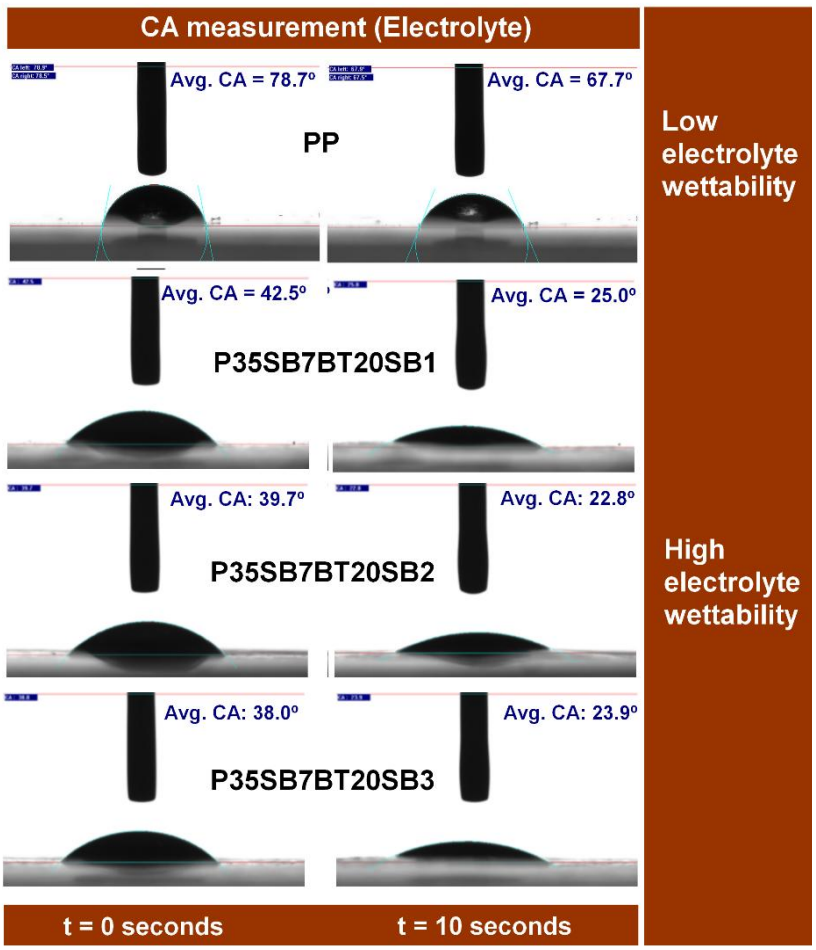

Figure 4.3 *Contact angles measured using standard electrolyte solution for (i) PP, (ii) P35SB7BT20SB1, (iii) P35SB7BT20SB2 and (iv) P35SB7BT20SB3 with respect to time*

Another most convincing method to assess wettability is to measure the angle of contact between the probe liquid (water or electrolyte) and the surface of the paper substrate[8]. The variation of electrolyte contact angles in terms of compositions of developed paper separators has been presented in ***Figure 4.3***. The image represents the time dependent changes in contact angles in electrolyte for commercial PP-based separator as well as P35SB7BT20SB1, P35SB7BT20SB2 and P35SB7BT20SB3 paper separators. The laminated separators showed low contact angle ranging from 38.0-42.5° at the moment of dropping electrolyte, which almost instantly reduced to 22-25° after 10 seconds while commercial PP-based separator showed contact angle of 78.7° initially, which decreased to the value of 67.7° after 10 seconds duration. Such lower contact angles of fabricated separators in comparison to the commercial one corroborates the findings obtained during estimation of electrolyte wettability. Lowering of contact angle basically relates to the higher spreading of liquid on substrate surface.

4.3.3 Mechanical Properties and Thermal Shrinkage Test

Tensile properties of the separator are important from cell manufacturing point of view wherein the separator has to endure certain tension of winding machine during cell assembly[9,10]. ***Figures 4.4(a) and (b)*** show the Load vs Extension plot of untreated paper (UP) and P35SB7BT20SB1, P35SB7BT20SB2 and P35SB7BT20SB3 paper separators both in (a) machine direction and (b) transverse direction. The mechanical properties as obtained are summarized in ***Table 4.1***.

Table 4.1 *Summary of mechanical properties of the developed paper separators*

Code	Width (mm)	Thickness (µm)	Max. Load (N)	Tensile stress at Max. Load (MPa)	Tensile strain at Max. Load (%)	Modulus (Automatic) (MPa)
UP-MD	10.00	20.000	9.253	46.26	1.75	5,200.81
UP-TD	5.00	20.000	1.183	11.83	2.97	921.58
P35-MD	10.00	0.02	10.140	50.70	4.37	3000.00
P35-TD	7.00	0.02	3.353	23.95	9.84	780.00
P35SB7BT20-MD	10.00	0.02	9.216	46.08	4.83	3290.00
P35SB7BT20-TD	6.00	0.02	3.220	26.84	8.61	900.00
P35SB7BT20SB1-MD	10.00	20.000	9.587	47.93	4.73	3,351.14
P35SB7BT20SB1-TD	5.00	20.000	2.768	27.68	8.50	842.51
P35SB7BT20SB2-MD	10.00	20.000	10.030	50.15	4.23	3,534.45
P35SB7BT20SB2-TD	5.00	20.000	2.821	28.21	8.44	940.71
P35SB7BT20SB3-MD	10.00	20.000	8.791	43.96	3.89	3,445.46
P35SB7BT20SB3-TD	5.00	20.000	2.657	26.57	6.98	970.50

It is revealed that the functionalization of paper separators using duo-polymer and ceramic offered marginal increase in their tensile stress at maximum load (43.96-50.15 MPa) compared to untreated paper substrate (46.26 MPa), however, two fold increase in tensile stress (paper separators: 26.57-28.21 MPa) was achieved in transverse direction (UP-TD: 11.83 MPa). A plot presenting variation of tensile strengths both in machine direction (MD) and transverse direction (TD) with respect to paper separator composition is shown in ***Figure 4.5*** for better understanding.

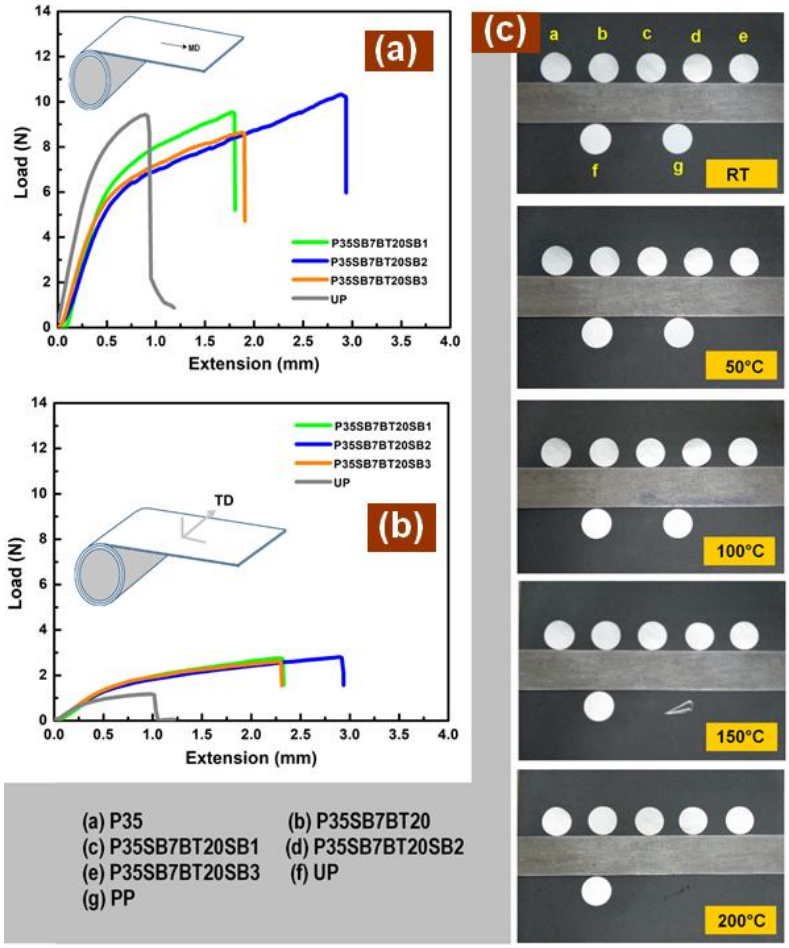

Figure 4.4 *Load vs extension curve (a) in machine direction (MD) and (b) in transverse direction (TD). (c) Digital images of thermal shrinkage up to 200°C for the separator specimen with code (a) P35, (b) P35SB7BT20, (c) P35SB7BT20SB1, (d) P35SB7BT20SB2, (e) P35SB7BT20SB3, (f) UP and (g) commercial PP based separator*

The increase in tensile strain as observed at maximum load both in (MD) and (TD) might be due to functionalization of paper substrate. It is worthy to mention here that mechanical properties of any paper-based material not only depend on the nature of the fiber, but also on

the bonding (H-bonding) between the fibers and their inherent strength[11]. Functionalization of paper substrate with polymers and filler materials can thus have limited effect in enhancing the mechanical properties. However, if the coating polymers are able to create new hydrogen bonding with the existing cellulosic fibers of paper matrix, an improvement in its mechanical property can be achieved[12].

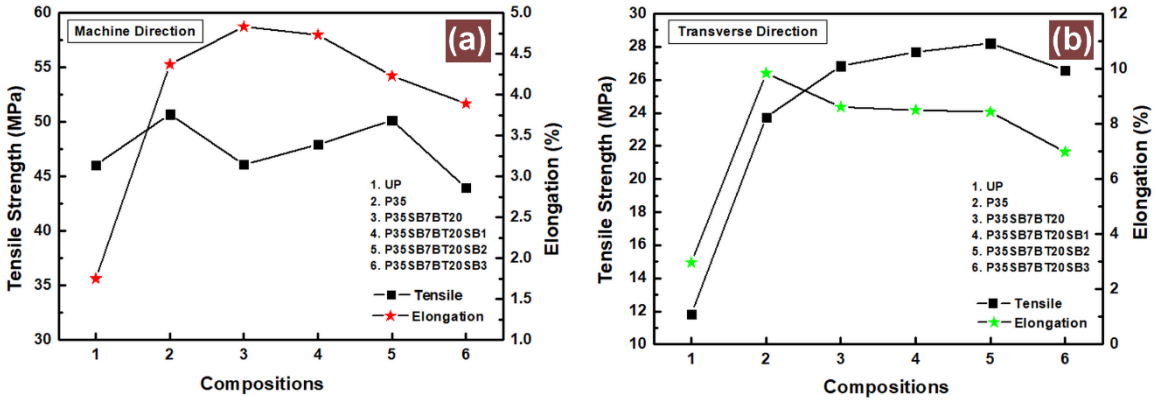

Figure 4.5 *Comparison Plots of Tensile Properties*

Therefore, enhancement in mechanical properties in terms of tensile strain (MD and TD) in fabricated paper separators is a combinational effect of both natural cellulosic fibers present in the paper substrate and inter- and intra H-bonding created by duo polymers (PVDF and SBR).

Also, the structural integrity of developed separators at elevated temperatures has been examined by qualitative thermal shrinkage test in an oven from 50°-200°C for UP, PP and fabricated separators-P35, P35SB7BT20, P35SB7BT20SB1, P35SB7BT20SB2 and P35SB7BT20SB3, as given in ***Figure 4.4(c)***. It has been observed that the commercial polyolefin membrane shows a dimensional shrinkage at ~120°C and it is totally degraded at 200°C, whereas our developed paper separators are able to hold their dimensional integrity even at 200°C and beyond. This is due to the fact that heat can readily dissipate though the fibrous cellulosic network of paper separator and ceramic filler materials can provide high thermal resistance. Apart from that, SBR also acts as binder material to maintain the structural integrity of the separator at elevated temperature. Thus, due to this improved thermal stability, fabricated paper separators can offer additional safety to the batteries by impeding short circuits at thermally abused state.

4.3.4 Electrical Properties

The various electrical tests performed for the developed paper separators are described as follows:

4.3.4.1 Ionic Conductivity

EIS was carried out using 2032 coin type symmetrical SS/Separator/SS cells and the frequency dependent impedance plot of the fabricated separators were shown in ***Figure 4.6(a)***. All the separators revealed straight line profiles inclined toward the Z′ axis representing electrode-electrolyte double-layer capacitance behaviour. The bulk resistance values of the fabricated separators were estimated from the high-frequency intercept of the Nyquist plot on the Z′ axis and presented in tabular form in the inset of ***Figure 4.6(a)***.

The effect of sizing, ceramic impregnation and lamination was quite evident with the increase in resistance values of fabricated paper separators-P35 (1.27Ω), P35SB7BT20 (1.70Ω), P35SB7BT20SB1 (4.23Ω), P35SB7BT20SB2 (5.84Ω), and P35SB7BT20SB3 (7.33Ω). The surface sizing in P35 resulted in lower impedance value of 1.27 Ω due to the presence of comparatively greater number of pore spaces than the ceramic impregnated and laminated separators. Ceramic impregnation of separator by introducing polymeric blend of nano-ceramic powder (SBR and BTO) although sacrificed few pore spaces in P35 separator matrix, the presence of ceramics on the other side facilitated the wettability of the separator. Thus, the dual competing effect resulted in a marginal change in impedance value in P35SB7BT20 separator. In laminated separators i.e., in P35SB7BT20SB1, P35SB7BT20SB2, and P35SB7BT20SB3, large number of pores were sacrificed with the increasing concentration of SBR (conc. range 1.0-3.0 w/v%) resulting in higher impedance values.

The corresponding ionic conductivities of electrolyte-soaked separators are also tabulated in the inset reflecting gradual decease in ionic conductivities. The EIS results in summary suggested that the manipulation of pore spaces definitely has adverse effect in separator resistance and ionic conductivities; however, an optimization is necessary to achieve a balance between wettability and separator impedance values. In that respect, all the paper separators might be qualified as good quality working separator with acceptable porosity, wettability and resistance.

4.3.4.2 Electrochemical Potential Window

The working electrochemical window for the paper separators were measured by Linear Sweep Voltammetry technique scanning from OCV to 6 V at 2.44 $mV.s^{-1}$ scan rate. For this experiment, 2032 type coin cells with cell configuration Li/Separator/SS using liquid electrolyte-soaked paper separators were fabricated. In current vs potential plots shown in ***Figure 4.6(b)***, small humps can be observed for all paper based composite separators nearly at 4.0 V. This can be due to the formation of passivation layer at the working electrode side. A sharp increase in current could be found above 5.1 V for the paper separators which might be due to the decomposition of the liquid electrolyte. On the other hand, the working potential window of untreated paper (UP) and commercial plastic separator (PP) were found to be around 5.0 V from their LSV profiles in ***Figure 4.6(b)***. Therefore, the working potential window as obtained for the paper separators was found to be nearly 5.1 V, which is suitable for almost every conventional commercial cathode material.

4.3.5 Electrochemical Tests

Electrochemical performance tests of the separators are conducted in both LIBs and SCs. The results are summarized below:

4.3.5.1 Full Cell Performance

A comparison of initial discharge profiles of 2032 coin cells with cell configuration of MCMB/separator/$LiFePO_4$ fabricated using untreated paper-UP, commercial PP and fabricated paper separators is given in ***Figure 4.6(c)***. Prior to cell fabrication all the separators were saturated with commercial standard $LiPF_6$ (EC:DMC = 1:2) electrolyte for two hours inside glove box. The specific discharge capacities of the cells were found to be 112 mAh/g (UP), 125 mAh/g (PP), 122 mAh/g (P35), 129 mAh/g (P35SB7BT20SB1), 117 mAh/g (P35SB7BT20SB2) and 133 mAh/g (P35SB7BT20SB13). The cycling performance at 0.2 mA/cm^2 current density was studied for all the fabricated separators including UP and commercial separator, PP. UP showed lower capacity values than PP and fabricated separators. A comparable cycling performance to that of PP was obtained for P35SB7BT20SB2 separator with similar capacity retention up to 100 cycles.

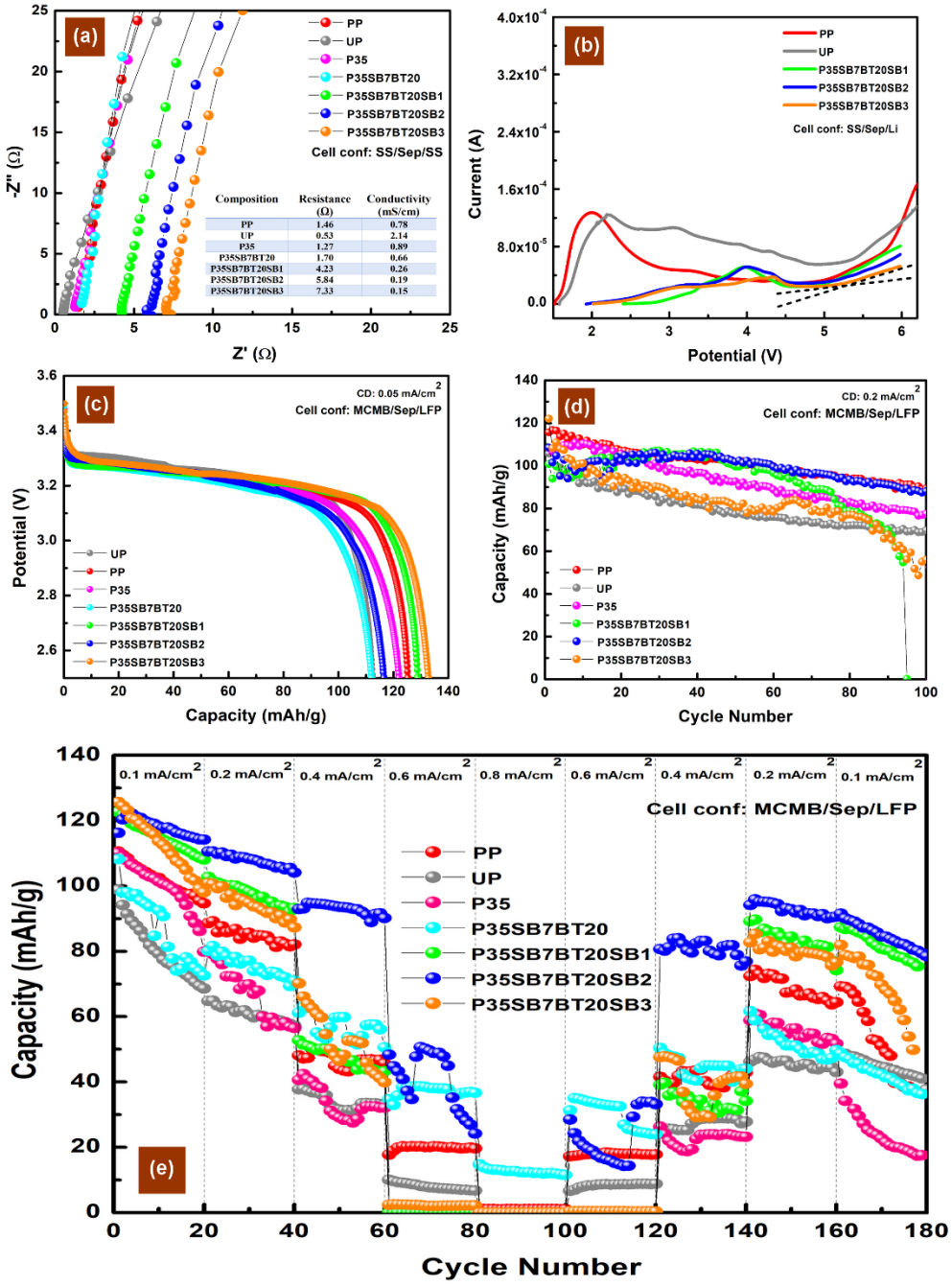

Figure 4.6 *(a) Nyquist plot of fabricated paper separators, (b) electrochemical stability window of fabricated paper separators at scan rate 2.44 mVs^{-1}; Electrochemical cell performance in 2032 coin type cell fabricated with MCMB anode, $LiPF_6$ (EC/DMC) liquid electrolyte soaked separators and $LiFePO_4$ cathode (c) initial charge-discharge profiles of UP, commercial PP along with fabricated separators (d) cycleability plot at current density of 0.2 mA/cm^2 and (e) cycling performance of UP, P35 and fabricated separators at current densities in the range of 0.1-0.8 mA/cm^2*

From ***Figure 4.6(d)***, it was also found that both lower and higher concentration (1.0 w/v% and 3 w/v%) of SBR used for lamination in P35SB7BT20SB1 and P35SB7BT20SB3 separator

could not performed well in cycling test. It is might be due to the fact that lower SBR concentration might not be sufficient to laminate the separator matrix homogeneously, whereas, a high SBR concentration of 3 w/v% suffered from uneven lamination coating along with polymeric segregation on separator surface leading to exposure of ceramic layer. An interesting result were found when the cells were cycled at increasing current densities from 0.1 mA/cm^2 to 0.8 mA/cm^2 and thereafter, reversing back to initial current density. All laminated separators- P35SB7BT20SB1, P35SB7BT20SB2, and P35SB7BT20SB3 delivered higher capacities at lower current densities than the UP-untreated paper, but failed to perform at very high current density of 0.8 mA/cm^2 for impedance developed due to lamination layer resulting in hindrance of Li-ion mobility across the separator membrane. On the contrary, separator without lamination-P35SB7BT20 still produced some capacities at 0.8 mA/cm^2. The results corroborated with the ionic conductivities found for different separator compositions. While reversing back to lower current densities, laminated separator was found to recover the capacity better than the UP and non-laminated paper separators (P35, P35SB7BT20).

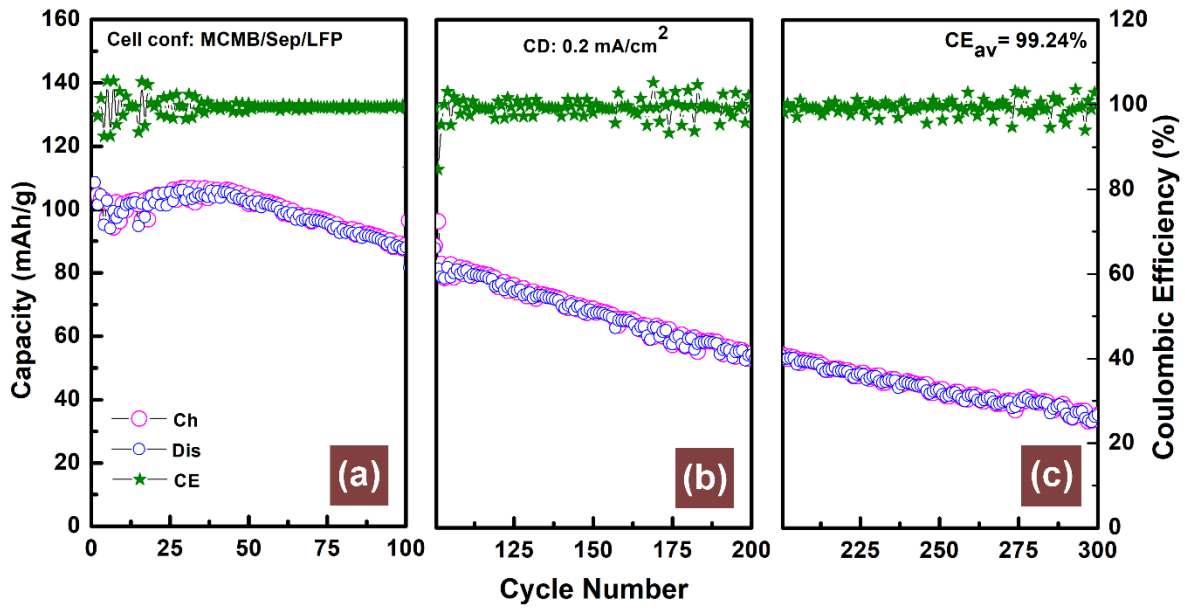

Figure 4.7 *Capacity vs cycle number plot of fabricated separator- P35SB7BT20SB2 up to 300 cycles. The Y axis represents the coulombic efficiency values in each charge-discharge cycle. Each plot from left to right represents the cycle numbers ranging from (a) 1-100th, (b) 101-200th and (c) 201-300th*

Figure 4.7 describes the long term cycling behaviour of laminated P35SB7BT20SB2 separator at current density of 0.2 mA/cm^2 up to 300 cycles including coulombic efficiency of the cell. The cell showed > 95% coulombic efficiency throughout cycling test.

4.3.5.2 Multi-cathode Compatibility of the Separators

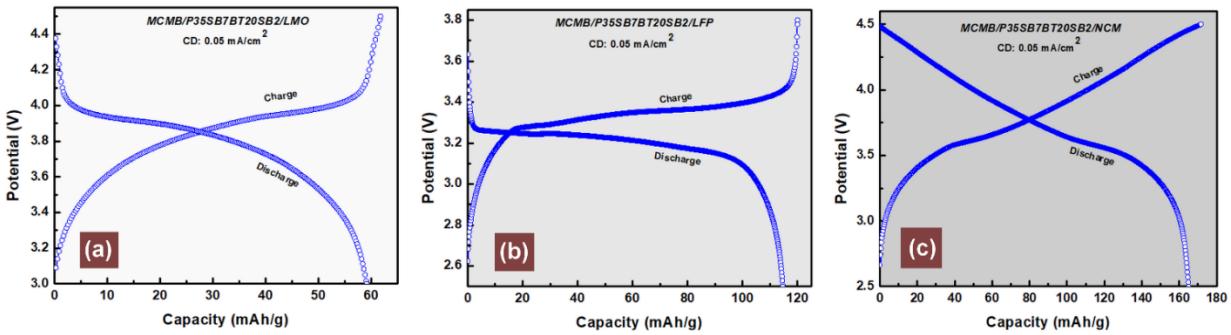

Figure 4.8 *Multi-cathode Compatibility: typical charge-discharge profiles of paper separator (P35SB7BT20SB2) against (a) $LiMn_2O_4$, (b) $LiFePO_4$ and (c) NCM111*

To evaluate multi-cathode compatibility, the developed composite paper separator (P35SB7BT20SB2) was tested in 2032 coin cell configuration using MCMB anode, standard electrolyte and three different commercial cathodes namely $LiFePO_4$ (LFP), $LiMn_2O_4$ (LMO) and $LiNi_{1/3}Co_{1/3}Mn_{1/3}O_2$ (NCM 111). Their typical charge-discharge profiles were presented in ***Figure 4.8***. It was found that the composite paper separator delivered a specific discharge capacity of 114.66 mAh/g, 59.18 mAh/g and 164.99 mAh/g with respect to LFP, LMP and NCM111 respectively. The obtained capacity values were found well matched with their practical achievable capacities in Li-ion Batteries.

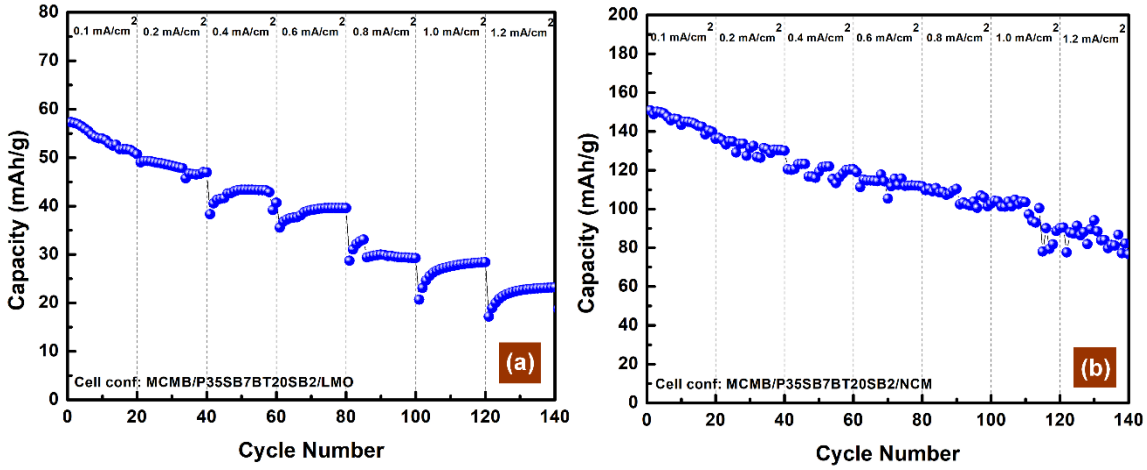

Figure 4.9 *Multi-cathode Compatibility: Capacity vs cycle number profiles of paper separator (P35SB7BT20SB2) against $LiMn_2O_4$ and NCM111 with step current density*

The capacity vs cycle number plots of MCMB/P35SB7BT20SB2/LMO and MCMB/P35SB7BT20SB2/NCM cells were presented in ***Figure 4.9***. Both the cells were cycled at different current densities ranging from 0.1-1.2 mA/cm^2 for 20 cycles at each current density and their performance shows good cycle retention of both electrodes with the designed separator.

4.3.5.3 Electrochemical Performance in Supercapacitors

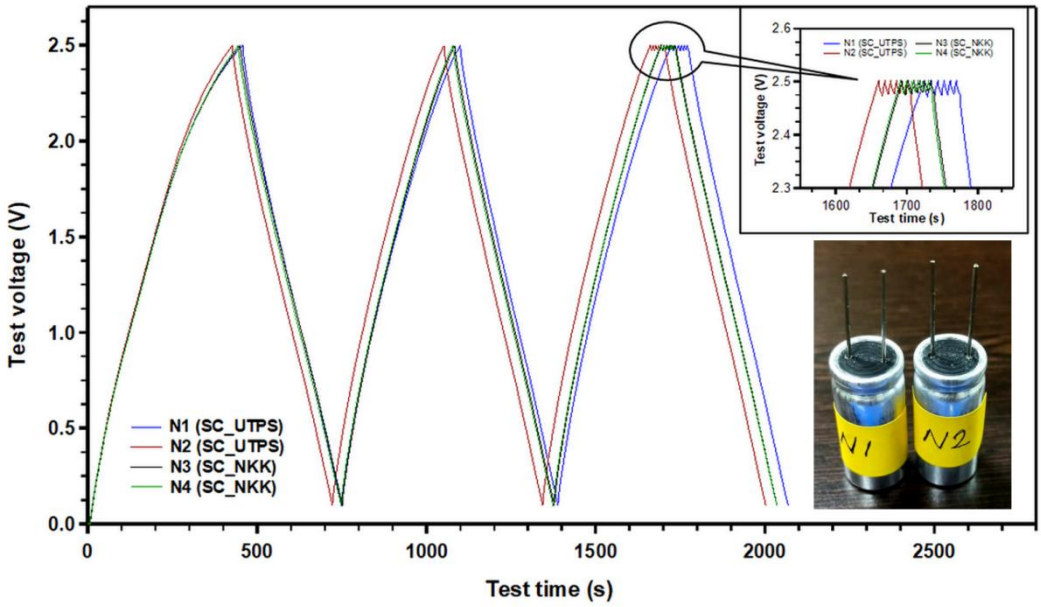

Figure 4.10 *Typical constant current charge-discharge (CDC @260 mA) patterns of SCs, made with (a) developed paper separator (N1-SC-UTPS & N2-SC-UTPS) and NKK branded commercial paper separator (N3-SC-NKK & N4-SC-NKK), carried out as per IEC 62391-1 (Class-II) by using the supercapacitor testing system. Inset represents the enlarged portion of CDC patterns during the constant current pulsing stage for measuring cell ESR of SCs*

The charge-discharge patterns of the SCs thus fabricated using UTPS were found to be identical and are highly reversible, that indicated no significant loss or disintegration of UTPS during the charge-discharge cyclying. The C_{eff} and ESR_{cell} of the UTPS based SC were found to be in the range of 25.79±0.2 F and 20.6±0.3 mΩ. In order to compare the UTPS performance in SC, two SCs were also fabricated by using two identical carbon aerogel based active electrodes and commercial cellulose based paper separator (NKK brand, Japan) in a similar fashion (labelled as N3-SC_NKK and N4-SC_NKK) and they were also tested in similar manner. The cell capacitances & ESR of the SCs made with NKK branded paper separator were found to be 26.1±0.06 F and 13.2±0.5 mΩ respectively. Typical charge-discharge plot of SC fabricated

using UTPS and NKK branded commercial paper separator is shown in ***Figure 4.10***, which clearly revealed that the newly developed paper separator (UTPS) are highly compatible with commercial products and possess high application potential for use as separator in wide range of electrochemical energy storage systems including Li-ion batteries and supercpacitors.

4.3.6 Calendar Ageing Test

The chemical stability of separator membrane inside cell environment needs to be addressed to examine its performance for long term cycleability. Inside the lithium-ion cell, both the surfaces of the separator are exposed to $LiPF_6$ (EC/DMC) based organic liquid electrolyte, different chemical constituents and of course, different redox environment (anodic and cathodic compartments) during cycling. Therefore, to observe the related changes in the microstructure, surface topology and electrical properties of separator calendaring ageing in full cell configuration (MCMB/Sep/LFP) has been studied here by using impedance spectroscopy (EIS) and microscopic imageing (FESEM and EDX) techniques. In contrast to cycling ageing, the results obtained in calendar ageing can be helpful to interpret the mechanism of formation of passivation layers (SEI), facts related to dissolution of electrode particles and chemical stability of separator membrane depending on the cell chemistries.

For this purpose, 2032 coin cells were fabricated using developed paper separator (P35SB7BT20SB2) both in full cell (MCMB/Sep/LFP) and symmetrical cell (SS/Sep/SS) configurations; and thereafter, measured their impedance in every one week interval throughout a total duration of eight weeks without electrochemical cycling. At the end of the study after eight weeks, the cells were dismantled and the separators were cleaned thoroughly several times with dimethyl carbonate (DMC) solvent to clear the soaked electrolytes. The surface properties of separator membrane thus examined and compared with the separator which was dismantled just after 24 hours of fabrication, and cleaned in the similar way as stated earlier.

The Nyquist plots representing the time dependent changes during ageing in electrolyte resistance (R_e) and charge transfer resistance (R_{ct}) of symmetrical cell fabricated with the developed separator is shown in ***Figure 4.11(a)***. It was observed that the electrolyte resistance of the cell was found to be apparently constant (6-8 Ω) throughout the ageing process, whereas, the charge transfer resistance (R_{ct}) gradually increased over time. The R_{ct} value of as fabricated cell was found to be 121.11 Ω which increased to a value of 1112.89 Ω after eight weeks. For better understanding, the results further plotted in ***Figure 4.11(b)*** and ***Figure 4.11(c)*** showing

the changes in impedance values of symmetric cell with respect to time. It suggested that the electrolyte resistance remained constant, where due to side reactions and SEI formation, the charge transfer resistance increased to higher values. This further indirectly confirmed that ceramic particles embedded in the paper separator composite matrix might not be leaching out from surface during ageing; otherwise incremental changes in electrolyte resistance might be observed due to dissolution of BTO particles in the electrolyte.

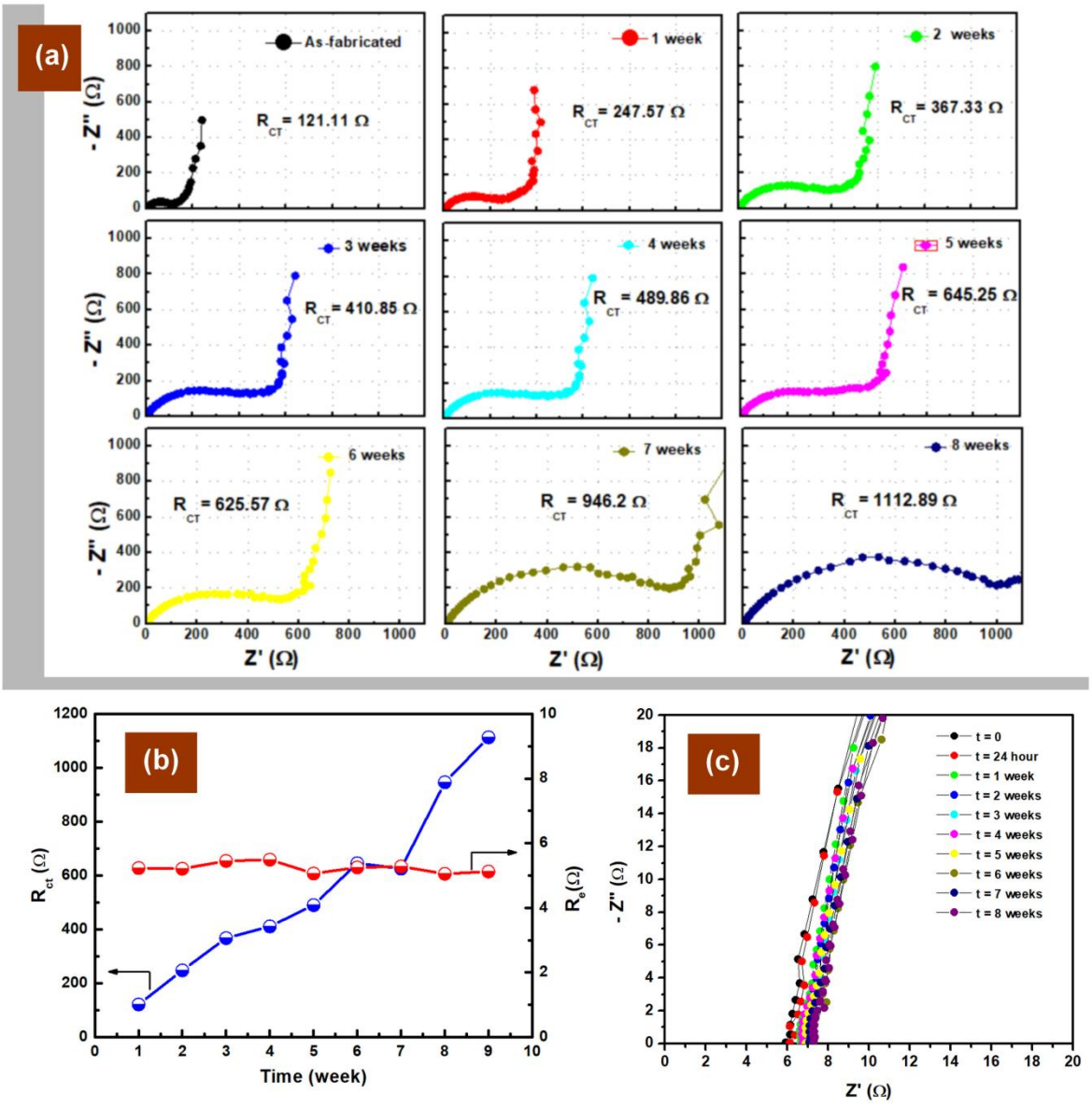

Figure 4.11 *(a) Nyquist plot of full cell (Configuration: MCMB/Sep/LFP) fabricated with paper separator P35SB7BT20SB2 during calendar ageing (0-8 weeks), (b) Time dependent plot of electrolyte resistance (R_e) and charge transfer resistance (R_{ct}) of symmetrical cell fabricated with the developed separator and (c) Nyquist plot taken at regular interval reflecting changes in bulk impedance of paper separator P35SB7BT20SB2 during calendar ageing*

Robert et al. reported that separator morphology (PP based) might be changed upon storage in a cell containing $LiPF_6$-EC-EMC electrolyte at elevated temperatures[13]. They argued such changes may affect the lithium movement across the separator membrane due to blocking/covering the pores of the separator resulting in increase in local ionic impedance. A non-uniform distribution of deposits originating from the liquid electrolyte was found in their study during ageing of full cell. In our case, we have dismantled the aged cell after eight weeks, and both the surfaces of aged paper separator (cathode facing surface and anode facing surface) were exposed under FESEM followed by elemental analysis by EDX as shown in ***Figure 4.12***. The surface topology of aged separator was duly compared with the non-aged separator dismantled after 24 hours of assembly. The micrographs of separator surfaces for freshly dismantled cells after 24 hours as shown in ***Figure 4.12(a-a1)*** and ***Figure 4.12(c-c1)*** for both anode and cathode facing surfaces, the morphology and microstructure looked apparently same as the surface of as-fabricated paper separator. However, cubic shaped particles could be found homogeneously deposited on both anode and cathode facing surfaces of the aged separator after eight weeks of calendar ageing at RT, as shown in ***Figure 4.12(b-b1)*** and ***Figure 4.12(d-d1)***. To identify the elemental composition of the deposits on paper separator surfaces, selected area EDX was carried out on freshly dismantled separator and eight weeks' aged separators and presented in ***Figure 4.12(a2-b2)*** and ***Figure 4.12(c2-d2)***.

The EDX profiles for both anode and cathode facing surfaces of freshly dismantled and aged separators revealed the presence of phosphorus along with other known elements like C, O, Ba, Ti, F, Si etc. The relative peak intensities of phosphorus were found to be increased on long term ageing. To probe this phenomenon, the EDX profile of as-fabricated separator was compared and it was found that no phosphorus peak could be detected in the spectrum (refer to ***Figure 4.1(e)***) of as-fabricated paper separator. These observations co-related that phosphorus might be deposited on both anode and cathode facing surfaces of the aged composite paper separator due to decomposition electrolyte salt in cell environment. The phosphorus containing precipitate as found uniformly distributed on the separator might be one of the reasons for capacity fading on long term cycling of the cells. It is also envisaged that such depositions could also be found on plastic PP/PE based separators.

Therefore, it is worthy to mention here that the reason of capacity fading on long term cycling might not be co-related with the developed paper based composite separator, rather it was the degradation property of liquid electrolyte during calendar ageing. Such depositions may block

the active pores of any such separator membrane impeding Li-ion transport and subsequently, capacity loss of the cell.

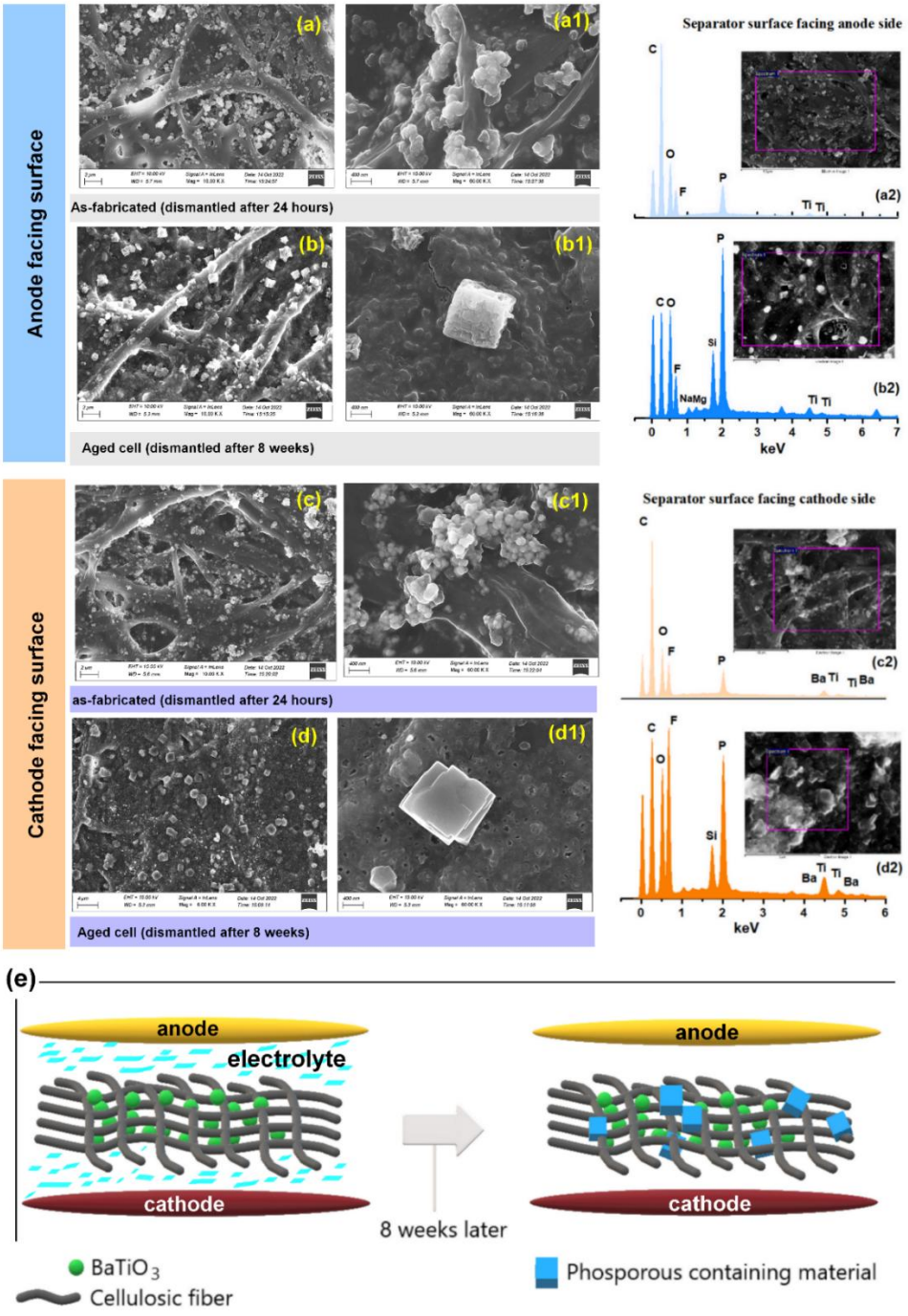

Figure 4.12 *FESEM micrographs of anode facing surface of (a)-(a1) as fabricated and (b)-(b1) aged cell dismantled after 8 weeks; FESEM micrographs of cathode facing surface of [(c)-(c1)] as fabricated and (d)-(d1) aged separator after 8 weeks, Corresponding selected area EDX profile of anode facing (a2-b2) and cathode facing surfaces (c2-d2) for both as-fabricated and aged separators, (e) A schematic illustration of phosphorous containing material deposition on separator surfaces after ageing*

4.3.6 Thermal Safety

The thermal safety tests are crucial for battery separators, since they determine the practical applicability inside a standard battery. We have performed several thermal tests for our developed separators, including thermogravimetric analysis (TGA), flame test and galvanostatic charge-discharge at elevated temperatures. The key findings and their possible causes are explained below;

4.3.6.1 Thermogravimetric Analysis

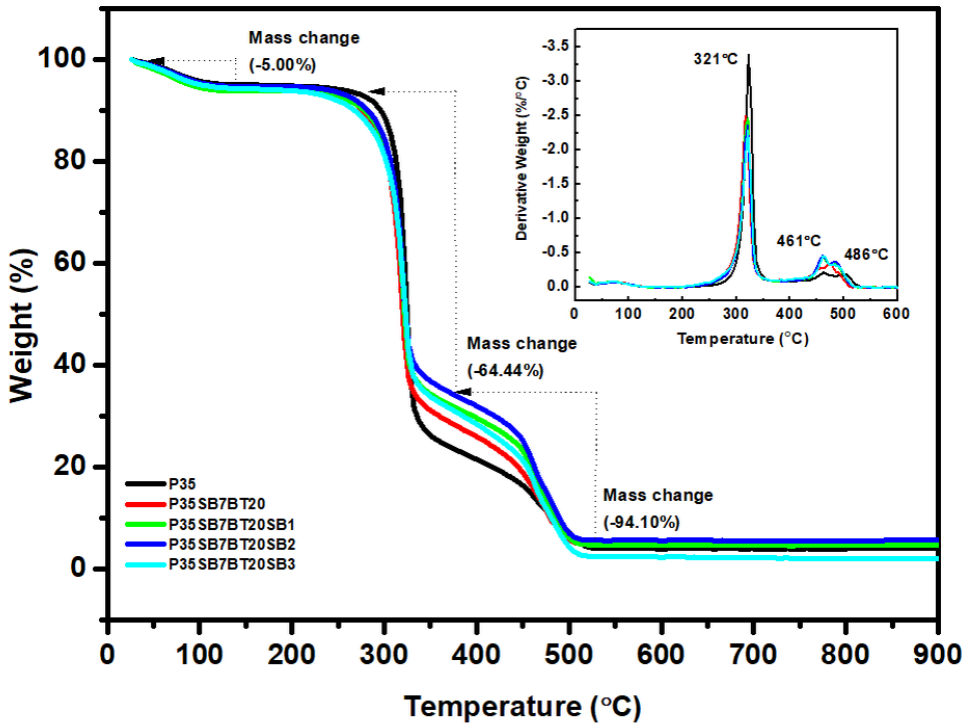

Figure 4.13 *TGA plot of paper separators samples; inset showing the differential weight loss from room temperature to 600℃*

For analysis of thermal degradation from RT to 600°C, TGA/DTA was performed for all the fabricated paper separators and shown in ***Figure 4.13***. A sharp peak of major weight loss could be observed in the inset of ***Figure 4.13*** for all the paper separators at 321°C followed by two small weight losses at about 461°C and 486°C. The major weight loss was attributed to the removal of surface and intrinsically H-bonded water molecules from cellulosic matrix. The later peaks correspond to the thermal degradation of polymers (PVDF and SBR) used as binders in paper separators.

4.3.6.2 Flame Safety Test

The internal short circuit is one of the major causes of battery failure, fire hazards and explosion. Short circuit (both internal and external) may lead to heat accumulation inside the cell causing decomposition of the transition oxide cathodes, and subsequently release gaseous oxygen[14,15]. Such phenomena may further result in oxidation of electrolyte and separator in exothermic fashion. Therefore, both separators and liquid electrolytes have to play a significant role in preventing thermal runaway in LIBs. In our case, the functionalized composite paper separator thus subjected to IEC 60695-11-10 vertical flame standard test of combustion to measure its fire retardant property. In our previous study, we observed that commercial polypropylene-based separator comprising an aliphatic hydrocarbon backbone burnt itself rapidly without leaving any residual "char" under flame[16]. The same is reported in other studies also[17]. Here, we compared the effect of functionalization on resisting flame and/or combustion by comparing the nature of decomposition on exposure to flame for 10s for both untreated paper and composite functionalized paper separator (P35SB7BT20SB2). As demonstrated in the ***Figure 4.14***, the untreated paper was seen to catch fire readily under flame due to intrinsic combustible nature of cellulose, whereas cellulose ceramic composite paper separator interestingly remained flame resistive throughout the total exposure time. Therefore, as per IEC 60695-11-10 vertical flame standard, the composite paper separator can be classified into V-0 ratings. Such flame retardant properties will add extra safety features to the developed composite separator in real time applications.

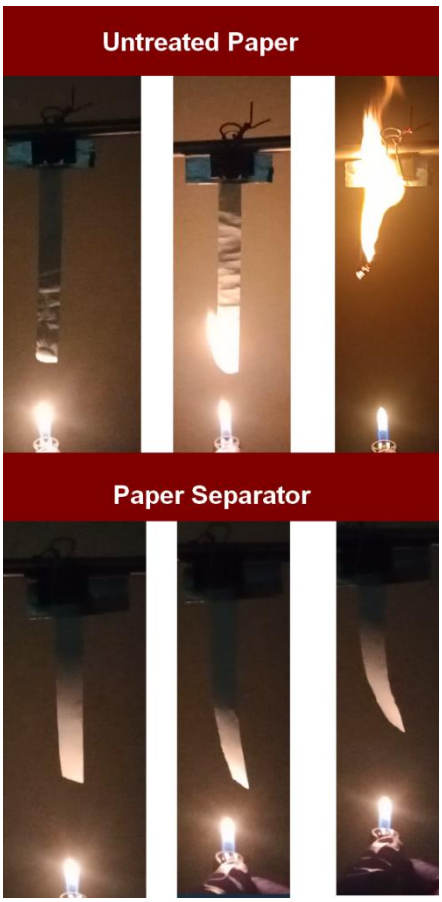

Figure 4.14 *Digital images taken during vertical flame test for both untreated (above) and functionalized paper separator (below)*

4.3.6.3 Electrochemical Cycling at Elevated Temperatures

In another attempt, electrochemical cycling performance at elevated temperature for the composite paper separator was evaluated from room temperature to 80°C and is duly compared

with cell performance of PP/PP based commercial separators. ***Figure 4.15(a)*** demonstrates the performance of commercial separator which revealed that the plastic separator initially performed well up to 60ºC, however, at 80°C it was showing false charging due to its dimensional degradation caused by intra-molecular motion of polymeric moieties present in plastic separator.

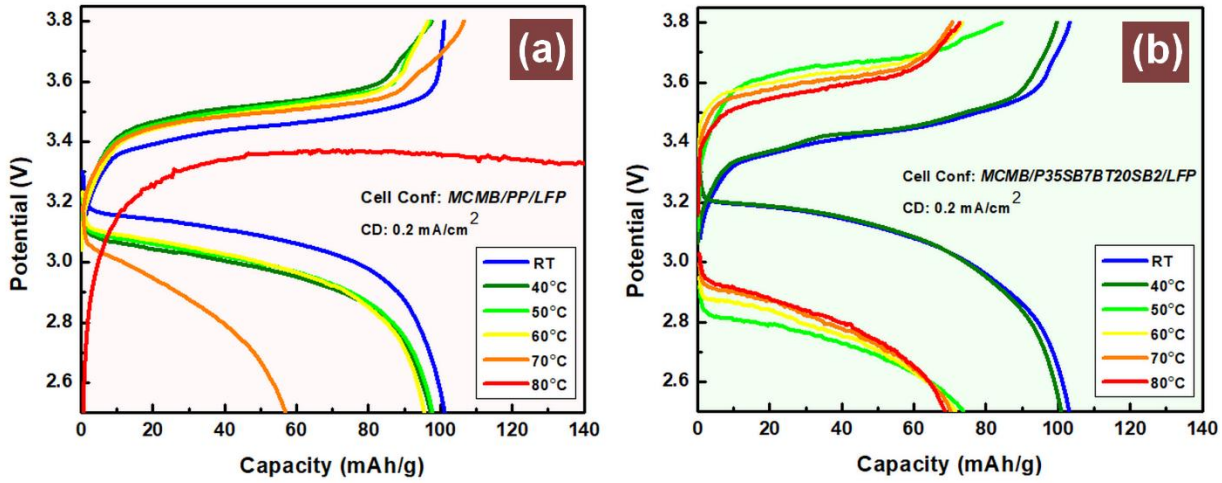

Figure 4.15 *A comparison of electrochemical performance of composite separator (P35SB7BT20SB2) with that of Commercial PP/PE based separator membrane at elevated temperatures RT- 80℃*

On the other hand, our developed paper based composite separator (P35SB7BT20SB2) satisfactorily cycling at 80°C ***[Figure 4.15(b)]***. The results further corroborate the intrinsic integrity of composite separator at elevated temperature in real cell environment.

4.4 Conclusion

A sustainable, economic and flexi paper based composite separator was developed by functionalizing low cost commercial paper applying three critical processing steps - sizing, ceramic impregnation and lamination. The wet coating method as designed to fabricate paper separator was intrinsically simple, single step and industry-friendly. The developed microporous paper separators showed excellent wettability (216-270%) with quicker saturation to the commercial liquid electrolyte and no dimensional shrinkage up to 200°C. The mechanical strength was found satisfactory to a value of 50.15 MPa in machine direction and 28.21 MPa in transverse direction.

Table 4.2 *Literature study and comparison of other relevant research work with this chapter work*

Composition	**Thickness (µm)**	**Porosity (%), Gurley (s)**	**Electrolyte Wettability (%)**	**Thermal stability (°C)**	**Tensile Strength (MPa)**	**Electrochemical Performance**	**Ref.**
Bacterial Cellulose	25	65	322	>300	-	140 mAg^{-1}; 89% retention after 100 cycles	*Huang et al.* [8]
Cellulose Acetate	20	84.6	318	-	56.2	148 mAg^{-1}; 89.5% retention after 50 cycles	Xu et al.[10]
Cellulose Nanofiber	33±2	58±2	≥ 200	150	56.2	123 mAg^{-1}; 94.31% retention after 100 cycles	Kim et al.[12]
Cellulose nanocrystal	150	75	≥200		Y:1860 ± 180	120 mAg^{-1} @ C/5	Gonçalves et al.[13]
Carboxyl methylcellulose	34 ± 4	62±3	≥200	>150	-	100 cycles @1C, Capacity 109.5 mAg^{-1}, (after 100 cycles), CD; 0.1C-5C	Kim et al. [11]
Rice paper	100	65	322	90/ (-0.26%)	13.8	Comparable to Celgard @ 0.2 C, 1 C, and 2 C	Zhang et al.[22]
Tissue paper	45-55	40-70	100-230	200	19.9	Capacity retention 86.89% after 200 cycles	Zeng et al.[15]
Pure Cellulose	35	308 s	195	300	49	Capacity retention 91% after 100 cycles	Lv et al.[23]
Paper	65/70	15-25 s	131-147	>200	34.8-.38.31	Cap. 84.71-120.94 $mAhg^{-1}$ at 0.05 $mA.cm^{-2}$; C.E. > 97%; Current Density range: 0.1-0.4 $mA.cm^{-2}$	Das et.al [17]
Paper	**20±5**	**120 s**	**270.21**	**>200**	**43.96-50.15**	**300 cycles, C.E.>96%, Current Density 0.1-0.8 $mA.cm^{-2}$, Capacity 117-133 $mAhg^{-1}$**	***This Work***

To establish the chemical stability of developed paper based composite separator in organic electrolyte, calendar ageing test via EIS was carried out, which showed that no chemical degradation or ceramic leaching even after eight weeks of ageing at room temperature. The electrochemical performance of composite paper separator in full cell configuration (MCMB/Sep/LFP) was found to be comparable to that of commercial PP/PE based plastic separator in terms of specific capacity, rate capability, coulombic efficiency (>95%) and long term cycling performance (>300 cycles). To check multi-device compatibility, developed separator was tested in supercapacitors as per IEC 62391-1 (Class-II) method. The performance was found comparable to that of commercial separator both in terms of effective capacitance (C_{eff}) and equivalent series resistance (ESR_{cell}). As per IEC 60695-11-10 vertical flame standard, developed composite paper separator was found to be flame retardant, a feature necessary in terms of safety aspects. The present research on engineered flexible composite paper separator thus provides an opportunity to develop sustainable "Better Batteries" for future applications.

References

1 X. Zeng, Y. Liu, R. He, T. Li, Y. Hu, C. Wang, J. Xu, L. Wang and H. Wang, *Cellulose*, 2022, **29**, 3985–4000.

2 Z. Li, W. Wang, X. Liang, J. Wang, Y. Xu and W. Li, *Journal of Energy Chemistry*, 2023, **79**, 92–100.

3 A. Gören, C. M. Costa, M. N. Tamaño Machiavello, D. Cíntora-Juárez, J. Nunes-Pereira, J. L. Tirado, M. M. Silva, J. L. Gomez Ribelles and S. Lanceros-Méndez, *Solid State Ion*, 2015, **280**, 1–9.

4 V. Deimede and C. Elmasides, *Energy Technology*, 2015, **3**, 453–468.

5 R. Dallaev, T. Pisarenko, D. Sobola, F. Orudzhev, S. Ramazanov and T. Trčka, *Polymers (Basel)*, 2022, **14**, 4793.

6 A. R, A. P. Vijaya Kumar Saroja and R. Sundara, *ACS Appl Mater Interfaces*, 2019, **11**, 3889–3896.

7 L. Spagnuolo, R. D'Orsi and A. Operamolla, *Chempluschem*, DOI:10.1002/cplu.202200204.

8 J. Zhang, L. Yue, Q. Kong, Z. Liu, X. Zhou, C. Zhang, Q. Xu, B. Zhang, G. Ding, B. Qin, Y. Duan, Q. Wang, J. Yao, G. Cui and L. Chen, *Sci Rep*, 2014, **4**, 3935.

9 Y. Li, Q. Li and Z. Tan, *J Power Sources*, 2019, **443**, 227262.

10 J. Xing, J. Li, W. Fan, T. Zhao, X. Chen, H. Li, Y. Cui, Z. Wei and Y. Zhao, *Compos B Eng*, 2022, **243**, 110105.

11 A. Li, A. C. Y. Yuen, W. Wang, I. M. De Cachinho Cordeiro, C. Wang, T. B. Y. Chen, J. Zhang, Q. N. Chan and G. H. Yeoh, *Molecules*, 2021, **26**, 478.

12 J. C. Roberts, *The Chemistry of Paper*, 1996.

13 S. Bourlot, P. Blanchard and S. Robert, *J Power Sources*, 2011, **196**, 6841–6846.

14 X. Liu, D. Ren, H. Hsu, X. Feng, G.-L. Xu, M. Zhuang, H. Gao, L. Lu, X. Han, Z. Chu, J. Li, X. He, K. Amine and M. Ouyang, *Joule*, 2018, **2**, 2047–2064.

15 S. Sharifi-Asl, J. Lu, K. Amine and R. Shahbazian-Yassar, *Adv Energy Mater*, 2019, **9**, 1900551.

16 M. Das, P. S. Das, R. N. Basu and M. W. Raja, *Cellulose*, 2022, **29**, 9899–9917.

17 C. Liao, W. Wang, L. Han, X. Mu, N. Wu, J. Wang, Z. Gui, Y. Hu, Y. Kan and L. Song, *Appl Mater Today*, 2020, **21**, 100793.

Chapter 5

Surface Charge-Directed Ceramic Impregnation in Cellulose Paper Separators

Highlights

- The intrinsic effect of different nanoceramics impregnation into cellulose paper matrix
- Variation of physico-chemical, thermal, and electrochemical properties as Li-ion battery separator
- Improved electrolyte wettability, ionic conductivity, and Li^+ transport phenomena
- Stable electrode-separator interfaces enabled by ZrO_2 incorporation

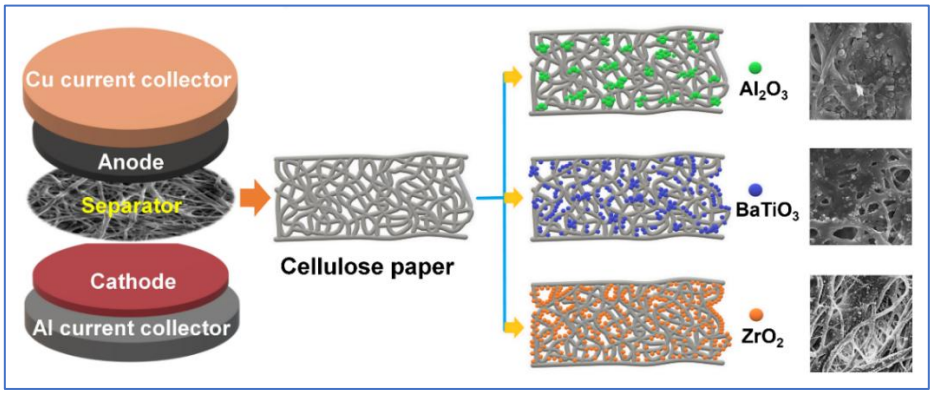

Figure 5.0 *Graphical Abstract showing the nature of ceramics impregnation in cellulose matrix*

This chapter presents the development and performance evaluation of cellulose-based paper separators impregnated with three different nano-structured ceramic fillers (Al_2O_3, $BaTiO_3$, and ZrO_2). The nature of ceramic impregnation, influenced by surface charge and morphology, impacts the physico-chemical, thermal, and mechanical properties of the separators. Electrochemical performance is assessed through full-cell configurations, highlighting the role of ceramic fillers in enhancing cycling stability, rate capability, and interfacial compatibility. It is well known that increase in SEI and charge transfer resistance are major issues in long-term Li-ion full cell operation. To mitigate these problems, the impregnated nanoceramics inside the separator matrix play a crucial role. Especially, the zirconia modification helps to create a stable interface between the separator and the electrode, which assists in long-term stable cycling and very negligible enhancement in SEI and charge-transfer resistance after several charge-discharge cycles. Particular emphasis is placed on the safety aspects of the developed separators, including dimensional stability at elevated temperatures, flame retardance, and thermal shutdown behavior.

5.1 Background and Overview

It can be stated from our experience so far that the reinforcement of ceramic particles on cellulose tissues of paper matrix can directly affect the dimensional integrity, thermal stability and to some extent the mechanical tension of the ceramic-based paper separator. Therefore, it is important to understand the nature of the impregnation while constructing paper-based separators [1,2]. The homogenous distribution of ceramic particles, surface charge and the type of deposition of ceramic particle on the surface of the entangled, cross-linked cellulose fibers play significant role on the performance of cellulose-ceramic based composite sseparators. Apart from these, there are various factors that can impact the cycle life and overall performance of a Li-ion battery, including the growth of the solid electrolyte interphase (SEI) layer, lithium plating, instability at the electrode-separator interface, electrode degradation, electrolyte decomposition etc[3].Over repeated charge-discharge cycles, these issues can lead to a notable increase in the internal charge transfer resistance degrading the efficiency of the battery. In this regard, Zeng et al[4] has demonstrated that tissue paper once modified with nano-SiO_2 hybrid cross-linked polymer electrolyte as coating layer can offer superior cycling performance. A paper-supported inorganic composite separator as developed by Wang et al.[5] also showed better electrochemical performance in Graphite/$LiCoO_2$ full cell than PE separator. Zhang et al[6] used a commercial rice paper in lithium-ion batteries showing improved electrochemical performance and multi-electrode compatibility.

In the study covered in the present chapter, an effort was made to produce three different types of paper-based ceramic separators employing nano-structured Al_2O_3, $BaTiO_3$, and ZrO_2. In previous reports, it was exhibited that aluminum oxide (Al_2O_3) can enhance cycling stability and lifetime of lithium-ion cells by preventing surface phase transitions of cathodes most probably by forming stable SEI layers[7,8]. Similarly, barium titanate ($BaTiO_3$ or BTO), being a dielectric material, can enhance Li^+ mobility owing to its ability to effectively ionize $LiPF_6$[9,10]. On the other hand, zirconium dioxide (ZrO_2) has gained considerable recognition for its ability to reduce charge transfer resistance by stabilizing electrode interfaces. Recently, various researchers exhibited increased battery performances when cathodes and anodes were coated with ZrO_2[11–13]. In our case, the above nano-structured ceramic particles were used as reinforcement fillers in paper matrix in presence of polymeric binder. Using an in-house designed double-decker dip-coating equipment together with an in-situ drying and calendaring process and scalable roll to roll technology, the cellulosic paper matrix was impregnated with

those ceramic materials in an optimized concentration. In terms of physical, structural, thermal, mechanical, and electrochemical properties, all the three developed separators showed either better or comparable performances with those of polyolefin based commercial separators. The exhaustive electrochemical tests were performed for all the paper separators along with their post-electrochemical analysis. The developed separators showed excellent cycling performance, high rate capabilities at different current densities and excellent columbic efficiencies. The multi-electrode compatibility studies clearly revealed that paper separators could be used for application specific cells. In terms of safety, the paper separators exhibited good flame retardant properties in standard flame tests. The current study thus as a whole showcases the feasibility of developing sustainable paper based ceramic separators for application in LIBs by probing physico-chemical and electrochemical cell performances of separators impregnated with various nano-structured ceramic materials.

5.2 Separator Fabrication Process

The paper separator fabrication process is mainly divided into three critical process steps; (1) de-moisturization of untreated paper roll, (2) preparation of ceramic-polymer suspension for dip-coating, and (3) coating of the paper substrate with in-situ drying and compaction. The commercial paper roll (W-62 mm, L-100 m) is initially kept in a vacuum oven at 80°C overnight for complete drying and moisture removal. Thereafter, a clear suspension comprising 3.0 w/v% of PVDF in NMP is prepared under constant heating at 70°C and stirring at 400 rpm. The bare cellulose paper substrate (hereafter termed as CP) first goes through a sizing process by coating with PVDF solution. An aqueous solution of 7.0 w/v% of SBR is prepared by continuous stirring at 400 rpm for 4h which was used for ceramic impregnation. The ceramic nanopowders namely aluminum oxide (Al_2O_3), barium titanate ($BaTiO_3$ or BTO) and zirconium oxide (ZrO_2) are added separately in the concentration level of 2.0 w/v% to make three different SBR-ceramic aqueous suspensions. Finally, the three different polymer-ceramic suspensions are uniformly coated on both sides of the dehydrated PVDF-coated sized paper using in-house designed semi-automated separator fabrication equipment as schematically represented in ***Figure 2.2*** in ***Chapter 2***. The coating, drying and compaction of the separators have been done following the procedure mentioned in *Section 2.3.2.2* of ***Chapter 2***. The thickness of the fabricated paper separators is measured to be in the range of 20-25 µm. The mass of each separator per unit volume is calculated after the fabrication process. Firstly, circular disks with diameter of 19 mm have been cut from the separator rolls as well as from

the untreated cellulose paper. They are dried under 60ºC inside a vacuum oven for overnight and their weights are measured. With the values of their thickness and radius, the volumes of those separator disks have been calculated. Dividing the mass of each separator with its respective volume, the mass per unit volume is calculated to exactly identify how the polymer and ceramic impregnation can affect the mass and volume composition of the separators. The values obtained are summarized in Table 5.3. All the experiment has been conducted with six different type of separator membranes – (i) untreated cellulose paper (CP), (ii) 3.0 w/v% PVDF coated paper (P3), (iii) 7.0 w/v% SBR coated P3 (P3S7), (iv) 2.0 w/v% Al_2O_3 and 7.0 w/v% SBR coated P3 (P3S7A2), (v) 2.0 w/v% $BaTiO_3$ and 7.0 w/v% SBR coated P3 (P3S7B2) and (vi) 2.0 w/v% ZrO_2 and 7.0 w/v% SBR coated P3 (P3S7Z2). Henceforth, the fabricated paper separators comprising three different nano ceramic particles will be termed as P3S7A2 (Al_2O_3), P3S7B2 ($BaTiO_3$), and P3S7Z2 (ZrO_2).

5.3 Results and Discussion

5.3.1 Microstructural Features

The microstructural features of different ceramic-impregnated paper separators namely P3S7A2, P3S7B2 and P3S7Z2 are shown in ***Figure 5.2***. For comparison, the FESEM images of the untreated cellulose paper (CP) and of the commercial PP based separator (PP) are also presented in ***Figure 5.1***. FESEM images of CP shown in ***Figures 5.1(a)*** and ***5.1(b)*** clearly reveal that the paper matrix is made up of cross-linked cellulose fibers and microfibers creating random pore spaces inside it, while the micrographs of commercial PP separator shown in ***Figures 5.1(c)*** and ***5.1(d)*** showcase the regular and ordered pores inside the polymeric matrix.

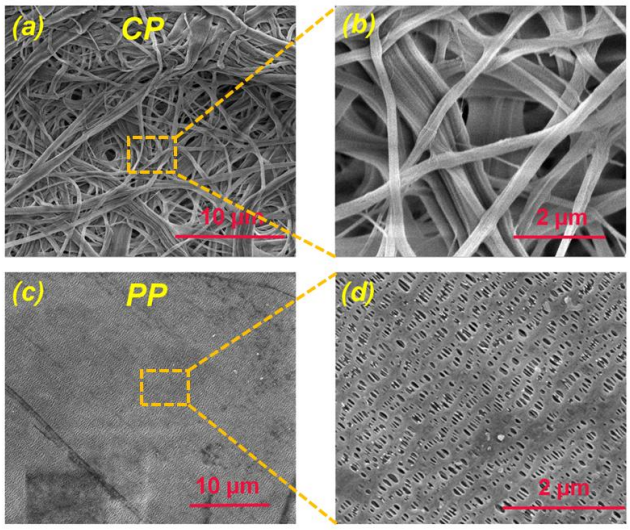

Figure 5.1 *(a)-(b) FESEM images of bare cellulose paper (CP) and (c)-(d) FESEM images of commercial separator (PP)*

In case of developed paper separators, ***Figures 5.2(a)*** and ***5.2(b)*** display the low and high magnification images of Al_2O_3 impregnated P3S7A2 paper separator. A fibrous mat composed

of cross-linked cellulosic fibers is visible. The nature of the deposition of Al_2O_3 nanoparticles on entangled fibers is found to be random and agglomerated. The corresponding EDX profile as shown in ***Figure 5.3(a)*** also indicates the presence of the constituent elements of P3S7A2. In same magnifications, as displayed in the micrographs in ***Figures 5.2(c)-(d)*** of P3S7B2, homogeneous deposition of $BaTiO_3$ nanoparticles is observed on the cellulosic surface. The BTO nanoparticles are found both on the fiber surface and also into their pore spaces as confirmed by the micrographs and their selected area EDX profile as shown in ***Figure 5.3(b)***. The deposition pattern of ZrO_2 in P3S7Z2 is found to be somewhat different than the other two. The particles of ZrO_2 adheres mainly to the cellulosic fibers, not in the pore spaces as displayed in ***Figures 5.2(e)-(f)***.

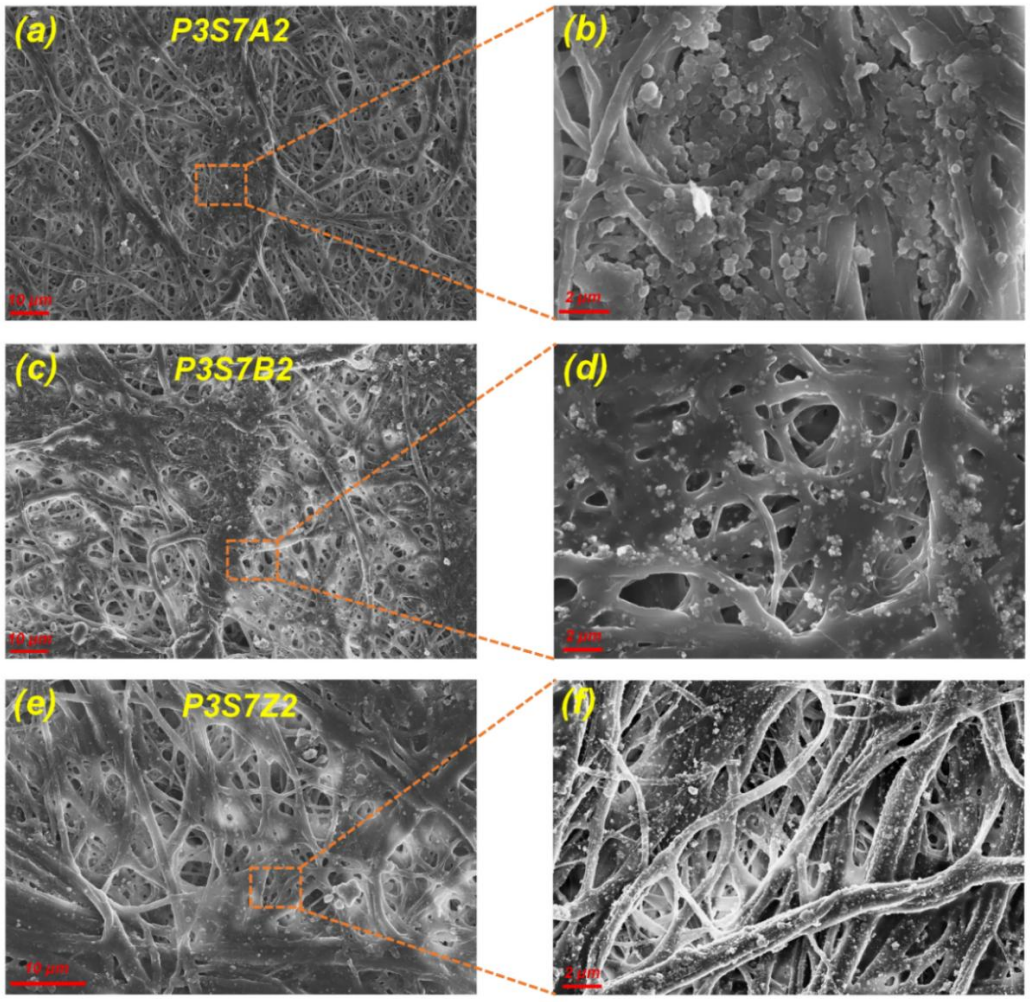

Figure 5.2 *(a)-(b) FESEM images of Al_2O_3 impregnated paper separator (P3S7A2) in low and high magnification respectively; (c)-(d) FESEM images of $BaTiO_3$ impregnated paper separator (P3S7B2) in low and high magnification respectively; (e)-(f) FESEM images of ZrO_2 impregnated paper separator (P3S7Z2) in low and high magnification respectively*

It suggests that the zirconia particles have an intrinsic affinity to interact with the cellulose fibers and/or microfibers and all the cross-linked fibers are found to be grafted with nano ZrO_2. Their presence is again confirmed by EDX as shown in ***Figure 5.3(c)***. Such different patterns of deposition of ceramic nanoparticles on cellulosic paper substrate are primarily due to their different morphologies associated with surface charges. The mechanism of deposition of ceramic particles on any substrate is well reported in the literature in terms of their zeta potential in a particular pH range. The cellulosic aqueous suspension consistently exhibits a negative zeta potential value in the entire pH range of 1-10[14], which signifies that cellulose fibers carry a negative surface charge across a broad pH range. In the case of SBR-Al_2O_3 aqueous coating suspension, the pH level is found to be 6-7, indicating that the developed wet-coating process during the fabrication of P3S7A2 separator occurs under mildly acidic conditions. It is reported at this pH range, alumina registers a zeta potential on the lower positive side, typically falling within the range of 10-20 mV[15]. It is worthy to mention here that zeta potential values >30 mV are typically indicative of a well-dispersed solution, while values <5 mV result in significant agglomeration of particles during deposition. The zeta potential in the intermediate range between 5mV to 30 mV typically shows a tendency towards forming agglomeration. Due to this, the alumina nanoparticles which have reported intermediate positive zeta potential value favors the interactions with negatively charged cellulose fibers and also shows their inherent inclination to form the agglomerates. In ***Figures 5.2(a)-(b)***, the micrographs clearly show such nature of the distribution of Al_2O_3 particles on the P3S7A2 separator surface. In contrast, the coating solution of SBR-$BaTiO_3$ aqueous suspension exhibits a pH value in the range of 4-5, within which the $BaTiO_3$ nanoparticles display a negative zeta potential ranging from -5 mV to -15 mV as reported in the literature[16,17]. Thus, in our case, the limited negative surface charged $BaTiO_3$ is found reluctant to interact with the negatively

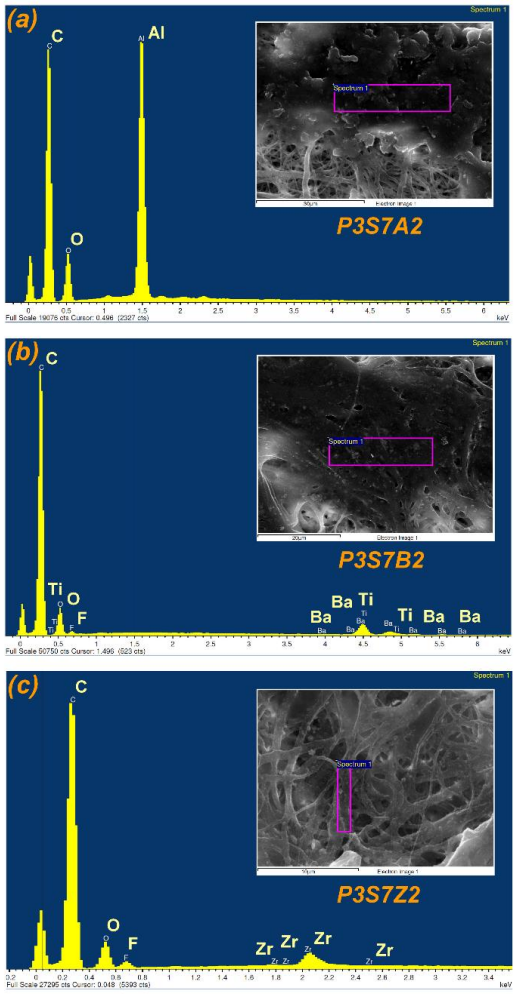

Figure 5.3 *EDX profiles of (a) P3S7A2, (b) P3S7B2 and (c) P3S7Z2 separators*

charged cellulose fibers. And, the $BaTiO_3$ particles are thus found distributed almost homogeneously on the surface of the paper substrate along with some agglomeration. It is known that nano-ZrO_2 particles typically possess a high positively charged surface in the working pH range of 4-5 and exhibit 30-40 mV of positive zeta potential value[18,19]. Such high positive zeta potential of ZrO_2 facilitates strong interaction with the negatively charged cellulose fibers and also demonstrates good deposition on the paper surface while fabricating paper separator. In summary, it can be inferred that the deposition pattern of ceramic nanoparticles on cellulosic paper substrate is primarily driven by the nature of surface charge, its magnitude and particle morphology, and such pattern will have genuine impacts on the physical and electrochemical characteristics of the P3S7A2, P3S7B2, and P3S7Z2 separators. We will explore the effects in detail in subsequent discussions.

5.3.2 Air permeability, Pore Characteristics and Electrolyte Uptake

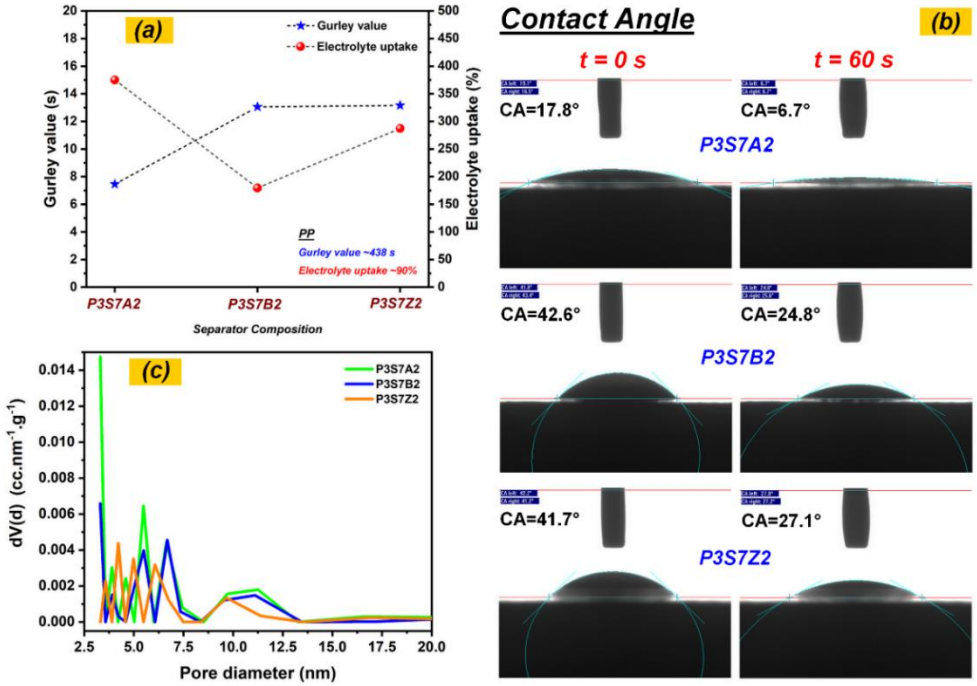

Figure 5.4 *(a) Gurley values and electrolyte uptake capabilities; (b) time dependent contact angles measured for developed paper separators (P3S7A2, P3S7B2 and P3S7Z2); (c) Variation of pore diameter with respect to separator compositions (BJH method)*

The Gurley value is a crucial technical parameter for assessing porous membranes in terms of their air permeability. It also plays a significant role in characterizing the separators for use in batteries, because a lower Gurley value signifies higher air permeability which in turn indicates

smooth Li-ion transport across the porous separator[20]. In this study, a highly porous cellulosic paper substrate is modified by incorporating duo-polymers (PVDF and SBR) as binders and ceramic nanoparticles (Al_2O_3, $BaTiO_3$ and ZrO_2) as fillers. Thus, it is expected that the introduction of such materials may affect the air permeability values of the separator membranes if the pore spaces within the paper substrate are blocked either by the polymer binders or by the formation of large aggregates originating from nanosized ceramic particles. The Gurley value of the untreated cellulose paper (CP) is measured to be 5s[21]. After sizing with 3.0 w/v% PVDF, the value increases to 7s. Such nominal change in Gurley value might be due to the fact that low concentration of polymer has a mere effect on the overall porosity of the sized paper. Even the incorporation of ceramics on PVDF coated paper for making paper separators results in minor alteration in Gurley values, i.e., 7.46s for P3S7A2, 13.05s for P3S7B2, and 13.16s for P3S7Z2. All the Gurley values as estimated for paper separators are cited in ***Figure 5.4(a)***. The curve explains a marginal change in air permeability concerning the nature of the ceramic particles. It is thus worthy to mention here that although the surface and morphological properties of nano-ceramic particles are different, their inclusion in the paper matrix did not change the porosity, keeping the facile path for Li^+-ion transaction across the paper separator membranes.

The electrolyte uptake capability serves as another critical indicator of separator membrane towards its wettability performance. Commercial separators comprising polyethylene or polypropylene typically exhibit lower electrolyte wettability resulting in extended periods for electrolyte absorption. Conversely, cellulose with its inherent hydrophilic properties bestows paper separators with the capacity of rapid and enhanced electrolyte absorption. P3S7A2 paper separator exhibits highest electrolyte uptake capacity of 375.00% compared to P3S7B2 (179.48%) and P3S7Z2 (287.17%) respectively. Another indirect method for assessing wettability involves measuring the contact angle between the probe liquid (liquid electrolyte) and the surface of the separators[22]. The variation of contact angle for the three different ceramic impregnated paper separators is presented in ***Figure 5.4(b)***. Notably, the contact angle values for the developed paper separators are found to be substantially lower than that of PP, as detailed in ***Table 5.3***. The contact angles as measured substantially corroborates the results found in their electrolyte uptake or soaking ability. For instance, P3S7A2, with the highest electrolyte uptake of 375.00%, registers the lowest initial contact angle of 17.8°, which further reduces to 6.7° after 60 s. Conversely, P3S7B2, with the lowest uptake of 179.48% among the three paper separators, exhibits the highest initial contact angle value of 42.6°, which further decreases to 24.8° after 60 s. As expected, P3S7Z2 demonstrates intermediate values for both

electrolyte uptake (287.17%) and also contact angle (41.7° initially and 27.1° after 60 s) among the three separators.

The pore size distributions of paper separators with different ceramic impregnation are presented in ***Figure 5.4(c)***. Also, their surface area, average pore diameter and total pore volume are summarized in ***Table 5.3***. The BJH plots of separator samples reveal the average pore radius of paper separators impregnated with different ceramic materials is mostly mesoporous in nature with their average pore diameters lying in the range of 3-4.5 nm. It is worthy to mention here that although BJH test results show the pore size in the range of <100 nm, SEM micrographs demonstrated much larger pores on separator matrix in the range of few micrometres. BJH method is most probably describing the small pores without taking into account the large pore spaces originated from cellulosic cross linking. Therefore, it will be good to consider the sizes of pore spaces of the separators in micron ranges as observed in their FESEM images.

5.3.3 Mechanical Properties and Flexibility

The separators must be mechanically strong enough to sustain the winding tension applied during lithium battery fabrication process. The mechanical properties are thus important parameters to be estimated for any developed separators. The ceramic impregnated paper separators as developed under this study are found to be easily rollable, bendable and twistable as shown in ***Figures 5.5(a)-(c)***. To estimate the tensile strength of the developed paper separators, load vs extension curves both in machine direction (MD) as well as in transverse direction (TD) are presented in ***Figures 5.5(d)*** and ***5.5(e)*** respectively. For comparison, the data obtained from untreated paper substrate are also included in the curves. Before discussing the mechanical strength of different paper separators, it is worthy to mention here that the tensile strength of any paper or paper modified matrix (e.g., paper separator) intrinsically depends on the strength of cellulosic tissue, their nature of cross linking and inter- and intra-hydrogen bonding among the cellulose units or functional polymers added to it[23–25]. It is considered paper to be a continuous network of hydrogen bonds with no other type of bond contributing to its mechanical strength. Therefore, any functionalization which creates opportunity of making more H-bonds, will only add values to their mechanical strength. In another assumption, we can consider the origin of mechanical strength of paper in terms of combination of fibre strength and fiber-to-fiber bonds[26].

In this case, the paper substrate including polymeric binders is same for all the compositions except impregnated ceramics- Al_2O_3, $BaTiO_3$ and ZrO_2. Here, the addition of polymeric binders (PVDF and SBR)in paper separators plays crucial role in making extra hydrogen bonds with the cellulosic hydroxyl groups which results in two-fold higher mechanical strength of 22.82 MPa-27.88 MPa compared to CP (11.2 MPa), particularly in the transverse direction.

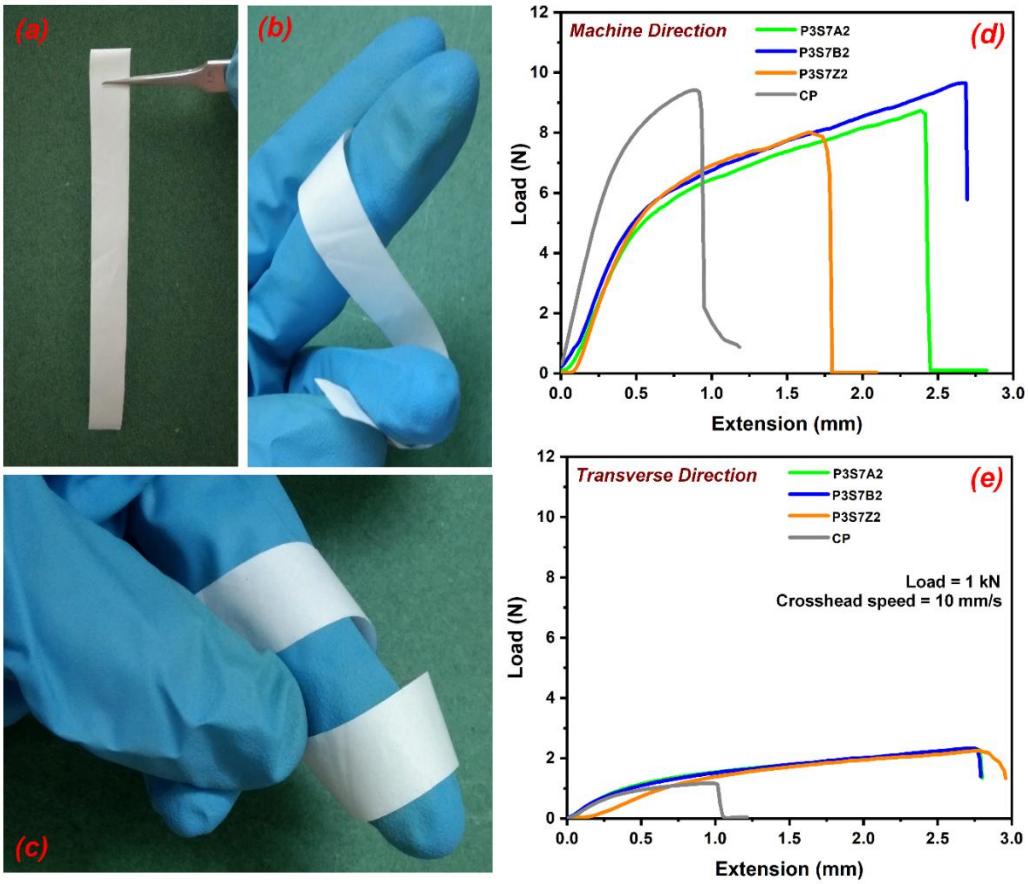

Figure 5.5 *The flexibility and mechanical properties of the developed paper separators: (a)-(c)a strand of paper separator showing utmost flexibility; (d)-(e)load vs extension curves of paper separators (P3S7A2, P3S7B2 and P3S7Z2) along with the untreated cellulose paper (CP) both in machine and transverse directions respectively*

On the other hand, impregnated ceramic nano-particles in paper substrate most probably providing structural integrity to the paper separators. The mechanical test data for paper separators reveals that the tensile strength in machine direction (MD) are in the range of 40-47 MPa. Such variation in their mechanical strength might be due to the variation in moisture content in the separators because the weakening effect of paper can arise due to temperature and moisture content in it[26]. However, the addition of polymeric binders and ceramic nanoparticles probably able to increase the elongation on stress up to 2.5 times in machine

direction (MD) and 3 times in transverse direction (TD) providing better structural integrity compared to CP.

5.3.4 Electrical Properties

The electrochemical impedance spectra (EIS) are recorded for symmetric cells comprising SS/Separator/SS and SS/PP/SS and the results are illustrated in ***Figure 5.6(a)***. All the developed separators exhibit linear profiles trending towards the Z′ axis, indicative of the characteristic behaviour of electrode-electrolyte double-layer capacitance. To quantify the bulk resistance, the low-frequency intercept on the Nyquist plot along the real axis is measured. From the obtained impedance data, the ionic conductivity of electrolyte-soaked paper separators is calculated using the conductivity equation given in ***Chapter 2***. The respective values are documented in ***Table 5.3***. The ionic conductivity estimated to be 1.24×10^{-3}, 0.99×10^{-3}, 1.08×10^{-3} and 0.83×10^{-3} $S.cm^{-1}$ for P3S7A2, P3S7B2, P3S7Z2, and PP respectively. It suggests that the developed paper separators having more and quick electrolyte soaking ability also demonstrates enhanced ionic conductivity to that of commercial polypropylene-based separator.

In order to assess the electrochemical stability of the developed paper separators, linear sweep voltammetry (LSV) has been carried out and described in ***Figure 5.6(b)***. The current vs potential plot infers that the working potential window for all the developed paper separators fall in the range of 4.7-4.8 V, which is comparable to that of commercial plastic separator. This wide potential window is highly required to ensure the optimal performance of the separators within real redox environment of the cell.

To understand the extent of Li^+-ion transport through the developed paper separators, the Li^+ transference number was calculated with the Bruce-Vincent method using the DC polarization technique for Li/Separator/Li symmetric cells[27]. The DC polarization curves along with the Nyquist plots taken before and after the polarization for PP, P3S7A2, P3S7B2 and P3S7Z2 are represented in ***Figures 5.6(c)-(f)***, respectively. The Li^+ transport number for PP is determined to compare and it is estimated to be t_{Li+}=0.21, while those values for P3S7A2 and P3S7B2 are found to be 0.29 and 0.30, respectively. In contrast, the P3S7Z2 separator exhibits a significantly higher lithium transference number of 0.51. The increase in Li^+ ion transference observed with the P3S7Z2 separator can be attributed to the interaction between the opposite surface charges of ZrO_2 and cellulose. This creates a smoother and hindrance free internal pathway allowing more facile movement of free Li^+ ions compared to the other matrices. The

structural modification of the cellulose fibers with ZrO_2 nanoparticles is thus proved to be the main catalyst for the improved electrical and electrochemical performance of the P3S7Z2 separator.

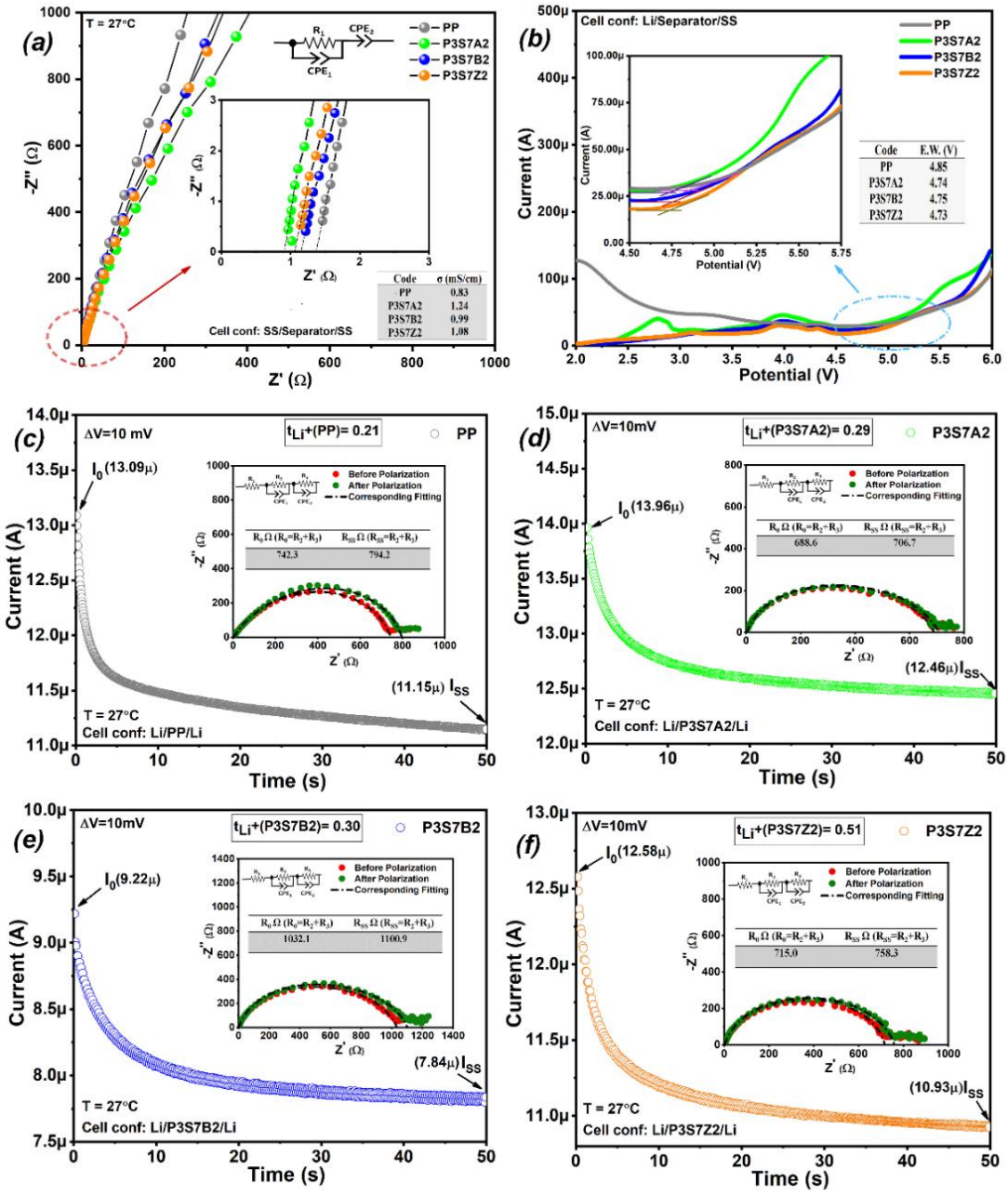

Figure 5.6 *Electrical properties of the developed paper separators along with the commercial separator: (a) ionic conductivity, (b)electrochemical potential window, (c) Li-ion transference number for PP, (d) Li-ion transference number for P3S7A2, (e) Li-ion transference number for P3S7B2, (f) Li-ion transference number for P3S7Z2*

5.3.5 Electrochemical Tests

Multiple electrochemical tests have been performed with the developed paper separators as well as commercial PP to compare and analyse their performances duly;

5.3.5.1 Full Cell Performance

To further investigate Li^+-ion transport during LIB operation, full cell performance is measured using developed paper separators (P3S7A2, P3S7B2 and P3S7Z2) with a cell configuration of NMC111/Separator/MCMB. Initially, three consecutive charge-discharge cycles are carried out at low current density of 0.05 $mAcm^{-2}$ for establishing smooth Li^+-ion migration pathway across the tortuous paper separators. The typical charge-discharge profiles in those formation cycles are displayed in ***Figure 5.7(a)***. The charge-discharge profile of commercial PP separator with similar cell configuration is also included for comparison. The initial discharge capacities as obtained using P3S7A2, P3S7B2 and P3S7Z2 separators are found to be 166.66 $mAhg^{-1}$, 158.97 $mAhg^{-1}$and 170.52 $mAhg^{-1}$ respectively, quite comparable to that of commercial PP based separator (169.26 $mAhg^{-1}$).

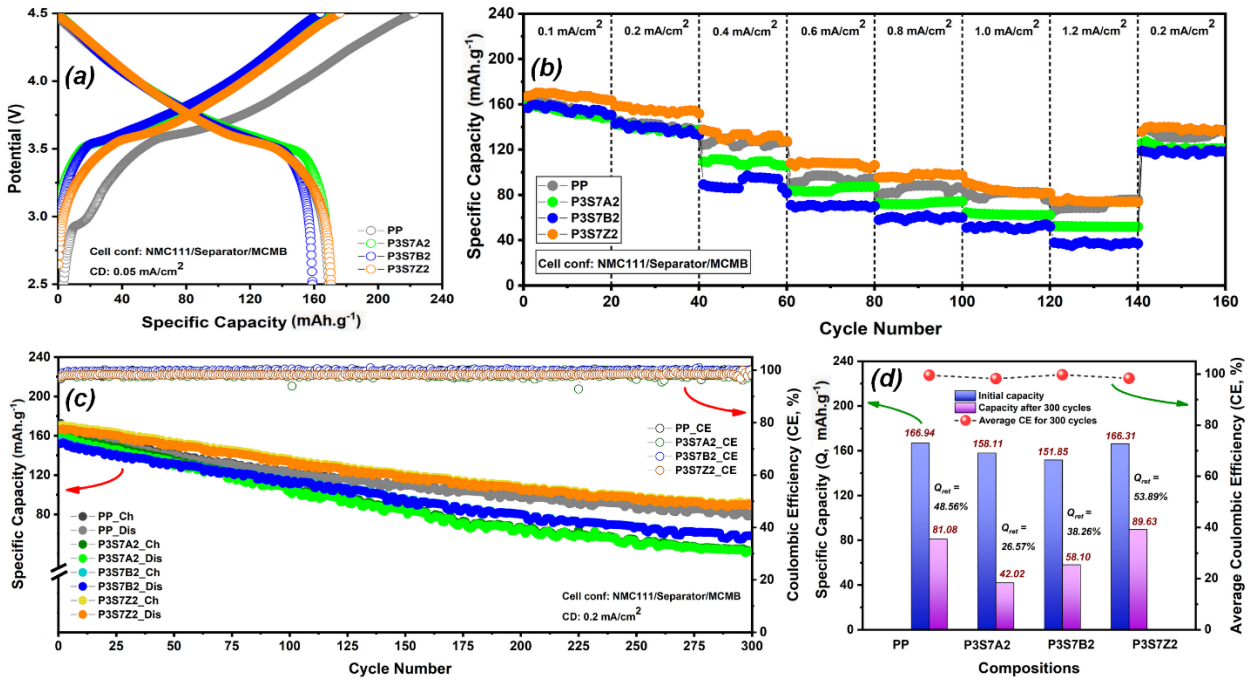

Figure 5.7 *Electrochemical properties of the developed paper separators in 2032coin cell with the configuration of NMC111/Separator/MCMB: (a) typical charge-discharge profiles at a low current density i.e., 0.05 $mAcm^{-2}$, (b) cycling performance at different current densities i.e., 0.1-1.2 $mAcm^{-2}$, (c) long cycling test at 0.2 $mAcm^{-2}$, (d) analysis of the long cycling plot for PP, P3S7A2, P3S7B2 and P3S7Z2 separators*

To further probe the performance of paper separators, the cells are cycled at various current densities ranging from 0.1-1.2 $mAcm^{-2}$. The average capacities obtained for P3S7A2, P3S7B2, P3S7Z2 and PP separators at various current densities are summarized in ***Table 5.1***. On analysis of ***Figure 5.7(b)***, it is found that at current densities ranging between 0.1-1.0 $mAcm^{-2}$, P3S7Z2 separator retains similar average discharge capacities to that of commercial separator. While the other two separators, P3S7A2 and P3S7B2 demonstrate somewhat lower average capacities. At a high current density of 1.2 $mAcm^{-2}$, while PP shows average capacity of 71.01 $mAhg^{-1}$, P3S7A2 and P3S7B2 delivers average capacities of 52.06 $mAhg^{-1}$ and 36.98 $mAhg^{-1}$ respectively. On the contrary, P3S7Z2 exhibits higher average capacity of 74.40 $mAhg^{-1}$. After completion of 140 cycles at step up current densities, the cells are again cycled at a lower current density of 0.2 $mAcm^{-2}$ to check their reversibility in terms of capacity recovery. It is further observed that P3S7Z2 retains almost 89.23% (138.16 $mAhg^{-1}$) of its initial average capacity when it is cycled at 0.2 $mAcm^{-2}$ (154.83$mAhg^{-1}$), a close match value to that of commercial separator. Other two paper separators although retain more than 85% of their average capacities at 0.2 $mAcm^{-2}$, however, specific capacities as obtained are still found to be lower than those of commercial PP and P3S7Z2 separators.

Table 5.1 *Average specific capacity of 20 cycles for PP, P3S7A2, P3S7B2 and P3S7Z2 at various current densities ranging from 0.1-1.2 $mAcm^{-2}$*

Current density ($mAcm^{-2}$)	**Average specific capacity ($mAhg^{-1}$) at different current densities**			
	PP	**P3S7A2**	**P3S7B2**	**P3S7Z2**
0.1	156.58	153.22	155.59	167.29
0.2	140.75	138.56	138.49	154.83
0.4	126.36	108.82	90.25	131.74
0.6	93.86	85.01	70.23	107.44
0.8	85.48	72.78	59.72	97.01
1.0	80.43	62.74	51.41	84.06
1.2	71.01	52.06	36.98	74.40
0.2	133.14	121.83	117.88	138.16

The long cycling characteristics of developed paper separators along with commercial PP are displayed in ***Figure 5.7(c)***. The plot also demonstrates the coulombic efficiencies of separators up to 300 cycles. All the developed paper separators show steady charge-discharge cycling profiles resulting in more than 98% coulombic efficacy. The capacity decay after 300 cycles is calculated and displayed in ***Figure 5.7(d)***. It reveals that P3S7Z2 separator demonstrates

capacity retention of 53.89%, higher than that of PP separator (48.56%). On the contrary, Al_2O_3 and $BaTiO_3$ impregnated paper separators demonstrate lower capacity retentions of 26.57% and 36.26% respectively. On compilation of obtained electrochemical performances, it is found that ZrO_2 based impregnation in paper separator has profound effect on cell performance. ZrO_2 nanoparticles have a tendency to incorporate Lewis acidic characteristics to the separator surface which interact with the Lewis basic site (PF_6^-) of $LiPF_6$ that slows down the decomposition of PF_6^-, thereby enhancing the electrochemical stability of the P3S7Z2 separator[28,29]. Also, the superior cycling stability and high rate capability of P3S7Z2 separator may be due to the fact that the nature of deposition of ZrO_2 particles is completely different than in cases of Al_2O_3 and $BaTiO_3$ ceramics. While $ZrO_2$is capable to coat the entangled cellulosic fibers without sacrificing porosity, other two ceramics either remain as agglomerated clusters deposited on pore spaces or completely block the mesopores. Such patterns of deposition of Al_2O_3 and $BaTiO_3$ ceramics probably hinder the Li-ion migration across the electrolyte-filled pore spaces during cycling, and also possibly fail to create compatible interface with the electrode surfaces resulting in higher interfacial resistances. In contrary, cellulose fibers coated with ZrO_2 particles created good ceramic-ceramic interfaces with electrode surfaces lowering the interfacial impedance. The EIS examination will be thus crucial to understand the intrinsic phenomena happening during cycling of the cells.

5.3.5.2 Pre- and Post-electrochemical EIS Study

Table 5.2 *Values of electrolyte resistance, SEI resistance and charge-transfer resistance before and after electrochemical cycling for the NMC111/Separator/MCMB cells comprising the three developed paper separators i.e., P3S7A2, P3S7B2 and P3S7Z2*

Composition	**R_e (Ω) (electrolyte resistance)**			**R_{SEI} (Ω) (SEI resistance)**			**R_{CT} (Ω) (charge-transfer resistance)**		
Separator	Before cycling	After cycling	Increase in resistance(%)	Before cycling	After cycling	Increase in resistance (%)	Before cycling	After cycling	Increase in resistance (%)
P3S7A2	0.85	2.79	228.23	4.88	12.37	153.48	8.64	429.80	4874.53 %
P3S7B2	1.61	4.19	152.66	4.77	139.50	2824.52	13.57	67.97	400.88 %
P3S7Z2	1.01	3.88	284.15	2.50	31.62	1164.80	6.67	8.50	27.44%

The reason behind better electrochemical performance of ZrO_2 based paper separator can be understood with respect to the impedance profiles obtained before and after cycling. The pre- and post-electrochemical EIS spectra are demonstrated in ***Figures 5.8(a)-(c)*** for P3S7A2, P3S7B2 and P3S7Z2 along with their equivalent circuit and enlarged view of profiles in the inset. The equivalent circuit as described in the graphs comprises of three components: (i) $R_e$as it denotes the bulk resistance or the electrolyte resistance, (ii) R_{SEI} attributes to the solid electrolyte interphase (SEI) formed at the cathode-separator interface and (iii) R_{CT} contributes to the charge transfer process[30]. On analysis of EIS data, it is found that the magnitude of each of these resistance components typically increases after 300 cycles compared to their pre-cycling values, however, the extent of increment significantly differs for different separators. These resistance values are presented in tabular form in ***Table 5.2***. While electrolyte resistance of the cell comprising three different separators increases more than two times after cycling, the increments in SEI and charge transfer resistances somewhat differ for three separators.

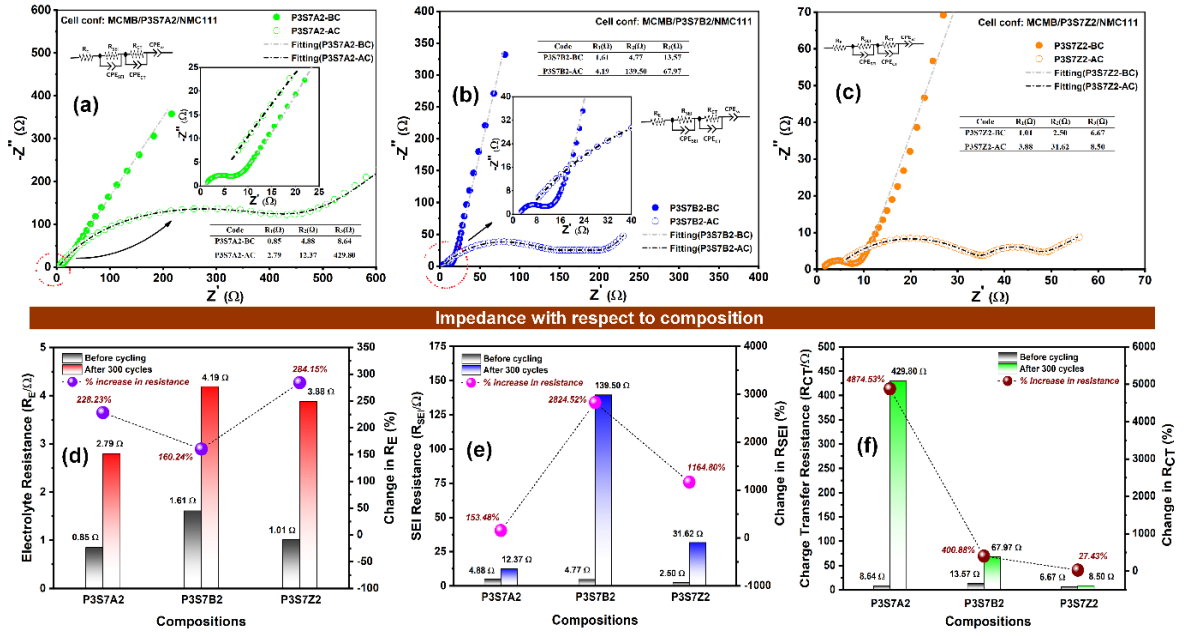

Figure 5.8 *Pre- and post-electrochemical impedance spectra of (a) P3S7A2, (b) P3S7B2 and (c) P3S7Z2 along with their equivalent circuit and enlarged view of profiles in the inset; The variation of different impedance components is displayed against paper separator compositions:(d) electrolyte resistance, (e) SEI resistance and (f) charge transfer resistances*

More interestingly, the charge transfer resistances are found to be markedly different for P3S7Z2 separator compared to the other two separators (P3S7A2 and P3S7B2). P3S7Z2 cells demonstrate slight increase in their charge transfer resistance from 6.67 Ω to 8.50Ω before and after cycling respectively. On the other hand, R_{CT} values for P3S7A2 and P3S7B2 are found to

increase from 8.64 Ω to 429.80 Ω and 13.57 Ω to 67.97 Ω respectively. Therefore, the EIS analysis clearly demonstrates the perfect compatibility of ZrO_2 impregnated separator with the electrodes (anode and cathode) resulting in facile charge transfer process at their interfaces.

5.3.5.3 Multi-electrode Compatibility of the Separators

To examine the multi-electrode compatibility of developed separators, 2032 coin cells are fabricated using mesocarbon microbead (MCMB), $Li_4Ti_5O_{12}$ (LTO) as anodes and $LiNi_{1/3}Mn_{1/3}Co_{1/3}O_2$ (NMC111), $LiFePO_4$ (LFP) and $LiMn_2O_4$(LMO) as cathode materials. For comparison, the commercial separator has also been cycled under same current densities. ***Figure 5.9*** demonstrates the typical charge-discharge profiles of P3S7A2, P3S7B2 & P3S7Z2 along with PP separator with cell configurations of LMO/separator/MCMB, LFP/separator/MCMB and LFP/separator/LTO. As shown in ***Figure 5.9(a)***, in a cell configuration of LMO/separator/MCMB, all the developed separators delivered similar specific discharge capacities ranging from 67-71 $mAhg^{-1}$, while PP delivered marginally higher capacity of 72.73 $mAhg^{-1}$.

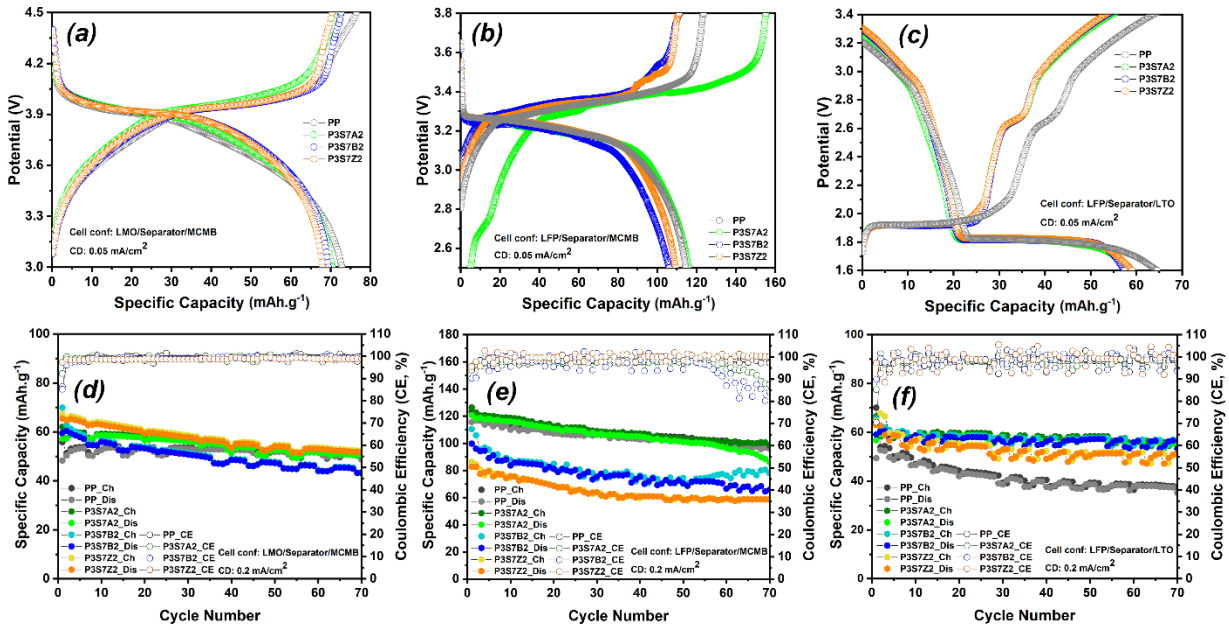

Figure 5.9 *Multielectrode compatibility of commercial and developed paper separators showing (a)-(c) typical charge-discharge profiles and (d)-(f) cycling performances with respect to different electrodes ($LiMn_2O_4$/Separator/MCMB, $LiFePO_4$/Separator/MCMB and$LiFePO_4$/Separator/$Li_4Ti_5O_{12}$)*

While Al_2O_3 and BTO based paper separators deliver comparable capacities of 120.78 $mAhg^{-1}$ and 110.76 $mAhg^{-1}$ with that of commercial separator (121.65 $mAhg^{-1}$) when tested in LFP/separator/MCMB configuration, ZrO_2 based separator delivered slightly lower capacity

of 81.65 $mAhg^{-1}$ (***Figure 5.9(e)***). In LFP/Separator/LTO configuration, all the three separators along with commercial one delivered comparable capacities ranging from 66-72 $mAhg^{-1}$ (***Figure 5.9(c)***). The cycle life test is also carried out using the similar cell configurations and the cycling profiles are demonstrated in ***Figures 5.9(d)-(f)***. In LMO/Separator/MCMB combination, all the paper separators showed fairly similar cycling profiles with that of commercial separator with >97% coulombic efficiency. As shown in ***Figure 5.9(e)***, using cell configuration of LFP/Separator/MCMB, initially P3S7A2 and P3S7B2 paper separators delivered higher discharge capacities than P3S7Z2 during cycling, however, on prolonged cycling, their discharge capacities drastically reduced and became comparable to that of P3S7Z2.While calculating the capacity loss on cycling, ZrO_2 impregnated paper separator showed lower capacity loss than that of Al_2O_3 and BTO based separators in LFP/MCMB combination. ***Figure 5.9(f)*** demonstrated the cycling patterns of P3S7A2, P3S7B2 and P3S7Z2 separators with cell combination of LFP/Separator/LTO. All the separators showcased better cycling ability and comparable coulombic efficiency than the commercial separator.

5.3.6 Thermal Safety Tests

A qualitative observation of thermal shrinkage at temperature of 200ºC for developed paper separators along with the commercial PP based separator and pristine cellulose paper (CP)is presented in ***Figures 5.10(a)-(b)***. It is observed that the bare paper and the developed paper separators retain their structural integrity at 200ºC, whereas the commercial PP based separator completely collapses. This demonstrates higher dimensional stability of the paper separators at elevated temperature ensuring safety of the battery. In addition to thermal shrinkage, the developed separators are exposed to flame to measure their flame resistance properties, as illustrated in ***Figures 5.10(c)-(d)***. The commercial PP separator, on exposure to flame, rapidly shrinks whereas the ceramic impregnated paper separators exhibit remarkable resistance to ignition either by char formation or by resisting the flame to achieve its ignition temperature. Interestingly, P3S7Z2 paper separator stands out as the top performer in flame among the developed three paper separators. Even during a prolonged exposure to flame for 25s, it does not undergo any char formation or catches flame.

The TGA curves as depicted in ***Figure 5.10(e)*** reveal thermal characteristics of all the paper separators. The thermal degradation of paper separators exhibits similar type of profiles with five distinct stages between the range of RT-1200ºC in air; (i) an initial weight loss occurs due to the removal of residual moisture between RT-150ºC, (ii) between 150-270ºC, the thermal

stabilization occurs followed by slow removal of hydrogen bonded water from the cellulosic bulk matrix, (iii) pyrolysis stage between 250-350ºC where the polymer binders used in paper separators start decomposing with notable weight loss, (iv) slow pyrolysis stage between 350-500ºC is characterized by gradual release of volatile substances and (v) at temperatures above 500ºC, the solid content in paper separators particularly ceramics remain without showing any further weight loss up to 1200°C [31]. This stage is often accompanied by a plateau in weight loss. In the inset of ***Figure 5.10(e)***, the corresponding DTA curves of the paper separators are shown.

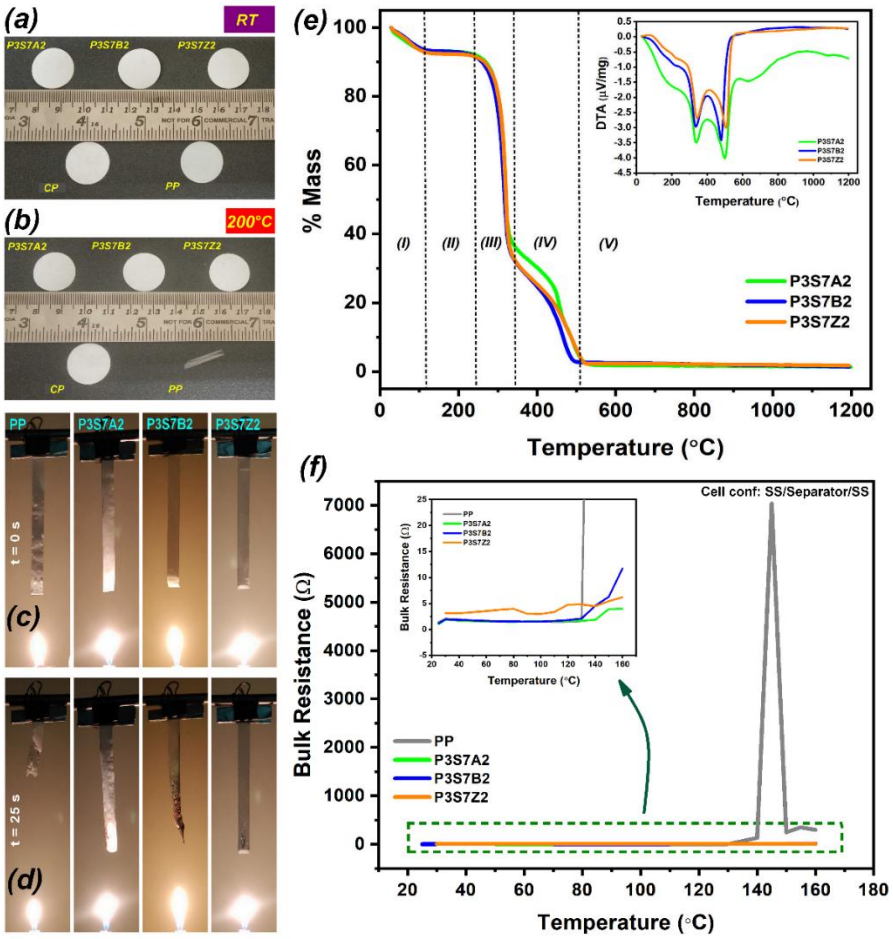

Figure 5.10 *Thermal behaviour of the developed paper separators: qualitative thermal shrinkage measurement (a) at room temperature and (b) at 200ºC; (c) & (d) flame safety test of the developed separators along with the commercial one; (e) thermogravimetric analysis (TGA) plot and differential thermal analysis (DTA) plot (inset of e); (f) Thermal shutdown properties via EIS method*

The temperature dependant impedance plot is given in ***Figure 5.10(f)*** to understand the shutdown properties of developed paper separators. For this purpose, the developed paper separators are sandwiched between two stainless (SS) electrodes and their resistivity is

measured with respect to incremental temperature ranging from RT-160ºC. It is observed that at about 140ºC, commercial separator demonstrates abrupt increase in resistance value, more than eighty times than its average resistance. On the other hand, a nominal two-fold increase in resistance value can be observed for paper-based ceramic separators. This further corroborates the high safety aspects of developed cellulosic separators.

Table 5.3 *Comparison chart of different properties of the developed paper separators (P3S7A2, P3S7B2 and P3S7Z2)*

Separator composition / Properties	**P3S7A2**	**P3S7B2**	**P3S7Z2**
Air permeability (Gurley, s)	7.46	13.05	13.16
Surface area (m^2g^{-1})	1.317	0.152	1.017
Average pore diameter (nm)	3.305	3.307	4.219
Pore volume ($cc.g^{-1}$)	0.01944	0.01311	0.01274
Electrolyte uptake (%)	375.00	179.48	287.17
Contact angle (0s/60s)	17.8º/6.7º	42.6º/24.8º	41.7º/27.1º
Tensile strength in MD/TD (MPa)	43.71/22.82	46.46/23.29	40.08/27.88
Ionic conductivity ($S.cm^{-1}$)	1.24×10^{-3}	0.99×10^{-3}	1.08×10^{-3}
Li^+ transference number	0.29	0.30	0.51
Typical specific capacity ($mAhg^{-1}$) (NMC111/Separator/MCMB)	166.66	158.97	170.52
Average coulombic efficiency for 300 cycles (%)	98.23	99.72	98.29

5.4 Conclusion

Sustainable, low cost, flexible ceramic-based paper separators have been developed under this study using an industry friendly wet coating process. Three different nano-structured ceramics (Al_2O_3, $BaTiO_3$ and ZrO_2) are impregnated into paper substrate along with polymeric binders to fabricate ceramic based paper separators. It is found that the nature of impregnation of different ceramics within the cross-linked cellulosic fibers of paper substrate heavily relies on their physical properties and surfaces charges and becomes crucial in determining physico-chemical properties as well as electrochemical performances of developed separators. All the three paper separators exhibit excellent porosity (8-14 Gurley s), electrolyte uptake capabilities (175-350%), dimensional stability at elevated temperature (>200ºC) and flame retardance

properties. Paper separators when tested in full cell configuration show remarkable performance in terms of cycleability (300 cycles), rate capability at different current densities (0.1-1.2 $mAcm^{-2}$) with excellent coulombic efficiency (>98%). When compared with commercial polyolefin-based separator, the developed paper separators demonstrate comparable electrochemical performances. While examining post-electrochemical results, it appears that although Al_2O_3 and $BaTiO_3$ impregnated paper separators show satisfactory performance in all other physical tests, ZrO_2 based paper separator exhibits more compatibility with commercial ceramic-based electrodes. It is understood that the impregnation of ceramics not only helps in enhancing structural integrity and electrolyte wettability of paper separators, but also incorporates flame resistance properties, a critical safety aspect for cellulose-based separators. In summary, the current study opens up a new horizon for developing functional ceramic based cellulosic separators for future sustainable metal-ion batteries.

References

1 X. Jiang, X. Zhu, X. Ai, H. Yang and Y. Cao, *ACS Appl Mater Interfaces*, DOI:10.1021/acsami.7b05535.

2 X. Zhu, X. Jiang, X. Ai, H. Yang and Y. Cao, *ACS Appl Mater Interfaces*, DOI:10.1021/acsami.5b07230.

3 J. S. Edge, S. O'Kane, R. Prosser, N. D. Kirkaldy, A. N. Patel, A. Hales, A. Ghosh, W. Ai, J. Chen, J. Yang, S. Li, M. C. Pang, L. Bravo Diaz, A. Tomaszewska, M. W. Marzook, K. N. Radhakrishnan, H. Wang, Y. Patel, B. Wu and G. J. Offer, 2021, preprint, DOI: 10.1039/d1cp00359c.

4 X. Zeng, Y. Liu, R. He, T. Li, Y. Hu, C. Wang, J. Xu, L. Wang and H. Wang, *Cellulose*, DOI:10.1007/s10570-022-04499-5.

5 Z. Wang, H. Xiang, L. Wang, R. Xia, S. Nie, C. Chen and H. Wang, *J Memb Sci*, DOI:10.1016/j.memsci.2018.02.040.

6 L. C. Zhang, X. Sun, Z. Hu, C. C. Yuan and C. H. Chen, *J Power Sources*, DOI:10.1016/j.jpowsour.2011.12.028.

7 L. David, K. Dahlberg, D. Mohanty, R. E. Ruther, A. Huq, M. Chi, S. J. An, C. Mao, D. M. King, L. Stevenson and D. L. Wood, *ACS Appl Energy Mater*, DOI:10.1021/acsaem.8b01877.

8 S. Casino, B. Heidrich, A. Makvandi, T. Beuse, T. Gallasch, M. Peterlechner, G. Wilde, M. Winter and P. Niehoff, *J Energy Storage*, DOI:10.1016/j.est.2021.103479.

9 R. Arunkumar, A. P. Vijaya Kumar Saroja and R. Sundara, *ACS Appl Mater Interfaces*, DOI:10.1021/acsami.8b17887.

10 D. Lv, J. Chai, P. Wang, L. Zhu, C. Liu, S. Nie, B. Li and G. Cui, *Carbohydr Polym*, DOI:10.1016/j.carbpol.2020.116975.

11 U. Nisar, R. Amin, R. Essehli, R. A. Shakoor, R. Kahraman, D. K. Kim, M. A. Khaleel and I. Belharouak, *J Power Sources*, DOI:10.1016/j.jpowsour.2018.06.065.

12 X. Li, K. Zhang, D. Mitlin, Z. Yang, M. Wang, Y. Tang, F. Jiang, Y. Du and J. Zheng, *Chemistry of Materials*, DOI:10.1021/acs.chemmater.7b04861.

13 J. Peng, X. Zeng, H. Zhu, K. Xia, J. Gong and K. Huang, *RSC Adv*, DOI:10.1039/d2ra05555d.

14 D. Myśliwiec, M. Chylińska, M. Szymańska-Chargot, S. Chibowski and A. Zdunek, *Cellulose*, 2016, **23**, 2819–2829.

15 A. A. Ivanov, V. A. Polyushko and A. Y. Khomyakov, in *IOP Conference Series: Materials Science and Engineering*, 2019, vol. 537.

16 W. Luan and L. Gao, *Ceram Int*, 2001, **27**, 645–648.

17 S. S. Tripathy and A. M. Raichur, *J Exp Nanosci*, 2011, **6**, 127–137.

18 C. Renger, P. Kuschel, A. Kristoffersson, B. Clauss, W. Oppermann and W. Sigmund, in *Physical Chemistry Chemical Physics*, 2004, vol. 6.

19 M. Hashiba, H. Okamoto, Y. Nurishi and K. Hiramatsu, *J Mater Sci*, DOI:10.1007/BF01148770.

20 J. Jang, J. Oh, H. Jeong, W. Kang and C. Jo, 2020, preprint, DOI: 10.3390/ma13204625.

21 M. Das, P. S. Das, N. C. Pramanik, R. N. Basu and M. Wasim Raja, *ACS Omega*, DOI:10.1021/acsomega.3c02859.

22 W. Lin, F. Wang, H. Wang, H. Li, Y. Fan, D. Chan, S. Chen, Y. Tang and Y. Zhang, 2022, preprint, DOI: 10.1002/cssc.202201464.

23 H. Seddiqi, E. Oliaei, H. Honarkar, J. Jin, L. C. Geonzon, R. G. Bacabac and J. Klein-Nulend, 2021, preprint, DOI: 10.1007/s10570-020-03674-w.

24 M. Wohlert, T. Benselfelt, L. Wågberg, I. Furó, L. A. Berglund and J. Wohlert, 2022, preprint, DOI: 10.1007/s10570-021-04325-4.

25 I. Francolini, L. Galantini, F. Rea, C. Di Cosimo and P. Di Cosimo, 2023, preprint, DOI: 10.3390/ijms24119268.

26 J. C. Roberts, *The Chemistry of Paper*, 1996.

27 J. Evans, C. A. Vincent and P. G. Bruce, *Polymer (Guildf)*, DOI:10.1016/0032-3861(87)90394-6.

28 A. K. Solarajan, V. Murugadoss and S. Angaiah, *Sci Rep*, 2017, **7**, 45390.

29 C. H. Park, D. W. Kim, J. Prakash and Y. K. Sun, *Solid State Ion*, DOI:10.1016/S0167-2738(03)00025-0.

30 W. Choi, H. C. Shin, J. M. Kim, J. Y. Choi and W. S. Yoon, 2020, preprint, DOI: 10.33961/jecst.2019.00528.

31 J. L. Yang, X. X. Zhao, W. Zhang, K. Ren, X. X. Luo, J. M. Cao, S. H. Zheng, W. L. Li and X. L. Wu, *Angewandte Chemie - International Edition*, DOI:10.1002/anie.202300258.

Chapter 6

Effect of Chelated ZrO_2 in Paper Separator

Highlights

- Chelated zirconia precursors with coordinatively unsaturated Zr^{4+}/Zr-OH sites
- Strong Lewis acid–base interactions enhance electrolyte affinity and promote efficient Li-salt dissociation
- Optimized balance of structural disruption, wettability, and mechanical reinforcement at moderate zirconia loading
- Cellulose-based separator integrates ceramic surface chemistry for superior electrochemical performance

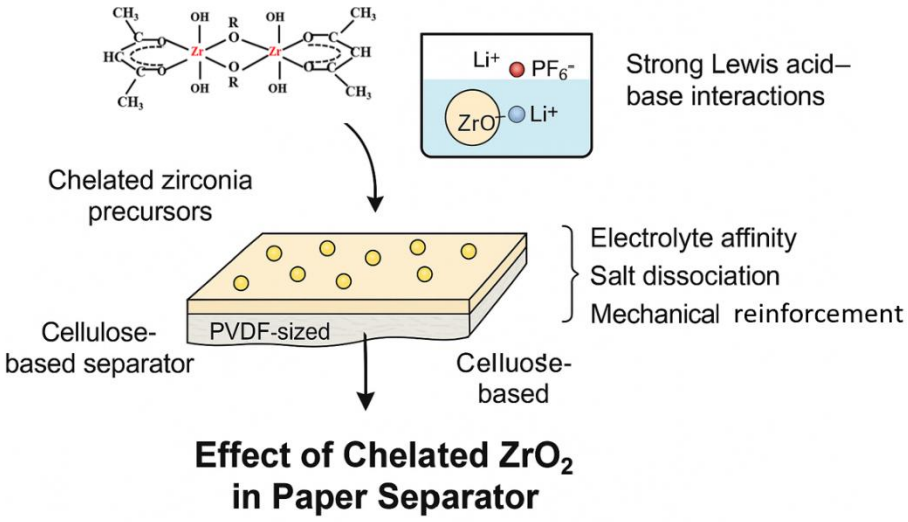

Figure 6.0 *Graphical representation of the chapter content*

This chapter explores the development of cellulose-based paper separators modified with chelated zirconia precursors. By employing acetylacetone-assisted chelation and controlled hydrolysis of zirconium isopropoxide, zirconia nanodomains with Lewis acid–base active sites were generated and uniformly integrated into a PVDF-sized cellulose matrix. These functional domains improved electrolyte affinity, promoted salt dissociation, and facilitated stable ionic conduction pathways, while simultaneously reinforcing mechanical integrity. The systematic evaluation of separators with varying zirconia loadings highlights the critical role of precursor chemistry and surface site engineering in optimizing performance for advanced lithium-ion battery applications.

6.1 Background and Overview

Lithium-ion batteries (LIBs) require separators that not only provide mechanical and thermal stability but also facilitate efficient ionic transport and stable electrode-electrolyte interfaces. Conventional polyolefin-based separators often suffer from limited wettability, poor electrolyte uptake, and safety concerns under high current densities, motivating the search for advanced alternatives[1,2]. Cellulose-based paper separators have emerged as a promising class owing to their renewable origin, porosity, mechanical flexibility, and inherent electrolyte affinity[3]. However, pristine cellulose suffers from uncontrolled swelling, lesser mechanical robustness than polyolefin, and limited ability to regulate ion-electrolyte interactions. These drawbacks can be overcome by introducing ceramic fillers, which enhance mechanical integrity, thermal resistance, and in certain cases, ion transport.

Zirconia (ZrO_2) has been widely investigated as a ceramic additive because of its high chemical stability and mechanical strength. Yet, bulk ZrO_2 nanoparticles tend to agglomerate and their surfaces are dominated by stable Zr–O–Zr linkages, with only limited densities of under-coordinated Zr^{4+} or hydroxyl (–OH) sites. Such surfaces are less effective in promoting lithium salt dissociation or in providing solvophilic sites for electrolyte wetting. Consequently, simple impregnation of bulk ZrO_2 often results in separators with restricted ionic conductivity and poor long-term electrochemical performance. To address these limitations, engineering the zirconia precursor chemistry to deliberately generate coordinatively unsaturated sites represents a rational design strategy.

Lewis acid–base interactions have recently been recognized as a powerful tool to modulate ion transport and interfacial behavior in polymer electrolytes and separators. Lewis acidic sites such as under-coordinated metal centers can coordinate to salt anions (e.g., PF_6^-), weakening ion pairing and thereby increasing the concentration of free Li^+ ions. Simultaneously, Lewis basic sites (–OH or O^{2-} groups) provide complementary coordination environments that stabilize solvated Li^+. This dual functionality enhances salt dissociation, lowers bulk resistance, and promotes selective Li^+ conduction pathways. Several recent studies exemplify this concept: An et al. demonstrated that incorporating molecular Lewis-acid centers into PEO electrolytes improves salt dissociation and extends oxidative stability up to 4.8 V, enabling stable cycling in high-voltage cells[4]. Zhou et al. reported yolk-shell Al_2O_3-coated separators where Lewis-acidic Al sites enhanced ionic conductivity (5.55×10^{-3} $S\cdot cm^{-1}$) and increased Li^+ transference number ($t_+=0.62$), while stabilizing symmetric Li/Li cycling for over 400h[5]. Wu et al.

highlighted that engineering pentacoordinated Al^{3+} sites in Al_2O_3 generates abundant Lewis-acidic centers, as confirmed by ^{27}Al MAS-NMR, directly correlating coordination state with ionic functionality[6]. Similarly, Hu et al. showed that introducing ZSM-5 nanosheets containing Si/Al–OH groups into PEO-based electrolytes improved conductivity (1.34×10^{-3} $S\cdot cm^{-1}$ at 60°C), Li^+ transference ($t_+ = 0.37$), and electrochemical stability (4.8 V), underscoring the role of Lewis-acidic fillers in tuning transport properties[7].

In this context, this chapter provides a comprehensive approach to design a chelated zirconia precursor via controlled acetylacetone chelation and subsequent hydrolysis of zirconium isopropoxide. This was done to suppress uncontrolled agglomeration and crystallization, while generating coordinatively unsaturated Zr^{4+} (Lewis acid) and Zr–OH (Lewis base) sites. These functional sites are expected to improve electrolyte affinity, promote Li-salt dissociation, and create stable ionic conduction pathways when embedded in a PVDF-sized cellulose paper matrix. The resulting composite paper separators were systematically evaluated in terms of structure, wettability, mechanical reinforcement, ionic conductivity, electrochemical stability, and cycling performance. The results show that moderate zirconia loading yields the most balanced and superior properties, highlighting the critical role of Lewis acid–base site engineering in separator design. By integrating concepts from recent literature with a tailored sol-gel route for zirconia, this work establishes a new framework for separator development that combines the sustainability of cellulose with the functional tunability of Lewis acidic ceramics.

6.2 Experimental Details

6.2.1 Preparation of Chelated Zirconia Precursor

For making 5 wt% zirconia (ZrO_2) sol, 19.23 g zirconium isopropoxide (ZIP) was added in 40 g 1-propanol solvent in a beaker and stirred for 10 minutes in room temperature (RT). Simultaneously, 2 g acetylacetone (acac) as a chelating agent and 15 g 1-propanol were obtained in another beaker. The mixer of acac solution was added slowly in ZIP solution with continued stirring for 1 h for partial chelation to stabilized ZIP solution in 1st step. The molar ratio of ZIP:acac was maintained at 1: 0.5. In 2nd step, mixer of 0.2 g 1(N) HNO_3, 1.70 g Millipore water, and 22 g 1-propanol were added in 1st step ZIP solution and mixed with proper stirring for 2 h in RT to complete the hydrolysis reaction. The equivalent 0.5, 1.0, 1.5, 2 and 2.5 wt % ZrO_2 sols were prepared from above 5 wt % sol. Finally, sols were kept in refrigerator before using for coating applications.

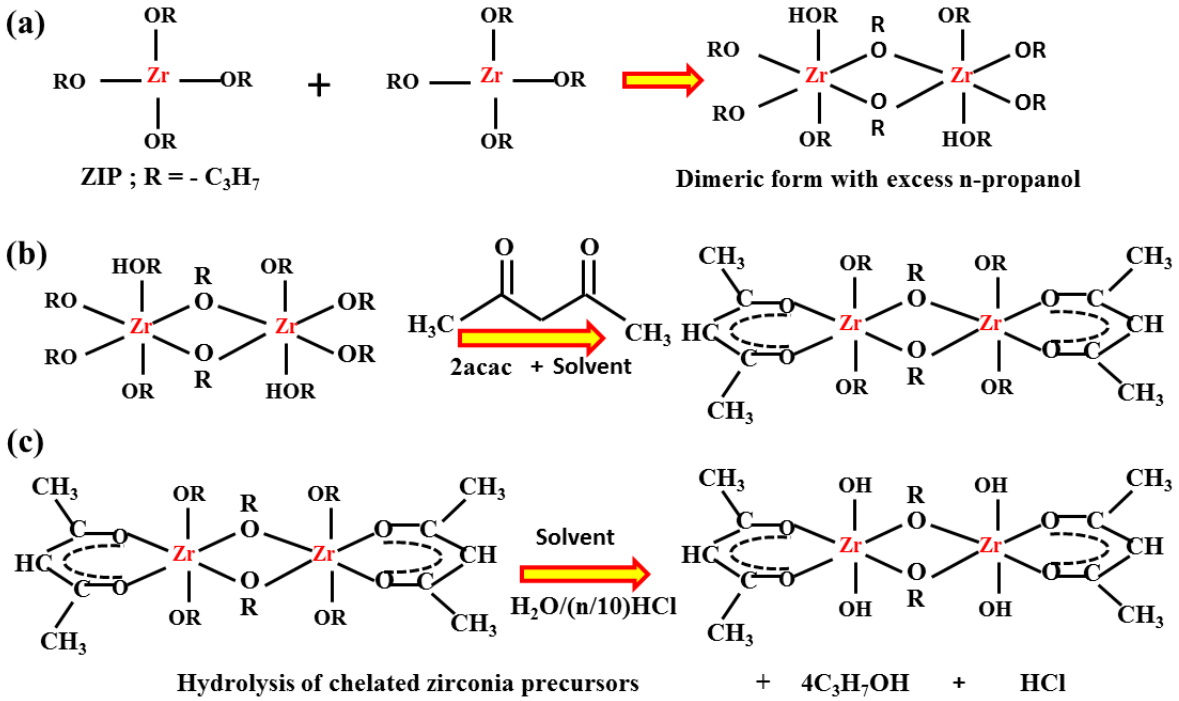

Figure 6.1 *Proposed reaction mechanism of ZIP during preparation of zirconia sol*

6.2.2 Fabrication of Paper Separators

Table 6.1 *Composition and codes for different paper separators developed under this study*

1st layer of coating on paper	2nd layer of coating on paper	Nomenclature
3.5 w/v% PVDF in NMP	7.0 w/v% SBR in de-ionized water	*HY00*
3.5 w/v% PVDF in NMP	7.0 w/v% SBR in de-ionized water : 0.5% zirconia precursor in 1-propanol	*HY05*
3.5 w/v% PVDF in NMP	7.0 w/v% SBR in de-ionized water : 1.0% zirconia precursor in 1-propanol	*HY10*
3.5 w/v% PVDF in NMP	7.0 w/v% SBR in de-ionized water : 1.5% zirconia precursor in 1-propanol	*HY15*
3.5 w/v% PVDF in NMP	7.0 w/v% SBR in de-ionized water : 2.0% zirconia precursor in 1-propanol	*HY20*
3.5 w/v% PVDF in NMP	7.0 w/v% SBR in de-ionized water : 2.5% zirconia precursor in 1-propanol	*HY25*

After preparing different concentration of chelated zirconia precursor, they are incorporated into paper matrix using the separator fabrication process described in ***Section 2.3.2.2*** of ***Chapter 2***. The zirconia sol precursors in 1-propanol are mixed in aqueous solution of styrene butadiene rubber (SBR) in 3:1 volume ratio. The 3.5 w/v% PVDF-coated paper is undergone another layer of wet-coating with the SBR-zirconia slurry. The SBR mainly acts as a binder here. The dried and compacted paper separators are then stored for further characterizations. The compositions and respective nomenclature used for the developed separators is mentioned in ***Table 6.1.***

6.3 Results and Discussion

Physical and electrochemical properties of the zirconia precursor as well as the developed paper separators have been determined and analysed by following the procedures mentioned in ***Chapter 2***.

6.3.1 Properties of the Zirconia Sol

Tentative reaction pathway of ZIP precursor in scheme 1 represented during preparation of sol through sol-gel wet chemical method. In Scheme 1(a), ZIP precursor forms in dimeric structure of it in the presence of excess coordinating alcohol molecules[8,9]. Dimeric ZIP alkoxide precursors partially chelated with acetyl acetone (ZIP:acac = 2:1) to retard the hydrolysis reaction rate and it control from first rate of reaction which shown in the scheme of ***Figure 6.1(b)***. In Hydrolysis reaction in the scheme of ***Figure 6.1(c)***, hydrolyzed the reactive prone –OR groups in dimeric ZIP structure with hydroxyl group (–OH) in acidic condition where –OH group have strong exchange ability.

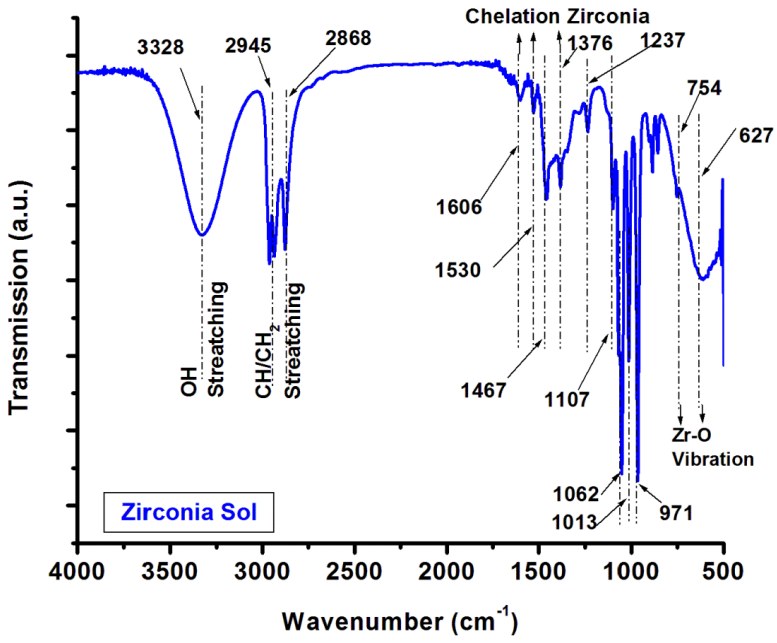

Figure 6.2 *ATR-FTIR spectra of zirconia sol*

Figure 6.2 showed that ATR-FTIR spectra of stable zirconium (IV) ions based solution which has

been prepared through sol-gel wet chemical technique. Solution was formulated from ZIP precursors with acetyl acetone to control rate of reaction and followed by hydrolysis reaction to create the active site of OH group in skeletal system of zirconium ions and OH group will participate to react with active species of various surface of substrates after deposition using different techniques likes dip and spray coating methods etc. Inorganic-organic network structures of zirconium ions were characterized by ATR-FTIR spectra (Bruker ECO, ALPHA) spectrometer (using a ZnSe crystal) in the spectral range of 500-4000 cm^{-1} with a resolution of 4 cm^{-1}. Stretching vibration band of O-H at 3328 $cm^{-1}$is associated with the network structure of zirconium ions[10]. C-O vibration absorption band in partially chelated zirconium ions are associated at 1237, 1062, 1013 and 971cm^{-1}[10]. The strong absorption stretching band C-H at 2945 and 2868 cm^{-1} can be attributed due to presence of $-CH_2/-CH_3$ group associates in ZIP and asymmetric C-H and C-C bands at 1467 and 1107 cm^{-1} can be assigned in isopropoxide part of zirconium respectively[10,11]. Zr-O or Zr-OH vibration peaks around were assigned to 627 and 754 cm^{-1} which proved that the presence of zirconium ions in solution. Chelated acac with zirconium precursors (ZIP) in solution stage can be assigned to the bands at 1606, 1530 and 1376 cm^{-1}[12].

6.3.2 Structural and Microstructural Properties of the Fabricated Separators

To understand the structural features of the chelated zirconia embedded paper separators, their XRD patterns are analysed first along with that of the pure cellulose-based pristine paper (CP). Fron the X-ray diffractogram shown in ***Figure 6.3***, it can be confirmed that CP exhibits the characteristic cellulose-I structure, with prominent diffraction peaks around $2\theta \approx 14–17°$ and 22–23°. These peaks are sharp and well defined, giving a crystallinity index (CI) of 58.29 %, which reflects the highly ordered arrangement of cellulose microfibrils and their extensive hydrogen-bonding network in native cellulose[13,14].

Upon introducing the chelated zirconia precursor into the PVDF-sized cellulose matrix, substantial changes in the diffraction profiles are observed for samples HY00-HY25. Although the characteristic cellulose-I reflections remain, the intensity of the peaks is significantly reduced, and they become broader. The CI value for HY00 appears to be 22.33%, which is much lower than that of the pure cellulose paper. This may happen because of the amorphous nature and polymer chain mobility of PVDF introduced into the cellulose matrix. The CI values for HY05, HY10, HY15, HY20 and HY25 are 26.66%, 29.86%, 15.63%, 23.19% and 22.59%,

respectively. This reduction in crystallinity as compared to CP indicates a considerable degree of lattice disorder. The most pronounced reduction is observed at HY15 (CI = 15.63%), which suggests maximal disruption of the native cellulose crystalline domains.

This disordering effect arises from the hydrolysis and condensation of the zirconia precursor within the cellulosic network. The acetylacetone stabilized chelate structure, undergoes controlled hydrolysis during the fabrication process to form Zr–OH and Zr–O–Zr bonds. These species intercalate between cellulose micro and nanofibrils, disrupting their hydrogen-bonding network and reducing cellulose crystallinity. Here, the absence of sharp crystalline zirconia peaks confirms that the chelation process suppresses uncontrolled crystallization, ensuring that zirconia remains in an amorphous or nanocrystalline state that is intimately dispersed within the cellulose matrix.

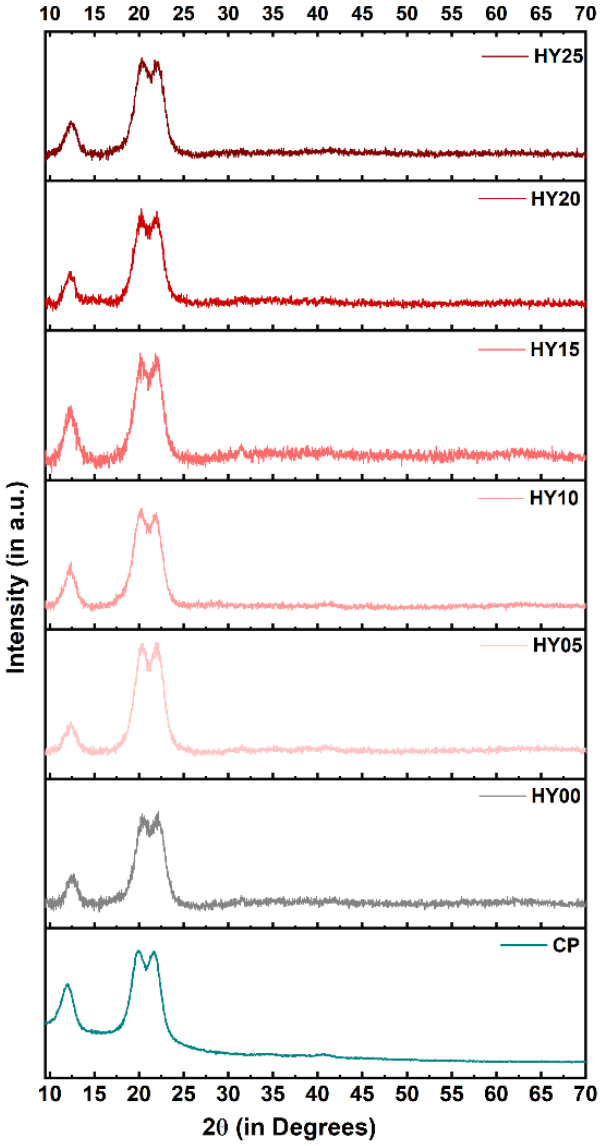

Figure 6.3 *X-ray Diffraction (XRD) patterns of all the developed paper separators (HY00, HY05, HY10, HY15, HY20 and HY25), along with pristine cellulose paper (CP)*

Interestingly, the CI values do not decrease monotonically with increasing zirconia content but instead show a minimum at HY15 before slightly recovering at higher loadings (HY20 and HY25). This non-linear trend suggests that moderate loadings allow maximum penetration and disruption of cellulose domains, while at higher loadings the zirconia network itself partially densifies and organizes, giving an apparent increase in order. Also, the hydroxyl moieties of the chelated precursor can create new

hydrogen bonds with the cellulose structure to give it a more ordered network at higher concentrations. Thus, the XRD data collectively indicate a strong interaction between cellulose crystallinity and the formation of zirconia nanodomains, which further help in enhancing ionic conductivity and electrochemical performance of the separators in battery environment.

The FTIR spectra in ***Figure 6.4*** further corroborate the XRD findings and provide substantial evidence of chemical interactions occurring within the composite separators. Several key regions of the spectra reveal systematic changes with increasing zirconia precursor content. Firstly, the broad peak at 3600–3300 cm^{-1} corresponding to O–H stretching appears for all the cellulose separators including CP. In modified separators, this band broadens further and intensifies progressively with increasing zirconia content. This enhancement is attributed not only to cellulose hydroxyl groups but also to newly generated Zr–OH groups formed during precursor hydrolysis. The peak at 3000–2850 cm^{-1} can be attributed to C–H stretching vibration of the aliphatic C–H bands associated with cellulose, PVDF, and residual alkoxide ligands. This band show a gradual reduction in intensity, indicating the progressive consumption of organic alkoxide groups (–OR) as they are converted into Zr–OH or Zr–O–Zr bonds. The reduced intensity also points to decreased organic ligand content within the network, corroborating the enhanced inorganic character of the modified paper. A distinct feature appears in this range of 1730–1650 cm^{-1}, which contributes to C=O stretching of the acetylacetone (acac) chelating ligand along with water bending. The persistence of this band across all modified samples confirms that chelation remains intact even after hydrolysis. This stabilization is critical, as it prevents uncontrolled growth and aggregation of zirconia particles, thereby ensuring uniform dispersion across the cellulose/PVDF network. Intensity is decreasing gradually for the peak at 1375–1350 cm^{-1}, which generally comes for CH_2 bending and ligand methyls. This region, linked to

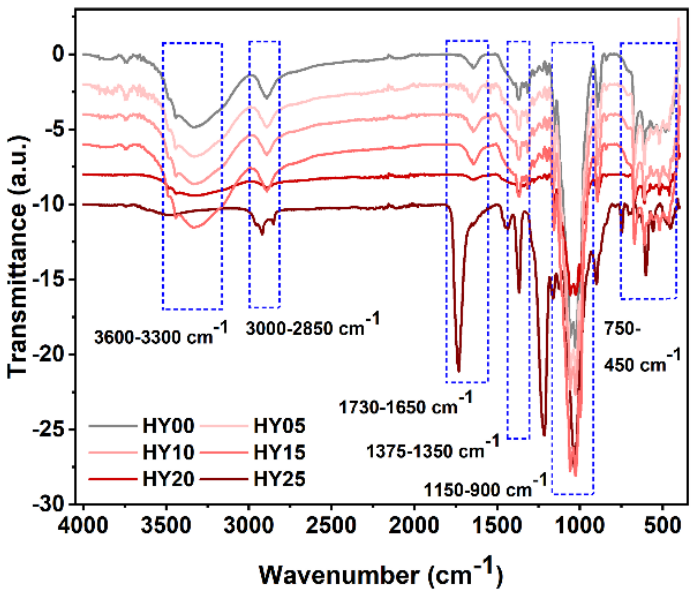

Figure 6.4 *Fourier Transformed Infrared (FTIR) Spectra in ATR mode for HY00, HY05, HY10, HY15, HY20, HY25 and CP*

δCH_2 vibrations in cellulose and residual ligand groups, shows a moderate decrease with increasing zirconia content. The loss of intensity suggests the consumption of alkoxide groups and reduced contribution of organic ligands. The cellulose-associated peaks remain visible, confirming the structural backbone of cellulose is preserved even though its crystallinity decreases. The signals at 1150–900 cm^{-1} correspond to C–O–C stretching, glycosidic linkages, and Zr–O–C stretching frequencies. This region is dominated by cellulose glycosidic vibrations (~1050–1030 cm^{-1}) in the pristine paper. But, in zirconia-containing samples, these features broaden and shift, indicating the overlap of cellulose bands with newly formed Zr–O–C and Zr–O vibrations. The evolution of this region reflects the chemical transformation of zirconia precursors from Zr–OR to Zr–OH and Zr–O–Zr. Zr–O–Zr lattice vibrations reflect in the region of 750–450 cm^{-1}. A clear set of bands emerges in this region with increasing precursor concentration, corresponding to Zr–O–Zr stretching vibrations of condensed zirconia nanodomains. These features become stronger and better defined at higher loadings, confirming the successful in-situ formation of zirconia oxide networks within the cellulose matrix.

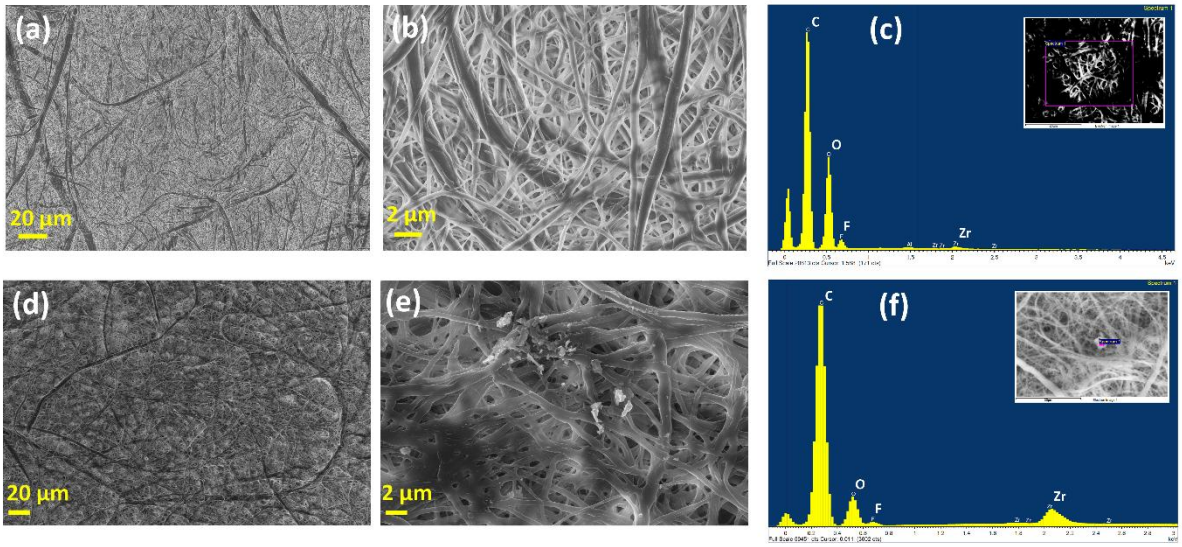

Figure 6.5 *FESEM micrographs (a)-(b) HY05 and (d)-(e) HY25; EDX profiles of (c) HY05 and (f) HY25, respectively*

Figure 6.5 shows the FESEM surface morphologies and EDX elemental profiles of HY05 and HY25 separators. Panels (a) and (b) correspond to HY05, revealing a relatively open and uniform fibrous cellulose network coated with thin PVDF layers. The fibers remain well-separated, and the surface appears smooth with minimal pore blocking. This structure facilitates effective electrolyte infiltration while retaining mechanical integrity. The

corresponding EDX profile in ***Figure 6.5(c)*** confirms the presence of dominant carbon and oxygen peaks from cellulose and PVDF, along with fluorine from PVDF sizing. A discernible but low-intensity zirconium peak indicates that at 0.5 wt% zirconia precursor loading (HY05), Zr species are present but sparsely distributed within the matrix. ***Figures 6.5(d)*** and ***(e)*** show the morphology of HY25. Compared to HY05, the higher zirconia content produces a denser and rougher surface, with visible clusters and particulate deposits embedded within the cellulose-PVDF network. These features suggest partial agglomeration or localized accumulation of zirconia domains at high loadings, which may block pores and reduce homogeneity. The EDX profile in ***Figure 6.5(f)*** exhibits stronger zirconium peaks relative to HY05, confirming higher Zr incorporation. The increase in Zr signal, together with intense fluorine peaks, verifies that zirconia is successfully impregnated into the PVDF-sized paper but with a tendency to form concentrated regions at high precursor concentrations.

Overall, the FESEM and EDX analyses demonstrate that low zirconia loadings (HY05) ensure homogeneous dispersion of chelated ZrO_2 within the fibrous matrix, while higher loadings (HY25) cause surface densification and partial aggregation. This microstructural evolution explains the observed performance trends: moderate loading (e.g., HY15) maximizes wettability, electrolyte uptake, and conductivity due to well-dispersed solvophilic Zr–OH sites, whereas excessive loading reduces structural uniformity and slightly compromises ionic transport.

6.3.3 Porosity, Wettability and Mechanical Properties of the Separators

Figure 6.6 presents the comparative wettability, permeability, electrolyte uptake, flexibility, and mechanical performance of the pristine cellulose paper (CP), PVDF-sized separator (HY00), and chelated ZrO_2-impregnated separators (HY05-HY25). Contact angle is the angle of contact formed at the interface of a substrate in contact with a liquid drop. Here, the experiment is done by putting a drop of liquid electrolyte on the paper or paper separator substrates, as mentioned in ***Chapter 2***. Pure cellulose shows high affinity for most of the solvents since cellulose can absorb liquids and get swelled very easily. This phenomenon is reflected in the contact angle value of CP that comes to be nearly 0° after instant soaking of the liquid electrolyte. However, PVDF-sized HY00 separator shows contact angle of nearly 22.9°, as can be seen in ***Figure 6.6(a)***. The PVDF sizing deposits a thin polar fluoropolymer layer that reduces immediate wetting and increases the contact angle. This observation can also be

corroborated from its electrolyte uptake of 266.98%, which is lower than that of CP (285.29 %).

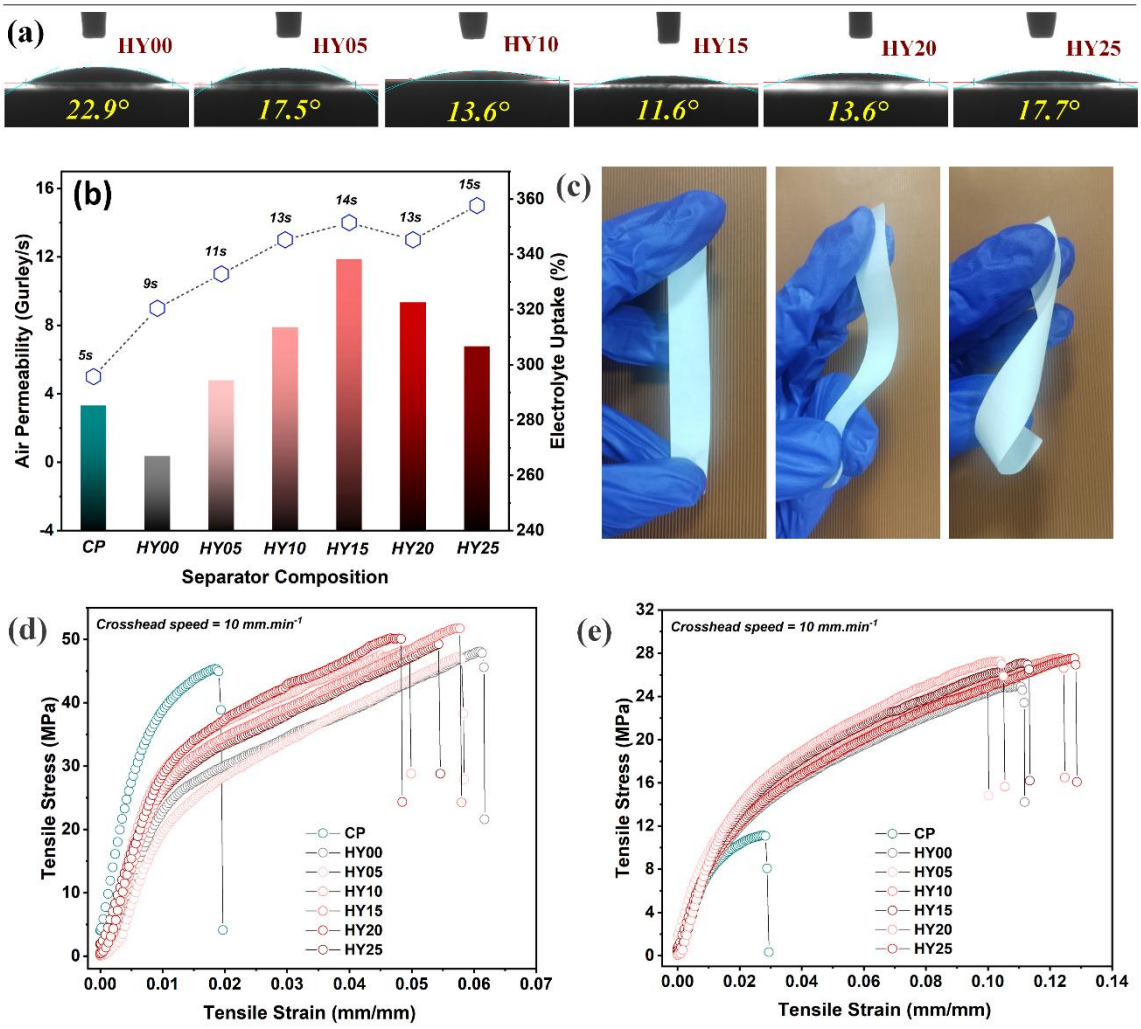

Figure 6.6 *(a) Contact angle in LIB liquid electrolyte (1M $LiPF_6$ in EC:DMC (1:2)), (b) Air permeability in terms of Gurley value and electrolyte uptake percentage, (c) flexibility of the developed paper separators demonstrated via stretching and bending activities, (d) demonstration of separator flexibility; Tensile stress vs tensile strain plots at (e) machine direction (MD) and (f) transverse direction (TD) for CP, HY00, HY05, HY10, HY15, HY20 and HY25, respectively*

The electrolyte uptake percentage along with air permeability data for all the paper separators are depicted in ***Figure 6.6(b)***. Coating the pristine paper with PVDF block the large pore spaces of the paper substrate partially and decrease the wettability, which is why the contact angle values for all the separators are higher than that of CP[15]. Addition of chelated Zr precursor progressively reduces the contact angle from HY05 to HY10 to HY15. The minimum contact angle occurs at HY15, which is 11.6°. This behavior is consistent with hydrolysis of chelated

precursor producing Zr-OH surface groups that are strongly polar and solvophilic in nature. Nonetheless, the contact angle increases again at slightly higher loadings, with the values of 13.6° and 17.7° for HY20 and HY25, respectively. This rise likely arises either from surface reorganization effect of PVDF or residual organics or from partial densification and organization of zirconia nanodomains. The Gurley value increases moderately with PVDF and zirconia impregnation, indicating slight pore blockage, but remains within a practical range for separator operation. Electrolyte uptake increases from 266.98% for HY00 to a maximum of 338.23% for HY15, reflecting the balance of porosity disruption and solvophilic Lewis acid/base surface sites. The slight decrease at HY20-HY25 indicates probable reduced solvent accessibility due to densification.

The digital images presented in ***Figure 6.6(c)*** demonstrate the excellent flexibility of the composite separators, which can be bent and folded without cracking or delamination, underscoring their suitability for practical battery assembly.

Figures 6.6(d) and ***(e)*** show the tensile stress-strain behavior in the machine direction (MD) and transverse direction (TD), respectively. CP exhibits anisotropic mechanical performance with higher MD (45.35 MPa) but poor TD strength (11.13 MPa). PVDF sizing and zirconia impregnation markedly reinforce the TD, nearly tripling the strength relative to CP. The maximum MD strength (51.73 MPa) and balanced TD strength (27.56 MPa) are obtained for HY15, confirming that moderate zirconia loading yields optimal mechanical reinforcement through strong filler-fiber-polymer interactions. Beyond HY15, mechanical gains plateau or slightly decline, suggesting that excessive zirconia might disrupt inter-fiber cohesion. Overall, HY15 demonstrates the most favorable combination of low contact angle, high electrolyte uptake, and superior mechanical strength, highlighting the synergistic role of chelated ZrO_2 nanodomains in tailoring both physicochemical and mechanical properties of cellulose-based paper separators.

6.3.4 Ionic Conductivity and Electrochemical Potential Window

Figure 6.7 represents the Nyquist plots of symmetric SS/Separator/SS cells assembled with pristine cellulose paper (CP), PVDF-sized separator (HY00), and the chelated-ZrO_2 impregnated separators (HY05-HY25). The equivalent circuit used for fitting, consisting of bulk resistance (R_b) and constant phase elements for electrode/electrolyte interfaces (CPE_w, CPE_b), is shown in the inset.

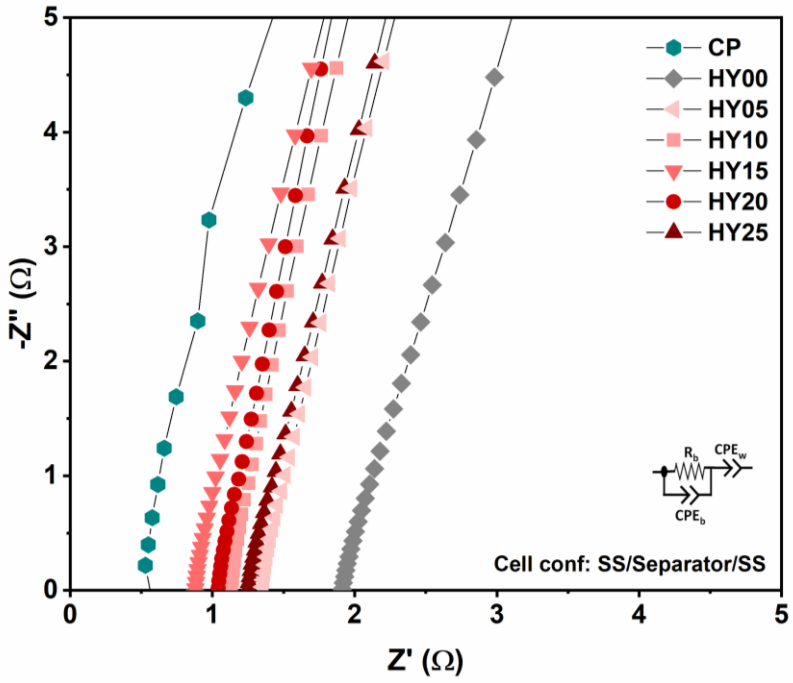

Figure 6.7 *Nyquist plots for all the developed paper separators along with CP*

The pristine cellulose separator (CP) exhibits the lowest bulk resistance (≈0.57 Ω), attributable to its highly porous and hydrophilic structure, which allows rapid electrolyte uptake and ionic conduction[15]. However, PVDF sizing (HY00) significantly increases the bulk resistance (≈1.92 Ω) due to pore blocking and the reduced wettability introduced by the fluoropolymer layer. Upon impregnation with chelated ZrO_2, a progressive decrease in bulk resistance is observed from HY05 (≈1.36 Ω) to HY15 (≈0.87 Ω), highlighting the beneficial role of polar Zr–OH and under-coordinated Zr^{4+} sites in enhancing effective Li-salt dissociation and facilitating Li^+ transport. HY15 exhibits the lowest resistance and highest ionic conductivity (1.30×10^{-3} $S.cm^{-1}$) among the modified samples, correlating directly with its highest electrolyte uptake (338.23%), minimal contact angle (11.6°), and lowest cellulose crystallinity index (15.63%). These synergistic structural and chemical modifications establish continuous ion transport pathways within the paper matrix.

At higher zirconia loadings (HY20 and HY25), the resistance increases slightly (≈1.04-1.26 Ω). This is consistent with FESEM observations (***Figure 6.5***), where excessive zirconia incorporation leads to surface densification and partial aggregation, which impede ion transport despite the presence of Lewis acid sites.

Overall, the Nyquist plots clearly establish that moderate zirconia loading (HY15) yields the most favorable ionic transport, balancing electrolyte affinity, structural disruption, and mechanical stability. This electrochemical evidence supports the conclusion that controlled incorporation of chelated ZrO_2 precursors optimizes separator performance, while excessive loading diminishes the benefits due to microstructural densification. The various properties of the developed paper separators as well those of commercial cellulose paper (CP) have been summarized in ***Table 6.2.***

Figure 6.8 illustrates the electrochemical stability window of the PVDF-sized separator (HY00) and the optimized zirconia-loaded separator (HY15), evaluated using linear sweep voltammetry (LSV) in an S/Separator/Li configuration. Both separators exhibit negligible current response up to ~5.5 V, indicating that they are electrochemically stable within the conventional operating window of lithium-ion batteries and also beyond that supporting high voltage cathode chemistries. Beyond this potential, a gradual rise in current is observed due to electrolyte decomposition. Notably, HY15 demonstrates a slightly delayed onset of decomposition and maintains a lower and more stable current than HY00 in the intermediate voltage range, suggesting improved oxidative stability. The enhanced stability of HY15 compared to HY00 can be attributed to the presence of polar Zr–OH and under-coordinated Zr^{4+} sites, which promote stronger Lewis acid–base interactions with electrolyte species. These interactions facilitate controlled salt dissociation and help suppress premature decomposition, thereby extending the safe operational voltage window. This improved electrochemical robustness complements the superior wettability, electrolyte uptake, and ionic conductivity previously demonstrated for HY15, underscoring its suitability as a high-performance separator material for advanced lithium-ion batteries.

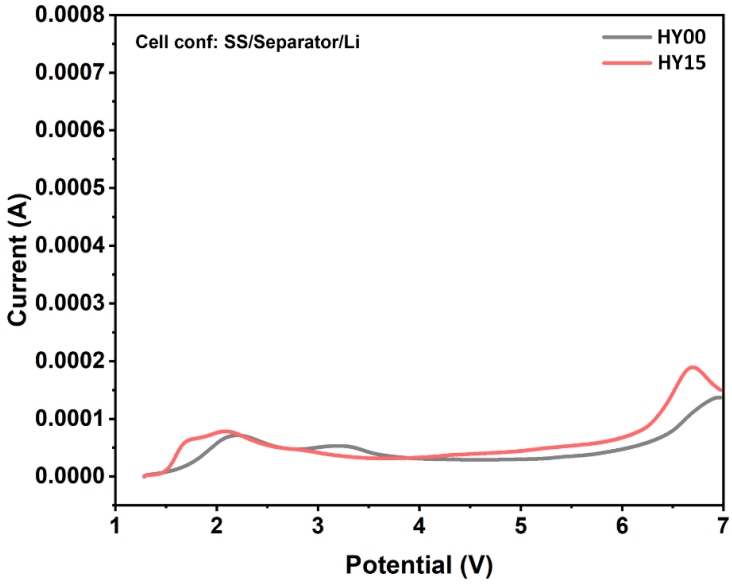

Figure 6.8 *Linear Sweep Voltammetry plots for HY00 and HY15, for determining electrochemical potential window*

Table 6.2 *Comparison of different properties of the chelated zirconia embedded paper separators with those of commercial cellulose paper*

Separator type / ***Property***	**CP**	**HY00**	**HY05**	**HY10**	**HY15**	**HY20**	**HY25**
Crystallinity Index (%)	58.29	22.33	26.66	29.86	15.63	23.19	22.59
Contact Angle	~0°	22.9°	17.5°	13.6°	11.6°	13.6°	17.7°
Air Permeability (Gurley/s)	5	9	11	13	14	13	15
Electrolyte Uptake (%)	285.29	266.98	294.43	313.68	338.23	322.59	306.71
Tensile Strength (MPa) MD/TD	45.35/ 11.13	46.16/ 24.97	47.18/ 25.97	48.28/ 27.28	51.73/ 27.56	50.18/ 27.53	49.26/ 27.09
Bulk Resistance/Ionic Conductivity	0.57 Ω/ 1.98×10^{-3} $S.cm^{-1}$	1.92 Ω/ 0.58×10^{-3} $S.cm^{-1}$	1.36 Ω/ 0.83×10^{-3} $S.cm^{-1}$	1.13 Ω/ 1.00×10^{-3} $S.cm^{-1}$	0.87 Ω/ 1.30×10^{-3} $S.cm^{-1}$	1.04 Ω/ 1.08×10^{-3} $S.cm^{-1}$	1.26 Ω/ 0.89×10^{-3} $S.cm^{-1}$

6.3.4 Electrochemical Performance

Figure 6.9 compares the electrochemical cycling stability and rate performance of PVDF-sized separator (HY00) and zirconia-impregnated separator (HY15) in MCMB/LFP full-cell configuration. ***Figure 6.9(a)*** shows the long-term cycling at a constant current density of 0.2 $mA\cdot cm^{-2}$. The HY00-based cell exhibits a rapid decline in discharge capacity from ~100 $mAh\cdot g^{-1}$ to below 40 $mAh\cdot g^{-1}$ within 300 cycles, reflecting poor electrolyte affinity and high interfacial resistance. In contrast, the HY15-based cell retains significantly higher discharge capacities (~60 $mAh\cdot g^{-1}$ after 400 cycles), indicating enhanced ionic conductivity, better electrolyte uptake, and a more stable electrode–separator interface. This pronounced improvement directly correlates with the optimized wettability, structural disruption, and Lewis acid-base interactions offered by the chelated zirconia domains.

The rate performance of the HY00-based cell is shown in ***Figure 6.9(b)*** across a wide range of current densities. At low rates (0.1-0.4 $mA\cdot cm^{-2}$), the cell delivers moderate capacity, but at higher current densities (>1.0 $mA\cdot cm^{-2}$), the capacity drops sharply and becomes negligible. This highlights the sluggish Li^{+} transport across the PVDF-sized separator with limited solvophilic surface functionality. On the other hand, the rate performance of the HY15-based

full cell under identical conditions is significantly better than HY00, as can be observed in ***Figure 6.9(c)***. Even at a high current density of 2.2 mA.cm^{-2}, the cell continues to deliver appreciable capacity and does not touch 20% depth-of-discharge threshold. The superior rate capability of HY15 validates the role of Zr–OH/Zr^{4+} surface sites in enhancing Li^{+} transport pathways and mitigating polarization under high current loads. Taken together, the galvanostatic results confirm that HY15 enables both long-term cycling stability and high-rate performance, outperforming the baseline PVDF-sized separator. The synergistic improvements arise from (i) increased electrolyte wettability and uptake, (ii) enhanced ionic conductivity via Lewis acid-base interaction induced salt dissociation, and (iii) reinforced mechanical stability that prevents structural collapse during repeated cycling.

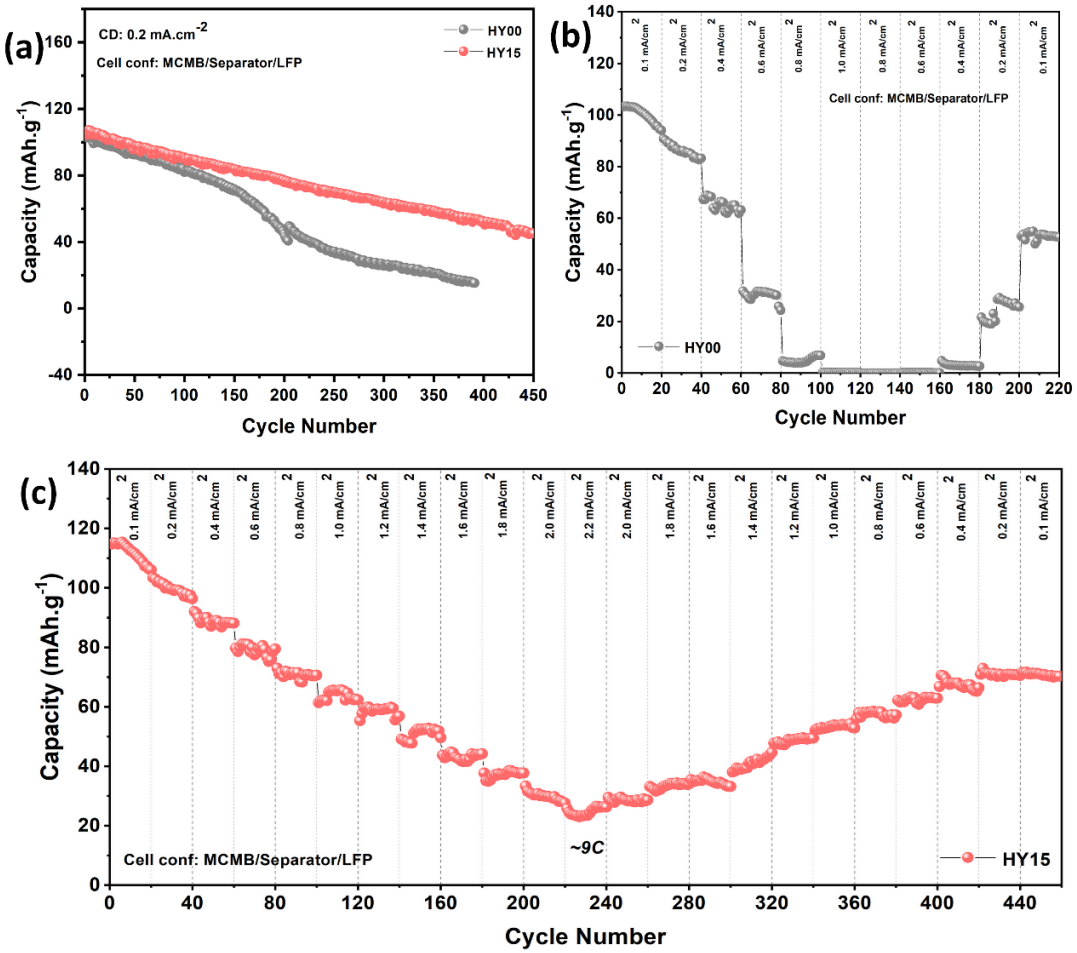

Figure 6.9 *Galvanostatic charge-discharge cycling of HY00 and HY15 in MCMB/LFP full cell configuration; (a) long term cycling at 0.2 mA.cm^{-2}, (b) cycling at varying current densities for HY00 and (c) cycling at varying current densities for HY15*

Table 6.3 *Literature review of Lewis acid-base interaction-driven performance modulation of electrochemical systems by various strategies*

Sl. No.	Material / Strategy	Mechanism	Key Performance	Ref.
1	Lewis-acid coordinated PEO-based electrolyte (molecular Lewis-acid centers in polymer)	Lewis-acid coordination to polymer backbone improved salt dissociation and oxidation stability up to high voltage	Demonstrated 4.8 V oxidative stability; device energy >580 $Wh.kg^{-1}$; stable cycling ~300 cycles in high-voltage cells	An et al.[4]
2	ST@Al_2O_3 (Ti-doped SiO_2@Al_2O_3) yolk-shell particles layered on PE separator - engineered Lewis acid sites on separator surface	Lewis acid sites tune Li plating/stripping and electrolyte interactions at separator interface	Ionic conductivity 5.55×10^{-3} $S\cdot cm^{-1}$; Li^+ transference $t_+ = 0.62$; Li/Li symmetric stable > 400 h at 1 $mA\cdot cm^{-2}$; improved cycling/rate	Zhou et al.[5]
3	Pentacoordinated Al^{3+}-enriched Al_2O_3 — demonstration that changing surface coordination creates abundant Lewis acidic sites	Surface spectroscopy (^{27}Al MAS-NMR) confirms high pentacoordination; correlated to high Lewis acidity and unusual reactivity (H_2 activation, catalysis)	Structural & surface-chemistry characterization (27Al MAS-NMR peaks at ~64, 33, 6 ppm indicating tetra/penta/octa coordination); proof that coordination tuning → new surface Lewis sites	Wu et al.[6]
4	2D ZSM-5 nanosheets as Lewis-acidic inorganic filler in PEO CPEs - unsaturated Si/Al–OH sites act as Lewis centers	Strong Lewis sites promoted salt dissociation and improved ion transport	$\sigma = 1.34\times10^{-3}$ $S\cdot cm^{-1}$ (at 60°C); $t_+ = 0.37$; electrochemical window 4.8 V; solid-state LFP/Li cells: initial capacity 152.3 $mAh\cdot g^{-1}$ with 91.4% retention after 200 cycles	Hu et al.[7]
5	Zirconium isoproxide chelated with acac is embedded in cellulose-based paper separator matrix	Co-ordinately unsaturated Zr^{4+} interacts with the anions of Li-salt, promoting effective salt dissociation and separator performance	$\sigma = 1.30\times10^{-3}$ $S.cm^{-1}$, extended potential window up to 5.5 V; long term cycling up to 450 cycles and high rate performance (~9C)	***This work***

6.4 Conclusion

This chapter has demonstrated the effectiveness of chelated zirconia precursors in tailoring the structural and electrochemical performance of cellulose-based paper separators for lithium-ion batteries. By employing acetylacetone-assisted chelation of zirconium isopropoxide followed by controlled hydrolysis, zirconia was introduced in a highly dispersed form with abundant coordinatively unsaturated Zr^{4+} and Zr–OH surface sites. These functional groups not only suppressed uncontrolled agglomeration but also provided Lewis acid–base centers capable of interacting strongly with electrolyte components. Such interactions promoted enhanced salt dissociation, improved electrolyte affinity, and facilitated continuous ionic transport pathways across the separator. Systematic evaluation revealed that moderate zirconia incorporation (HY15) delivered the most balanced performance. At this composition, the separator exhibited optimal structural disruption of cellulose crystallinity, superior wettability, and strong mechanical reinforcement. These properties collectively translated into reduced bulk resistance, enhanced ionic conductivity, and improved electrochemical stability. The galvanostatic cycling and rate capability results further confirmed that HY15 enabled stable long-term cycling and supported high current densities, in contrast to the baseline PVDF-sized separator.

Importantly, the findings align with recent literature on the role of Lewis acid–base interactions in improving ion transport and interfacial stability. The work establishes that rational design of ceramic precursors and their integration into sustainable cellulose substrates can yield separators that combine mechanical robustness, high electrolyte uptake, and electrochemical reliability. Thus, chelated ZrO_2 nanodomains represent a viable strategy for advancing paper-based separators toward high-performance and safe energy storage applications.

References

1 T. C. Turossi, H. L. O. Júnior, F. M. Monticeli, O. T. Dias and A. J. Zattera, *Polymers (Basel)*, 2025, **17**, 456.

2 P. Arora and Z. (John) Zhang, *Chem Rev*, 2004, **104**, 4419–4462.

3 E. Lizundia, C. M. Costa, R. Alves and S. Lanceros-Méndez, *Carbohydrate Polymer Technologies and Applications*, 2020, **1**, 100001.

4 H. An, M. Li, Q. Liu, Y. Song, J. Liu, Z. Yu, X. Liu, B. Deng and J. Wang, *Nat Commun*, 2024, **15**, 9150.

5 T. Zhou, W. Tang, J. Lv, Y. Deng, Q. Liu, L. Zhang and R. Liu, *Small*, DOI:10.1002/smll.202303924.

6 Q. Wu, R. Qin, M. Zhu, H. Shen, S. Yu, Y. Zhong, G. Fu, X. Yi and N. Zheng, *Chem Sci*, 2024, **15**, 3140–3147.

7 X. Hu, J. Liu and B. Zhang, *Polymers (Basel)*, 2024, **16**, 1604.

8 G. De, A. Chatterjee and D. Ganguli, *J Mater Sci Lett*, 1990, **9**, 845–846.

9 R. C. Mehrotra, *J Non Cryst Solids*, 1988, **100**, 1–15.

10 M. T. Colomer, *J Solgel Sci Technol*, 2013, **67**, 135–144.

11 U. K. H. Bangi, R. S. Gafari, R. C. Pawar, H.-N.-R. Jung and H.-H. Park, *ES Materials & Manufacturing*, DOI:10.30919/esmm5f937.

12 I. Das and G. De, *Sci Rep*, 2015, **5**, 18503.

13 K. S. Salem, N. K. Kasera, Md. A. Rahman, H. Jameel, Y. Habibi, S. J. Eichhorn, A. D. French, L. Pal and L. A. Lucia, *Chem Soc Rev*, 2023, **52**, 6417–6446.

14 S. Park, J. O. Baker, M. E. Himmel, P. A. Parilla and D. K. Johnson, *Biotechnol Biofuels*, 2010, **3**, 10.

15 M. Das, P. S. Das, N. C. Pramanik, R. N. Basu and M. Wasim Raja, *ACS Omega*, DOI:10.1021/acsomega.3c02859.

Chapter 7

Montmorillonite Clay Impregnated Sustainable Paper Separator

Highlights

- Natural cellulose paper is combined with montmorillonite clay to design sustainable battery separators
- Simple wet-coating fabrication for integrating clay platelets into paper matrix
- Detailed structural, mechanical, electrochemical, and thermal characterization of the developed separators
- Improved thermal stability, cycling performance, mechanical integrity

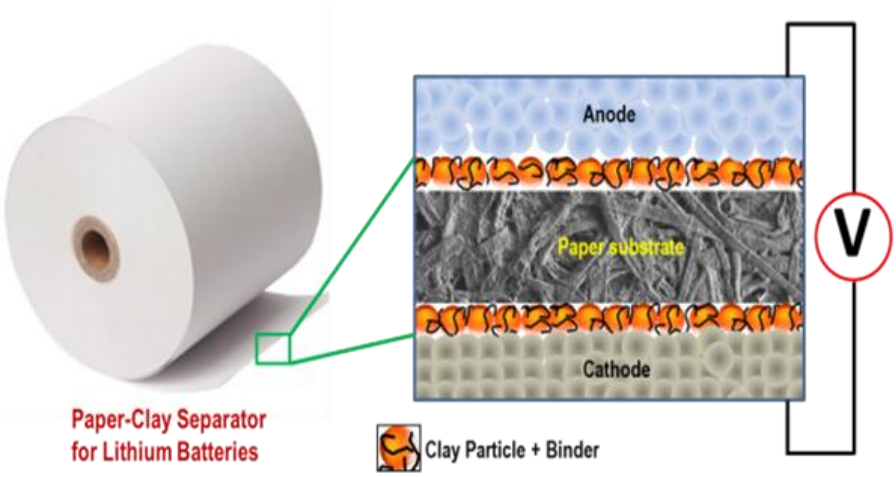

Figure 7.0 *A graphical demonstration of paper-clay separator*

This chapter reports the development of montmorillonite (MMT) impregnated paper–clay separators as cost-effective and sustainable alternatives to commercial polyolefin membranes in lithium-ion batteries. Structural and morphological studies confirmed uniform incorporation of clay platelets into cellulose networks, tuning porosity and enhancing electrolyte wettability. Mechanical tests revealed improved flexibility and isotropy, while electrochemical analysis demonstrated wide stability windows (>5 V) and excellent cycling with high coulombic efficiency. Thermal tests showed strong flame retardancy and self-extinguishing behavior, with the M15 composition retaining electrochemical functionality after flame exposure. These findings establish paper–clay separators as safe, sustainable, and high-performance candidates for next-generation batteries.

7.1. Background and Overview

The use of clay as raw materials by mankind is almost a 4000 year old story. These versatile minerals are now being used in many modern industrial applications such as paper, paint, petroleum, ceramic, cement, adhesive, asphalt, and health-care industry due to their wide abundance, lower cost and sustainability. Out of its many varieties, Montmorillonite (MMT) is widely being researched due to its high ion exchange capability, layered structure, large specific surface area and excellent adsorption properties. MMT is a layered structure sandwiching an alumina octahedral sheet by two silica tetrahedral sheets. The in-plane strong chemical bonds and weak van der Waals and electrostatic forces between the sandwiched layers provide MMT a strong ability to form freestanding exfoliated layers.

Recently, MMT is being studied extensively in energy storage devices mainly in metal ion batteries (MIBs) or lithium metal batteries (LMBs) as an additive material in electrolyte or in composite separator membrane. In a recent past, lithiophilic montmorillonite has been used as an additive in the ether-based electrolyte to regulate the lithium-ion concentration on the anode surface facilitating the uniform lithium deposition[1]. Para et al. showed a modification of commercial separator using montmorillonite/polyaniline composites resulting in an increase in ionic conductivity compared to the untreated one[2]. A separator membrane developed by Li et.al., using organically modified montmorillonite (OMMT) reinforced with polyimide (PI) demonstrated a significant enhancement in mechanical strength, superior electrolyte wettability and high ionic conductivity along with higher thermal stability[3]. Dong et al., successfully utilized MMT coated separator which showed minimization of the shuttle effect by preventing the diffusion of the polysulfide in Li-S batteries[4]. Poly(vinylidene fluoride) (PVDF)-MMT based separator membrane prepared by Pereira et al. also reported stable electrochemical performance compared to commercial PP membrane[5]. All these reports reveal that the presence of MMT has thus significant effect in battery performance due to its versatile capability of ionic exchange, particularly with Li-ions during electrochemical cycling.

In this chapter, we have attempted to fabricate MMT impregnated Paper-Clay separator for its application in Lithium-ion Batteries (LIBs). The combination of both low cost paper and cheap clay material for making sustainable Paper-Clay separator using wet-coating method for LIBs was found to be an interesting study. The Paper-Clay separator fabrication process carried out both in aqueous using an in-house designed double decker fabricating machine. The effect of

impregnation of bare MMT in different mass ratio in Paper-Clay separator was examined and the electrochemical performance of the separator evaluated using full cell configuration. Finally, a detail comparison of performances of developed Paper-Clay separator with that of commercial membrane was also presented here.

7.2 Experimental Details

7.2.1 Preparation of MMT Clay

The purification of raw clay was done via the following stages: i) removal of non- clay fraction through wet-sieving ii) destruction of organics and carbonates iii) separation of submicron fraction be repeated gravity settling and finally iv) ion exchange to form Na+ -MMT. Raw clay (50g) was dispersed in 5 Litre deionised water under stirring for 24 hours. The pH of the dispersion was decreased to 4.5 by adding 0.01N HCl to decompose carbonates. Then the dispersion was treated with H2O2 for decomposing the organics. Excess H2O2 was decomposed by heating. The dispersion was then was sieved through 150 Micron sieve to remove non-clay impurities. The pH was then adjusted to 6.5 with 0.01N NaOH. Then 0.02N Sodium hexametaphosphate solution was to added to it under stirring to disperse the clay fraction. The suspension was allowed to settle under gravity. The settling velocity of the particles was calculated as per the Stokes law

$$v = \frac{\rho - \rho_o}{18\eta} . g . d^2 \qquad (7.1)$$

Where v is the settling velocity of particle of diameter d and density ρ under gravitational acceleration g in a dispersion medium of density ρ_o and viscosity η[6].

Accordingly, the depth of settling of > 1 μm particles were calculated and the <1 μm particles were collected from the supernatant above 20 cm height after 53 hours of settling. This clay fraction was passed through ion-exhange resin Amberlite 120H in Na^+ form to generate Na^+ MMT particles.

7.2.2 Fabrication of Paper Separator

The purified Montmorillonite clay is dispersed in 7.0 w/v% SBR aqueous solution, in varying amounts, by stirring for 12h. The PVDF-coated paper substrate is again dip-coated with the SBR-MMT slurry in double-decker separator fabricator unit, as described in ***Chapter 2***. The

fabricated separators are dried, compacted and stored carefully for further experiments. The composition and codes for the developed separators have been provided in ***Table 1***.

Table 1 *Codes and compositions of the developed paper-clay separators*

Initial coating on paper substrate	Final coating on the paper	Code
3.5 w/v% PVDF in NMP	7.0 w/v% SBR + 0.5 w/v% MMT	M05
3.5 w/v% PVDF in NMP	7.0 w/v% SBR + 1.0 w/v% MMT	M10
3.5 w/v% PVDF in NMP	7.0 w/v% SBR + 1.5 w/v% MMT	M15
3.5 w/v% PVDF in NMP	7.0 w/v% SBR + 2.0 w/v% MMT	M20

7.3. Results & Discussions

7.3.1. Structural and Microstructural Features

7.3.1.1 MMT Clay

The chemical analysis of the purified clay shows presence of SiO_2, Al_2O_3 as major components, alongside fewer amounts of MgO, Na_2O, K_2O, TiO_2 and CaO[7]. The cation exchange capacity of the MMT was 64 $cmol.kg^{-1}$.

Figure 7.1 represents the structural and microstructural features of the purified sodium montmorillonite (Na-MMT). The XRD pattern in ***Figure 7.1(a)*** exhibits a sharp reflection at $2\theta \approx 5.2°$ corresponding to a basal spacing of ~1.7 nm, which is characteristic of montmorillonite (JCPDS 00-012-0219). The presence of this well-defined (001) reflection confirms the layered silicate structure, while the absence of significant impurity peaks demonstrates the high purity of the clay fraction obtained after ion-exchange treatment. A minor reflection around 12.4° indicates traces of kaolinite (JCPDS 00-014-0164), but its relative intensity suggests negligible contribution.

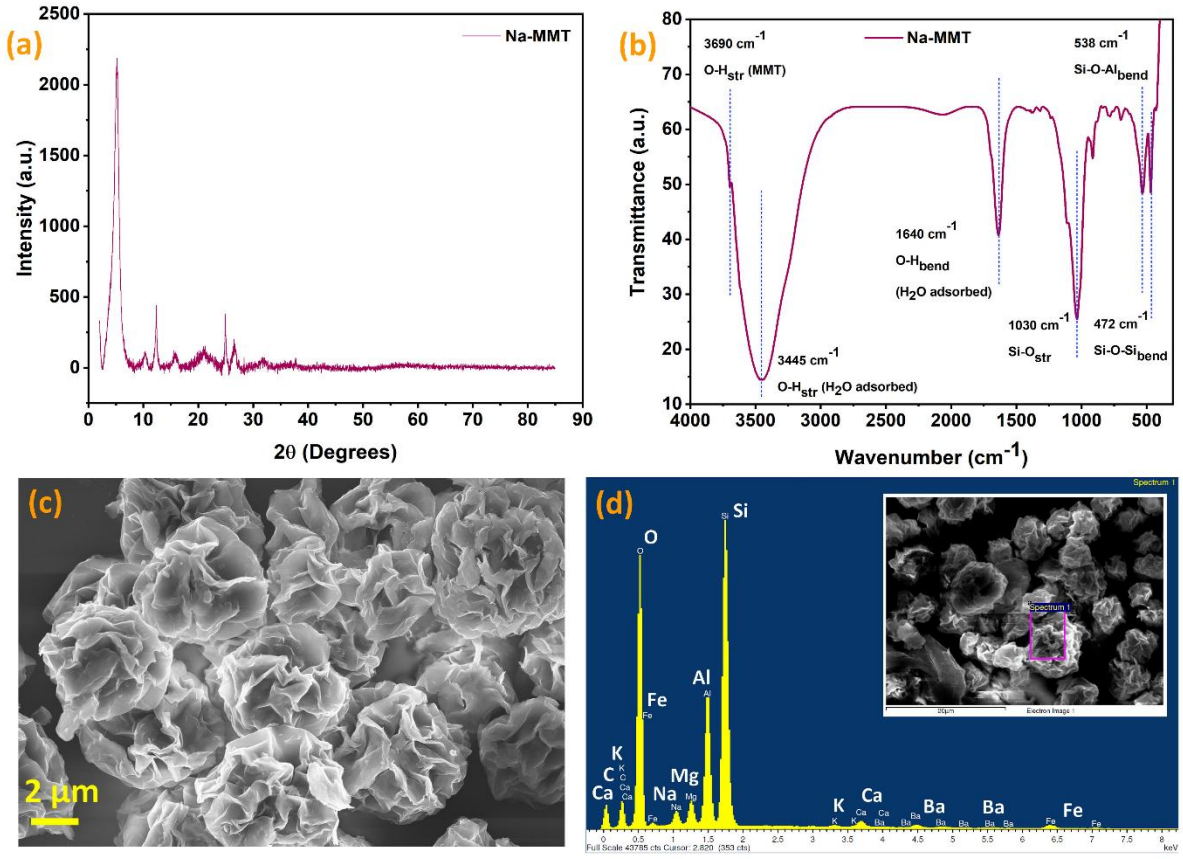

Figure 7.1 *Structural and microstructural features of Na-MMT powder; (a) X-ray diffraction pattern, (b) FTIR spectrum, (c) FESEM image and (d) EDX spectrum*

The FTIR spectrum of Na-MMT, demonstrated in Figure 7.1(b) further validates the structural integrity of the clay. The broad absorption band at 3445 cm^{-1} corresponds to O-H stretching of adsorbed water molecules, since the clay materials have an extremely hydrophilic nature. The shoulder at 3690 cm^{-1} arises from structural hydroxyl groups associated with octahedral cations (Al-OH). The bending vibration of interlayer water is observed at 1640 cm^{-1}. A strong peak at 1030 cm^{-1} corresponds to Si-O stretching vibration of the tetrahedral sheet, whereas the bands at 538 cm^{-1} and 472 cm^{-1} are attributed to Si-O-Al and Si-O-Si bending vibrations, respectively. These features are consistent with reported spectra of montmorillonite and confirm the retention of layered aluminosilicate framework[8].

The surface morphology, examined by FESEM, reveals typical aggregated platelet-like structures with curled, rose-petal-like edges, suggesting exfoliated and stacked lamellae of MMT, as can be observed in Figure 7.1(c). Such morphology provides a large accessible surface area and hierarchical porosity, beneficial for enhancing electrolyte uptake when incorporated into paper matrix. Elemental composition analyzed by EDX in Figure 7.1(d) confirms the presence of major constituents such as Si, Al, O, Mg, Fe, Na, K, and Ca, in agreement with the expected chemical composition of montmorillonite. The dominant Si and Al peaks correspond to the tetrahedral and octahedral sheets, while minor peaks of Fe, Mg, Ca, and K indicate isomorphic substitutions within the aluminosilicate lattice. The absence of significant extraneous elements reaffirms the purity of the processed Na-MMT.

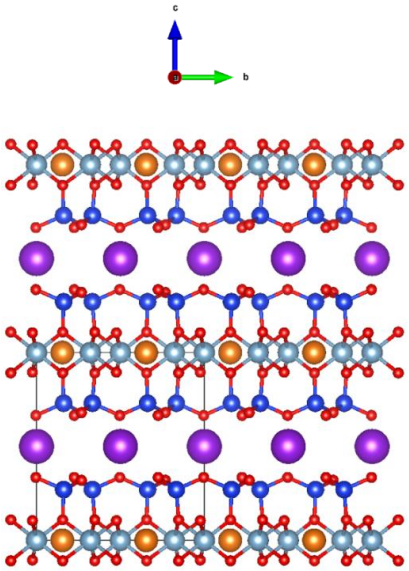

Figure 7.2 *Structure of Na-MMT clay, as obtained using the standard JCPDS file*

Thus, the combined XRD, FTIR, FESEM, and EDX analyses confirm the successful preparation of purified Na-MMT clay with preserved layered aluminosilicate structure, structural hydroxyl groups, and surface morphology, which might be beneficial for further incorporation into paper matrix as a low-cost functional filler.

7.3.1.2 MMT-incorporated Paper Separators

The XRD patterns of the pristine cellulose paper (CP) and MMT-impregnated paper separators with lowest and highest clay loadings (M05 and M20) are shown in Figure 7.3. The CP exhibits a broad diffraction peak at $2\theta \approx 22.5°$, which corresponds to the (200) crystalline plane of cellulose I structure, confirming the semi-crystalline nature of the fibrous network of cellulose. Upon incorporation of MMT into the paper matrix, additional reflections appear at lower angles ($2\theta \approx 5.8°–6.0°$), which can be attributed to the (001) basal plane of Na-MMT, indicating successful embedding of layered silicate within the fibrous substrate. The intensity of this

reflection becomes more pronounced with higher MMT content (M20), suggesting an increased degree of clay intercalation/exfoliation within the cellulose network. Simultaneously, the characteristic cellulose peak at 22.5° shows a reduction in relative intensity for both M05 nd M20, reflecting partial masking of cellulose crystallinity due to the homogeneous distribution of clay particles. The coexistence of characteristic peaks for cellulose and MMT confirms the formation of a composite paper–clay structure without altering the fundamental crystalline framework of cellulose, while the progressive enhancement of the clay signature peak validates the controlled impregnation of MMT into the fibrous matrix. These results provide strong evidence of successful fabrication of paper-clay separators with tunable clay incorporation, which is expected to improve thermal stability and ionic transport properties in subsequent electrochemical studies.

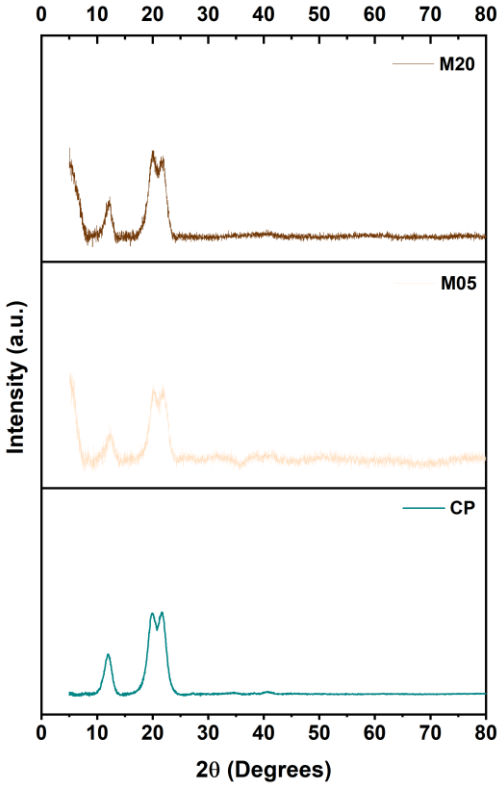

Figure 7.3 *X-ray diffractogram of CP, M05 and M20*

The surface morphology and elemental distribution of the lowest and highest MMT-incorporated paper separators were investigated using FESEM and EDX, as presented in Figure 7.4. The FESEM micrographs of M05 displayed in Figures 7.4(a) and (b) reveal a relatively smooth fibrous surface with well-entangled cellulose fibers. At this lower loading, the clay particles are sparsely distributed and predominantly located within the voids of the fibrous network, ensuring good structural integrity and porosity retention. The presence of fine lamellar MMT platelets attached to fiber surfaces are visible in Figure 7.4(b). In contrast, the morphology of M20, in Figures 7.4(d) and (e), exhibits denser coverage of clay particles across the cellulose matrix, resulting in a more compact structure. The stacked clay layers appear to bridge between adjacent cellulose fibers, leading to reduced surface roughness and smaller pore openings. It is also confirmed from Gurley values trends of the MMT-loaded paper substrates, described in next section. This microstructural change implies enhanced thermal stability and dimensional rigidity, but at the expense of slightly lower porosity compared to M05. Such

variation in microstructural features with clay loading highlights the tunability of the paper–clay separator architecture depending on performance requirements.

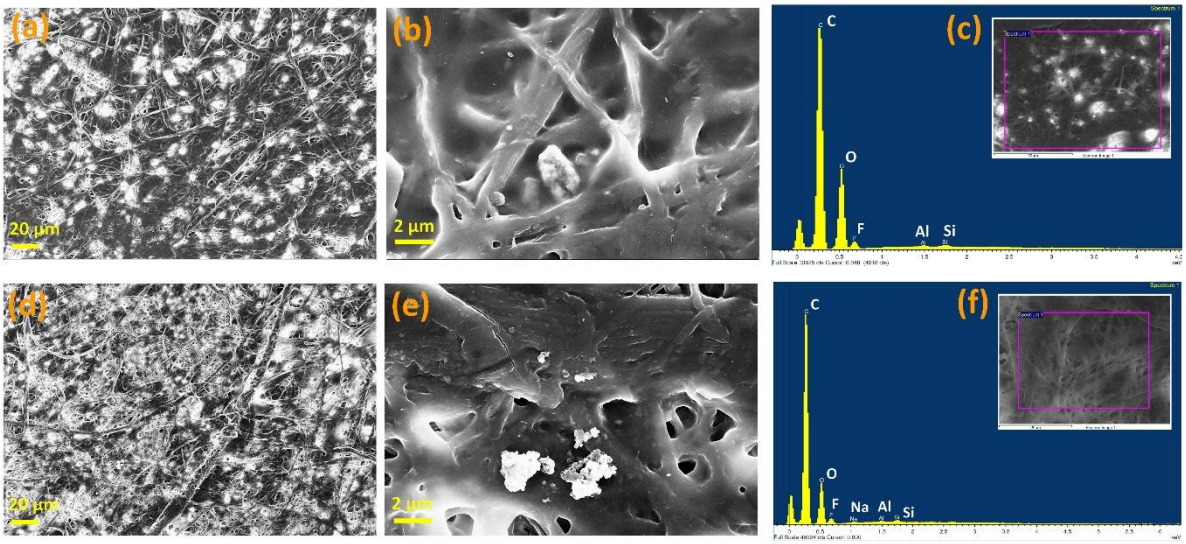

Figure 7.4 *FESEM micrographs of (a) & (b) M05, (d) & (e) M20; EDX profiles of (c) M05, (f) M20*

The EDX spectra for M05 and M20, presented in Figures 7.4(c) and (d) respectively, further confirm the successful incorporation of MMT within the paper matrix. For both M05 and M20, strong signals of Si, Al, and O are clearly evident, corresponding to the aluminosilicate layers of montmorillonite. Minor peaks of Mg, Na, K, and Fe are also detected, arising from isomorphic substitutions within the aluminosilicate lattice. The simultaneous presence of high intensity C and O peaks indicates the pure cellulose backbone of the paper. These results confirm that MMT has been effectively incorporated within the cellulose network, with its distribution density strongly dependent on the clay loading.

Overall, the combined FESEM and EDX analyses demonstrate that controlled incorporation of MMT into cellulose paper modifies the surface morphology and composition of the separator, enabling a balance between porosity, stability, and functional properties crucial for high-performance LIB applications.

7.3.2 Pore Characteristics and Electrolyte Wettability

Figure 7.5(a) illustrates the variation in air permeability in terms of Gurley value and electrolyte uptake of the developed Paper-Clay separators. The pristine cellulose paper (CP) shows the lowest Gurley value of 5s, indicating high porosity and easy air passage through the fibrous network[9]. With increasing MMT content, the Gurley value gradually increases, suggesting a

decrease in pore openness due to partial blocking and filling of inter-fiber pore spaces by clay particles and their agglomerates. This effect is more pronounced at highest loading (M20) with Gurley value of 57s, where dense packing of clay platelets restricts pore connectivity to a significant extent. Nevertheless, the Gurley values of all paper-clay separators remain significantly lower than that of commercial polyolefin membranes (Gurley value ~ 438s), confirming the superior intrinsic porosity of the cellulose-based matrix[10].

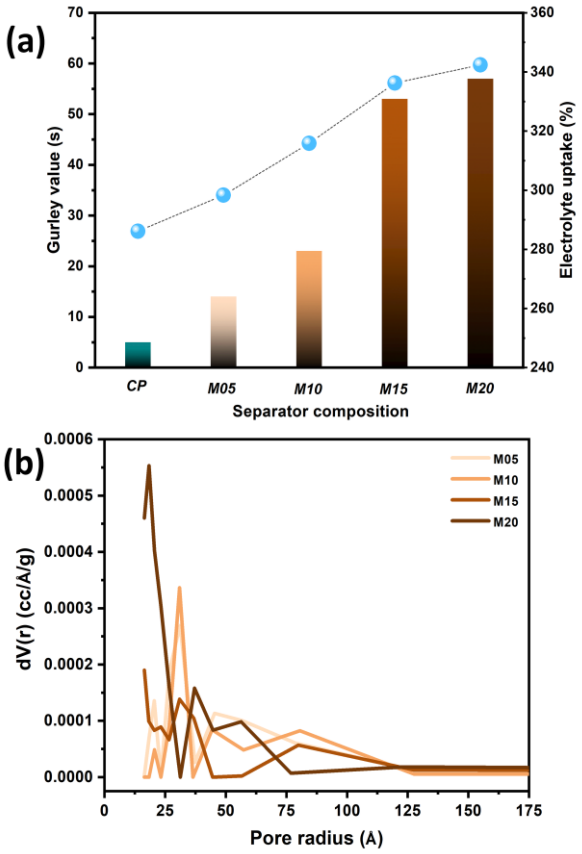

Figure 7.5 *(a) Air permeability in terms of Gurley value and electrolyte uptake, (b) BJH plots for M05, M10, M15 and M20 derived from BET adsorption*

Electrolyte uptake measurements reveal the opposite trend, as shown in Figure 7.5(a). The CP exhibits high electrolyte uptake of 286.15% owing to its hydrophilic cellulose fibers and open porous framework. Incorporation of a small amount of clay further enhances electrolyte uptake to 298.30% and 315.86% for M05 and M10, respectively, attributed to the hydrophilic nature and large surface area of MMT particles, which provide additional sites for electrolyte adsorption[11]. However, at higher loadings in M15 and M20, the electrolyte uptake although increases, but reaches a stagnant level of ~340%, likely due to significant pore filling and reduced free volume available for liquid absorption at highest loading. The balance between porosity and surface functionality therefore plays a critical role in optimizing electrolyte affinity in paper-clay separators.

The pore structure was further examined using nitrogen adsorption-desorption isotherms, as displayed in the BJH plots of Figure 7.5(b). All samples exhibit type-IV isotherms with H3 hysteresis loops, characteristic of slit-like pores associated with layered structures. The BET surface area increases for M05 and M10 compared to CP, reflecting the introduction of additional mesopores from well-dispersed clay platelets. At higher loading, the BET surface

area decreases, consistent with agglomeration and stacking of clay layers that reduce accessible surface sites. This trend correlates well with the air permeability and electrolyte uptake behavior.

Taken together, the air permeability, electrolyte uptake, and pore characteristics confirm that moderate incorporation of MMT provides an optimal balance of porosity, wettability, and surface area, making it promising for high-performance separators.

7.3.3 Separator Flexibility and Mechanical Properties

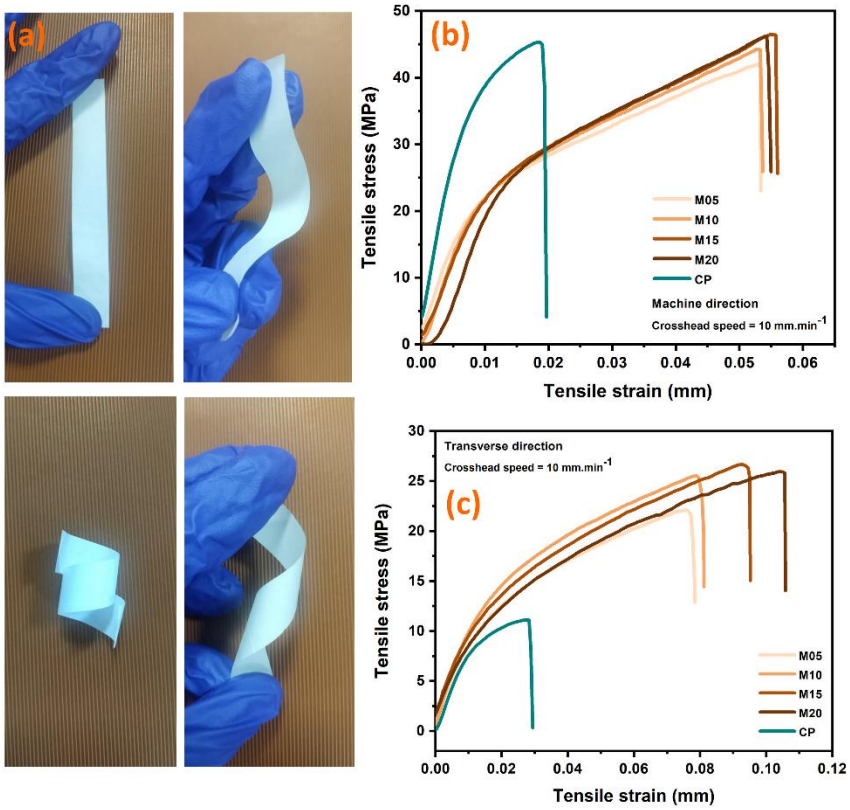

Figure 7.6 *Mechanical integrity of the developed separators: (a) bending and twisting experiments showing good flexibility; Tensile stress vs tensile strain curves along (b) machine direction and (c) transverse direction for M05, M10, M15, M20 and CP*

The flexibility of the paper-clay separators was first examined by simple folding and twisting experiments, as shown in Figure 7.6(a). The MMT-imperganted separators could be bent, twisted, and folded without any visible cracking or mechanical failure, demonstrating their inherent flexibility and mechanical integrity.

To quantify the mechanical strength of the developed separators, tensile stress-strain analysis was carried out in both the machine and transverse directions, as illustrated in Figures 7.5(b) and (c) respectively. In the machine direction, the pristine CP exhibited a tensile strength of 46.26 MPa with relatively low elongation at break. In comparison, the incorporation of MMT showed tensile strength values of 41.98 MPa, 44.30 MPa, 46.51 MPa and 46.17 MPa for M05, M10, M15 and M20 respective, with nearly three times more elongation. In the transverse direction, the effect of polymer and clay incorporation is even more pronounced. The CP displayed a low tensile strength of 11.13 MPa with premature fracture, highlighting the anisotropic mechanical character of commercial paper. In contrast, the PVDF and MMT-containing papers exhibited significantly improved strength of 22-26 MPa and much higher elongation. This suggests that the PVDF polymer reinforces the cellulose network effectively via new H-bonding interactions, while the clay particles also act as stress-distributing fillers, reducing localized stress concentration in the matrix and thereby enhancing toughness.

Overall, the incorporation of MMT and PVDF not only retains the flexibility of the paper substrate, but also enhances isotropy in mechanical properties by strengthening the transverse direction and enhancing the elongation at break. This improved balance of robustness and flexibility ensures that the paper–clay separators can withstand mechanical handling, battery winding tension, electrode contact pressure, and dimensional stress during battery operation, thereby making them suitable candidates for high-performance LIB separators.

7.3.4 Ionic Conductivity and Electrochemical Stability Window

The ionic conductivity and electrochemical stability of the fabricated paper-clay separators were evaluated by electrochemical impedance spectroscopy (EIS) and linear sweep voltammetry (LSV), respectively, as shown in Figure 7.7.

The Nyquist plots, demonstrated in Figure 7.7(a), for SS/Separator/SS symmetric cells reveal distinct differences in bulk resistance (R_b) among the separators. The commercial polypropylene (PP) membrane although exhibits the lowest bulk resistance of 2.47Ω, it suffers from very low electrolyte uptake capability of ~90%[12]. The ionic of conductivity of electrolyte-soaked commercial PP separator is 4.58×10^{-4} S.cm^{-1}, which is the highest among all, probably due to the isotropic porous structure of polypropylene. In contrast, the paper-clay separators show higher resistance values of 15.57Ω, 13.54Ω, 2.73Ω and 5.46Ω, resulting in ionic conductivities of 7.27×10^{-5} S.cm^{-1}, 8.36×10^{-5} S.cm^{-1}, 4.15×10^{-4} S.cm^{-1} and 2.07×10^{-4} S.cm^{-1},

for M05, M10, M15 and M20 respectively. Where M05 and M10 display relatively higher resistance as compared to M15 and M20, it suggests that moderate clay incorporation of 1.5 wt% preserves interconnected pore channels and facilitates ionic transport. M15 delivers nearly similar ionic conductivity as that of commercial PP and all the developed separators benefit from superior electrolyte wettability and uptake, which can offset resistance in practical battery operation. The corresponding equivalent circuit in inset of Figure 7.7(a) demonstrates that the overall impedance behavior is dominated by bulk electrolyte resistance and constant phase element contributions from electrode/electrolyte interfaces.

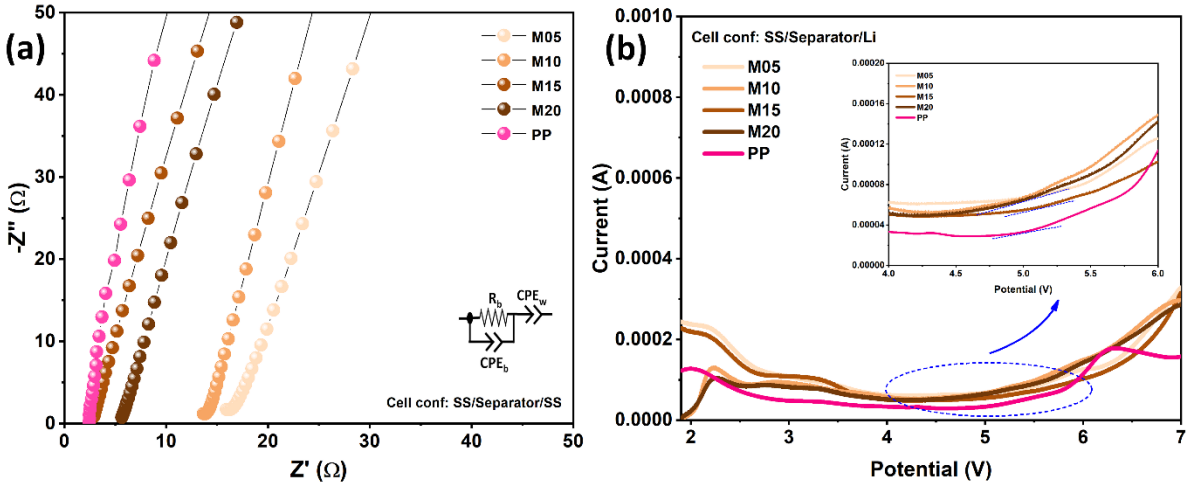

Figure 7.7 *Electrical properties: (a) Nyquist plots and (b) LSV plots for M05, M10, M15 and M20 along with commercial PP*

The electrochemical stability of the developed separators was further analyzed by Linear Sweep Voltammetry (LSV) using SS/separator/Li cell configuration. As per the LSV curves of Figure 7.7(b), all paper-clay separators exhibit a broad stability window extending beyond 5.0 V versus Li/Li$^+$, significantly wider than that of the PP separator. The inset of Figure 7.7(b) highlights the magnified view of the same plots, to show the difference in voltage windows of the different separators. The enhanced stability arises from the presence of inorganic MMT platelets, which act as thermal and electrochemical stabilizers within the cellulose network.

Overall, the EIS and LSV analyses confirm that the incorporation of MMT enhances the electrochemical robustness of the paper separators, providing a favorable trade-off between ionic conductivity, electrolyte wettability, and oxidative stability. The stability window above 5 V also demonstrates the suitability of paper-clay separators for next-generation high-voltage LIBs.

7.3.5 Electrochemical Performance

The charge-discharge characteristics of NMC111/MCMB full cells assembled with the fabricated paper-clay separators and commercial PP-based membrane are presented in ***Figure 7.8***. All separators exhibit typical voltage–capacity profiles of lithium-ion cells, with flat plateaus near 3.7 V, indicating stable electrochemical reactions. The commercial PP separator delivers a discharge capacity of ~165 mAh.g^{-1} at 0.05 mA.cm^{-2}, which is consistent with its limited electrolyte uptake. In comparison, cells employing the M15 separator shows higher discharge capacities of ~185 mAh.g^{-1}, attributed to its improved electrolyte wettability and ionic conductivity derived from the moderate incorporation of MMT platelets. However, for other loadings of MMT (M05, M10 and M20), the discharge capacity decreases slightly to ~170–175 mAh.g^{-1}. The superior performance of M15 demonstrates that an optimal clay concentration enhances both ionic conduction and electrode-electrolyte interface stability.

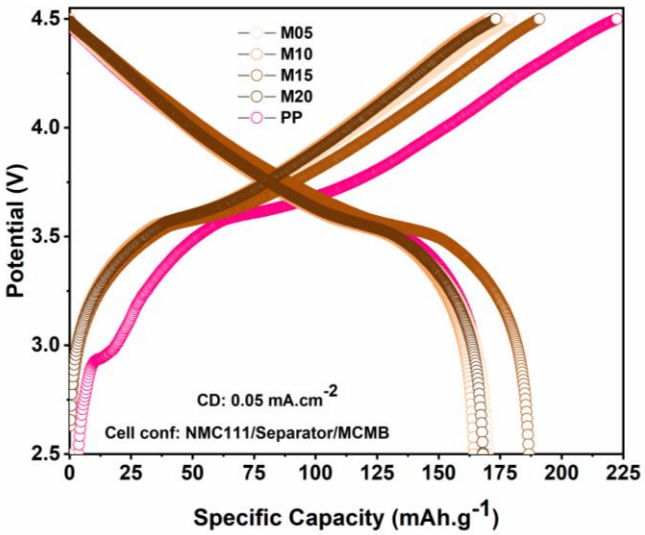

Figure 7.8 *Typical galvanostatic charge-discharge cycles for M05, M10, M15 and M20 along with commercial PP-based separator in NMC111/MCMB cell configuration*

The long-term cycling performance of these separators is depicted in ***Figure 7.9***. The PP separator shows a steady capacity fading, dropping below 60 mAh.g^{-1} after 400 cycles, with a coulombic efficiency stabilizing around 98%. In contrast, the MMT-impregnated separators exhibit much improved cycling stability, retaining specific capacities above 70-80 mAh.g^{-1} after 400 cycles with coulombic efficiency consistently exceeding 99%. This clearly highlights the advantage of paper–clay separators in sustaining reversible capacity over extended operation.

Overall, the electrochemical results demonstrate that controlled incorporation of MMT into cellulose paper significantly improves the ionic transport, electrolyte affinity, and long-term cycling stability of the separators. The optimized composition of M15 not only outperform the

commercial PP membrane but also provide sustainable and low-cost alternatives for next-generation lithium-ion batteries.

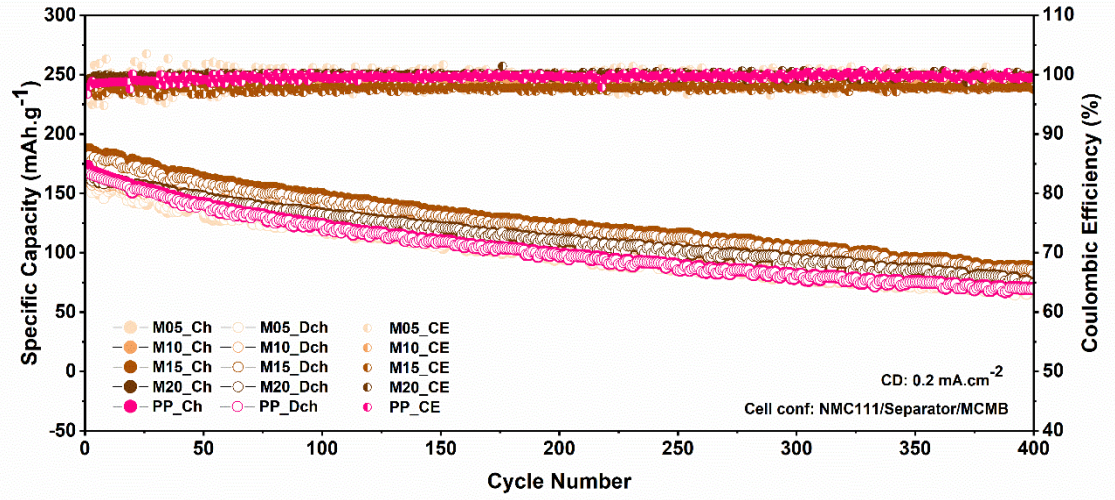

Figure 7.9 *Long cycling profiles for M05, M10, M15, M20 and PP in NMC111/MCMB cell configuration: charge and discharge capacity with coulombic efficiency*

7.3.6 Thermal Safety Tests

Even after good electrochemical stability, it is essential for a separator to become thermally stable for ensuring safety of an electrochemical cell.

The thermal stability of the pristine cellulose paper (CP) and the developed paper-clay separators was evaluated by thermogravimetric analysis (TGA) with corresponding differential thermal analysis (DTA) curves shown in ***Figure 7.10***. The CP exhibits an initial weight loss below 120°C, attributed to the evaporation of physically adsorbed water molecules.

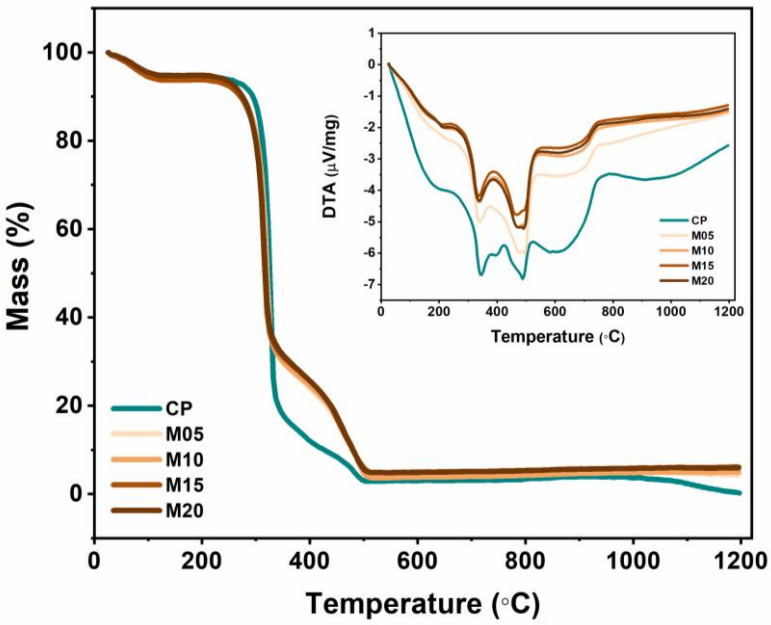

Figure 7.10 *Thermogravimetric analysis of the developed separators along with commercial cellulose paper; TGA plots along with the DTA curves in inset*

A major decomposition step occurs between 300-400 °C, corresponding to the pyrolysis of cellulose and hemicellulose, which results in significant mass loss and formation of volatile products. Beyond 500 °C, the CP sample shows almost complete degradation with negligible char residue, indicating poor thermal resistance of the pristine paper matrix. In contrast, all the paper-clay separators (M05–M20) exhibit markedly improved thermal stability. The onset of thermal degradation is shifted to slightly higher temperatures, and the overall decomposition rate is reduced compared to CP. This improvement arises from the barrier effect of montmorillonite platelets, which restrict the diffusion of volatile decomposition products and retard the thermal degradation process. Furthermore, the char yield at 800-1000°C is significantly higher in the clay-loaded separators (~15-20%), while CP shows almost no residual mass. The increased char residue reflects the inorganic contribution of MMT, which remains stable at high temperatures and provides structural reinforcement to the cellulose network.

The DTA curves displayed in the inset of ***Figure 7.10*** corroborate these observations. The sharp exothermic peak of CP at ~360°C, corresponding to cellulose pyrolysis, is broadened and reduced in intensity for the MMT-based separators, indicating a delayed and less severe thermal decomposition process. The extent of stabilization increases with clay content, with M15 and M20 showing the highest thermal resistance and most stable thermal behavior among the samples. Overall, the TGA-DTA analysis confirms that the incorporation of montmorillonite clay enhances the thermal robustness of the cellulose paper separator by improving char formation and retarding decomposition. This superior thermal stability is expected to play a vital role in enhancing the safety of lithium-ion batteries, particularly under high-temperature or thermal runaway conditions.

The flame-resistance of the developed separators was evaluated using the self-extinguishing time (SET) test, as shown in ***Figure 7.10***. For the M15 paper-clay separator ***(Figures 7.10(a)-(c))***, the sample initially ignites when exposed to the flame but quickly self-extinguishes within 4.50 seconds of removal of the ignition source. This behavior is attributed to the presence of inorganic MMT platelets, which provide a barrier effect by limiting heat transfer and volatile gas release from the cellulose matrix. The clay layers also contribute to char formation, thereby suppressing continuous combustion and enhancing the intrinsic flame-retardant property of the separator.

In stark contrast, the commercial PP separator, as observed in ***Figures 7.10(d)-(f)***, shows rapid melting, shrinkage, and sustained burning once ignited, without any tendency to self-extinguish. The poor thermal stability of PP arises from its low melting point (~165°C) and hydrocarbon backbone, which promote easy propagation of flames and complete combustion. The observed differences between M15 and PP highlight the superior fire safety of the paper-clay separator, demonstrating its ability to minimize thermal runaway risks in lithium-ion batteries.

Thus, the SET analysis confirms that incorporation of montmorillonite clay into the cellulose framework significantly improves the flame-retardant properties of the separator, providing a critical safety advantage over conventional polyolefin-based membranes.

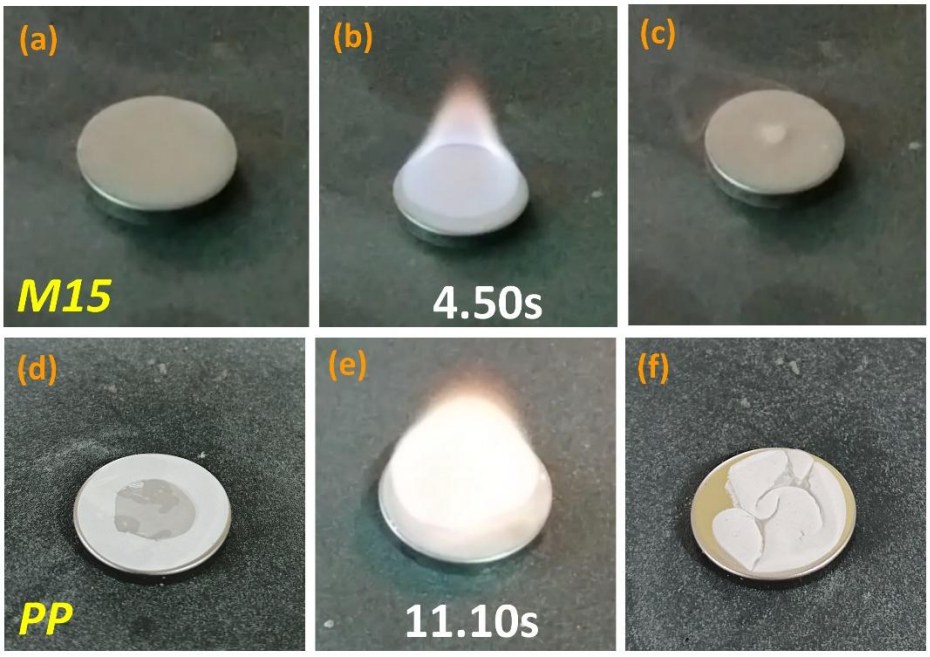

Figure 7.11 *Digital images of various stages of the self-extinguishing time measurement for (a)-(c) M15 and (d)-(f) PP*

The electrochemical stability of the separators before and after the flame-resistance test was further assessed through galvanostatic charge-discharge cycling, as shown in ***Figure 7.11***. For the PP separator ***(Figure 7.11(a))***, the cells fail to retain electrochemical functionality after the SET test. The discharge capacity in LFP/MCMB cell drops drastically and the voltage profile is highly distorted, reflecting severe thermal deformation of the PP membrane and resultant short-circuit of the cell during exposure to flame. The melting and shrinkage of PP not only compromise its mechanical integrity but also lead to increased internal resistance and poor ionic conduction, rendering the cell electrochemically unstable. In contrast, the M15 paper-

clay separator (Figure 7.11(b)) retains stable charge-discharge characteristics even after flame exposure. The voltage plateaus remain well-defined around 3.7 V, and the discharge capacity shows negligible deterioration compared to the pre-SET state. This superior retention of electrochemical behavior is directly linked to the flame-retardant capability of the clay-loaded cellulose network, which preserves separator morphology and maintains continuous ionic pathways under thermal stress.

These results clearly demonstrate that the paper-clay separators, particularly M15, offer substantial improvements in thermal safety over commercial PP membranes. The ability to self-extinguish and sustain electrochemical performance after flame exposure underscores their potential for safe operation in high-energy lithium-ion batteries, where safety concerns are paramount.

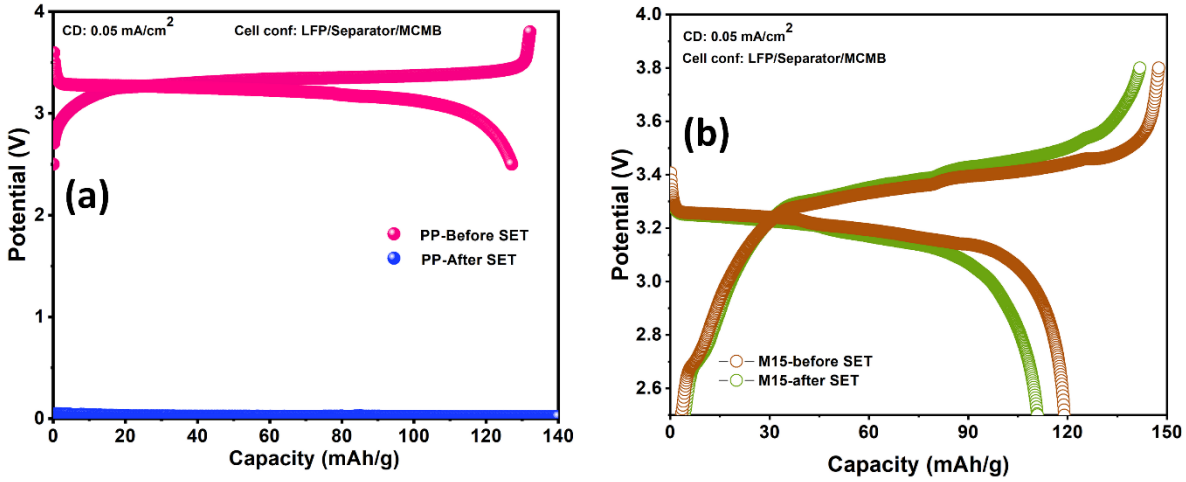

Figure 7.12 *Typical galvanostatic charge-discharge cycles for (a) PP and (b) M15 before and after SET test*

7.4 Conclusion

This chapter demonstrated the fabrication and evaluation of montmorillonite (MMT) impregnated paper-clay separators for lithium-ion batteries. Structural analysis confirmed the coexistence of cellulose and montmorillonite reflections in XRD, while FESEM–EDX revealed a progressive transition from sparse platelet distribution at low loading (M05) to dense stacking at higher loading (M20). This controlled incorporation modified the pore structure, improving electrolyte affinity and thermal stability. The separators retained excellent flexibility and showed significant reinforcement in the transverse direction, overcoming the anisotropy of pristine cellulose paper. Ionic conductivity and electrochemical stability measurements indicated that M15 offered the most balanced performance, with adequate porosity, strong

electrolyte uptake, and stability window exceeding 5.0 V, superior to the commercial PP separator. Full-cell studies further validated these findings. Cells assembled with M15 exhibited higher discharge capacities (~185-190 mAh g^{-1}) and superior cycling stability with >99% coulombic efficiency after 400 cycles. Even at higher clay loadings, the separators outperformed PP, demonstrating the inherent benefits of the cellulose–clay composite design. Thermal safety tests highlighted a clear advantage of the paper–clay separators. The M15 membrane quickly self-extinguished after flame exposure, while the PP separator sustained burning and structural collapse. Moreover, the M15-based cell retained stable charge–discharge profiles after the SET test, unlike PP, which showed catastrophic performance loss. TGA results corroborated these observations, showing delayed decomposition and higher char yield for clay-loaded membranes.

In summary, montmorillonite impregnation enhances the structural, electrochemical, and thermal properties of cellulose paper separators. 1.5% MMT impregnation in paper matrix delivers the best compromise between ionic conductivity, wettability, mechanical integrity, and safety, while higher loadings provide additional thermal robustness. These results demonstrate that low-cost, sustainable paper–clay separators can serve as safer and more efficient alternatives to commercial polyolefin membranes for next-generation lithium-ion batteries.

References

1 W. Chen, Y. Hu, W. Lv, T. Lei, X. Wang, Z. Li, M. Zhang, J. Huang, X. Du, Y. Yan, W. He, C. Liu, M. Liao, W. Zhang, J. Xiong and C. Yan, *Nat Commun*, 2019, **10**, 4973.

2 M. L. Para, D. Versaci, J. Amici, M. F. Caballero, M. V. Cozzarin, C. Francia, S. Bodoardo and M. Gamba, *Journal of Electroanalytical Chemistry*, 2021, **880**, 114876.

3 J. Li, J. Yu, Y. Wang, J. Zhu and Z. Hu, *Ind Eng Chem Res*, 2020, **59**, 12879–12888.

4 W. Dong, L. Ji, M. Zhao, X. Zhu, Z. Yang, D. Shen and S. Yang, *Diam Relat Mater*, 2023, **139**, 110265.

5 J. Nunes-Pereira, A. C. Lopes, C. M. Costa, R. Leones, M. M. Silva and S. Lanceros-Méndez, *Electroanalysis*, 2012, **24**, 2147–2156.

6 F. Bergaya, B. K. G. Theng and G. Lagaly, *Handbook of Clay Science*, 2006, vol. 1.

7 M. Sarkar, K. Dana, T. K. Mukhopadhyay and S. Ghatak, *Transactions of the Indian Ceramic Society*, 2011, **70**, 23–28.

8 T. Nazdracheva, A. Morozov, V. Yavna and A. Kochur, *J Mol Struct*, 2022, **1250**, 131871.

9 M. Das, P. S. Das, N. C. Pramanik, R. N. Basu and M. Wasim Raja, *ACS Omega*, DOI:10.1021/acsomega.3c02859.

10 M. W. Raja, R. N. Basu, N. C. Pramanik, P. S. Das and M. Das, *ACS Appl Energy Mater*, DOI:10.1021/acsaem.2c00188.

11 J.-H. Park, H.-J. Shin, M. H. Kim, J.-S. Kim, N. Kang, J.-Y. Lee, K.-T. Kim, J. I. Lee and D.-D. Kim, *J Pharm Investig*, 2016, **46**, 363–375.

12 M. Das, P. S. Das, R. N. Basu and M. W. Raja, *Cellulose*, DOI:10.1007/s10570-022-04873-3.

Chapter 8

Active Ceramic Impregnated Paper Separators for High-Performance LIBs

Highlights:

- Sustainable cellulose-based paper separators impregnated with varying concentrations of Li-ion conducting LLZO.
- Investigation of structural properties, ionic transport, electrochemical, and thermal stability of the separators
- Comparison with inert Al_2O_3-coated paper and commercial PP separators
- Enhanced thermal stability and safety

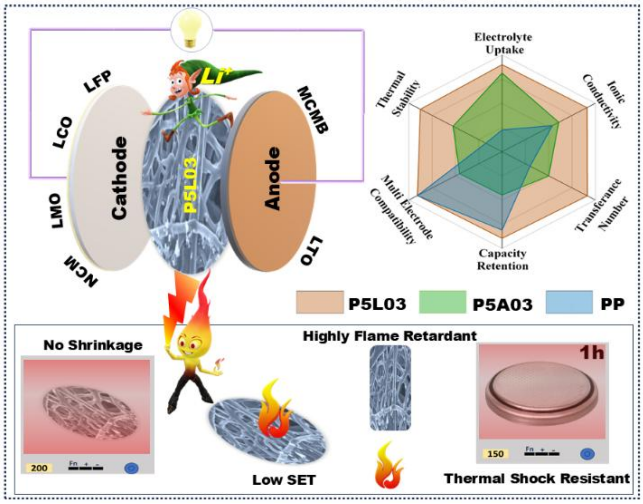

Figure 8.0*: Graphical abstract illustrating effect of LLZO impregnation in the cellulose matrix*

This chapter investigates the effect of active (LLZO) and inactive (Al_2O_3) ceramic impregnation in paper-based cellulose separators fabricated via an industry-friendly dip-coating process. Among the developed separators, the LLZO-loaded separator (P5L03) demonstrates superior ionic conductivity, Li-ion transport, and electrochemical stability compared to Al_2O_3-based and commercial PP separators. Its enhanced performance is mainly due to the intrinsic Li-ion conductivity of LLZO and PVDF chain modification in a Lewis basic environment. P5L03 further shows improved cycling stability, multi electrode compatibility, excellent flame retardancy, and resistance under self-extinguishing and thermal shock tests. In summary, LLZO-impregnated paper separators combine sustainability, safety, and cost-effectiveness, offering a promising alternative to conventional plastic separators for next-generation lithium-ion batteries.

8.1 Background and Overview

To mitigate environmental pollution contributed by petrol-diesel-driven transportation systems, a shift from internal combustion engines (ICE) to electric engines (EE) is imminent [1]. This typically requires powerful, long-life, and safe batteries for powering electric engines. Lithium-ion batteries (LIBs) are the first choice of energy storage systems among all other alternatives owing to their high power and energy densities[2]. However, the major bottleneck in current LIB technology is use of liquid electrolytes in the cell that poses a severe threat of thermal hazard and short-circuiting, further restricting its full-scale use in electric vehicles (EVs)[3,4]. Among the various battery component, separator though electrochemically inert, plays a critical role in both cell safety and Li-ion transport.

To address these limitations, three main strategies can be explored – firstly, to fabricate ceramic composite separators by coating inorganic particles such as Al_2O_3, SiO_2, and ZrO_2 onto polyolefin separators[5], secondly, to substitute polyolefin-based commercial separator with cellulose based sustainable separator[6] and thirdly, to explore all solid-state configuration of battery using lithium-ion conducting solid electrolytes[7]. While inorganic oxide coating in commercial separator shows better performance particularly in terms of safety but still possess a threat in challenging condition. On the other side, making functional solid-state batteries with inorganic solid electrolyte seems to be far from expected due to several challenges including complexity in manufacturing scalability. In this scenario, cellulose based materials show great potential for using as separator in metal ion batteries particularly for EV application.

Recently, researchers are exploring different types of cellulose-based materials by functionalizing them to use as separator. For example, Zeng et al.[8] modified tissue paper with nano-SiO_2 hybrid cross-linked polymer electrolyte as coating layer which offers superior cycling performance. One approach to overcome these limitations can be the introduction of any Li-ion conducting material such as lithium nitrate, lithium acetate, lithium lanthanum titanate (LLTO), lithium aluminum titanium phosphate (LATP) and lithium lanthanum zirconium oxide (LLZO) etc. into the separator matrix to enhance battery rate performance without compromising electrolyte wettability and thermal stability. A summary of separators developed with Li-ion active ceramic materials is given in ***Table 8.6***.

In this direction, the present study focuses on developing cellulosic paper separators impregnated with fast Li-ion conducting LLZO using an industry-friendly dip-coating process. The synergistic interactions between LLZO and PVDF binder enhance lithium transport

through structural modifications of the polymer backbone. The resulting separators demonstrate improved thermal stability, flame retardancy, and superior electrochemical performance, even under harsh conditions such as self-extinguishing and thermal shock tests. The developed LLZO paper separator also delivers superior performance against different cathodic (LFP, LMO, LCO, NMC) and anodic (LTO, MCMB) configurations and resulted in excellent compatibility. Thus, this chapter introduces an innovative approach of making paper supported LLZO impregnated separator for the development of sustainable, low cost, high performance and safe separator for advanced LIBs.

8.2 Experimental Details

8.2.1 Preparation of Cubic LLZO

To synthesize cubic phase of LLZO ($Li_7La_3Zr_2O_{12}$), a homogeneously mixed solution was first prepared by dissolving constituent metal salts $LiNO_3$, $La(NO)_3$, $ZrO(NO_3)_2$and a chelating agent alanine ($C_3H_7NO_2$) in deionized water. Through consistent stirring and heating at approximately 150°C, the solution eventually transformed into a thick, viscous gel which underwent a brief combustion phase, accompanied by the release of a significant volume of gaseous byproducts. This led to the formation of a light, fluffy white substance containing ultrafine particles, referred to as the as-synthesized powder. This as-synthesized powder was further calcined at 900°C for 10 hours in air to get cubic phase of LLZO powder. Digital image of cubic LLZO powder is presented in ***Figure 8.1***. Subsequently, the cubic LLZO powder was ground using a mortar pestle and then stored in a glove box to avoid any interference of moisture.

8.2.2 Fabrication of Paper Separators

The fabrication of paper separators in “Roll to Roll” form, relies heavily on the basic characteristics of the untreated paper such as its thickness, moisture absorption, overall porosity, mechanical strength etc. In this work, pure cellulose based commercial paper with thickness of 20 µm and porosity of nearly 65% was collected from local manufacturer. Initially, the commercial paper roll (W-62 mm, L-100 m) was kept at vacuum oven at 80°C overnight for its complete de-moisturization. Next day, a clear suspension comprising 5.0 w/v% of PVDF in NMP was prepared under constant heating at 70°C and stirring at 400 rpm for 6 hours. Different weight percentages of cubic LLZO powder (10, 30, 50 and 70 wt%) with respect to the total weight of the polymer was added to the solution. These solutions were ultrasonicated

for about 30 minutes followed by prolonged stirring. The process was repeated few times to get a homogenous slurry. It is worth mentioning here that dehydrofluorination of PVDF chains as discussed earlier could be clearly visualised by analysing the colour of the ceramic-polymer solution, where the colour of the solution turned to deep brown with the presence of higher concentration of white LLZO particles (70 wt%). The pH of the solution was measured to be around 12. However, lower concentration of LLZO (10 wt%) shows light brown colour with a pH of around 9. The colour of Al_2O_3 loaded PVDF solution was white with a pH in the acidic range same as 5 w/v% PVDF solution, suggesting no dehydrofluorination of PVDF chains. Finally, the polymer-ceramic suspensions were uniformly coated on both sides of the dehydrated commercial cellulose paper in an in-house designed semi-automated separator fabrication equipment. Following in-situ drying in the infrared heating zone within the fabricator machine, the ceramic-coated papers underwent compaction and were collected in roll form. Subsequent measurements revealed that the thickness of the fabricated paper separators fell within the range of 20 ± 2 µm. For comparison, a homogenous solution of 5 wt% PVDF in NMP and 30 wt% nano-Al_2O_3 powder was prepared and uniformly coated in the similar way. ***Table 8.1*** describes the nomenclature of various separators developed in this study. All the fabricated separators as well as the commercial PP separator were dried under vacuum at 60°C for overnight and stored in an Argon filled glove box for further characterizations.

Table 8.1 *Nomenclature of various composite paper separator developed in this study*

Ceramic	Concentration (wt%)	Nomenclature
LLZO	10	P5L01
	30	P5L03
	50	P5L05
	70	P5L07
Al_2O_3	30	P5A03

8.3 Results & Discussion

8.3.1 Structural, Microstructural and Surface Properties of LLZO Powder

X-ray diffractograms of calcined LLZO powder are plotted in ***Figure 8.1(a)*** along with the standard profile (JCPDS 00-064-0141). All the major intense peaks could be indexed as the

cubic LLZO (c-LLZO) along with the secondary impurity phases of $La(OH)_3$. The quantitative phase analysis as carried out revealed that the c-LLZO appeared as the major phase (73.7%) along with 26.3% of $La(OH)_3$. Typically, lanthanide impurity phases, such as $La(OH)_3$, La_2O_3 etc. are found in LLZO materials due to the exposure of the bulk powder in ambient atmosphere during synthesis and calcinations processes. The details of such phenomena have duly been described in some recent studies [9]. It is worthy to mention here that the rate of formation of such lanthanide impurities depends on the surface area and morphology of the bulk powder, as concluded by Fleming et al [10]. Although, presence of Li_2CO_3 is not detected in X-ray diffractogram, it may even remain as a surface impurity of LLZO powder due to the Li^+/H^+ exchange between the garnet material and moisture which is one of the reasons of reduced ionic conductivity of LLZO. The formation of cubic LLZO phase was further verified by FTIR and RAMAN spectroscopy as shown in ***Figure 8.1(b)*** and ***Figure 8.1(c)***. In FTIR spectra of calcined LLZO, the existence of $La(OH)_3$ could also be identified by the appearance of strong peak at 3609 cm^{-1}. The OH vibration at 3448 cm^{-1} and C-O stretching vibration at 1441 cm^{-1} and 866 cm^{-1} attribute to the absorbed moisture and presence of Li_2CO_3 respectively. Other stretching and bending vibrations at 1639, 1496, 1088 cm^{-1} etc are attributed to the presence of different hydrocarbon and organic moieties in the LLZO sample. Few more peaks below 800 cm^{-1} are found which reflect the presence of characteristics vibrations of La-O and Zr-O in LLZO [11,12].

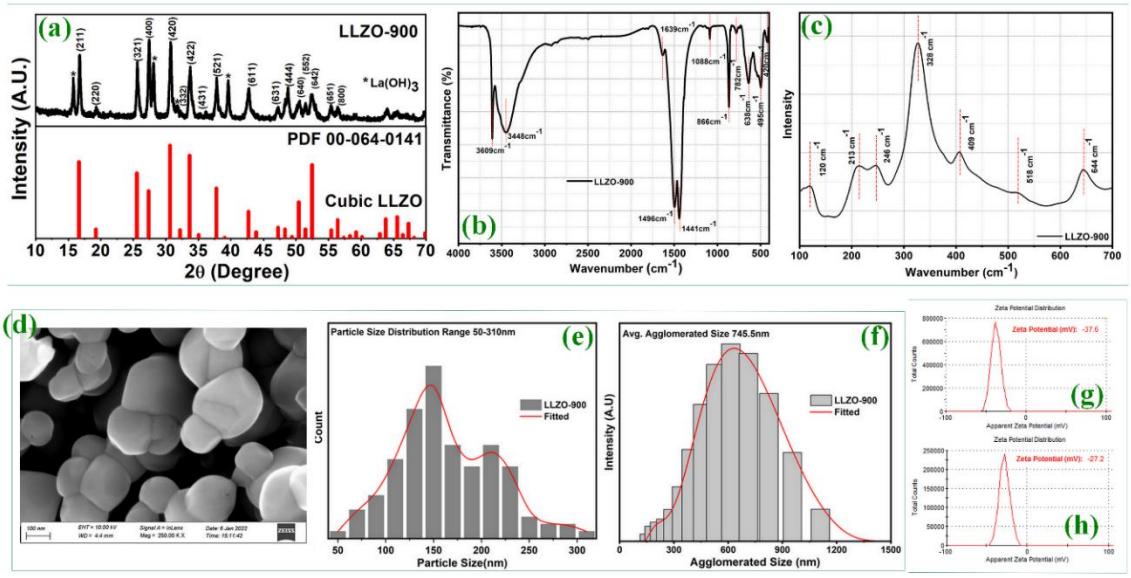

Figure 8.1 *(a)-(c) describes X-ray diffractogram, FTIR spectra and Raman spectra of LLZO powder calcined at 900°C respectively; (d) FESEM image of LLZO calcined powder; (e)*

Particle size distribution of LLZO powder calculated from the micrograph; (f) particle size distribution pattern of LLZO powder; Measured Zeta potential of (g) commercial cellulose paper and (h) LLZO powder

While carrying out RAMAN spectra as shown in ***Figure 8.1(c)***, the presence of cubic phase in pristine LLZO powder could also be evident. Here, signals at the low frequency vibration <300 cm^{-1} demonstrate the translation modes of the mobile cations and the presence of cubic phase is confirmed by obtaining a smaller number of broad and partially overlapping peaks at the mid frequency range of 300-550cm^{-1} [13]. The peaks at 644 cm^{-1} as shown could be assigned to the vibrational stretching of ZrO_6 octahedra in LLZO.

8.3.2 Microstructural Features of the Developed Separators

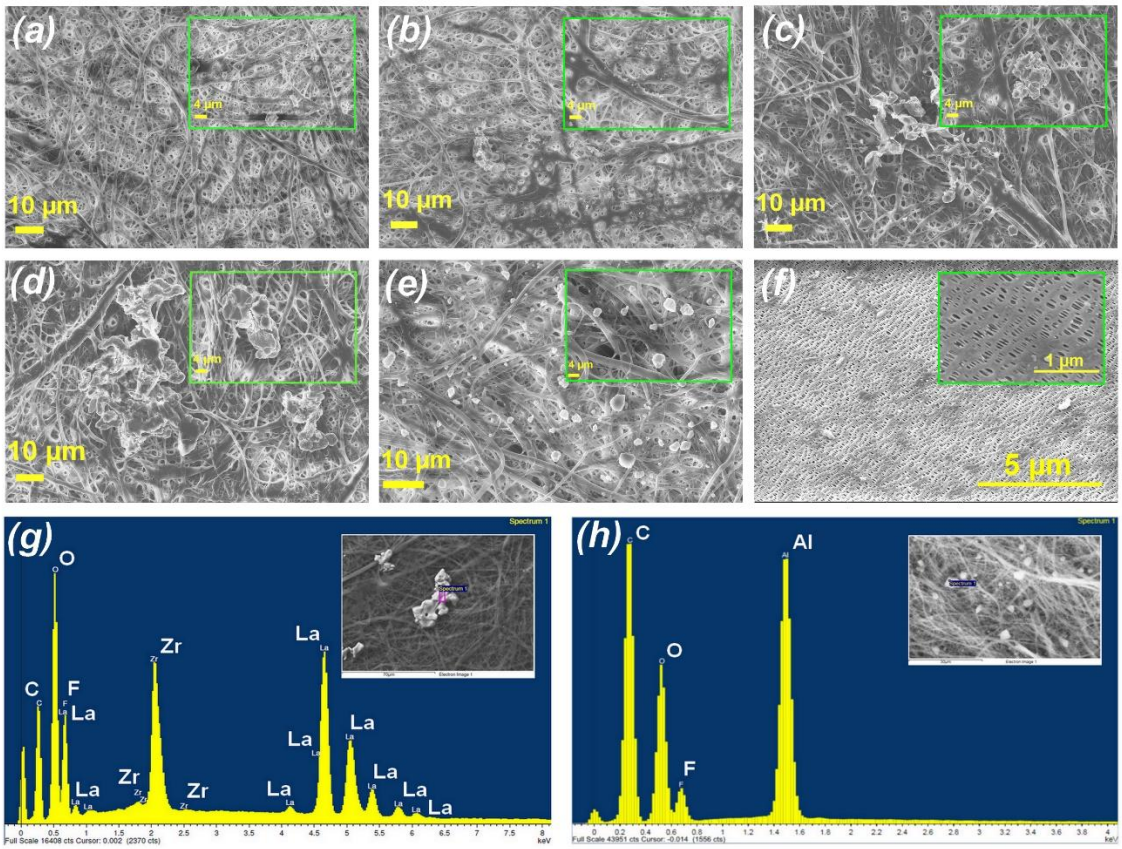

Figure 8.2 *FESEM micrographs of (a) P5L01, (b) P5L03, (c) P5L05, (d) P5L07, (e) P5A03 and (f) PP with their higher magnification images in the insets and EDX profiles of (g) P5L03 and (h) P5A03*

The microstructural features of the developed paper separators are shown in ***Figure 8.2***. ***Figures 8.2 (a)-(d)*** demonstrate the FESEM micrographs of LLZO impregnated paper

separators with different ceramic loading, namely P5L01, P5L03, P5L05 and P5L07 respectively. Their higher magnification images have also been displayed in the insets of the respective images. For comparison, FESEM images of the paper separator impregnated with Al_2O_3 nanoparticles named P5A03 are displayed in ***Figure 8.2(e)***. In a similar manner, microstructures of commercial PP separator are also shown in ***Figure 8.2(f)***. To ensure the presence of LLZO and Al_2O_3 nanoparticles inside the paper matrix, EDX spectra of P5L03 (LLZO based) as well as of P5A03 (Al_2O_3 based) have been presented in ***Figures 8.2(g)*** and ***(h)*** respectively. On the other hand, the FESEM micrograph of calcined LLZO powder as shown in ***Figure 8.1(d)*** shows a unique neck fused microstructure of LLZO grains. The particle size as measured using IMAGE J software from FESEM micrographs is presented in ***Figure 8.1(e)*** which shows a distribution of particles in the size range of 50-310 nm. It is obvious that such particles remain in agglomerated form in the bulk powder. The average agglomeration size of LLZO grains further measured by particle size analyzer (DLS) is shown in ***Figure 8.1(f)***. The size of the agglomerated particles corresponds to almost 745.5 nm.

Paper is typically made of cross-linked cellulose fibers which create randomly distributed pore spaces . Therefore, while impregnating ceramic, it is possible that the agglomerated ceramic particles will unevenly either block the pore spaces or remain in between the three-dimensional network of fibers. The FESEM micrographs as shown in ***Figures 8.2(a)-(d)***, display that LLZO nanoparticles reside on cellulose paper matrix randomly and in agglomerated forms. With increase in concentration of LLZO from 10 wt% to 70 wt%, the tendency and size of agglomeration increases. As shown in ***Figure 8.2(e)***, while impregnating Al_2O_3 nanoparticles the distribution of particles on the paper matrix found to be similar to that of LLZO, but reduced agglomeration size. The nature of deposition, the distribution of ceramic on paper matrix during wet coating process, and the effect of homogeneity of ceramic filler on paper separator is well reported in some recent reports [14,15]. It is important to probe the surface properties for both the filler material and the cellulosic surface while developing paper-based separator. The measurement of zeta potential is thus crucial before impregnation of ceramic filler in paper substrate. The zeta potential curves of aqueous suspension of pure cellulose paper as well as LLZO powder are displayed in ***Figures 8.1(g)*** and ***(h)*** respectively. Typically, the surface of a cellulose base matrix holds negative charge [16,17], which has been further confirmed by obtaining a highly negative zeta potential value of -37.6 mV for pure cellulose paper used in the present study. While measuring LLZO, it also shows a negative zeta potential value of -27.2 mV (***Figure 8.1(h)***); describing its Lewis base characteristics. As both the paper substrate as well

as LLZO particles are found to have negative zeta potentials, uneven ceramic distribution and particle agglomeration in between the cross-linked cellulosic fibers is expected. It is worthy to mention here that zeta potential values >30 mV are typically indicative of a well-dispersed solution, while values <5 mV result in significant agglomeration of particles during deposition. The zeta potential in the intermediate range between 5 mV and 30 mV typically shows a tendency towards forming agglomeration. Thus, alumina nanoparticles which have reportedly lower negative zeta potential value do not favor the interactions with negatively charged cellulose fibers and thus show their inherent inclination to form the random yet smaller agglomerates. In spite of the uneven distribution LLZO particles within the paper matrix, the presence of such ion-conducting LLZO significantly contributed in improving Li-ion transport phenomena as well as other required properties of separator materials.

8.3.3 Air permeability, Electrolyte Wettability and Mechanical Properties

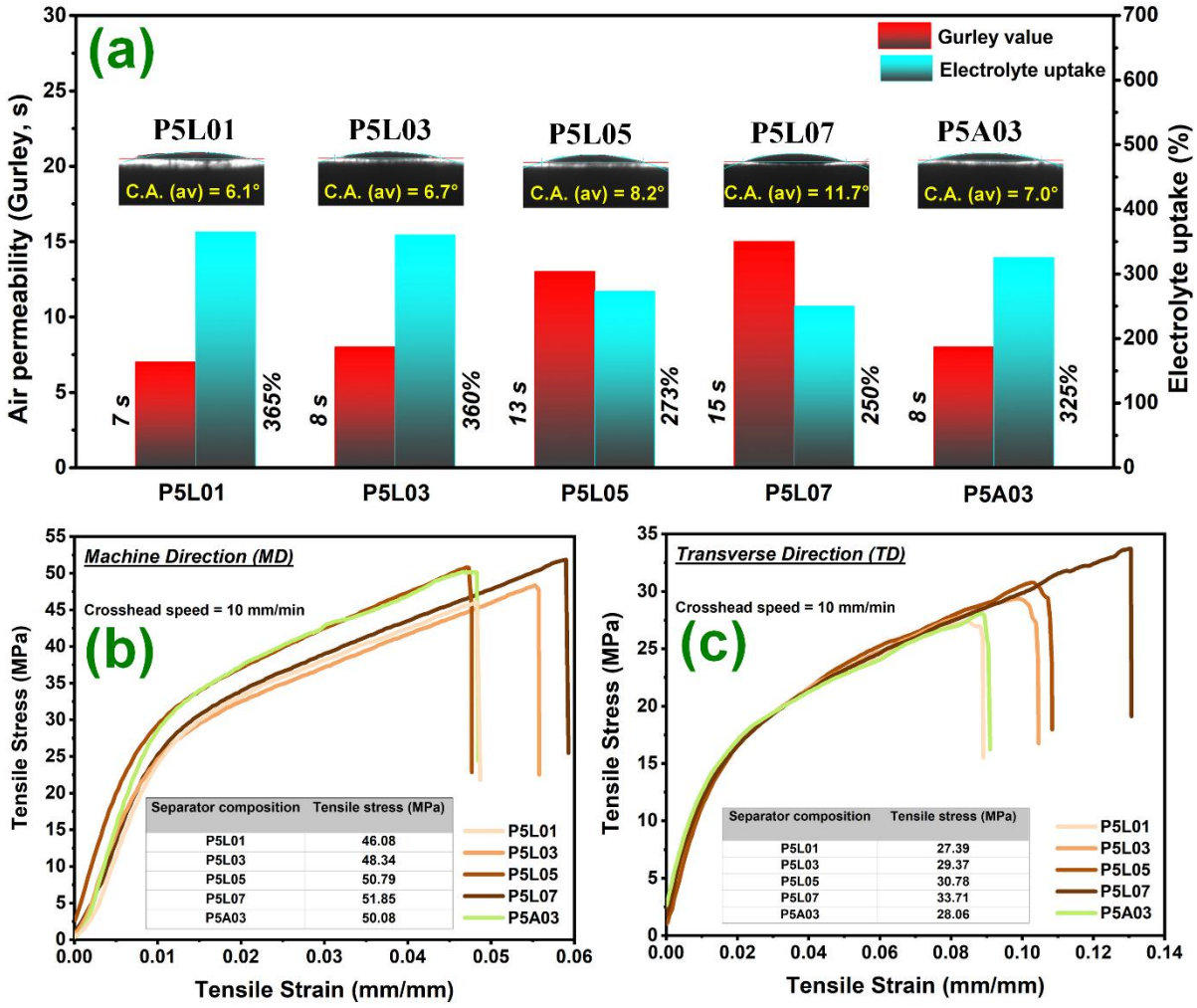

Figure 8.3 *(a) Gurley values and electrolyte uptake capabilities of our developed separators and the corresponding contact angle measurement was provided in the inset for each*

separator; Tensile stress vs tensile strain plot of developed paper-based separator in (b) machine direction (MD) and (c) transverse direction (TD)

Measurement of Gurley value indicates the air permeation ability of a porous membrane which is an important parameter to analyze the resistance of the battery separators towards movement of lithium ions [18]. Herein, the paper matrix being a highly porous matrix shows Gurley value of 5 s. Therefore, it is mandatory to examine the modified paper as we have introduced PVDF polymer as binder and LLZO, Al_2O_3 ceramic fillers because of their tendency to form agglomerates and block the pore spaces. On sizing the pure cellulose paper with 5.0 w/v% PVDF, the Gurley value increases marginally to ~7s. This nominal change suggests that the low concentration of polymer has minimal impact on the overall porosity of the paper. It is further observed that even with the introduction of ceramics on to the sized PVDF-coated paper, the change in Gurley values is not substantial; 7s for P5L01, 8s for P5L03, 13s for P5L05 and 15s for P5L07. ***Figure 8.3(a)*** demonstrates the change in air permeability values with respect to compositions. For reference, the air permeability value of P5A03, which is 8s, is also plotted. Therefore, it may be stated that the incorporation of ceramics (LLZO and Al_2O_3) in sized paper matrix does not significantly affect their air permeation efficiency, ensuring a facile pathway for Li^+-ion transport across the paper separator membranes.

The electrolyte uptake capability stands as another pivotal indicator of separator membrane performance regarding its wettability towards electrolyte. Traditional separators made from polyethylene or polypropylene often demonstrate limited electrolyte wettability, resulting in prolonged periods for electrolyte absorption. Conversely, cellulose, with its inherent hydrophilic properties, endows paper separators with the ability for rapid and enhanced electrolyte absorption [19]. Among the developed paper separators, P5L01 exhibits the highest electrolyte uptake capacity of 365%, whereas P5L07 demonstrates the lowest electrolyte uptake of 250% as shown in Y-axis of ***Figure 8.3(a)***. Similarly, P5A03 separator is also found to retain quite high liquid electrolyte uptake capacity of 325%. These results thus clearly indicate that cellulosic paper separator is far superior to that of commercial plastic separator which demonstrates only 90% electrolyte uptake capacity.

An alternative method for evaluating wettability involves measuring the contact angle between the liquid electrolyte and the surface of the separators [20,21]. The variation of contact angle for the three different ceramic-impregnated paper separators is displayed in the inset of ***Figure 8.3(a)***. Notably, the contact angle values as summarized in ***Table 8.2*** for the developed paper

separators are significantly lower than that of commercial polypropylene (PP) [22]. The measured contact angles strongly correlate with the observed electrolyte uptake or soaking ability. For instance, P5L01, with the highest electrolyte uptake of 365%, exhibits the lowest contact angle of 6.1°. Conversely, P5L07, with the lowest electrolyte uptake of 250%, shows the higher contact angle value of 11.7°.

Table 8.2 *A summary of different physical parameters of our developed paper separators*

Code	d (µm)	Gurley Value (s)	Contact Angle (°)	Electrolyte Uptake (%)	Tensile (MPa)	
					MD	TD
P5L01	20±2	7	6.1	365	46.08	27.39
P5L03	20±2	8	6.7	360	48.34	29.37
P5L05	20±2	13	8.2	273	50.79	30.78
P5L07	20±2	15	11.7	250	51.85	33.71
P5A03	20±2	8	7.0	325	50.08	28.06

Here, d stands for the thickness of separator.

The mechanical properties of a separator hold immense significance to ensure the safety and efficiency of a battery [23]. Any separator needs to withstand the winding tension during battery manufacturing process; thus, it should have to acquire sufficient structural integrity towards tension in machine direction. The tensile properties of all the developed paper separators are estimated and presented in ***Figure 8.3(b)*** and ***(c)*** in terms of tensile stress vs strain curve both in machine direction and transverse direction respectively. It is worthy to discuss here that the mechanical strength in any paper-based matrix is intrinsically depends on the three key points; strength of cellulosic tissue, the degree of cross-linking of cellulose fiber and the inter- and intra-molecular hydrogen bonds among cellulose units, or any added functional polymers. As mechanical strength of paper comes only from the continuous H-bonding, so any functionalization that create more and more H-bonds will eventually increase the mechanical strength of the system[24]. Herein, the concentration of polymeric binder (5 wt% PVDF) in all the paper separators is kept identical; however, only the concentration of ceramic particles in the separator matrix has been systematically varied. The tensile strength for untreated paper is found to be 11.83 MPa in transverse direction (TD) and 46.26 MPa in machine direction (MD) [22]. It is worthy to mention here that the additions of polymeric binder along with ceramic particle has significantly enhanced the tensile strength in transverse direction (almost three times for P5L07), however, the tensile strength in machine direction found to be somewhat

similar in nature, in the range of 46-52 MPa. Thus, it suggests that the polymeric binder is probably making few extra hydrogen bonds with the cellulosic hydroxyl groups to enhance their tensile strength. With the increase in concentration of LLZO filler from 10.0-70.0 wt% in paper matrix, the increase in tensile strength is found to be in the range of 12-13% in MD and 23-24% in TD. This suggests that the impregnated ceramic particles are probably contributing to the structural integrity in the paper matrix resulting in changes in tensile strength.

8.3.4 Electrical Properties

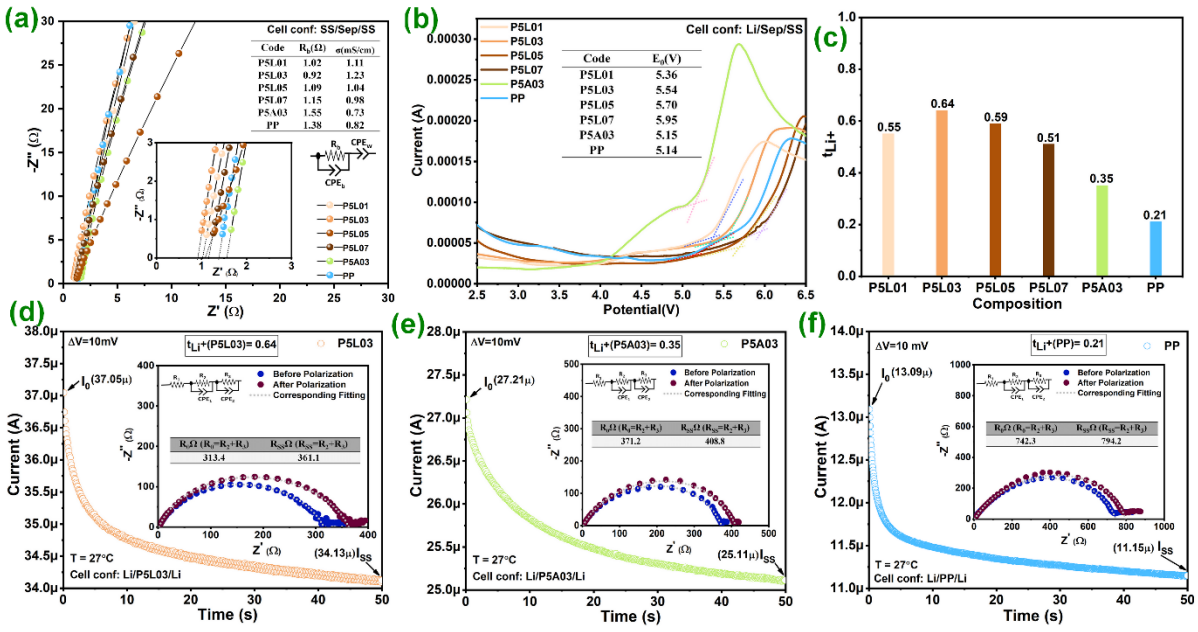

Figure 8.4 *Electrical properties of developed paper separator along with the commercial separator, (a) EIS spectra along with the corresponding equivalent circuit of SS/Separator/SS cell for measurement of ionic conductivity, (b) Current vs Potential sweep voltammetry (LSV) for measurement of electrochemical potential window, (c) Lithium-ion transference number (t_{Li}^{+}) calculated using Bruce-Vincent-Evans equation, DC polarization with the EIS spectra before and after polarization along with its corresponding equivalent circuit in the inset for (d) P5L03, (e) P5A03 and (f) PP respectively*

The function of a separator is not just to prevent the direct contact between anode and cathode, rather it directly impacts on the lithium-ion transport properties and consequently, the overall performance and safety of the cell. So, it's important to measure the lithium-ion transport properties of all the developed separator along with the commercial PP separator. ***Figure 8.4(a)*** represents the EIS spectra of electrolyte soaked LLZO and Al_2O_3 coated paper separators along with commercial separators, measured using symmetrical blocking electrodes (SS). The

corresponding equivalent circuit is also given in the inset of ***Figure 8.4(a)***. All the EIS spectra of different separators show a straight-line profile describing characteristic behaviour of electrode-electrolyte double layer capacitance. At the lower frequency region, the intercept on the real axis gives the bulk resistance value. The corresponding ionic conductivities of fabricated separators are estimated to be 1.11 mS/cm, 1.23 mS/cm, 1.04 mS/cm, 0.98 mS/cm, 0.73 mS/cm and 0.82 mS/cm for P5L01, P5L03, P5L05, P5L07, P5A03 and PP separator respectively. These values suggest that the inclusion of Li-ion active LLZO in the paper matrix is showing significantly higher ionic conductivities compared to inactive Al_2O_3. The insulating nature of Al_2O_3 particles in P5A03 thus may contribute to offer higher resistance, which may limit its overall electrochemical effectiveness.

Separator's electrochemical stability against the overall potential of the cell may affect the durability of lithium-ion battery and its compatibility against any commercial cathode or anode materials. The linear sweep voltammetry (LSV) of all the developed and commercial separator has been carried out ranging from 0 to 6.5 V at room temperature and displayed in ***Figure 8.4(b)***. The electrochemical potential window of LLZO separator is estimated to be in the range of 5.0-6.0V and appears to be suitable for high voltage lithium-ion batteries. It is worthy to mention here that with the increasing content of LLZO particles in the paper matrix the electrochemical potential window increases systematically which suggest that LLZO particle collectively improving the stability of the electrolyte-soaked paper separator by preventing its electrochemical decomposition at voltages >5V.

The understanding of transport phenomena through lithium-ion transference number is essential as it describes the ion transport efficacy, reduction of concentration polarization which in turn enhances the cycle life and power density of a battery. ***Figures 8.4(e)-(g)*** represent the DC polarization curve along with the EIS spectra before and after polarization, and its corresponding equivalent circuit is displayed in the inset for specimens P5L03, P5A03 and PP respectively. Lithium-ion transference number calculated using Bruce-Vincent-Evans equation as described in experimental chapter and found to be 0.21 for PP, 0.35 for P5A03 and 0.64 for P5L03 separators. A significant enhancement in lithium-ion transference number for LLZO coated paper separator (P5L03) is observed which suggests that an additional conduction pathway for lithium ions exists in the separator matrix which may facilitate ionic mobility in synchronization to the electrolyte pathway. However, such benefit is absent in Al_2O_3 coated paper-based, as well as in commercial PP separator. ***Figure 8.4(c)*** represents variation of lithium-ion transference number of developed paper-based separators and commercial

separator. It is interesting to observe that with the increasing content of LLZO in paper-based separators, the lithium-ion transference number first increases, reaches to a maximum value and then decreases. It may be due to the factors associated with the blocking pathways by LLZO agglomerates in paper matrix, followed by less electrolyte wettability. In summary, it can inferred that the optimum concentration of LLZO particle in paper separator is 30 wt% loading based on the parameters such as ionic conductivity and lithium-ion transport efficacy at room temperature. The in-cell electrochemical performance of developed LLZO paper may clear this fact more profoundly.

8.3.5 Electrochemical Performance

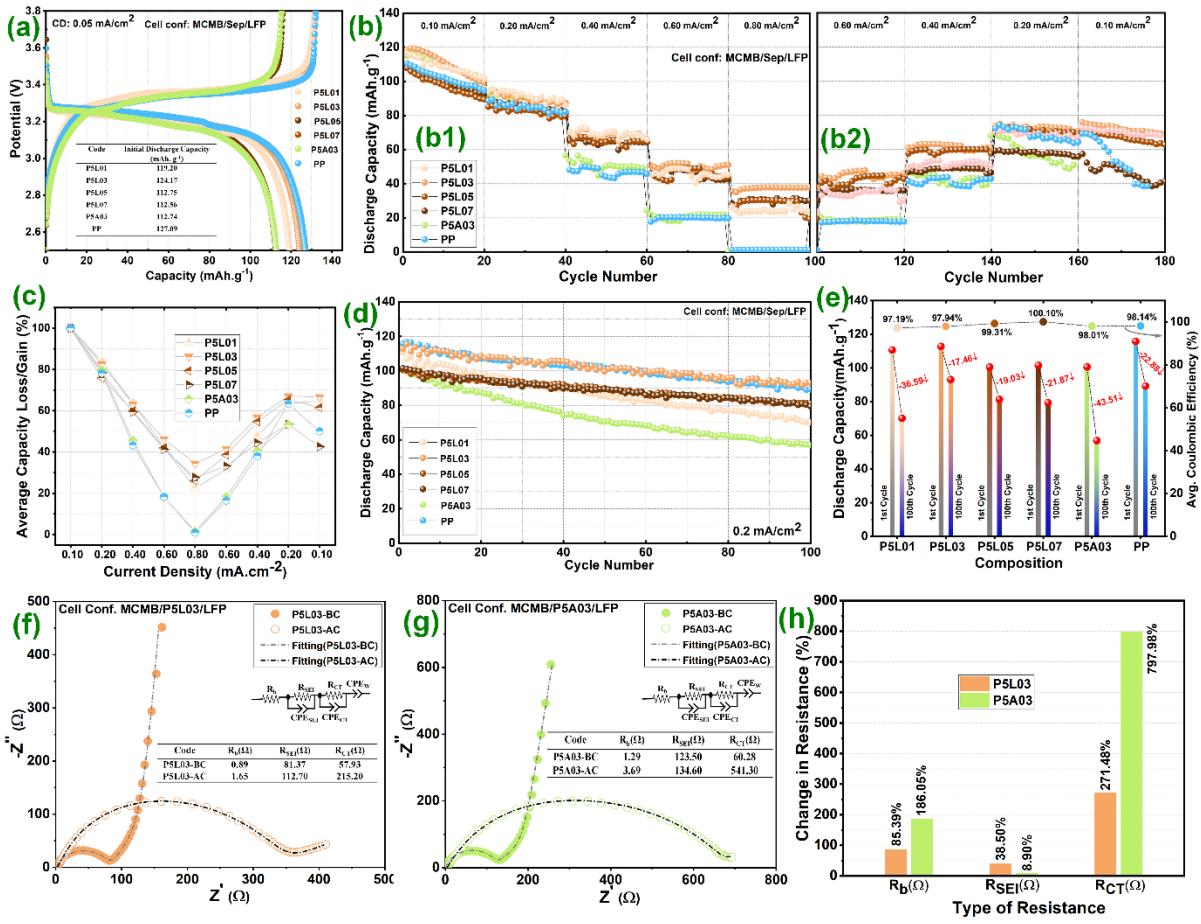

Figure 8.5 *Electrochemical characterizations of all the developed paper separators (P5L01, P5L03, P5L05, P5L07 and P5A03) as well as of the commercial separator (PP): (a) typical charge-discharge profiles, (b) capacity vs cycle number plots with varying current densities from 0.1 mA.cm^{-2} to 0.8 mA.cm^{-2} in (b1) forward and (b2) reverse directions, (c) summary of average capacity loss or gain in different current densities, (d) long cycling profiles and (e) their summary for the different separators, (f) EIS spectra of MCMB/P5L03/LFP cell before*

cycling (BC) and after cycling (AC), (g) EIS spectra of MCMB/P5A03/LFP cell before cycling and after cycling, (h) summary plot of change in different type of resistance values before and after cycling

The full cell performances have been carried out using the developed separators as well as the commercial PP separator in 2032 type coil cells with MCMB/separator/LFP configuration. Each cell is initially cycled at a very low current density of 0.05 $mAcm^{-2}$ to form smooth migration paths for the Li-ions. The typical charge-discharge profiles of these formation cycles for all the separators are shown in **Figure 8.5(a)**. The discharge capacities of P5L01, P5L03, P5L05 and P5L07 separators are found to be 119.20 $mAhg^{-1}$, 124.17 $mAhg^{-1}$, 112.75 $mAhg^{-1}$ and 112.56 $mAhg^{-1}$ respectively. The discharge capacity of P5A03 separator (112.74 $mAhg^{-1}$) also fall in the similar region, whereas the commercial PP separator shows a much higher capacity of 127.09 $mAhg^{-1}$. Analyzing all the specific capacity values, it is understood that the P5L03 separator with 30 wt% LLZO impregnation gives almost similar capacity as that of the commercial separator (PP).

To further examine the correlation of LLZO impregnation with full cell performance, the MCMB/LFP cells are cycled at various current densities ranging from 0.10 $mAcm^{-2}$ to 0.80 $mA.cm^{-2}$ and the profiles are displayed in ***Figure 8.5(b1)***. The cells are undergone to lower current densities stepwise to estimate the reversible capacity losses during cycling for a particular current density, as shown in ***Figure 8.5(b2)***. As the current density is gradually increased, the average capacities of the cells got decreased irrespective of the separator compositions and vice versa. The percentages of loss or gain in the average capacity values obtained from ***Figure 8.5(b)*** are summarized in ***Figure 8.5(c)***. It is clearly visible that PP and P5A03 face capacity loss of almost 100% in the highest current density of 0.80 $mAcm^{-2}$, whereas the all LLZO impregnated paper separators can retain up to 20-35% capacity at that current density. Although all LLZO based paper separators cycles better than PP and P5A03 (with inert filler) at higher current densities, 30 wt% LLZO impregnation delivers the best capacity retention among all. The electrochemical cycling performance of P5L03 is thus corroborates to its superior physical and electrical performances compared to its analogous varieties. Compared to P5L03, the capacity degradation in 50 wt% and 70 wt% LLZO may be due their large agglomeration which leads to the blocking of pore spaces in separator matrix, comparatively lower electrolyte wettability, and lithium transference numbers. Different electrical and electrochemical parameters of P5L01, P5L03, P5L05, P5L07, P5A03 and commercial PP separators are summarized in ***Table 8.3***.

Table 8.3 *A summary of different electrical and electrochemical parameters of P5L01, P5L03, P5L05, P5L07, P5A03 and commercial PP separators*

Code	Electrical Performance			Electrochemical performance	
	σ_i (mS. cm^{-1})	Window (V)	t_{Li}^+	Initial Capacity (mAh.g-1)	Capacity Retention @100 Cycles (%)
P5L01	1.11	5.36	0.55	119.20	63.41
P5L03	1.23	5.54	0.64	124.17	82.54
P5L05	1.04	5.70	0.59	112.75	80.97
P5L07	0.98	5.95	0.51	112.56	78.13
P5A03	0.73	5.15	0.35	112.74	56.49
PP	0.82	5.14	0.21	127.09	77.12

Here, σ_i stands for the ionic conductivity of electrolyte.

The long cycling profiles of the developed paper separators (P5L01, P5L03, P5L05, P5L07 and P5A03) as well as the commercial separator (PP) at a current density of 0.20 mA.cm^{-2} are displayed in ***Figure 8.5(d)***. P5L03 separator shows superior cycling performance compared to all other paper separators and almost reflecting the similar cycling profile like PP up to 100 cycles as examined. Among all, the full cell with commercial PP separator shows the highest initial capacity of 115.67 mAh.g^{-1} which decreases to 89.20 mAh.g^{-1} after 100 cycles, showing 22.88% decay in the capacity. The full cell with P5L03 separator starts with slightly lower initial capacity of 112.76 mAh.g^{-1} than PP, however it shows more stable cycling performance with only 17.46% capacity degradation even after 100 cycles. LLZO impregnated other separators such as P5L01, P5L05 and P5L07 show higher losses in capacities, i.e., 36.59%, 19.03% and 21.87% respectively. On the other hand, alumina coated paper separator P5A03 shows the highest capacity loss of 43.51% with respect to their initial capacity. All the data are summarized in ***Figure 8.5(e)*** which further corroborates that the introduction of Li-ion conducting material in paper matrix has profound effect in cycling life as well as cell performances.

To further pinpoint the causes of capacity degradation phenomena in Al_2O_3 coated paper separator and LLZO coated paper separator, EIS spectra was taken before and after the long cycling. ***Figure 8.5(f)*** and ***(g)*** represent the EIS spectra before and after cycling along with the equivalent circuit in the inset for P5L03 and P5A03 respectively. Here, the equivalent circuit comprises of three distinct resistance components: (i) R_b which denotes the bulk resistance or

the electrolyte resistance of the cell, (ii) R_{SEI} originates due to the solid electrolyte interphase (SEI) formed at the cathode-separator interface and (iii) R_{CT} attributes to the charge transfer resistances. After analyzing in Zview software, a summary plot has been given in ***Figure 8.5(h)*** describe the change of resistance in percentage due to electrochemical cycling for P5L03 and P5A03 separators. On analysis of EIS data, it is observed that all the three distinct resistances increase after the completion of 100 cycles. While the electrolyte resistance increases more than 85.39% for P5L03 and 186.05% for P5A03 separator before and after cycling, the SEI resistance changes from 81.37Ω to 112.70Ω for P5L03 and 123.50Ω to 134.60Ω for P5A03. More interestingly, the charge transfer resistance increases 797.98% for Al_2O_3 coated paper separator, whereas it increases only 271.48% for LLZO coated separator. Therefore, higher increment in electrolyte resistance and charge transfer resistance for Al_2O_3 coated paper separator causes the capacity degradation which may be due to the insulating nature of the Al_2O_3 particle that might create a barrier for lithium-ion movement at the electrode-electrolyte interface. In a similar fashion, thinner SEI layer due to less interaction with the electrolyte leads to no significant increment in SEI resistance for Al_2O_3 coated paper separator during cycling. On the other side, LLZO, being an ionic conductor, can provide more uniform and efficient ion transport, further lowering the electrolyte and charge transfer resistance. Also, LLZO can react with the electrolyte to form a stable SEI layer, leading to higher SEI resistance during cycling. Therefore, the EIS analysis further corroborates that the LLZO impregnated paper separator has superior compatibilities than the Al_2O_3 coating paper separator with the electrodes (anode and cathode).

8.3.6 Multielectrode Compatibility

Figure 8.6 describes the typical charge discharge profile and long cycling plots of the developed separators (P5L03 and P5A03) along with commercial PP using LTO anode and four different cathodes. As shown in ***Figure 8.6(a)***, for a cell configuration of LCO/Separator/LTO, LLZO coated paper separator delivers initial specific discharge capacity of 123.46 $mAh.g^{-1}$, whereas Al_2O_3 coated paper separator and commercial PP separator delivers capacities of 113.43 $mAh.g^{-1}$and 125.54 $mAh.g^{-1}$ respectively at a current density of 0.05 $mA.cm^{-2}$. The long cycling test in ***Figure 8.6(b)*** suggests that an impressive capacity retention of 94.99% was observed for LLZO coated paper separator. In comparison, capacity retentions of 80.20% and 88.67% are observed for Al_2O_3 coated paper separator and commercial PP separator. In LMO/Separator/LTO cells, all the separators deliver an initial discharge capacity in the range of 92-86 $mAh.g^{-1}$ as shown in ***Figure 8.6(c)***. Although, during cycling at 0.2 $mA.cm^{-2}$, LLZO

coated paper separator exhibits no capacity loss, whereas, Al_2O_3 coated paper separator and commercial PP separator retain more than 75% capacity after 100 cycles as shown ***in Figure 8.6(d)***.

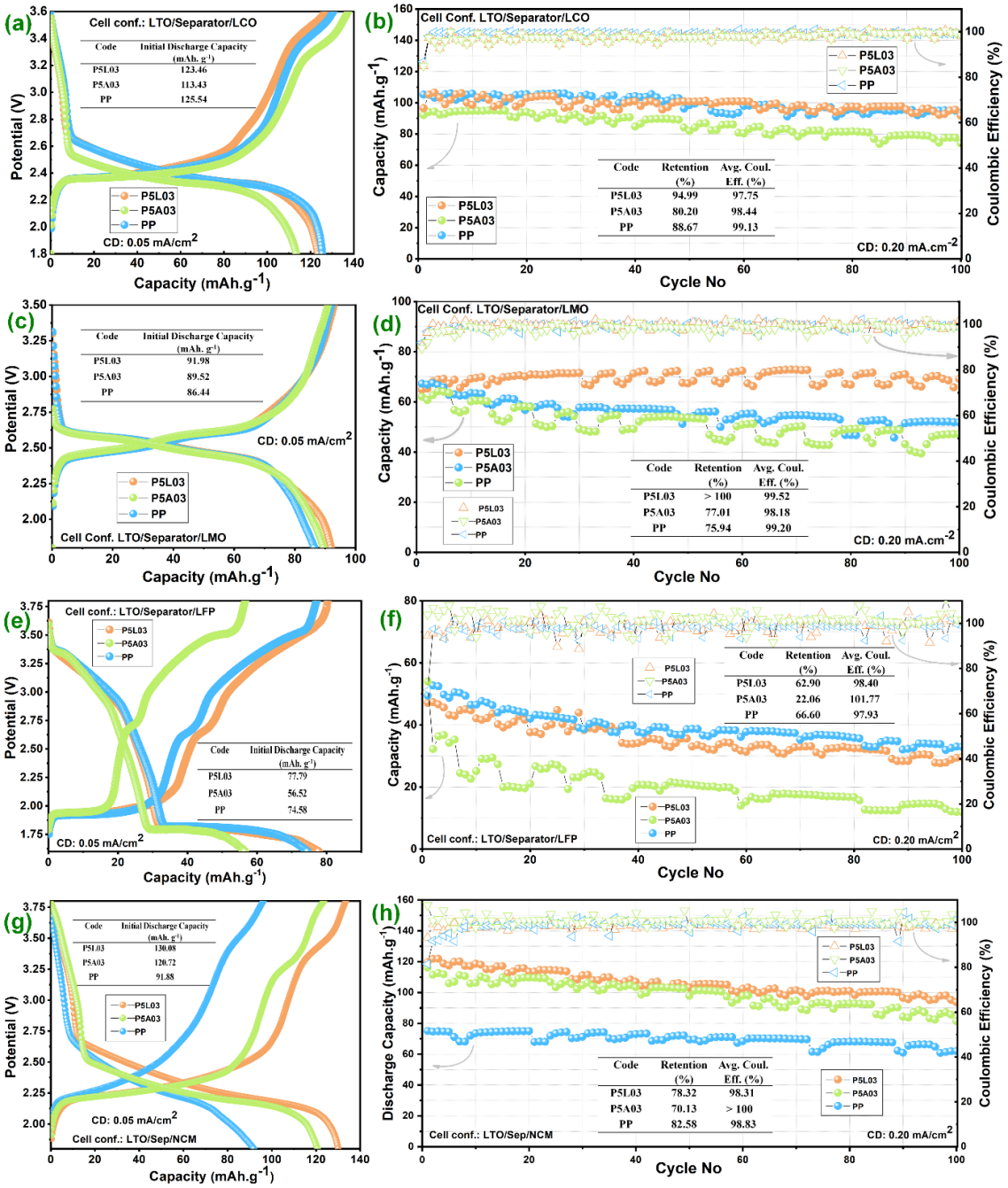

Figure 8.6 *Electrochemical compatibility of developed paper separators (P5L03, P5A03) and commercial separator (PP) with LTO anode and different cathodes; showing typical charge discharge profile and long cycling behavior against (a) & (b) LCO, (c) & (d) LMO, (e) & (f) LFP and (g) & (h) NCM respectively*

For LFP/Separator/LTO cell configuration, LLZO coated paper separator and commercial PP separator show an initial discharge capacity in the range of 74-78 mAh.g^{-1}, but Al_2O_3 coated paper separator delivers an initial discharge capacity of 56.52 mAh.g^{-1} as shown in ***Figure 8.6(e)***. In the similar manner at long cycling, Al_2O_3 coated paper separator shows a poor capacity retention of 22.06%, whereas LLZO coated paper separator and commercial PP separator retain more than 60% capacity after 100 cycles as shown in ***Figure 8.6(f)***. In a cell configuration of NCM/Separator/LTO, LLZO coated and Al_2O_3 coated paper separator deliver an initial discharge capacity of 130.08 mAh.g^{-1}and 120.72 mAh.g^{-1} respectively, although commercial PP separator delivers a poor capacity of 91.88 mAh.g^{-1} as shown in ***Figure 8.6(g)***. In long cycling in ***Figure 8.6(h)***, all the cells retain more than 70% capacity after 100 cycles. All the separators maintain an impressive average coulombic efficiency of more than 97% over any combination of cathode used against LTO anode.

Figure 8.7 shows the electrode compatibility of our developed and commercial separators using MCMB anode and four different cathodes (LCO, LMO, LFP, NCM). In LCO/Separator/MCMB cells, LLZO coated paper separator i.e. P5L03 delivers an impressive initial discharge capacity of 195.47 mAh.g^{-1}, whereas P5A03 and commercial PP separator deliver initial capacity in the range of 184-186 mAh.g^{-1} at a current density of 0.05 mA.cm^{-2} as shown in ***Figure 8.7(a)***, although very poor coulombic efficiencies at initial cycle are observed for all the fabricated cells. During long cycling at 0.20 mA.cm^{-2}, all the cells are unable to retain their capacity which leads to rapid rate of discharge as shown in ***Figure 8.7(b)***. For a cell configuration of LMO/Separator/MCMB, developed paper separators and commercial PP separator deliver an initial discharge capacity in the range of 68-76 mAh.g^{-1} as shown in ***Figure 8.7(c)*** and during long cycling at a current density of 0.20 mA.cm^{-2}, all the separator retains more than 70% of capacities as presented in ***Figure 8.7(d)***. In an LFP/Separator/MCMB cell combination, P5L03 and commercial PP separators deliver higher initial capacities than the Al_2O_3 coated paper separator as shown in ***Figure 8.7(e)***. In similar fashion, P5A03 shows very poor performance and only retained 56.49% of capacity after 100 cycles, whereas LLZO coated paper separator and commercial PP separator retain more than 75% of capacity as shown in ***Figure 8.7(f)***. For NCM/Separator/MCMB cells, P5L03 separator delivers a higher initial capacity of 176.92 mAh.g^{-1} than P5A03 and commercial PP separator as shown in ***Figure 8.7(g)***. During cycling at 0.20 mA.cm^{-2}, all the separator shows consistent performances in terms of capacity retention of more than 70% as shown in ***Figure 8.7(h)***. All the developed paper separators and commercial separator maintain an excellent average coulombic efficiency

of more than 97% over any combination of cathode used against MCMB anode. A summary of electrochemical performances of three different separator (P5L03, P5A03 and PP) during multi electrodes compatibility test is presented in ***Table 8.4***. Among all the separators, LLZO coated paper separator shows a better and more consistent performance against the combination of two different anodes and four cathodes.

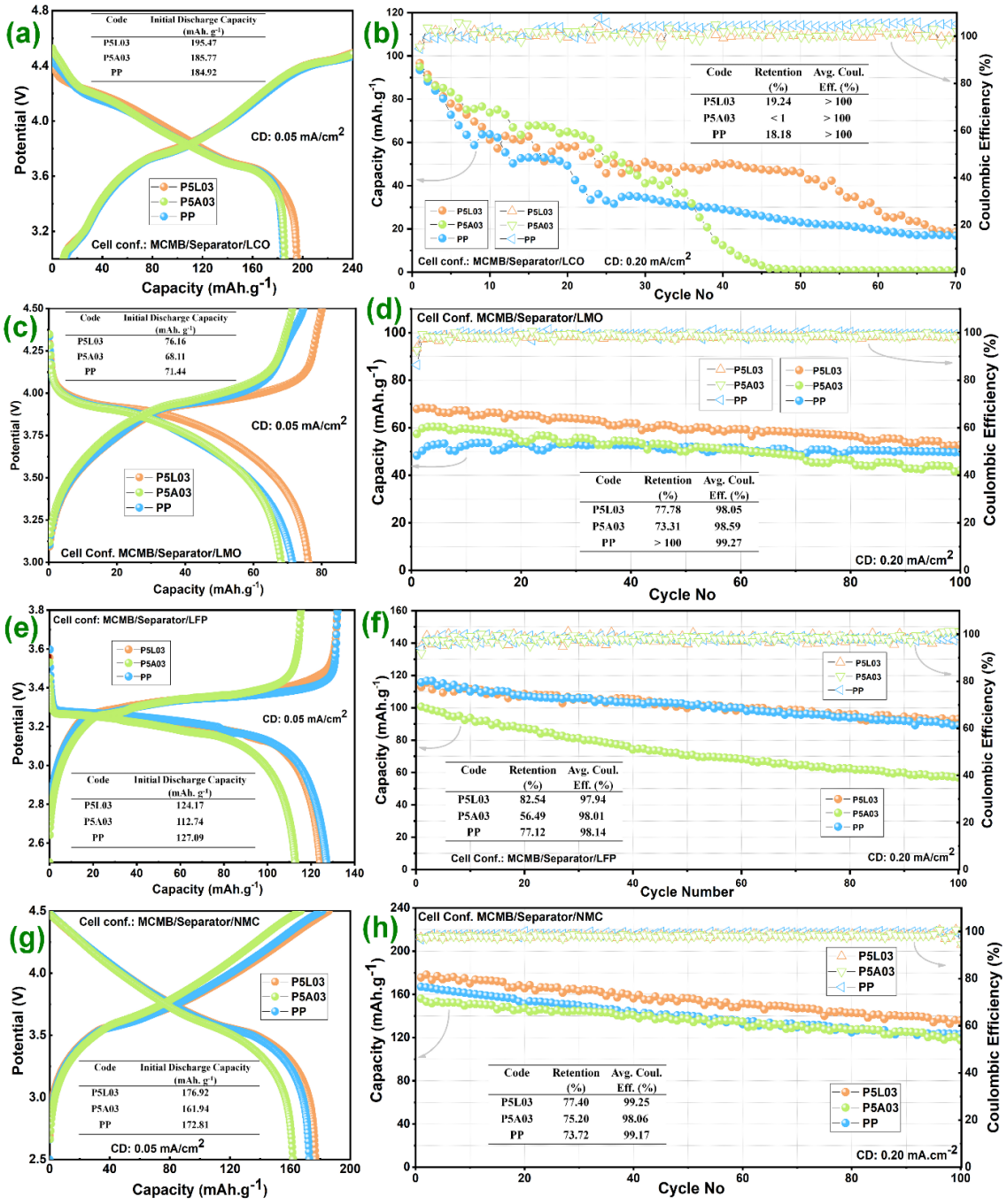

Figure 8.7 *Electrochemical compatibility of developed paper separators (P5L03, P5A03) and commercial separator (PP) with MCMB anode and different cathodes; showing typical charge*

discharge profile and long cycling behavior against (a) & (b) LCO, (c) & (d) LMO, (e) & (f) LFP and (g) & (h) NCM respectively

Table 8.4 *A summary of electrochemical performances of three different separator (P5L03, P5A03 and PP) during multi electrodes compatibility test*

Cell Conf.	Sep.	Initial Capacity ($mAh.g^{-1}$)	Avg Cou. Effi. (%)	Capacity retention (%)
LTO/Sep./LCO	P5L03	123.5	97.8	94.9
	P5A03	113.4	98.4	80.2
	PP	125.5	99.1	88.7
LTO/Sep./LMO	P5L03	91.9	99.5	>100
	P5A03	89.5	98.2	77.0
	PP	86.4	99.2	75.9
LTO/Sep./LFP	P5L03	77.8	98.4	62.9
	P5A03	56.5	>100	22.1
	PP	74.6	97.9	66.6
LTO/Sep./NMC	P5L03	130.1	98.3	78.3
	P5A03	120.7	>100	70.1
	PP	91.9	98.8	82.6
MCMB/Sep./LCO	P5L03	195.5	>100*	19.2*
	P5A03	185.8	>100*	<1*
	PP	184.9	>100*	18.18*
MCMB/Sep./LMO	P5L03	76.2	98.1	77.8
	P5A03	68.1	98.6	73.3
	PP	71.4	99.3	>100
MCMB/Sep./LFP	P5L03	124.2	97.9	82.5
	P5A03	112.7	98.0	56.5
	PP	127.1	98.1	77.1
MCMB/Sep./NMC	P5L03	176.9	99.3	77.4
	P5A03	161.9	98.1	75.2
	PP	172.8	99.2	73.7

Capacity retention and average coulombic efficiency were calculated after 70 cycles.

8.3.7 Thermal, Flame-Retardant, and Shock-Resistant Properties

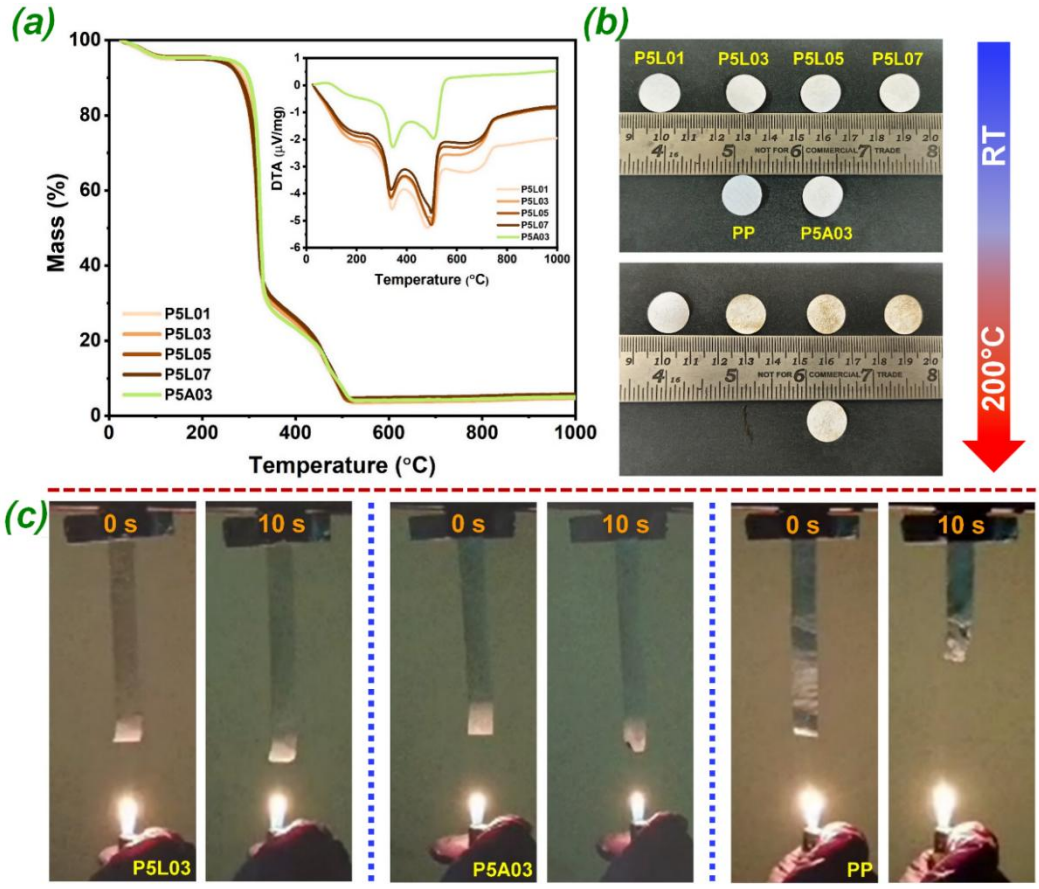

Figure 8.8 *(a) Thermogravimetric Analysis (TGA) plots of the developed paper separators (P5L01, P5L03, P5L05, P5L07 and P5A03) with their Differential Thermal Analysis (DTA) plots in the inset; (b) Qualitative thermal shrinkage analysis of the developed paper separators and commercial PP separator at room temperature (RT) and at 200ºC (30 min at each temperature); (c) Flame test for P5L03, P5A03 and PP*

Even after achieving good ionic conductivity, long cycle life, high-rate capability and multielectrode compatibility, it still remains very important for a separator to achieve high thermal stability and flame-retardant characteristics for its practical use in a lithium-ion battery. Thermogravimetric analysis can test the thermal stability of a separator in a broad range of temperature. It also helps to detect the presence of moisture or any volatile substance inside the separator matrix. In ***Figure 8.8(a)***, the degradation in masses of the separators from RT to 120ºC temperature is mainly due to the removal of surface moisture that was present on the separator surfaces. Apart from that, there is intrinsic moisture also present inside the paper matrices, which gets removed in the region of 120-280ºC. After this stage, pyrolysis of polymer binder used during separator fabrication takes place with a remarkable weight loss in between

280ºC to 360ºC. And the last stage where the separators again lose majority of their remaining masses lies between 360ºC to 500ºC. Here, only the volatile substances present inside the separators release gradually. After 500ºC, there is no significant loss in the separator weights as only the thermally stable ceramic particles remain inside the matrices[25]. The TGA curves in ***Figure 8.8(a)*** and the DTA curves in its inset deliver nearly similar thermal characteristics for all the developed paper separators. From the TG analysis, an idea of how the paper separators can behave in high temperatures can be derived easily. To compare their behavior with the commercial separator, a qualitative thermal shrinkage experiment has been carried out and depicted in ***Figure 8.8(b)***. Although all the separators maintain same dimension at room temperature, the commercial separator shows a huge dimensional shrinkage when the temperature rises to 200ºC. On the other hand, there was no notable change in the dimensions of any of the paper separators at such this elevated temperature. This ensures the safety and lesser chances of short-circuit inside the Li-ion cells when paper-based separators are used.

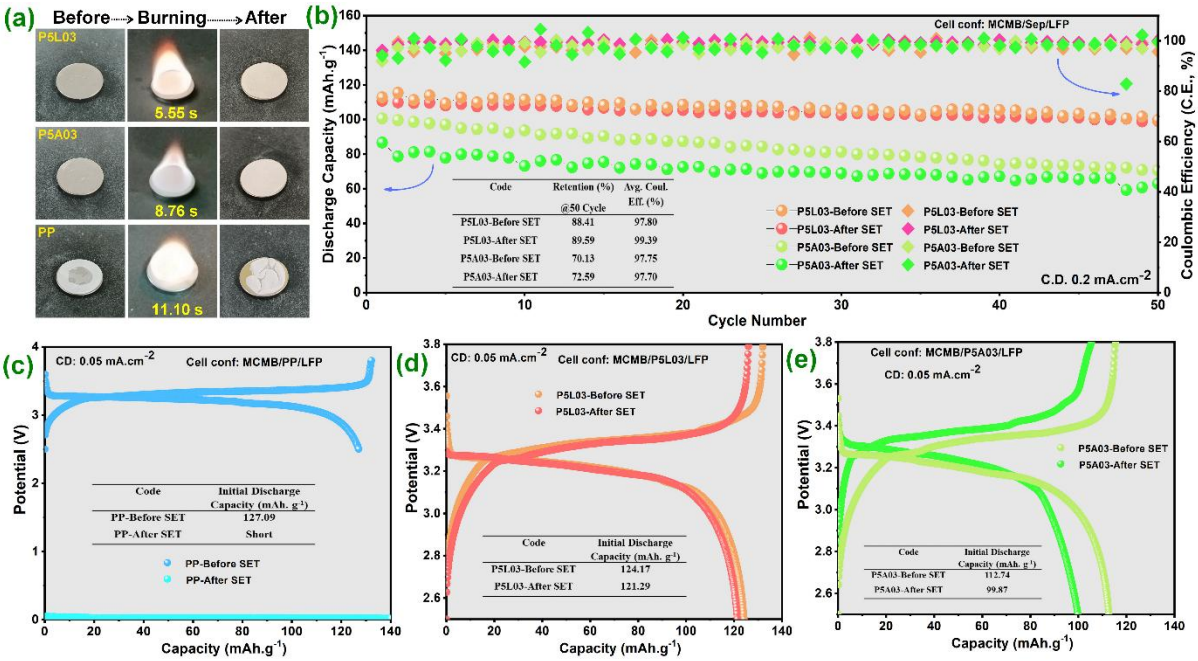

Figure 8.9 *(a) Visualization of self-extinguishing time (SET) test for P5L03, P5A03 and PP separators; (b) Electrochemical long cycling of the separators before and after SET in MCMB/separator/LFP configuration; Typical charge-discharge profiles before and after SET for (c) PP, (d) P5L03 and (e) P5A03*

Polypropylene and cellulose both have tendency to catch fire very easily, however treatment with certain polymer and ceramic can make the separator membranes flame resistant and safe. To clarify this fact, a vertical burning test was carried out by keeping the flame at a certain

distance from the separator specimens. This time also, P5L03 separator outperformed the other two by remaining dimensionally intact even after exposure of more than 10 seconds. When alumina-based paper separator P5A03 although performs well with a very little amount of char formation at the end, the electrolyte-soaked commercial separator catches fire after 2-3 seconds only as can be observed in ***Figure 8.8(c).***

Apart from the separator, another safety component in LIBs is the flammable organic liquid electrolyte which may catch fire very easily. Even after using cellulose based separators, some unavoidable risks may arise where the electrolyte soaked by the separator would catch fire. In such circumstances, a flame-retardant separator would be highly effective for ensuring the ultimate safety for the battery. Self-extinguishing time (SET) is an important parameter which can determine the fire resistance characteristics of separators as well as for electrolytes[26]. Since we are using commercial liquid electrolyte, i.e., $LiPF_6$ in EC: DMC in our cells, the SET is measured only for the separators. The less time a separator takes to fully extinguish the fire, the more effectively it can retard the flame on it. From Figure 6(a), it can be observed that the LLZO based paper separator P5L03 registers the least SET of 5.55 s among the three, making it the most suitable and safe separator for practical use inside LIBs. The SETs for P5A03 and PP are 8.76 s and 11.10 s respectively. Although, dimensions of P5L03 and P5A03 separator is not changed but commercial PP separator failed to maintained its dimensional stability in SET measurement as visualized in ***Figure 8.9(a)***. After the SET measurement, all the separators are vacuum dried over 48h and then stored in a glove box for electrochemical measurement. ***Figure 8.9(b)*** shows the electrochemical cycling behavior of P5L03 and P5A03 separators before and after the SET measurements in MCMB/separator/LFP full cell configuration. As compared to the before SET measurement, both the cells are maintained almost similar capacity retention. However, the discharge capacity is found to be less for P5A03 and almost identical for P5L03. Typical charge-discharge profile at a current density of 0.05 $mA.cm^{-2}$ are also shown in ***Figure 8.9(c)*** for PP, ***(d)*** for P5L03 and ***(e)*** for P5A03. As expected, the cell fabricated using commercial PP separator after the SET measurement is short circuit. As earlier, cell with P5A03 separator delivered less initial discharge capacity whereas P5L03 delivered similar discharge capacity before and after SET measurement suggesting that the LLZO coated paper separator shows better thermal retardant properties as compared to Al_2O_3 coated paper separator.

LLZO coated paper separator shows excellent thermal retardant and self-extinguishing properties for thermally durable high-performance batteries. While, it is equally important to evaluate the electrochemical and electrical performance of battery cells using various separator

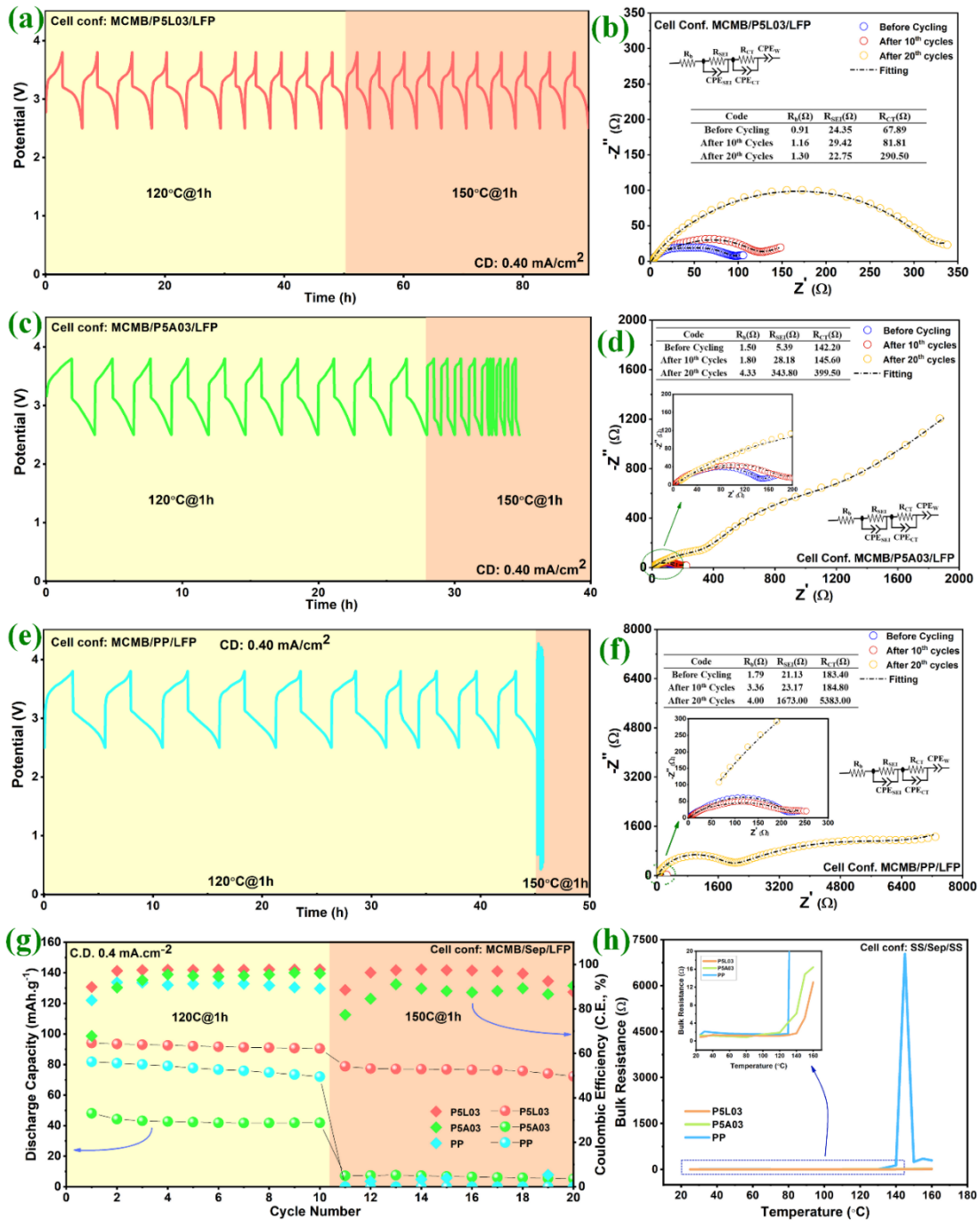

Figure 8.10 *Investigation of electrochemical and electrical properties of paper based develop separator along with commercial separator under vigorous thermal treatment; (a) & (b) Potential vs time plot after thermal shock treatment at two different temperature and corresponding changes in EIS spectra after cycling for P5L03 respectively. (c) & (d) Potential vs time plot after thermal shock treatment at two different temperature and corresponding changes in EIS spectra after cycling for P5A03 respectively. (e) & (f) Potential vs time plot after thermal shock treatment at two different temperature and corresponding changes in EIS spectra after cycling for P5L03 respectively. (g) Cycling behavior of developed separator and*

commercial PP separator after thermal shock treatment. (h) Thermal shutdown measurement by EIS method with temperature variation for P5L03, P5A03 and PP.

under vigorous thermal treatment to simulate real world thermal shock. Such measurement is essential to predict and understand any changes which is occur during thermal stress, particularly important for EV application where it is expected that the battery would operate at different challenging condition. In this scenario, full cells with LFP/Separators/MCMB configuration are fabricated using P5L03, P5A03 and commercial PP separator and undergone 10 cycles each after two different thermal shock treatment. All the cells are kept for 1h at 120°C and 150°C under vacuum and kept 24 hours in room temperature. After each thermal shock treatment, the electrochemical and electrical properties are carefully measured and summarized in ***Figure 8.10***. Cells with P5L03 separator shows no significant changes in electrochemical charge discharge profile at 0.40 $mA.cm^{-2}$ after two thermal shock treatment as shown in ***Figure 8.10(a)***. However, EIS studies reveled that no significant changes in electrolyte resistance and SEI resistance are observed but charge transfer resistance is increased almost ~ 330% for LLZO coated paper separator after 20 cycling as shown in ***Figure 8.10(b)***. Cell with P5A03 separator, shows stable potential vs time plot after thermal shock treatment at 120°C as presented in ***Figure 8.10(c)***. Although, unstable behavior of charge-discharge profile is observed after 150°C due to abrupt change in electrolyte, SEI and charge-transfer resistance as measured after 20 cycles, presented in ***Figure 8.10(d)***. For commercial PP separator, the cell delivers stable galvanostatic charge-discharge profile after thermal shock treatment at 120°C as shown in ***Figure 8.10(e)***, but lost all its capacity which is a sign of premature cell failure when the cell undergone thermal shock treatment at a temperature above the melting temperature of PP separator. The EIS studies reveled that significant rise in SEI and charge transfer resistance after 20 cycles, as presented in ***Figure 8.10(f)***. Cycling behavior of P5L03, P5A03 and PP separator after thermal treatment shown in ***Figure 8.10(g)***. Among all the cells, the cell with P5L03 separator delivers a stable cycling behavior with an average discharge capacity of around 92 and 78 $mAh.g^{-1}$ after 10 and 20 Cycles respectively. It also maintained a good average coulombic efficiencies of ~97% and ~95% after subsequent thermal treatment. Whereas, PP and P5A03 delivers an average discharge capacity of around 77 and 43 $mAh.g^{-1}$ and average coulombic efficiencies of ~90% and ~92% respectively after thermal shock treatment at 120°C. After 150°C, cell with PP separator loss it's all capacity and P5A03 delivers a poor average discharge capacity of around 7 $mAh.g^{-1}$ and average coulombic efficiencies of ~87%. So, LLZO coated paper separator delivers excellent electrochemical performance under

vigorous thermal treatment. Different behavior obtained for P5L03, P5A03 and PP separator during thermal stability test are summarized in ***Table 8.5***.

Table 8.5 *An overview of different behavior observed for P5L03, P5A03 and PP separator during thermal stability test*

Code	Shrinkage at 200°C	Flame retardant properties	Self-extinguishing (SE) properties		Electrical and electrochemical study after thermal shock treatment	
			SE time(s)	cell study	120°C/1h	150°C/1h
P5L03	No shrinkage	No flame or chur	5.55	No change	Stable charge-discharge cycling	Stable charge-discharge cycling, rise in R_{CT}
P5A03	No shrinkage	No flame but char formed	8.76	Initial capacity decreases	Stable cycling but significant rise in R_{SEI}	Rapid decay in discharge capacity, rise in R_b, R_{SEI} and R_{CT}
PP	Melted and shrink	Shrink/catches fire within 2-3 sec	11.10	Short after SE test	Stable cycling but rise in R_b	Lost all capacity, abruptly rise in R_{SEI} and R_{CT}

Figure 8.10(h) describes the shutdown characteristics of the separators. When there is a sudden rise in the environmental temperature of a battery, the polymer-based separators with their melting points in between 120ºC to 160ºC show a natural tendency to melt, due to which their pores get blocked and Li-ions face hindrance to move. This phenomenon of commercial polyolefin-based separators force to increase the resistance of the Li-ion cells at elevated temperatures. But natural polymer cellulose consists of a much higher melting temperature, due to which it shows no such shutdown phenomenon. These facts are clearly visible in ***Figure 8.10(h)*** where PP shows nearly 8000% increase in its resistance value at 140ºC, the paper separators P5L03 and P5A03 show only 30% and 118% increase respectively. In ***Table 8.5***, a comparison chart of Li ion active ceramic material coated separator developed in recent times are summarized along with the present work for better understanding.Analyzing the various thermal properties for the separators, it can be safely inferred that the LLZO coated paper separators not only show superior electrical and electrochemical performances, they hold significant thermal stability and flame resistivity which make them safe and suitable separator to be successfully used in commercial LIBs as well as in EV battery packs.

Table 8.6 *Comparison of Li-ion active ceramic-coated separators and their key properties*

Separator composition	d (µm)	σ_i (mS.cm^{-1})	Electrochemical cell performance	Thermal Stability	Ref
PVDF-HFP/LLZO thin film with 80% LLZO content	30	1.10	148.8 mAh.g^{-1} against $LiCoO_2$/graphite pouch cell, 92.3% retention @ 300 cycles at 0.5C	No thermal shrinkage at 160°C for 60mins, a thermal trigger for self-heating around 80°C and ignited after 1107 min	27
LTO coated on Al_2O_3 coated PE separator (PEAO-LTO)	32	0.72	173.2 mAh.g^{-1} in Li/LTO cell at 0.5C, 90.2% retention @100 cycles at 0.5C	Shrink only 1.1% at 160°C, consistent thermal distributions, highly flame retardant	28
$LiFePO_4$ coated PE separator with coating thickness is 28 µm	40	0.85	168.4 mAh.g^{-1} in Li/LFP cell at 0.5C, lower cycling stability that PE	Shrink only 1.1% at 140°C, uniform thermal distributions, highly flame resistance	29
LLTO coated PE separator	12	0.38	157.2 mAh.g^{-1} in NCM523/Graphite pouch cell at 0.5C,88.7% retention @1000 cycles at 1C.	Good thermal stability and no melting at 160°C	30
LLZO based polymer in ceramic membrane	75	2.80	Discharge capacity decreases rapidly in Li/NMC811 cell	Higher thermal stability and better retardation thermal runway propagation	31
LLZO-PVDF based nonwoven composite separator using electrospinning method	30	1.97	168 mAh.g^{-1} in NCM622/Graphite cell at 0.1C,97% retention @100 cycles at 3C in full cell and 86% retention @250 cycles at 0.5C at half cell	No thermal shrinkage at 150°C/30mins	32
PVDF-HFP-LLZO composite separator (4.29wt%)	25± 3	0.74	165.8 mAh.g^{-1} in Li/LFP cell at 0.1C, ~140 mAh.g^{-1} even after 500 cycles at 2C, ~160 mAh.g^{-1} even after 100 cycles at 0.5C	Uniform thermal distribution and no noticeable thermal shrinkage still 160°C	33
PVDF-LLZO (30wt%) coated paper separator	20± 2	1.23	124.17 mAh.g^{-1} in MCMB/LFP cell at 0.05 mA.cm^{-2}, 82.54% retention @100 cycles at 0.20 mA.cm^{-2}, Excellent Multi-electrode compatibility	No shrinkage at 200°C, Low Self-extinguishing time (SET), Highly flame retardant and thermal shock resistive even at 150°C	This Work

Here, d stands for the thickness of separator and σ_i for the ionic conductivity of electrolyte.

8.4 Conclusion

This study demonstrates the successful development of an eco-friendly, cost-effective, and flexible paper-based separator impregnated with Li-ion active LLZO using a scalable wet-coating process. The LLZO powders were synthesized through an aqueous alanine-assisted auto-combustion method and incorporated into cellulose matrices with various loadings. All the fabricated separators showed high porosity, excellent electrolyte uptake, good mechanical robustness, and remarkable dimensional stability above 200 °C.

Among the developed separator, the 30 wt% LLZO-loaded paper separator (P5L03) proved optimal, delivering the highest ionic conductivity (1.23 mS cm^{-1}), superior Li-ion transference number (0.64), and excellent electrochemical stability across diverse cell configurations. In contrast, the Al_2O_3-based separator (P5A03) showed only moderate transport properties and poor long-term cycling behavior. Comparative studies further confirmed that LLZO impregnation enhances the ionic transport, thermal durability, flame retardancy, and self-extinguishing ability, outperforming both Al_2O_3-based and commercial PP separators.

Overall, this chapter highlights the dual role of LLZO as both a structural stabilizer and an active ion conductor within a sustainable cellulose framework. The developed LLZO-paper separator offers a balance between safety and electrochemical performances. Thus, LLZO impregnated paper separator emerging as a promising candidate to replace the conventional polyolefin separators in next-generation lithium-ion batteries.

References

1 P. Albrechtowicz, *Energy Reports*, DOI:10.1016/j.egyr.2023.02.088.

2 Y. Gao, Z. Pan, J. Sun, Z. Liu and J. Wang, 2022, preprint, DOI: 10.1007/s40820-022-00844-2.

3 B. Kennedy, D. Patterson and S. Camilleri, *J Power Sources*, DOI:10.1016/S0378-7753(00)00402-X.

4 Y. Miao, P. Hynan, A. Von Jouanne and A. Yokochi, 2019, preprint, DOI: 10.3390/en12061074.

5 J. Li, Y. Zhang, R. Shang, C. Cheng, Y. Cheng, J. Xing, Z. Wei and Y. Zhao, 2021, preprint, DOI: 10.1016/j.ensm.2021.08.046.

6 H. Chen, Z. Wang, Y. Feng, S. Cai, H. Gao, Z. Wei and Y. Zhao, 2023, preprint, DOI: 10.1016/j.cej.2023.144593.

7 W. Zhao, J. Yi, P. He and H. Zhou, 2019, preprint, DOI: 10.1007/s41918-019-00048-0.

8 X. Zeng, Y. Liu, R. He, T. Li, Y. Hu, C. Wang, J. Xu, L. Wang and H. Wang, *Cellulose*, DOI:10.1007/s10570-022-04499-5.

9 K. Ghosh and M. Wasim Raja, *ACS Appl Energy Mater*, DOI:10.1021/acsaem.3c00291.

10 P. Fleming, R. A. Farrell, J. D. Holmes and M. A. Morris, *Journal of the American Ceramic Society*, DOI:10.1111/j.1551-2916.2009.03564.x.

11 K. Ghosh and M. Wasim Raja, *ACS Omega*, DOI:10.1021/acsomega.2c04012.

12 A. Ansari, A. Ali, M. Asif and Shamsuzzaman, *New Journal of Chemistry*, DOI:10.1039/c7nj03742b.

13 K. Ghosh and M. Wasim Raja, *Chemical Engineering Journal*, DOI:10.1016/j.cej.2023.148200.

14 D. Bossert, C. Geers, M. I. P. Peña, T. Volkmer, B. Rothen-Rutishauser and A. Petri-Fink, *Chemistry (Switzerland)*, DOI:10.3390/chemistry2020023.

15 M. Das, P. S. Das, N. C. Pramanik, R. N. Basu and M. Wasim Raja, *ACS Omega*, DOI:10.1021/acsomega.3c02859.

16 D. Myśliwiec, M. Chylińska, M. Szymańska-Chargot, S. Chibowski and A. Zdunek, *Cellulose*, 2016, **23**, 2819–2829.

17 F. Cheng, M. Lorch, S. M. Sajedin, S. M. Kelly and A. Kornherr, *ChemSusChem*, DOI:10.1002/cssc.201300305.

18 D. M. D. Babiker, C. Wan, B. Mansoor, Z. R. Usha, R. Yu, J. C. Habumugisha, W. Chen, X. Chen and L. Li, *Compos B Eng*, DOI:10.1016/j.compositesb.2021.108658.

19 E. Lizundia, C. M. Costa, R. Alves and S. Lanceros-Méndez, *Carbohydrate Polymer Technologies and Applications*, 2020, **1**, 100001.

20 W. Lin, F. Wang, H. Wang, H. Li, Y. Fan, D. Chan, S. Chen, Y. Tang and Y. Zhang, 2022, preprint, DOI: 10.1002/cssc.202201464.

21 R. Xu, H. Huang, Z. Tian, J. Xie and C. Lei, *Polymers (Basel)*, DOI:10.3390/polym12010117.

22 M. Das, P. S. Das, R. N. Basu and M. W. Raja, *Cellulose*, DOI:10.1007/s10570-022-04873-3.

23 J. Xing, J. Li, W. Fan, T. Zhao, X. Chen, H. Li, Y. Cui, Z. Wei and Y. Zhao, 2022, preprint, DOI: 10.1016/j.compositesb.2022.110105.

24 J. C. Roberts, *The Chemistry of Paper*, 1996.

25 J. L. Yang, X. X. Zhao, W. Zhang, K. Ren, X. X. Luo, J. M. Cao, S. H. Zheng, W. L. Li and X. L. Wu, *Angewandte Chemie - International Edition*, DOI:10.1002/anie.202300258.

26 Y. Roh, D. Kim, D. Jin, D. Kim, C. Han, J. Choi, H. Lee, Y. G. Lee and Y. M. Lee, *Chemical Engineering Journal*, DOI:10.1016/j.cej.2023.145937.

27 Y. C. Jung, S. K. Kim, M. S. Kim, J. H. Lee, M. S. Han, D. H. Kim, W. C. Shin, M. Ue and D. W. Kim, *J Power Sources*, 2015, **293**, 675–683.

28 M. V. M. Nitou, M. Tang, Y. Niu, Y. Pang, Z. Wan, S. E. Mawuli, J. A. Leoba, F. Xiaodong and W. Lv, *J Power Sources*, 2024, **602**, 234406.

29 M. V. M. Nitou, Y. Pang, Z. Wan, W. Li, Z. Zhong, W. Muhammad, S. Muhammad, S. Muhammad, Y. Niu and W. Lv, *Journal of Energy Chemistry*, 2023, **86**, 490–498.

30 Y. Feng, M. Wang, L. Gao, Z. He, K. Chen, Z. Li, H. He and Y. Lin, *Journal of Materiomics*, 2022, **8**, 1184–1190.

31 E. J. Cheng, K. Nishikawa, T. Abe and K. Kanamura, *Ionics (Kiel)*, 2022, **28**, 5089–5097.

32 J. Kim, S. Lee, W. J. Song and K. J. Lee, *J Alloys Compd*, 2023, **968**, 171882.

33 X. Shi, Q. Sun, B. Boateng, Y. Niu, Y. Han, W. Lv and W. He, *J Power Sources*, 2019, **414**, 225–232.

Chapter 9

Composite Solid Polymer Electrolytes for Paper-Supported Solid-State Li-metal Batteries

Highlights

- Ceramic fillers in polymer electrolytes tune crystallinity, interfacial stability, and overall electrochemical performance
- Zirconia-incorporation induces superior conductivity, mechanical robustness, and stable Li-metal cycling
- Duo-polymer design enhances ionic transport, while cellulose reinforcement provides mechanical strength and safety
- Paper-based CSPEs emerge as scalable and flexible electrolytes for next-generation all solid-state flexible paper batteries

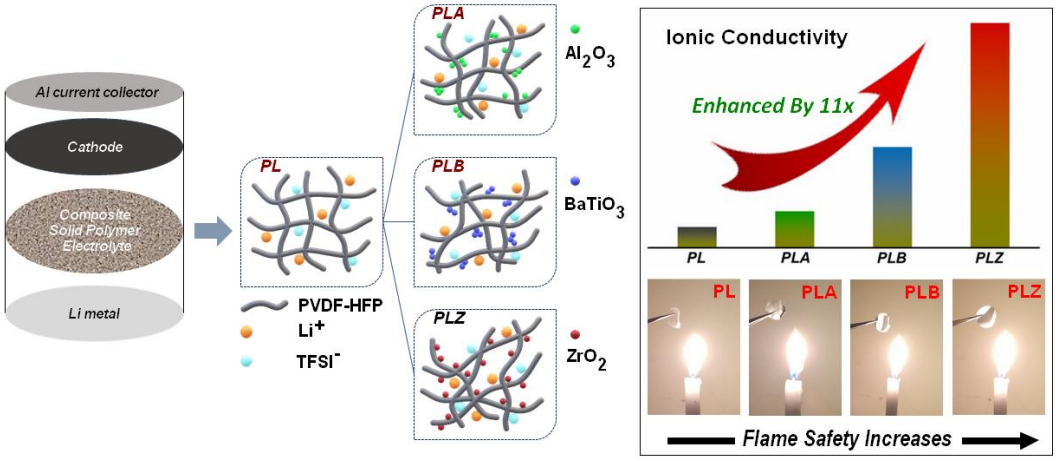

Figure 9.0 *Graphical abstract*

This chapter presents the development of composite solid polymer electrolytes tailored for safe and flexible solid-state lithium batteries. By incorporating ceramic fillers into a PVDF-HFP matrix, the study demonstrates how polymer–ceramic interactions govern conductivity, stability, and mechanical strength. Zirconia emerged as the most effective filler, offering enhanced ionic transport and interfacial stability. A duo-polymer strategy with PEO further improved conductivity, while cellulose reinforcement enabled scalable, robust, and flame-safe paper-based membranes. Together, these approaches establish a pathway toward next-generation electrolytes that balance performance, safety, and sustainability for advanced lithium-metal and paper-based battery technologies.

9.1 Background and Overview

Both liquid electrolyte and polyolefin-based separator pose serious safety concerns on applicability of LIBs, especially in EVs and high safety applications like medical devices, portable electronics etc. Here, solid electrolytes can be an effective alternative of both, since they do not present any risk of leakage and flammability, and can additionally provide a wider electrochemical stability window, high performance, and good compatibility with Lithium metal anodes[1]. Solid electrolytes can be of three major types: (a) inorganic solid electrolytes (ISEs), (b) solid polymer electrolytes (SPEs), and (c) composite solid polymer electrolytes (CSPEs)[2,3]. The inorganic solid electrolytes like oxides (LLZO, LLTO), phosphates (LATP), sulfides (LSPSCl), etc, mostly have high ionic conductivity and excellent thermal stability, suitable for high-performance and high-safety applications[4–6]. However, ISEs could not become the ultimate choice in various cases due to their lack of flexibility, air and moisture sensitivity, and scalability issues[7]. These drawbacks can be made up by solid polymer electrolytes (SPEs) which consist of a polymer backbone (PVDF, PEO etc) along with a Lithium salt (LiTFSI, $LiClO_4$ etc)[3,8]. Although SPEs are easily scalable and flexible in nature, their low ionic conductivity, poor mechanical strength and high interfacial resistance compel researchers to think about incorporating ceramic particles, ionic liquids, and plasticizers into them[9–11]. This introduces the concept of composite solid polymer electrolytes (CSPEs) that contain polymer, Li-salt, and some additive like inorganic ceramic filler or plasticizer as necessary components[12]. When ceramic particles are incorporated, they impose the appropriate flexibility, robustness, and improved ionic conductivity in the CSPEs, which are suitable for applicability in high-performance Lithium metal batteries.

While active ceramic fillers (LLZO, LATP, LSPSCl etc) enhance ionic conductivity of CSPEs by providing additional pathways for Li-ion transport[13], passive ceramic fillers (Al_2O_3, TiO_2, $BaTiO_3$, ZrO_2 etc) help in Li-ion migration in a different way. They reduce the crystallinity of the polymer backbone and increase the amorphous content, leading to facile Li-ion transport and enhanced electrochemical stability[14,15]. The ceramic fillers also help to increase the mechanical integrity and thermal stability of the CSPEs, which is essential for ensuring the cell safety. Recently, Liu et al. fabricated a CSPE by incorporating Co-doped cubic-ZrO_2 (C-ZrO_{2-x}) into a PVDF/PVDF-HFP matrix[16]. ZrO_2 provides oxygen vacancies as well as Lewis acidic characteristics, which are beneficial to capture $TFSI^-$ and Li^+ respectively, thus escalating LiTFSI dissociation rate. The enhanced salt dissociation later helped in increasing ionic conductivity and cycle life. In another research conducted by Erwei Tan and group, the

introduction of a metal-organic framework named ZIF-8 and PVDF-HFP in PEO-based SPE helps to decrease the crystallinity of PEO and promotes facile Li-ion transport[17]. SiO_2 can also help to provide excellent ionic conductivity of 2.4×10^{-4} $S.cm^{-1}$ and high Li-ion transport number of 0.54, along with stable cell performance, when incorporated into PVDF-HFP/PEA/PEGDE matrix as a cross-linking agent[18]. Another work by Tao Wei and group showed the incorporation of metal-organic frameworks (MOFs, UiO-66-NH_2) and superacid ZrO_2 (S-ZrO_2) fillers into PVDF-HFP matrix as anion-immobilizing agents through Lewis acid-base interactions, and they have got high ionic conductivity, enhanced Li-ion transport number, and better electrochemical properties as a result[19]. Researchers have also worked with Al_2O_3 and $BaTiO_3$-based CSPEs and observed significant increments in ionic conductivity, Li-ion transport and electrochemical stability[20,21].

In view of the recent research works, it has been observed that PVDF-HFP is a potential polymer backbone for developing efficient polymer electrolytes, as it can provide good ionic conductivity and it is compatible with a wide range of ceramic materials. While various studies are available where CSPEs have been successfully developed by incorporating an active or passive ceramic in PVDF-HFP, there is a lack of comparison of CSPEs with different ceramic materials incorporated in the PVDF-HFP matrix. In the initial part of this chapter, we have incorporated three different ceramic nanopowders, namely aluminium oxide (Al_2O_3), barium titanium oxide ($BaTiO_3$), and zirconium dioxide (ZrO_2), and incorporated them into the PVDF-HFP-LiTFSI system to develop three different CSPEs. Upon this introduction, mechanical strength, ionic conductivity, and thermal stability were increased in all three CSPEs from the pristine SPE. However, their microstructural, physical, and electrochemical properties varied within themselves to a significant extent, most probably due to the different kinds of surface interaction of the ceramics with the polymer chain structure. In the later stage, we moved forward to the development of paper-based electrolytes and finally to all solid-state flexible paper battery configuration. The paper matrix provides sufficient flexibility and mechanical robustness to the system to impede Li-dendrite growth for a long cycle life.

9.2 Fabrication Process

The fabrication of composite electrolytes under this research has undergone two stages, which are as follows:

9.2.1 Development of CSPEs

The composite solid polymer electrolytes (CSPEs) were fabricated using a simple solution casting method, as schematically described in ***Figure 9.2.3*** of ***Chapter 2***. All the reagents were previously vacuum dried for 24h to remove residual moisture. The PVDF-HFP was then dissolved in DMF via stirring at high temperature. After dissolving, LiTFSI was added, and the solution was stirred for a few more hours. Then, 10 wt% of the three ceramic nanopowders, namely Al_2O_3, $BaTiO_3$, and ZrO_2, were added to the solution to obtain the three CSPE solutions. Those were then cast on a PTFE substrate using a doctor's blade, following the process described in *Section 2.4.1* of ***Chapter 2***. The free-standing CSPE films were vacuum dried and then collected for further testing. Digital images of those films were taken with a mobile camera and they are displayed in ***Figure 9.1(a)***. The CSPE films were named as PLA, PLB, and PLZ for Al_2O_3, $BaTiO_3$, and ZrO_2, respectively. Only in the case of ZrO_2, three different CSPEs were developed with 5wt%, 10wt%, and 15wt% ZrO_2 incorporation to optimize the ceramic concentration. Along with them, the PVDF-HFP and LiTFSI-based CSPE film with no added ceramic was also fabricated for comparison. The composition and codes used for all the developed CSPEs are given in Table 9.1. The thickness of the membranes varied within the range of 40-60 μm.

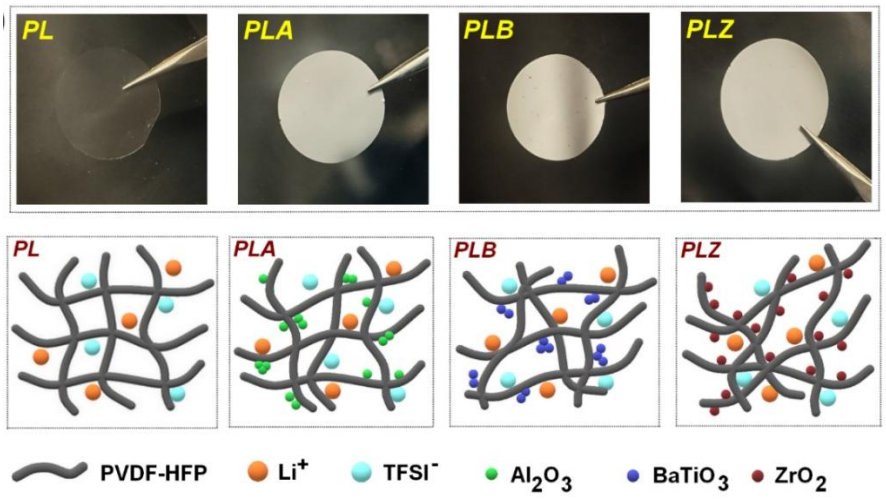

Figure 9.1 *(a) Digital images of the four developed membranes; (b) Schematic representation of the orientation of polymer, Li-salt, and ceramic nanoparticles inside the CSPEs*

9.2.2 Development of Paper-based CSPEs (p-CSPEs)

Before proceeding with the paper-supported CSPE, a duo-polymer-based CSPE has been developed to enhance the room temperature ionic conductivity to a significant extent. For this purpose, an optimal 30 wt% polyethylene oxide (PEO) of the total polymer was added in the

primary solution of PVDF-HFP in DMF. After homogeneous mixing, the optimized amount of ZrO_2 was added to it and dispersed well via prolonged stirring. Some portion of this solution was cast as it is to get a free-standing CSPE film, further named as PELZ. The remaining portion is put in the sample chamber of the semi-automated double-decker separator fabricator unit, presented in ***Figure 2.1*** of ***Chapter 2***. The oven-dried pure cellulose paper roll (thickness ~ 20 µm) is coated by the solution in both sides and air dried in the IR drying zone of the same instrument. After initial drying, the paper-based CSPE membrane is transferred to a vacuum oven. The coated paper is further compacted and collected in roll form with a uniform thickness of ~60±5 µm.

Table 9.1 *Composition of the developed CSPEs along with the codes assigned to them*

Sl No.	Base matrix	Li-salt	Ceramic Nanopowder	Amount of ceramic added	Code of the CSPE
1	PVDF-HFP	LiTFSI	-	-	**PL**
2	PVDF-HFP	LiTFSI	Al_2O_3	10 wt%	**PLA**
3	PVDF-HFP	LiTFSI	$BaTiO_3$	10 wt%	**PLB**
4	PVDF-HFP	LiTFSI	ZrO_2	5 wt%	**PLZ05**
5	PVDF-HFP	LiTFSI	ZrO_2	10 wt%	**PLZ10/PLZ**
6	PVDF-HFP	LiTFSI	ZrO_2	15 wt%	**PLZ15**
7	PVDF-HFP, PEO	LiTFSI	ZrO_2	10 wt%	**PELZ/CSPE**
8	PVDF-HFP and PEO reinforced in cellulose paper	LiTFSI	ZrO_2	10 wt%	**p-PELZ/p-CSPE**

This unique paper-based electrolyte configuration provides a promising platform for the development of next-generation flexible solid-state lithium batteries.

9.3 Results and Discussion

The structural, microstructural, mechanical and electrochemical test results help us better understand the effect of dual polymer and ceramic in the paper matrix.

9.3.1 Structural, Microstructural and Mechanical Features

The microstructural features of the PL, PLA, PLB, and PLZ films can be observed in their FESEM images. ***Figures 9.2(a)*** and ***9.2(b)*** represent the FESEM micrographs of the PL membrane in lower and higher magnifications, respectively, while ***Figure 9.2(c)*** shows the corresponding EDX spectrum. In ***Figure 9.2(a)***, some agglomeration of the polymer can be

observed in the pristine PVDF-HFP-LiTFSI film (PL), indicating the presence of crystalline regions in the untreated polymer matrix.

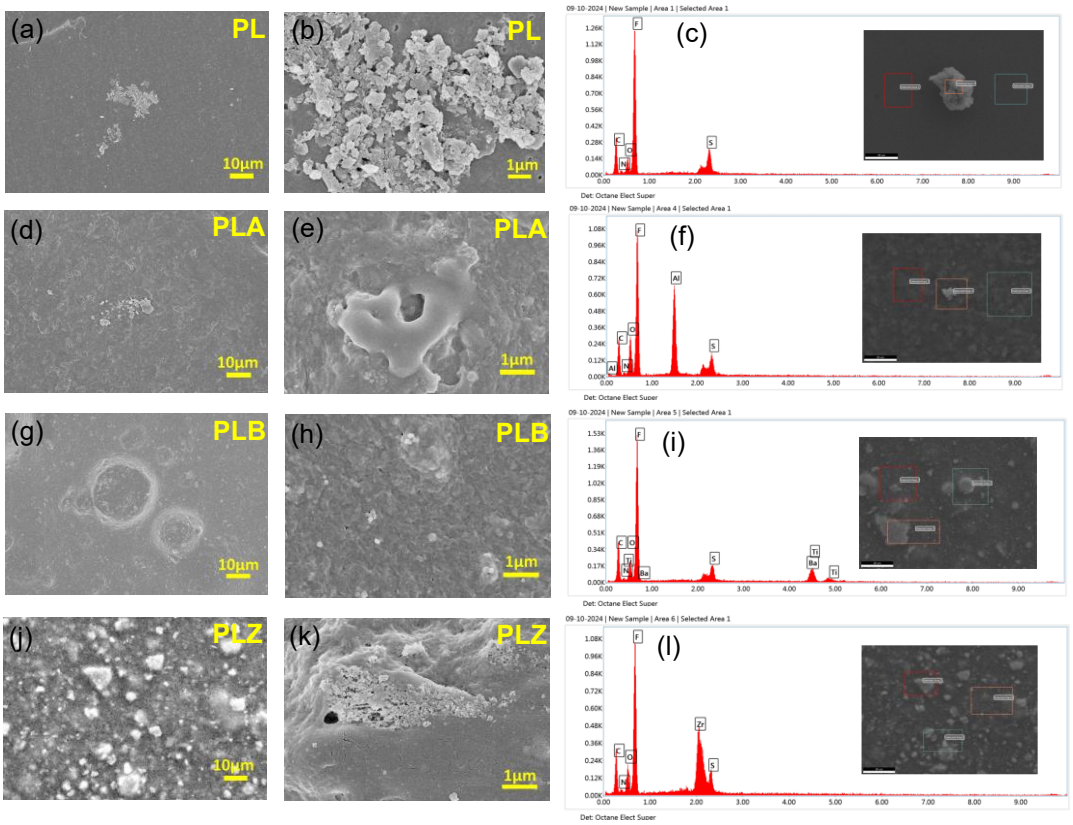

Figure 9.2 *Microstructural features of the developed CSPEs: Low and high magnification FESEM images of (a) & (b) PL, (d) & (e) PLA, (g) & (h) PLB (j) & (k) PLZ; EDX profile of (c) PL, (f) PLA, (i) PLB, (l) PLZ*

The corresponding EDX profile consists of characteristic peaks of C, O, and F, confirming the presence of PVDF-HFP, while the additional peaks associated with N and S suggest the successful incorporation of LiTFSI in the membrane. In a similar way, ***Figures 9.2(d)-(f), 9.2(g)-(i),*** and ***9.2(j)-(l)*** represent the series of low and high magnification images with corresponding EDX spectra for PLA, PLB, and PLZ membranes, respectively. While analysing the different microstructural features of the polymeric films, the surface charge of PVDF-HFP, Al_2O_3, $BaTiO_3$ and ZrO_2 will play a significant role. The three solutions of polymer, Li-salt, and ceramics in DMF typically register pH values within the range of 4-6, which signifies that the overall solution casting process takes place in acidic conditions. In this pH range, PVDF-HFP registers a highly negative surface charge with an approximate zeta potential value of -50mV or less [22]. It is reported in the literature that at this pH range, alumina shows a lower positive surface charge with zeta potential value falling within the range of 10–20 mV [23]. It is to be noted here that zeta potential above ±30 mV typically indicates a well-dispersed and

stable colloidal system, whereas values below ±5 mV are associated with significant particle agglomeration during deposition. Zeta potential values in the intermediate range (±5–30 mV) generally suggest a moderate tendency towards forming agglomeration[24].

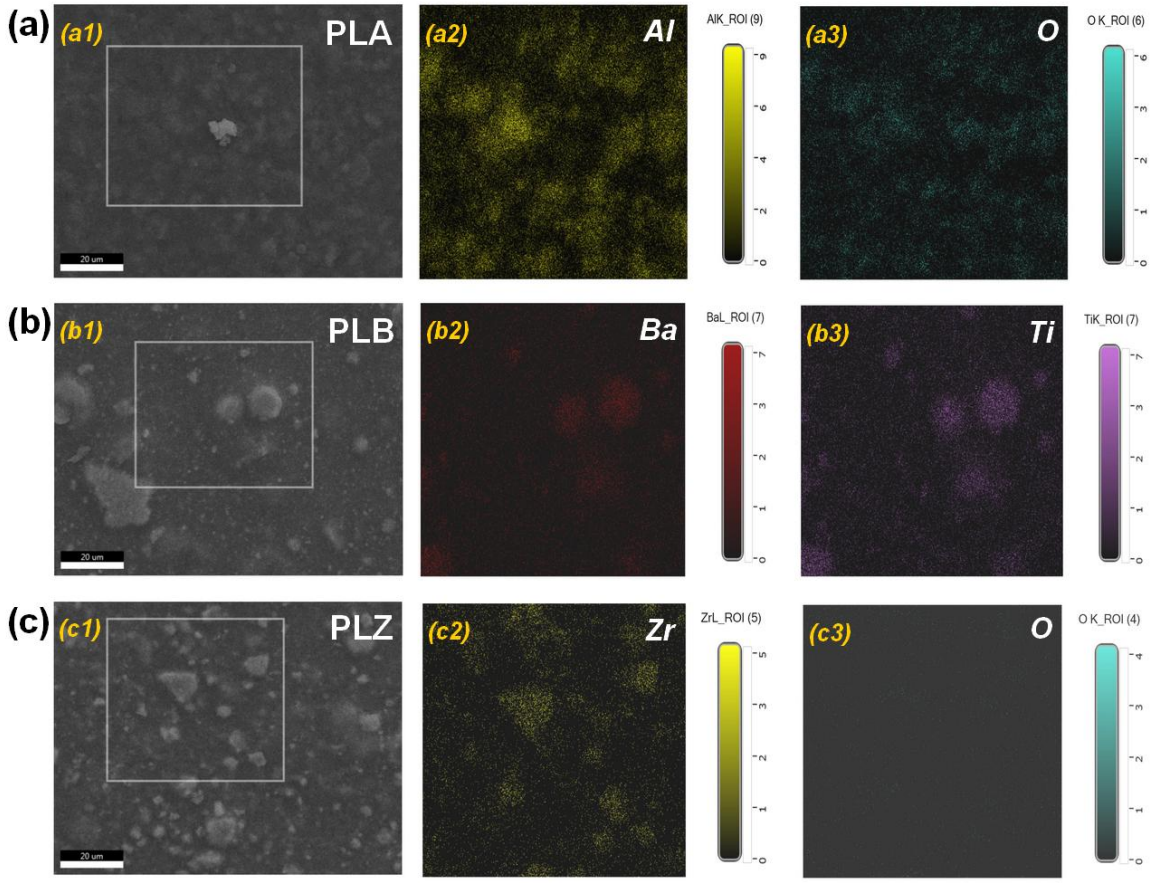

Figure 9.3 *Elemental mapping from EDX for (a) PLA, (b) PLB, and (c) PLZ: (a1), (b1) and (c1) are the selected area from SEM for EDX analysis, (a2) and (a3) mapping for Al and O, (b2) and (b3) mapping for Ba and Ti, (c2) and (c3) mapping for Zr and O, respectively*

This is the primary reason that alumina nanoparticles with intermediate positive zeta potential show a tendency of agglomeration as well as good interaction with negatively charged PVDF-HFP matrix, as shown in ***Figures 9.2(d)*** and ***9.2(e)***. The corresponding EDX spectrum in ***Figure 9.2(f)*** confirms the presence of Al along with the other characteristic elements of polymer and Li-salt. Furthermore, the elemental mapping of Al and O shown in ***Figures 9.3(a1)-(a3)*** confirms the distribution pattern of Al_2O_3 nanoceramics in the CSPE membrane. In the similar pH region, $BaTiO_3$ shows zeta potential value on a lower negative side, generally between -5 mV to -15 mV [25,26]. That is why the negatively charged barium titanate nanoparticles show reluctance to interact with another negatively charged matrix of PVDF-

HFP. Instead, they agglomerate within themselves and reside on the polymer matrix randomly, as can be seen in ***Figures 9.2(g)*** and ***9.2(h)***.

The characteristic peaks of Ba and Ti in the EDX profile of PLB presented in ***Figure 9.2(i)*** give confirmation of the presence of $BaTiO_3$ nanoparticles in the PLB membrane. The elemental mapping of Ba and Ti given in ***Figures 9.3(b1)-(b3)*** emphasizes the agglomeration and random distribution of the $BaTiO_3$ nanoparticles.

On the other hand, the surface of ZrO_2 nanoparticles with zeta potential value of 20-30 mV within pH 4-5, is moderately positive in nature[27,28]. This leads to good interaction of ZrO_2 with highly negative charged PVDF-HFP. The homogeneous distribution of ZrO_2 nanoparticles within the polymer matrix as displayed in ***Figures 9.2(j)*** and ***9.2(k)***, can also be attributed to the strong interaction between Lewis acidic sites of ZrO_2 and the electron-rich regions of the polymer or LiTFSI. The homogeneous distribution of ZrO_2 can also be confirmed from the elemental mapping of Zr and O represented in ***Figures 9.3(c1)-(c3)***. Similar interaction can also be observed in some relevant studies of composite polymer electrolytes in solid-state lithium batteries [29–31]. The probable nature of deposition of ceramic particles are represented via a schematic diagram in ***Figure 9.1(c)***. ***Figure 9.2(l)*** depicts the EDX profile of the PLZ film where the peaks of Zr and O confirm the presence of zirconia in the system.

The structural properties of the developed CSPE films are analysed using X-ray diffraction (XRD) pattern and Fourier transformed infrared (FTIR) spectroscopy, which are represented in ***Figures 9.4(a)*** and ***9.4(c)***, respectively. The XRD pattern shows the characteristic peak of PVDF-HFP at ~20º, which is highlighted separately in Figure 9.4(b). This broad peak indicates towards the semicrystalline nature of the polymer [32,33].

The crystallinity index (CI) of the polymer is calculated by from this peak for all the CSPE films. As the crystallinity index decreases, the amorphous content of the polymer increases, and hence, the conductivity enhances with an increase in disorder inside the polymeric matrix. Being an ion-conducting polymer, PVDF-HFP exhibits a predominantly amorphous structure, as reflected by its crystallinity index (%CI) of 37.2. Apart from this, the downward trend of %CI values in PLA, PLB, and PLZ indicates that BTO and ZrO_2 successfully disrupt the crystalline region with significantly lower CI values of 7.7% and 4.2%, respectively. In contrast, Al_2O_3 with a CI value of 33.8% appears less effective in inducing amorphous characteristics within the polymer matrix.

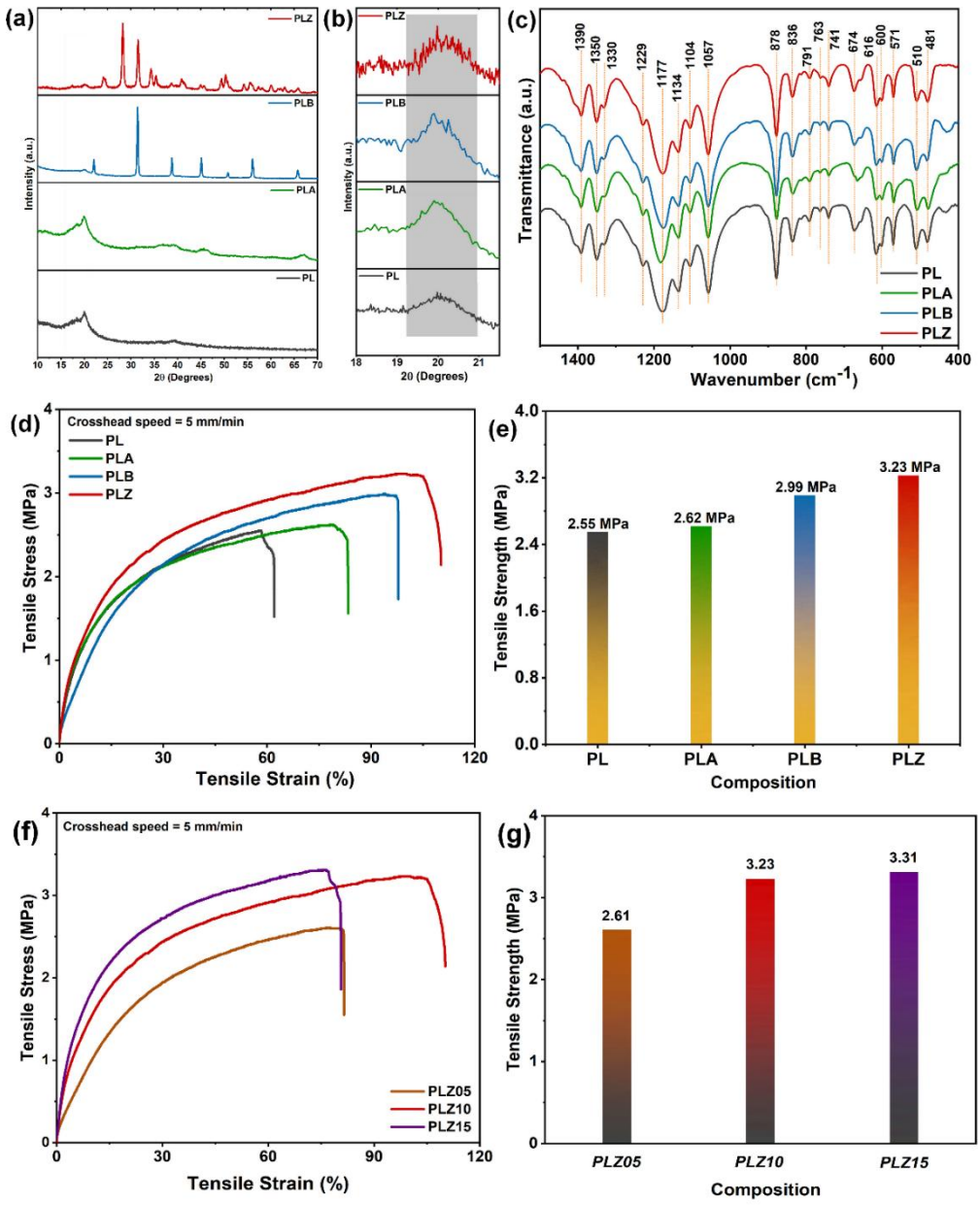

Figure 9.4 *(a) X-ray diffraction patterns, (b) XRD peak corresponding to PVDF-HFP, (c) FTIR spectra, (d) Tensile stress vs tensile strain curves, (e) Summary of tensile strength for PL, PLA, PLB and PLZ; (f) Tensile stress vs tensile strain profiles for PLZ05, PLZ10 and PLZ15, (g) Summary of tensile strength values for PLZ05, PLZ10 and PLZ15*

FTIR spectra of PL, PLA, PLB, and PLZ composite solid polymer electrolytes are shown in ***Figure 9.4(c)*** to understand the chemical changes in the polymer matrix after the incorporation of different ceramic materials. The PL electrolytes show characteristic bands at 1177 and 840 cm^{-1}, attributed to the CF_2 stretching and bending vibrations of PVDF-HFP[34,35]. Also, a distinct band at 1057 cm^{-1} corresponding to the SO_2 asymmetric stretching of LiTFSI[36,37]. After incorporation of ceramic materials in the polymer matrix, peak broadening along with reduced

intensity is observed in the 1229-510 cm^{-1} region. This is due to the strong interactions between the polymer matrix and ceramic particles. These interactions suggest reduced crystallinity and enhanced amorphous character, which is beneficial for Li^+ ion transport. Sharper and pronounced peaks at 1134, 1057, 836, and 600 cm^{-1} were observed for PLZ electrolytes, which suggests good compatibility between the polymer matrix and ceramic material. Zr-O or Ti-O metal-oxygen vibration at 674 and 481 cm^{-1} from ZrO_2 and $BaTiO_3$ is clearly observed in PLZ and PLB CSPE, respectively[38,39]. In summary, the FTIR results further confirm that the incorporation of filler particles in the polymer matrix has the potential to enhance the ion transport phenomena, which will be measured in the later section.

The safety performance of the battery comprising the flexible electrolyte films largely depends on the robustness of the CSPE membranes. The mechanical strength of the developed CSPE films was measured using a Universal Testing Machine. The stress vs strain plots for PL, PLA, PLB, and PLZ are represented in ***Figure 9.4(d)***. A similar plot for the CSPEs developed with three different concentrations of ZrO_2 is shown in ***Figure 9.4(f)***. The tensile strength values are also summarised in ***Figures 9.4(e)*** and ***9.4(g)***, respectively, for better understanding. For the pristine PL membrane, the tensile strength value is 2.55 MPa, which is enhanced to 2.62 MPa, 2.99 MPa, and 3.23 MPa for Al_2O_3, $BaTiO_3$, and ZrO_2 incorporation, respectively. The suitable interaction of ZrO_2 nanoparticles with PVDF-HFP polymeric matrix has helped in increasing the mechanical strength of PLZ to a greater extent. Also, the elongation upon stretching is quite high for the ceramic incorporated CSPEs, especially for PLZ as compared to PL (nearly two times). ZrO_2 exhibits stronger Lewis acidity compared to Al_2O_3 and $BaTiO_3$, which promotes stronger interactions with the electron-rich -CF_2- groups in the PVDF-HFP backbone[19,31]. Additionally, its smaller particle size (~100 nm) ensures more uniform dispersion and better interfacial adhesion within the polymer matrix, leading to improved stress transfer under load. These combined effects not only enhance the tensile strength but also improve elongation at break, as observed for the PLZ composite electrolyte. In case of variation of tensile strength with ceramic concentration, there is a noticeable enhancement in the strength when ceramic loading increases. This is probably due to better reinforcement and improved robustness in the polymer membranes in the presence of ceramic nanoparticles[40]. However, the lower and higher concentrations of ZrO_2, although they provide good mechanical strength (2.61 MPa and 3.31 MPa), the elongation for the PLZ05 and PLZ15 samples is quite lower than that of PLZ10 or PLZ. This gives an idea that the optimal concentration of the incorporated ceramic might be nearly 10 wt% for the PVDF-HFP/LiTFSI-based composite electrolytes.

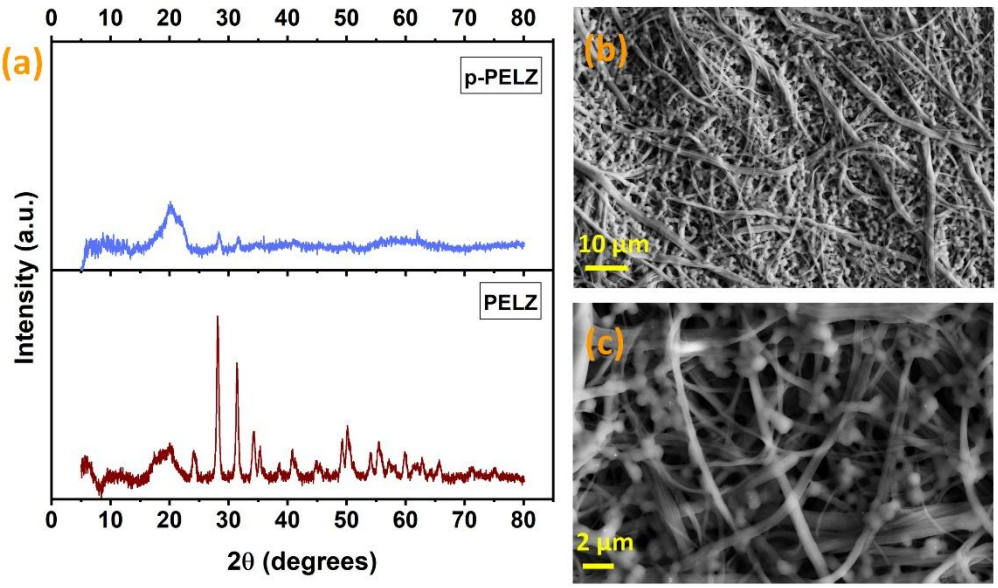

Figure 9.5 *(a) X-ray diffractograms of PELZ and paper-based PELZ (p-PELZ), (b) & (c) FESEM micrographs of p-PELZ at lower and higher magnifications, respectively*

The XRD patterns in ***Figure 9.5(a)*** demonstrate the structural changes introduced by (i) adding PEO to the PVDF-HFP/LiTFSI matrix and (ii) impregnating that composite into a cellulose paper support. The free-standing PELZ film shows a broadening and clear reduction in intensity of the PVDF-HFP characteristic reflection (previously noted at ≈ 20°), consistent with a substantial increase in the amorphous fraction after PEO addition and ZrO_2 incorporation. The expected crystalline reflections from PEO are weak or substantially merged into the broad polymer halo, which indicates strong polymer-polymer and polymer-ceramic interactions that suppress long-range PEO crystallinity and therefore promote segmental mobility of polymer chains - a structural change that facilitates Li^+ transport. In the p-PELZ diffractogram, the polymer halo remains broadened but superposes with low-intensity cellulose reflections arising from the underlying paper; overall the polymer peaks in p-PELZ are equal or further attenuated relative to free PELZ, indicating that the coating or impregnation process and the constrained environment of the fibre network further hinder polymer crystallization and favor an amorphous, ion-conducting matrix.

The FESEM images, presented in ***Figures 9.5(b)-(c)***, provide the morphological basis for the XRD observations. At low magnification the cellulose fibre mat is seen to be uniformly coated: the original fibrous texture is preserved but the inter-fibre pores are filled by the composite polymer, producing a continuous, conformal film over the paper network. High-magnification

micrographs show a smooth polymer film enveloping individual fibres and reveal bright, granular contrasts consistent with ZrO_2 nanoparticles anchored at the polymer-fibre interface. There is no evidence of large ceramic agglomerates or delamination; instead, the particles appear well-distributed and intimately adhered to fibre surfaces. These microstructural features explain (i) why the diffractogram shows reduced polymer crystallinity, and (ii) why the paper-supported membrane combines continuous ionic pathways with improved dimensional and mechanical stability. Taken together, the XRD and FESEM data explain the electrochemical behaviour observed elsewhere in this chapter: PELZ's increased amorphous fraction correlates with the targeted rise in room-temperature ionic conductivity, while the p-PELZ architecture preserves comparable ionic pathways but adds macroscopic reinforcement, thickness uniformity and handling robustness, making p-PELZ an attractive, scalable electrolyte for flexible solid-state paper cells.

9.3.2 Electrical Properties

Previously, the variation in mechanical strength with ceramic concentration provided a preliminary insight about the optimal ceramic content in composite polymer electrolyte system. To confirm the findings further, EIS studies were performed with SS/SS symmetric cells prepared using the CSPEs incorporated with varying amounts of ZrO_2 (PLZ05, PLZ10 and PLZ15). The ionic conductivities of the CSPE films at 30°C are calculated from the bulk resistance values extracted from the high frequency intercept on the real axis of the Nyquist plots given in ***Figure 9.6(a)***. At 30°C, the ionic conductivity increased from PLZ05 (6.35×10^{-5} $S.cm^{-1}$) to PLZ10 (9.26×10^{-5} $S.cm^{-1}$), probably due to the improved dispersion of ZrO_2 nanoparticles, which increases amorphous domains in the polymer matrix and facilitate segmental motion of the polymer chains. However, the ionic conductivity further decreases to 7.13×10^{-5} $S.cm^{-1}$ for PLZ15, likely because of the agglomeration effect of nanoceramics and resultant impediment in Li-ion transport at high ceramic loading.

Temperature-dependent Nyquist plots for PLZ05, PLZ10, and PLZ15 (given in ***Figures 9.6(d)–(f)***) were recorded within 30-90°C, and the corresponding bulk resistances were used to construct Arrhenius plots given in Figure 6(b).The activation energy values (E_a) of the three CSPEs, calculated using Arrhenius equation (4), are summarised in Figure 6(c). The lowest activation energy obtained for PLZ10 (0.23 eV) indicates a low energy barrier for ion migration, which facilitates the better electrical and electrochemical performance in 10 wt% ceramic loading in the CSPEs.

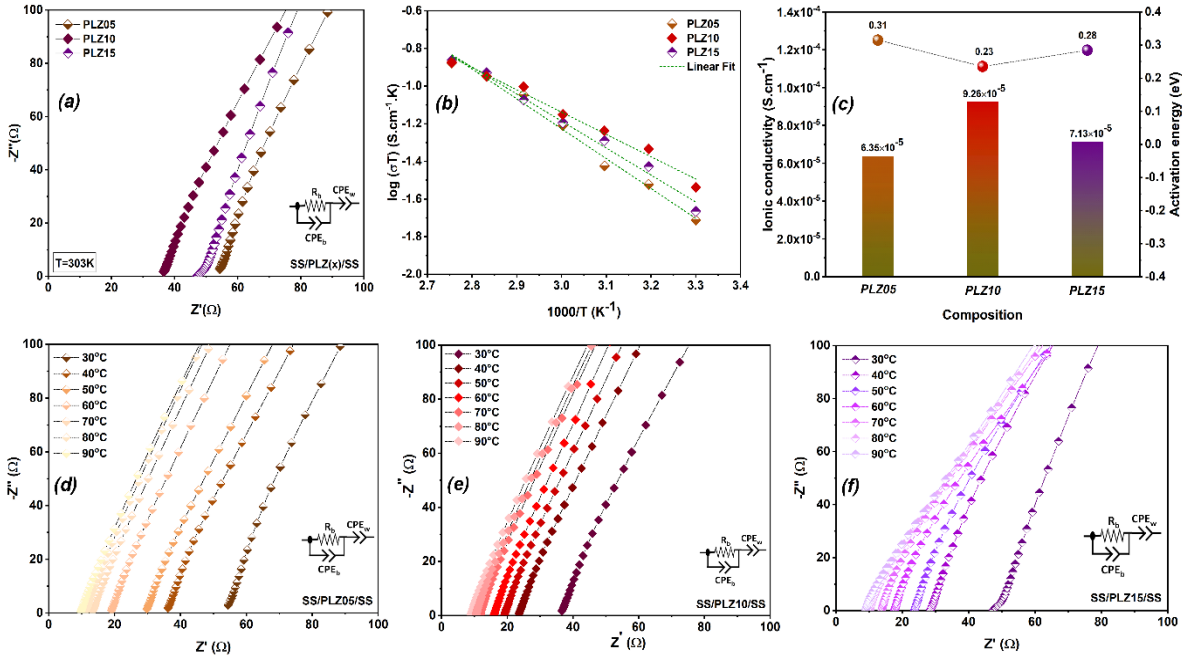

Figure 9.6 *Variation of electrical properties with respect to ZrO_2 variation in the CSPEs named as PLZ05, PLZ10 and PLZ15; (a) Nyquist plots at 303K, (b) Arrhenius plots, (c) Summary plot consisting of ionic conductivity for the three CSPEs at 303K along with their activation energy; Nyquist plots at temperatures ranging from 303 K to 363 K for (d) PLZ05, (e) PLZ10, and (f) PLZ15*

The Nyquist plots for the four CSPE films incorporated with 10 wt% of three different ceramic materials as well as the bare film, are represented in ***Figure 9.7(a)***. The pristine PVDF-HFP-LiTFSI film (PL) shows lower ionic conductivity (σ=0.82×10^{-5} S.cm^{-1}) at 30°C due to the presence of crystalline regions in the polymer. However, the introduction of ceramic fillers into the matrix helps to enhance the amorphous content of the polymer, and thus, ionic conductivity also increases. EIS was also conducted at higher temperatures up to 90ºC for all the samples, and the ionic conductivity values with respect to temperature are represented in ***Figure 9.7(b)*** in Arrhenius plots. Their activation energy (E_a) values were also calculated, and a summary of ionic conductivity (at 30ºC) and activation energy has been presented in ***Figure 9.7(c)***. As far as the ionic conductivity is concerned, the alumina incorporated PLA film consists of ionic conductivity of 1.50×10^{-5} S.cm^{-1} at 30ºC, which is higher than PL but significantly lower than the other two films. Although $BaTiO_3$ incorporation enhances the ionic conductivity to a significant extent of 4.15×10^{-5} S.cm^{-1}, the highest conductivity is reached for ZrO_2 grafted PLZ membrane with the σ value of 9.26×10^{-5} S.cm^{-1}. This trend is the direct reflection of surface charge interactions of PVDF-HFP with different ceramics and the resultant alteration of the crystallinity index of the polymer.

The high temperature ionic conductivities, as well as the activation energy values, vary for the four CSPEs in a similar fashion, as observed in ***Figures 9.7(b)*** and ***9.7(c)***. The activation energy (E_a)values for all the developed CSPEs are calculated. PL shows the highest E_a value of 0.40 eV, which largely drops down to 0.29 eV, 0.24 eV, and 0.23 eV for PLA, PLB, and PLZ, respectively. The Nyquist plots of PL, PLA, PLB, and PLZ at various temperatures ranging from 30-90°C are given ***in Figures 9.7(d), 9.7(e), 9.7(f),*** and ***9.6(e)***, respectively.

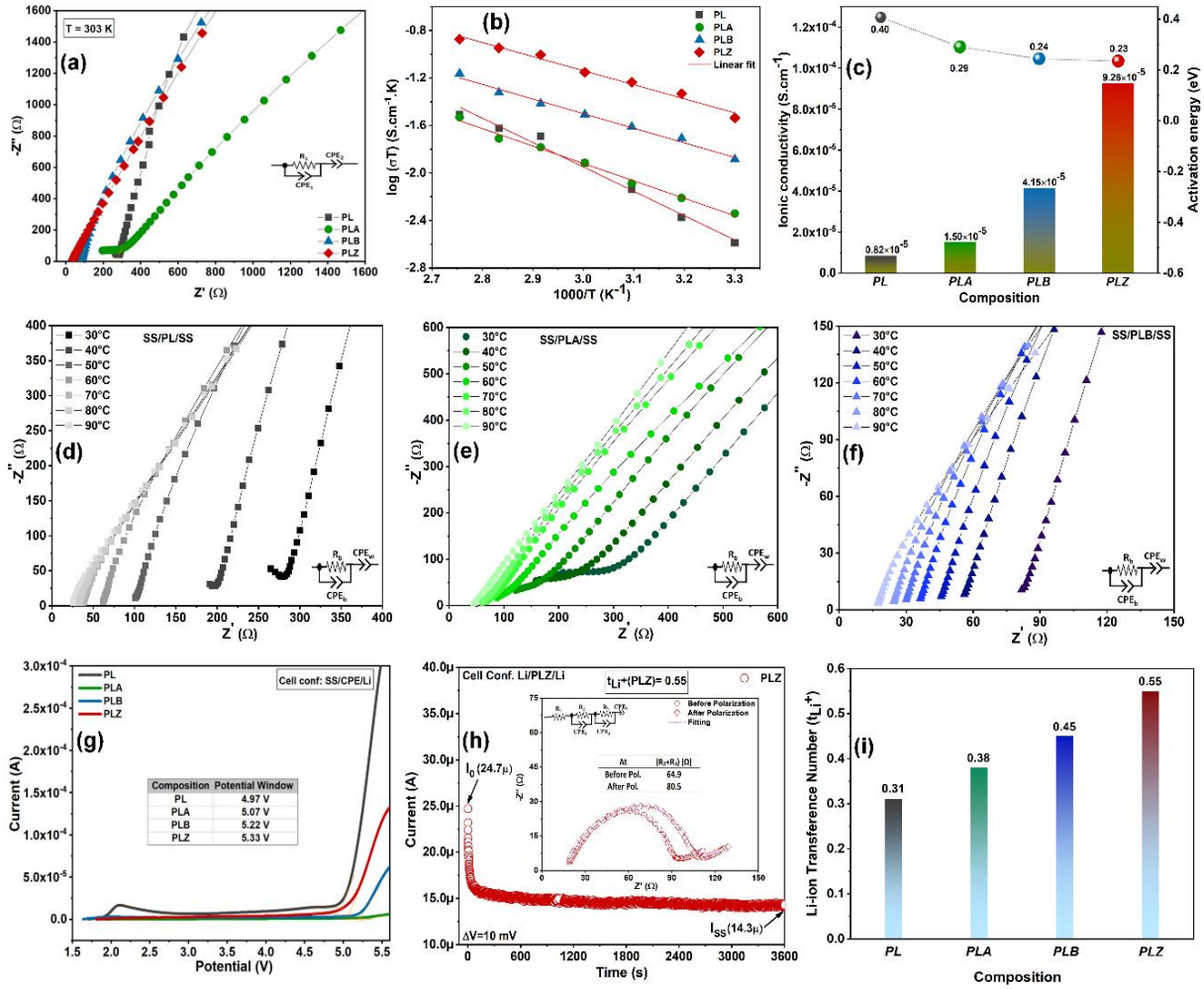

Figure 9.7 *Electrical properties of PL, PLA, PLB, and PLZ: (a) Nyquist plots at 30°C, (b) Arrhenius plots, (c) Summary plot of ionic conductivity and activation energy, (d) – (f) Nyquist plots in the temperature range of 30-90°C for PL, PLA and PLB, respectively, (g) Linear Sweep Voltammetry (LSV) plots, for PL, PLA, PLB, and PLZ, (h) DC polarization of Li/PLZ/Li cell, (i) Summary of Li-ion transference numbers for all the four developed CSPEs*

Figure 9.7(g) represents the Linear Sweep Voltammetry (LSV) curves, which give an idea about the working potential window of the CSPEs for safe electrochemical operations.

Although the values do not differ much, a significant change is observed between the untreated polymer film (PL) and the ceramic incorporated films (PLA, PLB, and PLZ). All the Li/SS asymmetric cells comprising the developed CSPEs remained stable in the potential range of 2.0-4.8 V. However, the electrochemical window for PL comes to be 4.97 V, which is further increased to 5.07 V, 5.22 V, and 5.33 V for Al_2O_3, $BaTiO_3$, and ZrO_2 incorporation, respectively.

Li-ion transference number (t_{Li+}) is a critical parameter for an electrolyte, which quantifies the fraction of the total ionic current carried by Li^+ ions during electrochemical operation[41]. ***Figure 9.7(h)*** demonstrates the DC polarization curve for Li/PLZ/Li at 60°C which helps to calculate the Li^+ transport number using Bruce-Vincent method, given in ***Chapter 2***[42]. t_{Li+} is calculated for all the four CSPEs in the same procedure and the values are summarised in ***Figure 9.7(i)***. The EIS test results for DC polarization for all the four cells are provided in ***Table 9.2***. The PL film exhibited the lowest Li^+ transference number of 0.31, indicating a relatively high contribution from anion movement.

Upon incorporation of nanoceramic fillers, the value further increases to 0.38 for PLA, 0.45 for PLB and 0.55 for PLZ. These results corroborate with the crystallinity index values and ionic conductivity of the CSPEs. The ceramic materials help to reduce the crystallinity of PVDF-HFP and facilitate Li-ion migration through segmental mobility of polymer chains. The significant enhancement of t_{Li+} in PLZ can be attributed to the suppression of anion mobility through Lewis acid–base interactions in presence of ZrO_2, that helps in smoother Li^+ conduction pathways by improving salt dissociation and polymer segmental dynamics[31].

The Nyquist plots in ***Figure 9.8(a)*** compare the room-temperature ionic conductivities of the free-standing PELZ membrane (PVDF-HFP/PEO/LiTFSI with ZrO_2) and its cellulose paper-supported counterpart p-PELZ. The bulk resistance values extracted from the high-frequency intercepts reveal that PELZ exhibits an ionic conductivity of 6.7×10^{-4} S·cm^{-1} at 303 K, whereas p-PELZ shows a slightly lower conductivity of 4.3×10^{-4} S·cm^{-1}.

Incorporation of an optimal amount of PEO in the PLZ matrix helped to enhance the ionic conduction significantly, while the lower conductivity of the paper-supported film can be attributed to partial restriction of polymer chain mobility within the cellulose fibre framework.

Table 9.2 *Li-ion transference number and corresponding EIS test results of the CSPEs*

CSPE	I_0 (A)	I_{ss} (A)	R_0 (Ω)	R_{ss} (Ω)	Li-ion Transference Number (t_{Li+})
PL	25.5×10^{-6}	13.5×10^{-6}	251.2	283.0	0.31
PLA	25.6×10^{-6}	14.6×10^{-6}	218.6	234.9	0.38
PLB	26.5×10^{-6}	15.7×10^{-6}	180.1	196.6	0.45
PLZ	24.7×10^{-6}	14.3×10^{-6}	64.9	80.5	0.55

Nevertheless, the conductivity value of p-PELZ remains sufficiently high for practical solid-state battery applications, while offering additional mechanical robustness and dimensional stability from the cellulose scaffold.

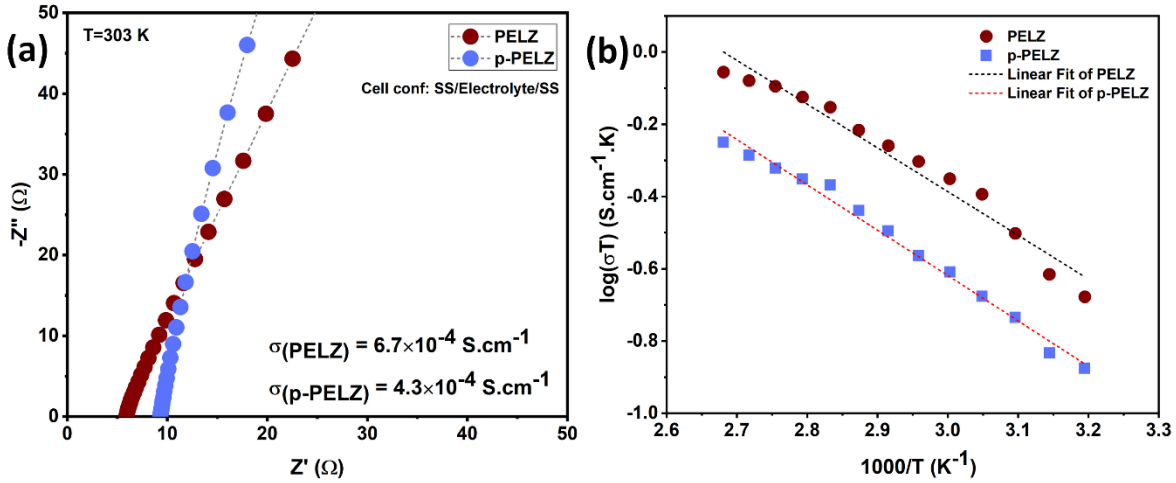

Figure 9.8 *(a) Nyquist plots and (b) Arrhenius plots for PELZ and p-PELZ*

Figure 9.8(b) presents Arrhenius plots of log(σT) versus 1000/T for both electrolytes in the temperature range 30–90 °C. Both systems follow thermally activated ionic transport behaviour with a near-linear dependence, confirming that Li^+ conduction is governed by polymer segmental dynamics. The activation energy (Ea), calculated from the slopes of the linear fits, is lower for PELZ (0.24 eV) as compared to p-PELZ (0.26 eV), consistent with its higher conductivity at room temperature.

Taken together, these results indicate that while the incorporation of cellulose paper slightly decreases the ionic conductivity, it significantly enhances the structural integrity, processability, and flexibility of the composite electrolyte. Thus, p-PELZ provides a balanced

trade-off between ionic transport properties and mechanical reinforcement, making it a practical candidate for paper-supported solid-state lithium-metal batteries.

9.3.3 Electrochemical Tests

To understand the interface compatibility between composite solid polymer electrolytes and Li metal, EIS spectra before a long stability test are taken and presented in ***Figure 9.9(b)*** along with the corresponding equivalent circuit. It is worth mentioning here that the R_1 in the equivalent circuit fitting is the bulk electrolyte resistance, and (R_2+R_3) is the total interfacial resistance, which is the probable contribution of SEI and charge transfer resistance. CPEs are the constant phase elements. The electrolyte-metal interface resistance, which constitutes about half of the total interface resistance [(R_2+R_3)/2] of a cell, is estimated to be 140.6Ω, 115.8Ω, 93.9Ω, and 48.3Ω for PL, PLA, PLB, and PLZ electrolytes, respectively. So, incorporation of ceramic material in a PVDF-HFP-LITFSI matrix has reduced the metal-electrolyte interface resistance. Among all the incorporations, ZrO_2 ceramic incorporated CSPE shows the lowest metal-electrolyte interfacial resistance due to its strong Lewis acid-base interaction with PVDF-HFP chains and LiTFSI anions, which promotes effective salt dissociation and stable SEI formation. Such interfacial compatibilities between the electrolyte and Li metal are expected to benefit electrochemical cell performance, which will be discussed later.

The electrochemical stability test of the developed CSPEs was evaluated using Li/Li symmetric cells. The voltage vs time profiles of Li/Li symmetric cells developed using PL, PLA, PLB, and PLZ as electrolyte are demonstrated in ***Figure 9.9(a)***. All the cells are showing stable Li plating-stripping characteristics for 480 hours continuously without a short-circuit at a current density of 0.10 $mA.cm^{-2}$ and an elevated temperature of 60ºC for better performance. From the enlarged views (I) and (II) presented in the inset of ***Figure 9.9(a)***, it can be observed that the PLZ electrolyte exhibits the lowest and most stable overpotential (~8 mV) among all throughout the duration of the test. In the initial stage, the order of overpotential value is PL>PLB>PLA>PLZ, where the values for PL and PLB are quite similar (~20 mV).

However, a significant shift is observed toward the end of the cycling period, where the PL cell exhibits a substantial increase in overpotential of upto 38 mV, likely due to progressive polarization of the electrochemical species. While PLA also displays a hike in polarization voltage (~21 mV), PLB shows a reduction (~15 mV), and PLZ consistently maintains low and stable overpotential (~7 mV), underscoring its electrochemical stability.

Electrochemical impedance spectroscopy (EIS) was conducted on all the symmetric cells before and after cycling to gain deeper insights into the charge transfer process. By examining the Nyquist plots and fitting the data with appropriate equivalent circuit models, we can monitor the changes in electrolyte bulk resistance and metal-electrolyte interface resistance due to prolonged cycling. ***Figures 9.9(c)- 8(f)*** represent the Nyquist plot before and after the cycling process, along with the equivalent circuit for PL, PLA, PLB, and PLZ, respectively. It is observed that the bulk resistance does not increase for all the developed electrolytes, suggesting that the structural and compositional stability of the polymer matrix is well maintained during cycling.

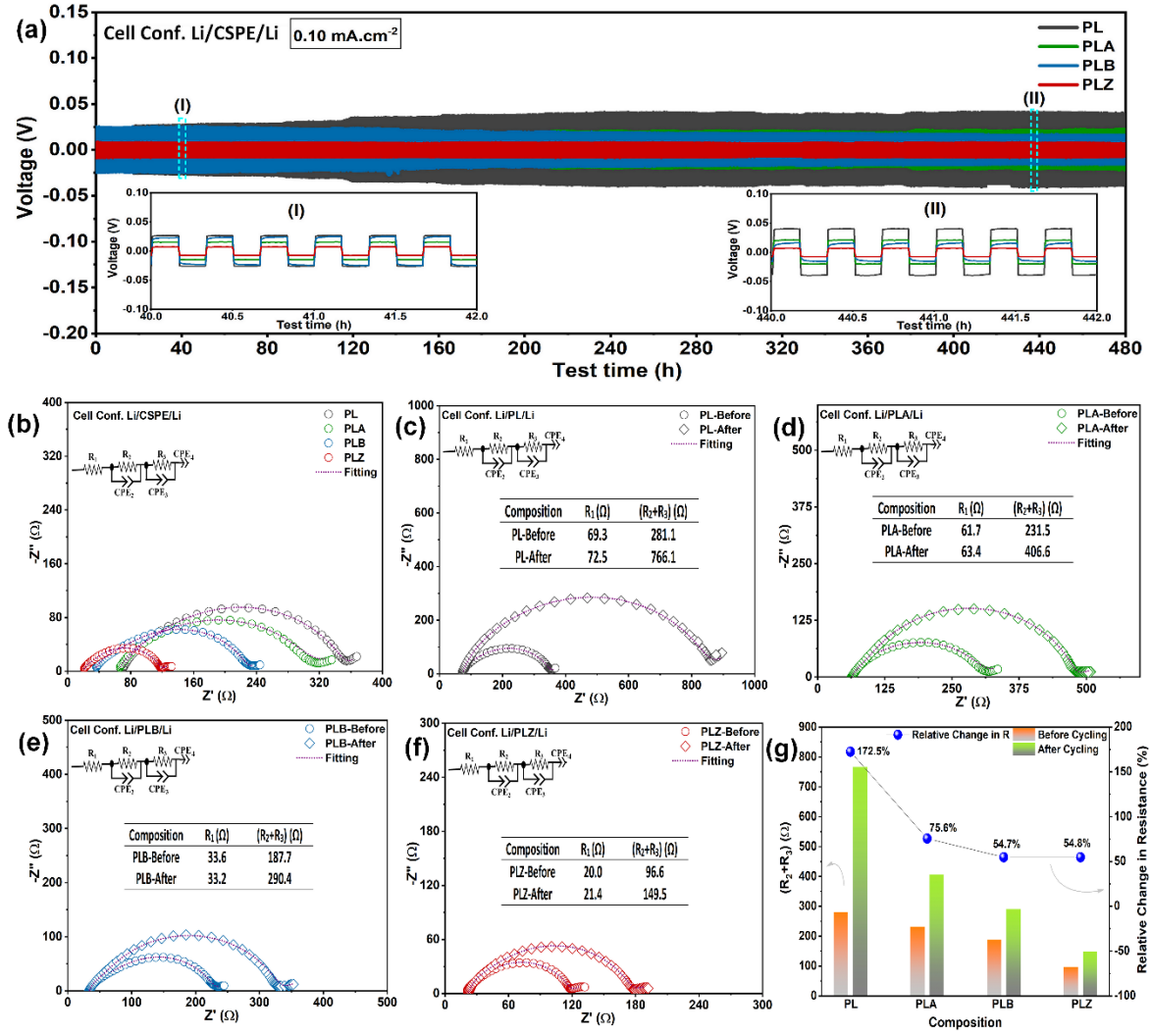

Figure 9.9 *(a) Voltage vs time profiles for Li/Li symmetric cells of PL, PLA, PLB, and PLZ at 60°C, (b) Nyquist plot of all the developed CSPEs in Li/Li symmetric cells for the variation of electrolyte-metal interface resistance, EIS spectra before and after long-term cycling for (c) PL, (d) PLA, (e) PLB, and (f) PLZ, (g) Variation of interfacial resistance for developed CSPEs before and after a long cycling test*

However, a significant rise in interfacial resistance at the metal/electrolyte boundary is evident, likely due to the gradual formation of resistive surface layers or solid electrolyte interphase (SEI) components, which hinder charge transfer kinetics at the interface. Although among all the developed CSPEs, this rise is more prominent for the PL composite electrolyte, as shown in ***Figure 9.9(g)***, and PLZ and PLB show the lowest change in interfacial resistance. The variation of this interfacial resistance is summarized in ***Figure 9.9(g)***. Thus, the incorporation of ceramic fillers plays a crucial role in stabilizing the electrode-electrolyte interface by mitigating interfacial degradation, leading to improved long-term electrochemical performance.

Figure 9.10 represents the comparative impedance evolution and DRT analysis of Li/CSPE/Li symmetric cells using ZrO_2-incorporated PVDF-HFP–LiTFSI electrolyte (PLZ) and bare PVDF-HFP–LiTFSI electrolyte (PL) during 60 h of cycling. The Nyquist plots in ***Figures 9.10(a)*** and ***9.10(b)*** demonstrate that the PLZ cell shows a lower interfacial resistance compared to PL throughout the cycling process, as observed earlier. This is due to the incorporation of ZrO_2 nanoparticles, which successfully reduces the initial charge-transfer resistance and stabilizes the electrode–electrolyte interface under repeated Li plating/stripping. It is worth mentioning here that the Electrochemical impedance spectroscopy (EIS) helps to analyze the different electrochemical processes during electrochemical cycling. However, resolving the electrochemical processes using conventional equivalent circuit models (ECMs) is challenging due to overlapping time constants in the EIS spectra[43,44]. In contrast, the distribution of relaxation times (DRT) method simplifies the EIS analysis. It also distinguishes each individual electrochemical process through unique time constants.

Here, ***Figures 9.10(c)*** and ***9.10(d)*** present the DRT spectra of PLZ and PL CPSE during symmetric cell performance. The spectra are easily deconvoluted into distinct relaxation regions associated with electrolyte bulk/ion transport ($\tau \sim 10^{-6}$-10^{-5}s), SEI formation ($\tau \sim 10^{-5}$-10^{-4}s), charge-transfer process ($\tau \sim 10^{-3}$-10^{-2}s), and Li-ion diffusion ($\tau > 100$ s) [44].

For the PLZ system (***Figure 9.10(c)***), the SEI peak remains relatively small and stable. Initially, it increases, then once stabilized, it decreases and remains stable, which suggests the formation of a robust and thin SEI layer. The intensity corresponding to the charge-transfer process also remains lower. This may be due to uniform Li-ion flux and suppressed dendrite nucleation over cycling. The diffusion-related peak at longer relaxation times also remains stable, implying facile ionic transport through the composite matrix. In contrast, the PL system (***Figure 9.10(d)***)

displays dynamic interfacial behavior. The SEI peak increases and broadens substantially with cycling, pointing to continuous SEI repair and instability caused by localized Li plating/stripping. The charge-transfer peak broadens and intensifies over time, correlating with interfacial heterogeneity and high overpotentials. It is interesting to observe that changes in the peak correspond to diffusion phenomena in PL system. It appears earlier and at lower τ (~10^{-1}-10 s), but broadening in over cycling may be due to interfacial instability (voids, uneven SEI).

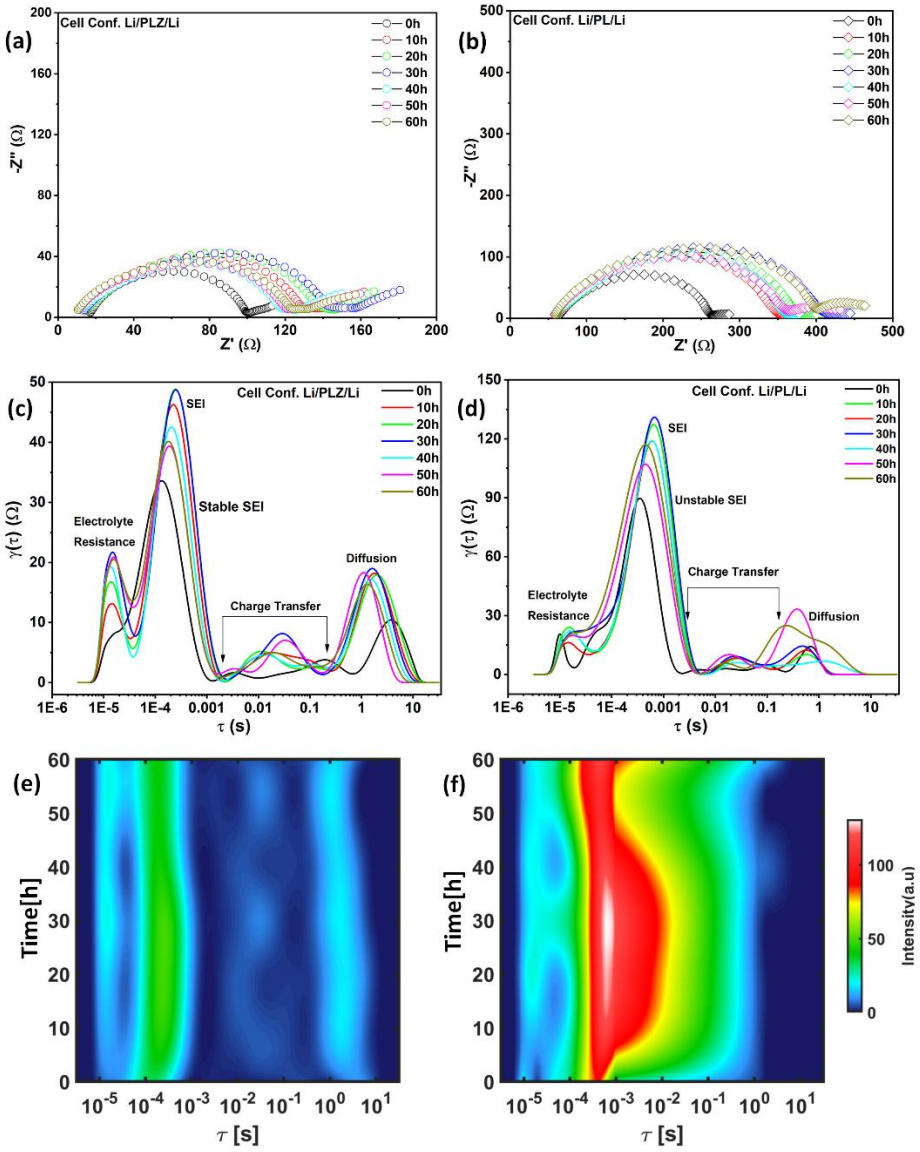

Figure 9.10 *(a), (b) Nyquist plots of Li/PLZ/Li and Li/PL/Li symmetric cells during cycling up to 60 h. (c), (d) Corresponding DRT spectra at various cycling times, decoupling the contributions from electrolyte resistance, SEI resistance, charge transfer, and diffusion processes. (e), (f) 2D contour plots of DRT intensity vs. time show the stable interfacial kinetics for PLZL composite and unstable SEI for bare PL electrolyte*

The cycle-resolved DRT contour plots in ***Figures 9.10(e)*** and ***9.10(f)*** illustrate these trends more clearly. The PLZ electrolyte maintains a narrow and stable SEI signature, whereas the PL system exhibits a progressive shift of interfacial resistance domains, particularly in the charge-transfer and diffusion regions. The SEI is also broadening and at the higher polarization side for PL. Thus, the enhanced performance of PLZ can be attributed to: (i) Lewis acid–base interactions between ZrO_2 and $TFSI^-$ anions, leading to higher ionic conductivity, (ii) the formation of a stable SEI, and (iii) suppressed polymer segmental motion crystallization, providing a flexible yet mechanically reinforced interphase. These factors collectively facilitate faster Li-ion transport and mitigate interfacial fluctuations, as evidenced by the stable SEI and minimal diffusion polarization in PLZ.

The practical applicability of the developed CSPEs can only be proven if they perform well in full cell configuration. To check that, Li/LFP cells were fabricated using all four CSPE membranes. The as-fabricated EIS spectra are taken for all the developed cells before the cycling test at 60ºC to check the various interfacial/charge-transfer resistance. Nyquist plots, along with the equivalent circuit, are presented in ***Figure 9.11(f)***. Here, R_1 denotes the bulk resistance of the developed CSPEs, and R_2 and R_3 represent the anodic and cathodic charge transfer/interfacial resistance. The values of R_1 and R_2 are consistent with those observed in the Li/Li and SS/SS symmetric cells, suggesting that the ionic transport through the bulk electrolyte and across the lithium interface remains stable and reproducible. Among all the developed CSPEs, PL exhibits the highest cathodic charge-transfer resistance, while PLZ demonstrates the lowest, indicating superior interfacial kinetics. The R_3 value of PL, PLA, PLB, and PLZ is found to be 353.7Ω, 259.7Ω, 187.3Ω, and 150.3Ω, respectively, reflecting a significant reduction in interfacial resistance with the incorporation of ceramic fillers.
The cells are cycled at three different current densities of 0.05, 0.10, and 0.20 $mA.cm^{-2}$ at 60ºC. The potential vs specific capacity profiles are represented in ***Figures 9.11(a), (b),*** and ***(c)***, respectively. The discharge capacities of the four developed CSPEs at different current densities are summarised in ***Figure 9.11(d)***, which helps to understand the trend in their capacity values with varying current. At 0.05 $mA.cm^{-2}$, the specific capacity for PL, PLA, PLB, and PLZ are 132.9, 140.9, 148.3 and 151.3 $mAh.g^{-1}$ respectively. These values change to 124.5, 133.3, 135.7 and 144.4 $mAh.g^{-1}$ respectively at 0.10 $mA.cm^{-2}$. At the highest current density of 0.20 $mA.cm^{-2}$, the capacity values decrease drastically to 109.4, 121.7, 132.1 and 141.9 $mAh.g^{-1}$ for PL, PLA, PLB, and PLZ, respectively. From the full cell performance of the developed CSPEs at different current densities, it can be well understood that PLZ membrane

demonstrates the highest specific capacity values and the least capacity loss across the current range, likely because of the befitting interaction of ZrO_2 nanoparticles with PVDF-HFP matrix.

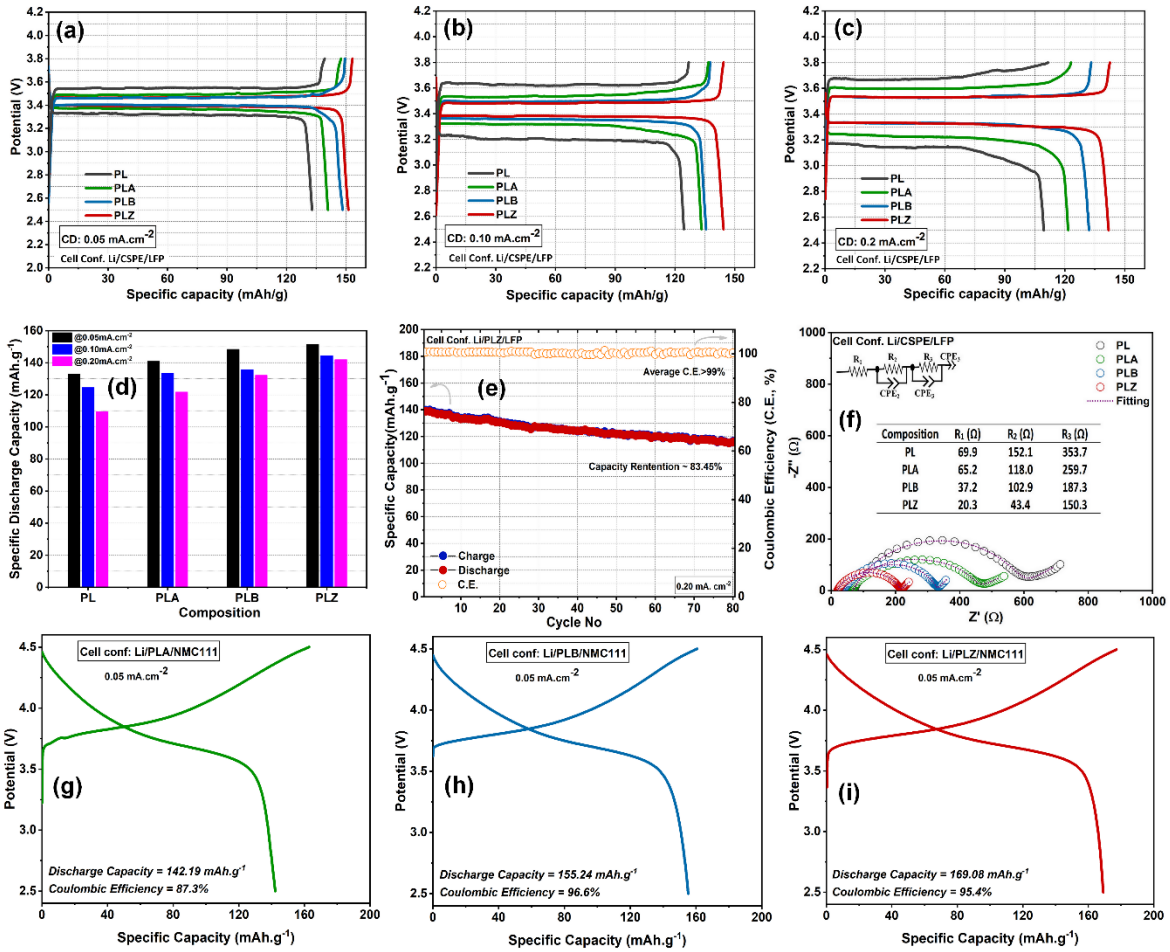

Figure 9.11 *(a), (b) and (c) Typical charge-discharge profiles of Li/LFP cells of PL, PLA, PLB, and PLZ at 0.05, 0.10 and 0.20 mA.cm^{-2} current densities respectively; (d) Comparison among specific discharge capacities of the different CSPEs in the three current densities; (e) Specific capacity vs cycle number plot of Li/PLZ/LFP cell along with coulombic efficiency; (f) Comparison of Nyquist plots for as fabricated Li/LFP cells of PL, PLA, PLB and PLZ*

When the Li/PLZ/LFP cell is further cycled at 0.20 mA.cm^{-2}, it runs smoothly for 80 cycles with more than 99% average coulombic efficiency, as can be observed in ***Figure 9.11(e)***. It is observed that the 83.45% capacity is retained after 80 cycles. To check the multi-cathode computability of the developed CSPEs, the Li/NMC111 cell was fabricated using PLA, PLB, and PLZ CSPEs as presented in ***Figures 9.11(g)-(i)***. Among all the electrolytes, PLZ delivers the highest discharge capacity of 169.02 mAh.g^{-1} at 0.05mA.cm^{-2} current density. Whereas,

PLA and PLB deliver a discharge capacity of 142.19 $mAh.g^{-1}$ and 155.24 $mAh.g^{-1}$ at the same current density of operation.

A comparison chart of the different properties of the CSPEs developed by various researchers worldwide is provided in ***Table 9.3***. Thus, the symmetric cell as well as full cell operations of the developed composite solid polymer electrolytes help to demonstrate the potential of the ZrO_2-incorporated CSPE membrane for application in all solid-state Li-metal batteries.

The electrochemical stability and practicality of the paper-supported composite solid polymer electrolyte (p-PELZ) were further demonstrated in all-paper-based battery configurations. The full cell cycling performance, shown in ***Figure 9.12***, demonstrates that the p-LFP/p-PELZ/p-MCMB cell delivers stable discharge capacities over 100 cycles at a current density of 0.10 $mA \cdot cm^{-2}$ with a ~90% capacity retention. Importantly, the cell maintains a coulombic efficiency consistently above 99%, indicating highly reversible Li^+ intercalation processes in the paper-based electrodes and minimal parasitic side reactions during cycling. The sustained performance underscores the ability of the cellulose-reinforced polymer electrolyte to provide uniform ion transport while preserving interfacial stability at both electrodes.

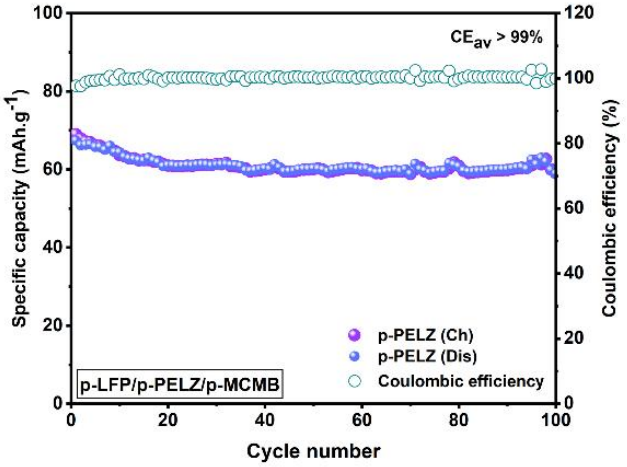

Figure 9.12 *Full cell performance in paper-based LFP/p-CSPE/paper-based MCMB configuration*

Figure 9.13 further validates the interfacial robustness of p-PELZ through symmetric Li/p-PELZ/Li cell testing. The cell exhibits highly stable Li plating-stripping behaviour for more than 1200h at 0.10 $mA \cdot cm^{-2}$ without any short-circuiting or dendritic failure. The enlarged insets of the voltage profiles reveal minimal hysteresis and steady overpotentials of ~15 mV at initial cycles and ~10 mV at the later stage, signifying the establishment of a uniform and stable solid-electrolyte interphase (SEI) on the Li metal electrodes. These findings confirm that the cellulose-supported CSPE not only retains sufficient ionic conductivity, but also ensures mechanical integrity and dendrite suppression over extended cycling. Collectively, the results

in ***Figures 9.12*** and ***9.13*** establish p-PELZ as a viable electrolyte system for next-generation all-solid-state paper batteries, combining safety, scalability, and long-term cycling stability with environmentally benign and mechanically flexible components.

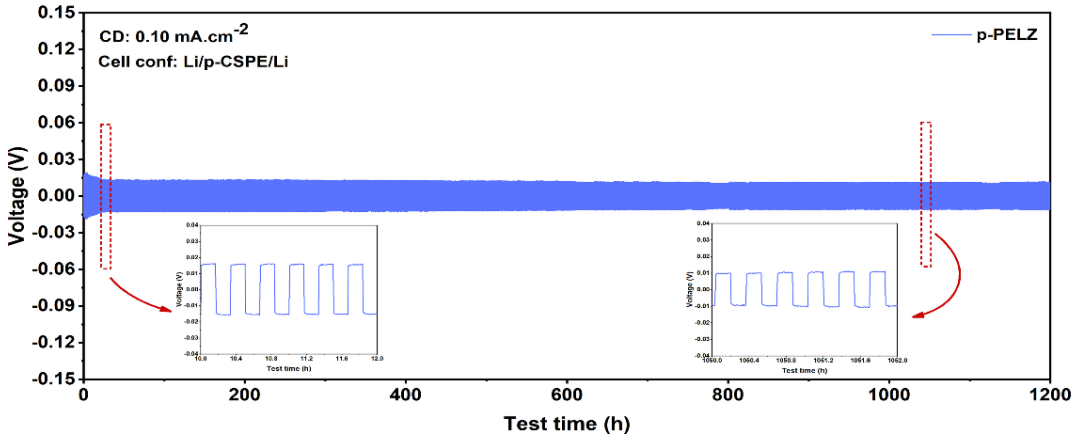

Figure 9.13 *Stable Li plating-stripping for 1200h without any short-circuit*

9.3.4 Thermal Properties

Thermogravimetric analysis (TGA) of PL, PLA, PLB, and PLZ films was conducted with a heating rate of 10ºC min^{-1} up to 1200ºC to evaluate thermal stability. The TGA plots, along with DTA curves of the samples, are depicted in ***Figures 9.14(a)*** and ***9.14(b)***, respectively. As can be observed in ***Figure 9.14(a)***, the initial weight loss of the samples up to 150ºC is primarily attributed to the moisture loss. Although the CSPE films have been prepared under moisture-free and vacuum conditions inside a glove box, they need to be fetched outside the glove box for thermogravimetric analysis. The samples may have caught some moisture at that point. The inherent trapped solvent (here DMF) evaporation may also contribute to this degradation. Additionally, the weight loss up to 300ºC is primarily due to the decomposition of LiTFSI salt, whose melting point is 234ºC [47]. Significant weight loss after 450ºC corresponds to degradation of PVDF-HFP, with the remaining mass attributable to the ceramic particles. The Differential Thermal Analysis (DTA) plots in ***Figure 9.14(b)*** confirm the mass losses due to the above-mentioned degradation processes taking place in the CSPE systems.

Flame safety is an important and critical parameter due to the thermal runaway and flammability in metal batteries. Thus, to evaluate the fire safety, direct flame tests are conducted on all the developed electrolyte samples by exposing them to a near-open flame for 30 seconds as shown in Figures 5(c)-(f) [48,49]. Among them, PL and PLA film shows visible

deformation and shrinkage. PLB shows a little char formation at about 25 seconds and the PLZ film maintains its shape without any burning, ignition or char formation even after 30 seconds, which confirms enhanced flame resistance with $BaTiO_3$ and ZrO_2 ceramic loading.

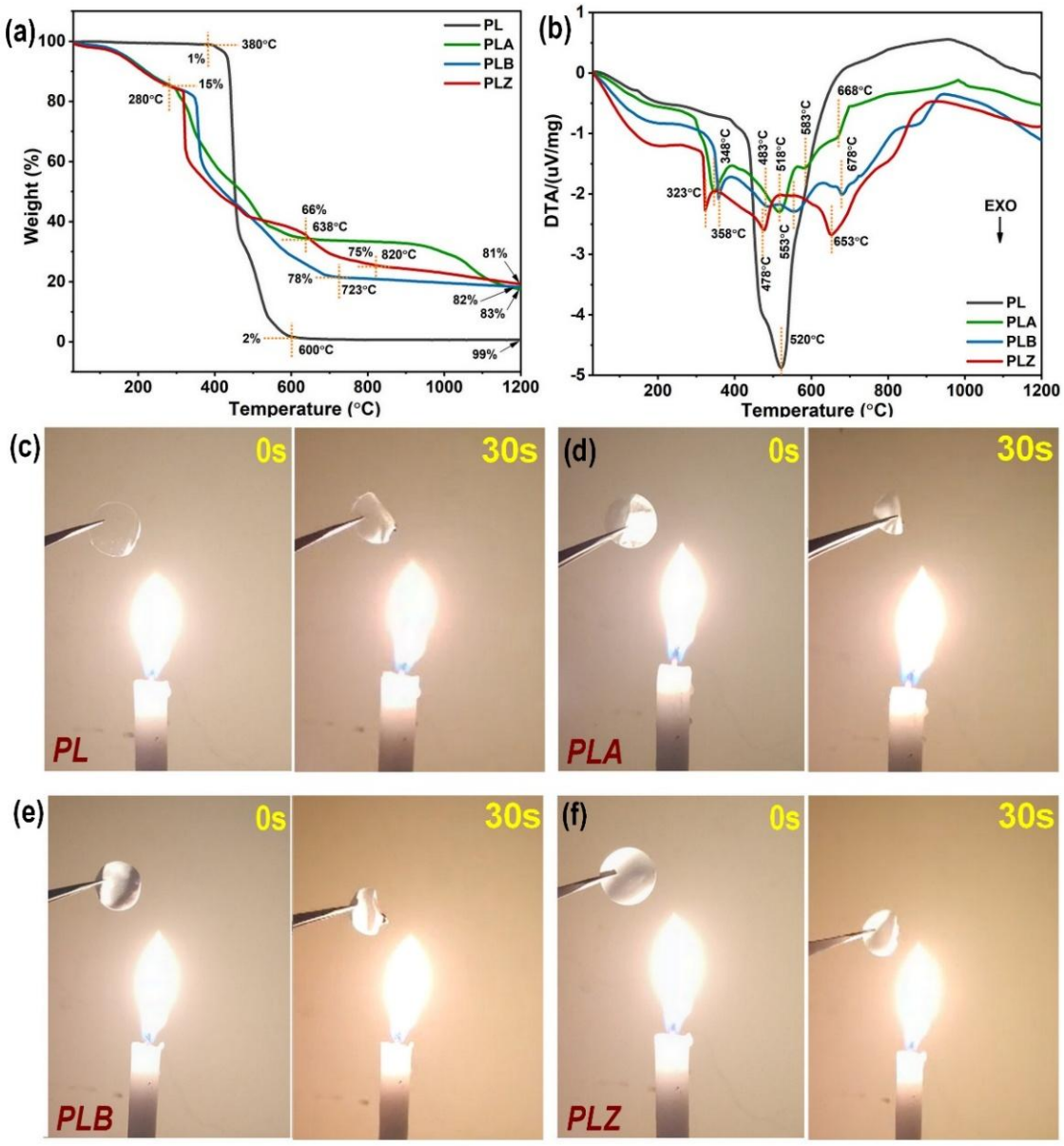

Figure 9.14 *Thermal studies of the developed CSPEs: (a) Thermogravimetric Analysis (TGA) plots; (b) Differential Thermal Analysis (DTA) plots; Flame safety tests for (c) PL, (d) PLA, (e) PLB, and (f) PLZ at 0 and 30 seconds*

Table 9.3 *Comparison among various properties of passive ceramic filler-based composite solid polymer electrolytes for solid-state lithium batteries*

Sl No	CSPE Composition	Thickness (µm)	Ionic Conductivity/ Activation Energy	Electrochemical Stability	Ref.
1	PEO/PVDF-HFP/LiTFSI/ZIF-8	52	6.8×10^{-5} S.cm^{-1} (RT)/0.59 eV	Li/Li cell: polarization ~28.3 mV at 0.1 mA.cm^{-2}, short-circuit after 500h of cycling; Li/LCO cell retains 85.3% capacity after 200 cycles at 0.2C	Tan et al.[17]
2	PVDF/PVDF-HFP/LiTFSI/C-ZrO_{2-x}/$C_3H_6N_6$	90-100	4.7×10^{-4} S.cm^{-1} (25°C)/0.3 V	Critical current density increased from 0.9 mA.cm^{-2} to 1.4 mA.cm^{-2} at 25ºC with ZrO_2; Li/Li cell cycled for 730h with overpotential<60mV; Li/LFP cell ran for 550 cycles at 1 C, 92.13% capacity retention	Liu et al.[16]
3	PVDF-HFP/PEGDE/PEA/LiTFSI/SiO_2	480	2.4×10^{-4} S.cm^{-1}/0.06 eV	Minor interfacial polarization of 0.09 V after 1000h for Li/Li symmetrical cell; for Li/$LiFePO_4$ cell, a capacity retention of 93.8% achieved after 100 cycles at 0.2 C	Xu et al.[18]
6	PVDF-HFP/LiTFSI/UIO-66-F_4(Zr)	90	4.37×10^{-4} S.cm^{-1} (60°C)/0.311 eV	Li/Li cell stably cycles at a current density of 0.1 mA.cm^{-2} for over 1000h, with overpotential of 20–30 mV; 1.15 mA.cm^{-2} critical current density achieved; Li/LFP cell shows a capacity retention of 93.2% after 300 cycles	He et al. [45]
7	PVDF-HFP/LiTFSI/[P_{P13}][TFSI]/UiO-66-NH_2	75	4.842×10^{-4} S·cm^{-1} (60°C)/0.549 eV	Li plating and stripping at 0.05 mA·cm^{-2} for up to 1000h with an overpotential of 50–60 mV without an internal short circuit; Li/LFP cells ran for more than 100 cylces at 2C	Wei et al. [46]
8	PVDF-HFP/LiTFSI/nanoceramics (Al_2O_3, $BaTiO_3$ and ZrO_2)	40-60	9.26×10^{-5} S.cm^{-1} (30ºC)/0.23 eV	For ZrO_2-based CSPE, Li/Li symmetric cell shows stable plating-stripping behaviour at 60ºC for 480h with lowest overpotential of 7 mV; Li/LFP cell runs smoothly at 0.20 mA.cm^{-2} for 30 cycles with more than 99% average coulombic efficiency	This work

9.4 Conclusion

This chapter compared three different passive ceramic fillers (Al_2O_3, $BaTiO_3$, ZrO_2) in a PVDF-HFP/LiTFSI matrix and developed a duo-polymer (PVDF-HFP:PEO) CSPE and its paper-reinforced analogue (p-PELZ) for scalable, flexible solid-state Li-metal batteries. Among the passive fillers, 10 wt% ZrO_2 (PLZ) gave the best balance of properties: highest room-temperature ionic conductivity (9.26×10^{-5} S·cm^{-1}), lowest activation energy (0.23 eV), improved tensile strength (3.23 MPa), Li^+ transference number ($tLi^+ \approx 0.55$), and an extended electrochemical window (~5.33 V). PLZ exhibited stable Li plating/stripping for 480h at 0.10 mA·cm^{-2} (60°C) with minimal overpotential (~7–8 mV), and in Li/LFP full cells delivered the highest specific capacities across 0.05–0.20 mA·cm^{-2} and retained ~83.5% capacity after 80 cycles with >99% coulombic efficiency. Addition of PEO (PELZ) substantially raised bulk ionic conductivity (PELZ ≈ 6.7×10^{-4} S·cm^{-1} at 303 K), while roll-coated p-PELZ (paper-reinforced CSPE) retained practical conductivities (≈4.3×10^{-4} S·cm^{-1}). p-PELZ demonstrated exceptional interfacial stability, with Li/p-PELZ/Li symmetric cells cycling for more than 1200h without shorting, and all solid-state paper-based p-LFP/p-PELZ/p-MCMB full cells retained ~90% capacity and >99% coulombic efficiency over 100 cycles. Mechanistically, superior performance of ZrO_2-containing systems is assigned to favorable surface charge and Lewis acid-base interactions that promote Li-salt dissociation, suppress anion mobility, increase polymer amorphicity and segmental motion, and stabilize the SEI. The paper-supported architecture offers a scalable route, combining continuous ionic pathways with macroscopic reinforcement and flame resistance.

In summary, 10 wt% ZrO_2 in PVDF-HFP (and its PEO-modified, paper-reinforced variants) provides a practical, scalable pathway toward safer, flexible, all-solid-state paper batteries. Future work should focus on interface engineering at ambient temperature, long-term full-cell testing with high-voltage cathodes, and process optimization for roll-to-roll manufacturing.

References:

1 T. Yang, C. Wang, W. Zhang, Y. Xia, H. Huang, Y. Gan, X. He, X. Xia, X. Tao and J. Zhang, *Journal of Energy Chemistry*, DOI:10.1016/j.jechem.2023.05.011.

2 A. G. Nguyen and C. J. Park, 2023, preprint, DOI: 10.1016/j.memsci.2023.121552.

3 S.-H. Kim, M.-H. Woo, S. Omkar, A. Javid, D.-R. Chang and C.-J. Park, *J Power Sources*, 2025, **640**, 236716.

4 C. Hei Chan, H. Ho Wong, S. Liang, M. Sun, T. Wu, Q. Lu, L. Lu, B. Chen and B. Huang, *Batter Supercaps*, DOI:10.1002/batt.202400432.

5 K. Ghosh and M. Wasim Raja, *Chemical Engineering Journal*, DOI:10.1016/j.cej.2023.148200.

6 K. Ghosh and M. Wasim Raja, *ACS Appl Energy Mater*, DOI:10.1021/acsaem.3c00291.

7 M. Muzakir, K. Manickavasakam, E. J. Cheng, F. Yang, Z. Wang, H. Li, X. Zhang and J. Qin, *J Mater Chem A Mater*, 2025, **13**, 73–135.

8 D. Zhou, D. Shanmukaraj, A. Tkacheva, M. Armand and G. Wang, 2019, preprint, DOI: 10.1016/j.chempr.2019.05.009.

9 Z. Song, F. Chen, M. Martinez-Ibañez, W. Feng, M. Forsyth, Z. Zhou, M. Armand and H. Zhang, *Nat Commun*, DOI:10.1038/s41467-023-40609-y.

10 X. Yu and A. Manthiram, 2021, preprint, DOI: 10.1016/j.ensm.2020.10.006.

11 S. Wang, A. La Monaca and G. P. Demopoulos, *Energy Advances*, 2025, **4**, 11–36.

12 C. Hei Chan, H. Ho Wong, S. Liang, M. Sun, T. Wu, Q. Lu, L. Lu, B. Chen and B. Huang, *Batter Supercaps*, DOI:10.1002/batt.202400432.

13 H. Liang, L. Wang, A. Wang, Y. Song, Y. Wu, Y. Yang and X. He, 2023, preprint, DOI: 10.1007/s40820-022-00996-1.

14 V. P. H. Huy, S. So and J. Hur, 2021, preprint, DOI: 10.3390/nano11030614.

15 X. Yang, J. Liu, N. Pei, Z. Chen, R. Li, L. Fu, P. Zhang and J. Zhao, *Nanomicro Lett*, 2023, **15**, 74.

16 Y. Liu, H. Xu, Z. Chen, B. Li, Q. Liu, S. V. Savilov and M. Chen, *J Alloys Compd*, 2025, **1022**, 179925.

17 E. Tan, W. Peng, Q. Li, D. Wang, X. Li, J. Duan, H. Guo, G. Yan, J. Wang and Z. Wang, *Electrochim Acta*, DOI:10.1016/j.electacta.2023.143469.

18 C. Xu, Z. Wang, W. Jiao, Q. Sun, Q. Zhang, C. Li, S. Wang, Y. Ma, Z. He, D. Song, H. Zhang, X. Shi, C. Li and L. Zhang, *J Alloys Compd*, DOI:10.1016/j.jallcom.2023.171548.

19 T. Wei, Z. hong Zhang, Q. Zhang, J. hao Lu, Q. ming Xiong, F. yue Wang, X. ping Zhou, W. jia Zhao and X. yun Qiu, *International Journal of Minerals, Metallurgy and Materials*, DOI:10.1007/s12613-021-2289-z.

20 L. Lee, S. J. Park and S. Kim, *Solid State Ion*, DOI:10.1016/j.ssi.2012.12.011.

21 A. S. Ulihin, N. F. Uvarov, K. S. Rabadanov, M. M. Gafurov and K. B. Gerasimov, *Solid State Ion*, DOI:10.1016/j.ssi.2022.115889.

22 M. Alhoshan, A. K. Shukla and J. Alam, *Water Air Soil Pollut*, DOI:10.1007/s11270-023-06455-w.

23 A. A. Ivanov, V. A. Polyushko and A. Y. Khomyakov, in *IOP Conference Series: Materials Science and Engineering*, 2019, vol. 537.

24 M. Das, K. Ghosh and M. W. Raja, *J Power Sources*, 2024, **606**, 234573.

25 W. Luan and L. Gao, *Ceram Int*, 2001, **27**, 645–648.

26 S. S. Tripathy and A. M. Raichur, *J Exp Nanosci*, 2011, **6**, 127–137.

27 M. Hashiba, H. Okamoto, Y. Nurishi and K. Hiramatsu, *J Mater Sci*, DOI:10.1007/BF01148770.

28 C. Renger, P. Kuschel, A. Kristoffersson, B. Clauss, W. Oppermann and W. Sigmund, in *Physical Chemistry Chemical Physics*, 2004, vol. 6.

29 J. Lu, Z. Wang, Q. Zhang, C. Sun, Y. Zhou, S. Wang, X. Qiu, S. Xu, R. Chen and T. Wei, *Chin J Chem Eng*, DOI:10.1016/j.cjche.2023.01.011.

30 T. Wei, Z. Wang, M. Zhang, Q. Zhang, J. Lu, Y. Zhou, C. Sun, Z. Yu, Y. Wang, M. Qiao and S. Qin, *Mater Today Commun*, DOI:10.1016/j.mtcomm.2022.103518.

31 W. Liu, D. Lin, J. Sun, G. Zhou and Y. Cui, *ACS Nano*, DOI:10.1021/acsnano.6b06797.

32 J. K. Nayak, U. Shankar and K. Samal, *Chemical Engineering Journal Advances*, DOI:10.1016/j.ceja.2023.100459.

33 M. Tripathi, S. M. Bobade and A. Kumar, *Bulletin of Materials Science*, DOI:10.1007/s12034-018-1685-0.

34 A. Gupta, A. Jain and S. K. Tripathi, *Journal of Polymer Research*, DOI:10.1007/s10965-021-02597-9.

35 B. Jamoussi, M. N. M. Al-Sharif, L. Gzara, H. Organji, T. B. Almeelbi, R. Chakroun, B. A. Al-Mur, N. H. M. Al Makishah, M. H. F. Madkour, F. A. Aloufi and R. F. Halawani, *Polymers (Basel)*, 2024, **16**, 1738.

36 N. Zhang, J. He, W. Han and Y. Wang, *J Mater Sci*, 2019, **54**, 9603–9612.

37 A. Narita, W. Shibayama and H. Ohno, *J Mater Chem*, 2006, **16**, 1475.

38 S. Bhaskar, E. W. Awin, K. C. H. Kumar, A. Lale, S. Bernard and R. Kumar, *Sci Rep*, DOI:10.1038/s41598-019-57394-8.

39 D.-T. Van-Pham, V. V. Phat, N. T. Q. Hoa, N. H. Ngoc, D. T. Thao Ngan, T. N. Don, N. T. N. Mai, T. T. B. Quyen and D. V. H. Thien, *IOP Conf Ser Earth Environ Sci*, 2021, **947**, 012017.

40 Y. Chen, J. Niu, S. Zhang, Z. Dong, J. Xu and C. Lei, *J Power Sources*, 2024, **624**, 235569.

41 K. M. Diederichsen, E. J. McShane and B. D. McCloskey, *ACS Energy Lett*, DOI:10.1021/acsenergylett.7b00792.

42 J. Evans, C. A. Vincent and P. G. Bruce, *Polymer (Guildf)*, DOI:10.1016/0032-3861(87)90394-6.

43 C. Plank, T. Rüther, L. Jahn, M. Schamel, J. P. Schmidt, F. Ciucci and M. A. Danzer, *J Power Sources*, DOI:10.1016/j.jpowsour.2023.233845.

44 Y. Lu, C. Z. Zhao, J. Q. Huang and Q. Zhang, 2022, preprint, DOI: 10.1016/j.joule.2022.05.005.

45 L. He, Z. Di, J. Li, S. Wang, W. Kong, R. Li, A. Proskurin, C. Lv and T. Wei, *Chemical Communications*, 2024, **60**, 14637–14640.

46 T. Wei, Q. Zhang, S. Wang, M. Wang, Y. Liu, C. Sun, Y. Zhou, Q. Huang, X. Qiu and F. Tian, *International Journal of Minerals, Metallurgy and Materials*, DOI:10.1007/s12613-023-2639-0.

47 V. van Laack, F. Langer, A. Hartwig and K. Koschek, *ACS Omega*, 2023, **8**, 9058–9066.

48 K. Ghosh, M. Das and M. W. Raja, *J Power Sources*, 2025, **654**, 237838.

49 M. Das, P. S. Das, R. N. Basu and M. W. Raja, *Cellulose*, DOI:10.1007/s10570-022-04873-3.

Chapter 10

Conclusions & Future Perspectives

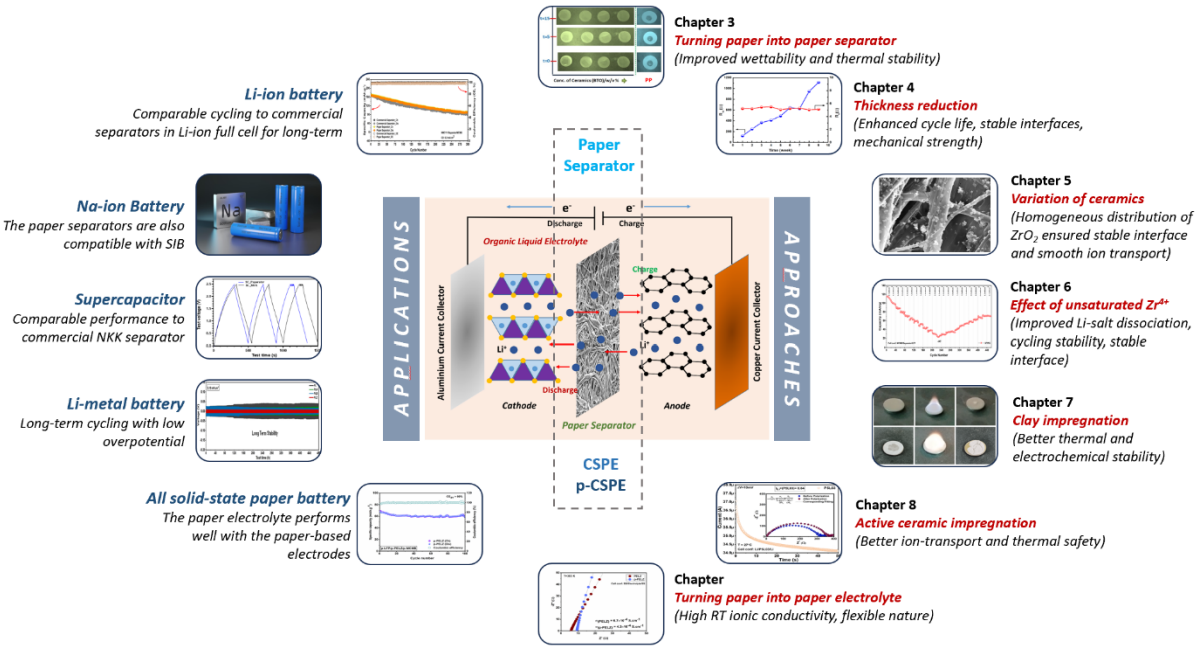

Figure 10.0 *Graphical overview of the research works conducted under this thesis and their major outcomes*

The present research has successfully demonstrated the potential of cellulose paper as a sustainable platform for next-generation battery separators and electrolyte membranes. Starting from locally available commercial paper, the work has progressively advanced through polymer reinforcement, ceramic impregnation, hybrid functionalization, and clay-based fillers, ultimately leading to the development of high-performance paper separators with excellent safety, thermal stability, and electrochemical compatibility.

10.1 Conclusions

The main objective of this thesis was to develop a sustainable alternative of the commercial polyolefin-based separator, which owing to its limited electrolyte wettability and low thermal stability, lacks the potential and safety needs required for use in EV battery packs. In spite of these drawbacks, PP/PE-based membranes are ruling the global separator market, in the absence of any suitable alternative that truly holds the potential to replace polyolefin. Also, amidst the increasing pollution and environmental concerns, replacing plastic-based separator with some sustainable alternative is crucial to move a step towards carbon neutrality.

In this scenario, cellulose can be a game changer, especially if we consider its excellent wettability, robustness, natural abundance and ability to be functionalized. Paper contains all the advantages of cellulose materials, along with the structural integrity as add on. To convert paper into paper separator, we have tried to modify its surface by polymer and ceramic incorporation. An easy-to-reproduce and industry-friendly wet-coating process has been developed and optimized for this purpose. Apart from the commercial aspects and performance related parameters, the scientific and chemistry aspects of the research have also been quested in this thesis.

With its uniform pore distribution and smooth surface, polyolefin is able to establish stable interfaces with the electrodes, that result in efficient electrochemical cycling in a cell. However, the surface of raw paper is rough in nature. Sizing with suitable polymers help to make paper surface smoother and the matrix stronger. Incorporation of different passive ceramics helps in stabilizing separator-electrode interfaces, depending on their surface charge and nature of distribution. The ceramic nanoparticles also help to modify the crystallinity of polymer matrices and control the ionic conductivity of polymer electrolytes. On the other hand, ion-conducting active ceramic materials help to provide alternative ion-conduction pathways through separator, thereby increasing the effective ionic conductivity and ion-transport number. The physico-chemical and electrochemical performances and their possible reasons have thoroughly been discussed in the previous chapters of the thesis.

Chapter 1 is the introductory part of the thesis, where the motivation of this research has been explained in detail. The world is moving towards e-mobility and the demand and research on materials used in rechargeable batteries are increasing exponentially. Separator, although an electrochemically inert component in energy storage systems, can influence the safety and performance of the systems significantly. Both commercially used separator and liquid

electrolyte in Lithium-ion batteries pose environmental concerns and safety issues, which compel the researchers worldwide to search for their sustainable alternatives, especially for electric vehicle applications. The government of India, with its electric mobility mission, net zero targets and Atmanirbhar Bharat programme, is emphasizing on self-reliance and sustainability in case of battery components. Hence, the development of cellulose paper-based separator and electrolyte membranes is important in both global and domestic perspectives.

Chapter 2 elaborates the research methods and experimental works conducted throughout the study.

- **The Early Stage of Paper to Paperator journey**

Developing a new material requires a lot of composition variation and optimization, which have been discussed in ***Chapter 3***. The journey of paper separator development started with a locally outsourced commercial paper, which had several impurities and a much higher thickness (~80/90 μm) than the commercial separator standard. Those impurities had been anchored and the paper had been reinforced by two suitable polymers, chitosan and polyvinyl alcohol. The concentration of the two polymers has been varied and optimized to a standard ratio. Two different ceramic materials have also been impregnated in the paper matrix separately according to their functionalities: (i) $BaTiO_3$ for its ferroelectric nature and ability to dissociate Li-salts present in the liquid electrolyte, which helps in enhancing ionic conductivity and (ii) SiO_2 for its low cost, stability, porous nature and thermal stability, which provide high electrolyte wettability and flame resistance. Both the paper separators show improved performance in an optimal ceramic concentration:

(a) An industry-friendly aqueous wet-coating process is developed and optimized to fabricate the paper separators in roll form.
(b) Ceramic impregnated paper separators show dimensional stability up to 200°C, outperforming PP-based commercial separator which degrades at about 150°C.
(c) The paper separators show instant surface wetting by the liquid electrolyte and much lower electrolyte contact angle than the commercial separator, suggesting their excellent wettability. Commercial separator takes prolonged time in soaking and it can retain much lesser amount of electrolyte than cellulose-based separators.
(d) In LIB cells, the developed separators delivered satisfactory charge-discharge cycling, excellent coulombic efficiency (>98%), and comparable discharge capacities to PP

separators, especially for 0.1 w/v% BTO and 1.5 w/v% SiO_2, with slightly lower capacity attributed to higher thickness (60–70 μm) and tortuous cellulose pathways.

(e) The BTO-based separator (C25PV1BT01) also functioned effectively as separator in supercapacitors (tested to IEC 62391-1), achieving cell capacitance ~17.2 F and ESR ~76 mΩ, comparable to commercial cellulose separators.

(f) Both BTO and SiO_2-based paper separators exhibit excellent flame safety characteristics.

- **Trilayer Separator with Pure Cellulose Substrate: Suppressing the Effect of Ceramic Dissolution**

In ***Chapter 4***, we have substituted the ~80 μm paper substrate with a ~20 μm NKK-grade paper which has no added impurities. The new substrate consists of 100% cellulose, that has been confirmed from its FESEM and EDX analysis. While this purity is beneficial in electrochemical cycling, it does to not allow the paper to go through aqueous processing. That is why the paper is functionalized with PVDF in NMP solution along with ceramic nanoparticles. In this particular research work, a trilayer separator has been developed by three process steps: (i) sizing the paper with 3.5 w/v% PVDF in NMP solution, (ii) ceramic ($BaTiO_3$) impregnation in 2.0 w/v% in 7.0 w/v% SBR aqueous solution and (iii) lamination by varying concentrations (1.0-3.0 w/v%) of SBR aqueous solution. The developed paper separators exhibit optimal and sometimes better performance as compared to the commercial separator:

(a) The trilayer paper separator demonstrated much higher electrolyte wettability (216–270%) than the commercial separator (~90%), rapid saturation, and enhanced dimensional stability up to 200°C without shrinkage.

(b) In MCMB/LFP full cells, the separator showed comparable capacity, rate capability, coulombic efficiency (>95–96%), and long-term cycleability (>300 cycles) versus commercial PP/PE separators.

(c) Calendar ageing test for 8 weeks revealed no significant change in resistivity or morphology for the paper separator, while the PP-based separator showed a significant enhancement in bulk resistance.

(d) Flame tests (IEC 60695-11-10) confirmed excellent flame-retardant behaviour.

(e) The separator also functioned effectively in supercapacitors (IEC 62391-1, Class II standard), achieving capacitance and ESR values comparable to commercial separators, demonstrating versatility beyond LIBs

- **Role of Different Ceramic Fillers (Al_2O_3, $BaTiO_3$ and ZrO_2)**

While the ceramic particles had helped to improve separator functionalities significantly so far, the exact role of ceramics on separator properties and overall battery performance was yet to be discovered. In ***Chapter 5***, we have chosen three different ceramic nanopowders (Al_2O_3, $BaTiO_3$ and ZrO_2) to impregnate in paper matrix, based on their surface charge. The zeta potential and morphology of ceramic nanoparticles dictated their deposition pattern on cellulose fibers, as confirmed from FESEM images. Al_2O_3, with a lower positive zeta potential value, although interacts with negatively charged cellulose surface but shows a high tendency to form agglomerates. $BaTiO_3$ shows poor interaction with cellulose due to its lower negative zeta potential in our working pH range, and resides randomly on paper matrix in agglomerated form. ZrO_2, on the other hand, registers a highly positive zeta potential, thus interacting strongly with every individual cellulose fibers.

As a result, the ZrO2-impreganted paper separator (P3S7Z2) shows better Li-ion transport, electrochemical cycling and interface stabilization than the other two separators (P3S7A2 and P3S7B2):

(a) P3S7Z2 achieved the best performance with ionic conductivity ~1.08×10^{-3} $S\cdot cm^{-1}$, high Li^+ transference number ~0.51, and excellent electrolyte uptake (~287%).
(b) In full-cell (NMC111/MCMB) configurations, P3S7Z2 delivered higher rate capability and superior long-term stability (300 cycles, >98% CE) compared to Al_2O_3 and $BaTiO_3$ counterparts, which showed faster degradation.
(c) Post-cycling EIS revealed that charge-transfer resistance increased minimally for ZrO_2-based separators, while Al_2O_3 and $BaTiO_3$ systems showed large resistance growth, confirming superior electrode compatibility of zirconia nanoparticles.
(d) All ceramic-based paper separators exhibited dimensional stability at 200°C and strong flame resistance, but P3S7Z2 stood out as the most flame-tolerant, resisting ignition as well as char formation even under extended flame exposure.

- **Functionalization of Paper with Chelated ZrO_2**

While ZrO_2 impregnation significantly assists in enhancing separator performance, the saturated coordination of Zr^{4+} by O^{2-} reduces the Lewis acid-base interaction and compromises the Li-salt ($LiPF_6$) dissociation. To further enhance the electrochemical cycleability and interface compatibility, ***Chapter 6*** focuses on the preparation of a zirconium isopropoxide–

acetylacetone sol via controlled hydrolysis to generate under-saturated Zr^{4+} sites and Zr–OH groups, and its incorporation within the cellulose paper matrix. The organo-inorgano hybrid zirconia incorporated paper separators (HY05-20) undergo some inherent structural and chemical changes and significant performance enhancement as a result:

(a) XRD and FTIR showed that incorporation of chelated ZrO_2 reduced cellulose crystallinity (from CI ~ 58.3 % for cellulose paper to minimum of CI ~ 15.6% at HY15) significantly. It helped to disrupt hydrogen-bonding networks, and introduced abundant Zr–OH sites, creating favorable ion-conduction pathways.
(b) Contact angle decreased from 22.9° (PVDF-sized HY00) to 11.6° at HY15, correlating with its maximum electrolyte uptake (~338%).
(c) The optimal HY15 separator delivered ionic conductivity ≈ 1.30×10^{-3} $S\cdot cm^{-1}$ with reduced bulk resistance (~0.87 Ω), much better than those of HY00.
(d) Wider electrochemical potential window (>5V) achieved.
(e) Chelated ZrO_2 incorporation improved tensile strength (up to ~52 MPa in machine direction) and created Lewis acid–base sites (Zr^{4+}/O^{2-}/–OH) that enhance Li^+ salt dissociation, suppress dendrite growth, and improve interfacial stability under cycling.

- **Impregnation of Natural Clay in Paper Separator**

The commercial ceramic nano-powders although provide enhanced characteristics in paper separators, their costs are typically high which limits the development of a sustainable paper separator in true sense. This is the reason we have explored a natural clay material as reinforcing filler inside the cellulose matrix in ***Chapter 7***.

We have chosen low cost and naturally abundant Montmorillonite (MMT) clay and impregnated it in paper matrix alongside PVDF and SBR. Montmorillonite is also a well known flame retardant material, which helps to modify the cellulose surface in such a way that the heat can be dissipated uniformly in presence of flame. Other physical and electrochemical properties have also benefitted from the incorporation of MMT, which are summarised as follows:

(a) High thermal and electrochemical stability achieved.
(b) 1.5 wt% MMT impregnation provided the best performance.
(c) Cycling stability for up to 500 cycles with >99% coulombic efficiency

- **Probing the Impregnation of Ion-conducting Ceramic: Active Filler ($Li_7La_3Zr_2O_{12}$)**

So far, we had explored the 'passive' fillers that indirectly helped in improving Li-ion conductivity and transport phenomena, but could not directly influence them. This time, in the study elaborated in ***Chapter 8***, a Li-ion conducting high temperature ceramic material $Li_7La_3Zr_2O_{12}$ (LLZO) has been incorporated in cellulose paper matrix to see the effect of such 'active' fillers in separator performance. LLZO is a well known garnet type inorganic solid oxide, whose ionic conductivity is high and electronic conductivity is low, inducing its potential to be used as an electrolyte in solid state batteries (SSBs). We have prepared LLZO via a wet chemical combustion reaction and incorporated the calcined LLZO powder in varying concentrations (10-70 wt%) in paper matrix by the same dip-coating process as previous. The physico-chemical alterations of the cellulosic matrix and their effect on overall cell and safety performance have been elaborated in ***Chapter 8***, along with comparison with commercial separator and an Al_2O_3-based passive separator. To summarize,

(a) The composition with 30 wt% LLZO (P5L03) was identified as optimal, delivering high ionic conductivity (~1.23 $mS \cdot cm^{-1}$) and a lithium transference number of ~0.64, significantly outperforming Al_2O_3-based paper separators and even commercial PP membranes.
(b) LLZO-containing separators exhibited excellent electrolyte uptake (~250-365%), rapid wettability, and favorable Gurley values (7-15s), ensuring smooth ion transport through the paper matrix.
(c) In full-cell tests, P5L03 enabled stable cycling, reduced polarization, and low interfacial resistance growth during long-term operation, also showing broad compatibility with multiple electrode chemistries.
(d) The LLZO-paper separators maintained structural integrity above 200°C, displayed very high self-extinguishing flame resistance, and effectively suppressed shrinkage, highlighting their safety superiority over commercial PP/PE membranes and Al_2O_3-based separator.

Functionalization of cellulose paper matrix with suitable polymers, active and passive ceramics fillers and sustainable clay materials successfully integrate superior electrolyte wettability, optimal mechanical strength, high thermal safety, enhanced ion transport along with stable cycling in cathode/anode (graphite-based) full cell configurations. But such modifications

cannot enable the paper separator to cycle against Li-metal anode, which provide highest possible capacity and energy density for a cell. Also, the paper-based separators require organic liquid electrolyte, which is flammable in nature and thus limits the safety of the battery. If we want a membrane which will produce improved performance with ultimate safety and stability, we have to substitute both plastic separator and carbonate-based electrolyte with paper-based material.

- **Towards Solid-State Paper Electrolyte**

With the aim of developing paper-based electrolyte-cum-separator membrane, we have explored composite solid polymer electrolytes (CSPEs) initially in ***Chapter 9***. PVDF-HFP and LiTFSI-based CSPE systems provided optimal ionic conductivity, Li-ion transference number and stable cycling against Li-metal. Here also, three different ceramics (Al_2O_3, $BaTiO_3$ and ZrO_2) have been used as fillers and their compositions are optimized and performances are compared duly. Maintaining the previous trend of *Chapter 5*, here also ZrO_2 has outperformed the other two ceramics in every aspect. Due to the limited room temperature ionic conductivity (highest achieved 9.26×10^{-5} $S\cdot cm^{-1}$ at 30°C for ZrO_2-based membrane) of these CSPEs, another polymer (PEO) has been introduced to the base PVDF-HFP matrix to enhance polymer chain mobility and effective ion transport. After optimizing the CSPE composition, the same has been transferred to paper substrate for developing a paper-based composite solid polymer electrolyte (p-CSPE). This electrolyte shows high Li-ion conductivity and stable cycling performance at room temperature. At the same time, paper has been functionalized with in-situ polymerization of aniline, to produce electronic conductivity to the matrix. This paper has been used as the substrate for casting cathode and anode, thereby ultimately moving towards the goal of producing all solid-state paper cell, whose all the major components (i.e., cathode, electrolyte and anode) is paper-based. To summarize the chapter contents,

(a) A simple solution casting method was followed for developing the CSPE membranes.
(b) The 10 wt% ZrO_2-based CSPE showed the best balance of properties — highest ionic conductivity (9.26×10^{-5} $S\cdot cm^{-1}$ at 30°C), wide potential window (5.33 V), tensile strength (3.23 MPa), and Li^+ transference number (0.55).
(c) Li/PLZ/Li symmetric cells exhibited stable plating–stripping for >480 h at 0.10 $mA\cdot cm^{-2}$, maintaining the lowest overpotential (~7-8 mV) and minimal rise in interfacial resistance, confirmed by EIS and DRT analyses.

(d) ZrO_2- and $BaTiO_3$-based CSPEs demonstrated superior flame resistance, retaining membrane integrity even after 30 s of direct flame exposure, unlike pristine PVDF-HFP electrolytes.

(e) We have prepared a prototype paper cell with p-LFP, p-MCMB and p-CSPE, that produced stable cycling and high ionic conductivity at room temperature.

10.2 Key Insights

This thesis contains a comprehensive and detailed research on development and performance optimization of paper-based separators, primarily developed for rechargeable Li-ion batteries. The applicability of the developed separators has also been extended to other energy storage devices, like supercapacitors and Na-ion batteries. Almost 10 different types of paper separators have been developed here, with different compositions and functionalities. Each of them showed some distinct characteristics, both inside and outside of electrochemical cells. While studying the different phenomena of the paper-based systems, some key insights have caught the particular attention, which include;

- ***Paper → high-performance separator by simple surface engineering:***
  A pragmatic polymer-sizing + ceramic-impregnation route via easy wet-coating process converts commercial cellulose paper into LIB separators with greatly improved electrolyte wettability, uptake, tensile strength and dimensional stability (no shrinkage up to ~200°C), delivering full-cell cycling and supercapacitor performance comparable to commercial separators.
- ***Choice of ceramics and surface chemistry-controlled interface and ion transport:***
  The deposition behavior of ceramics on cellulose matrix, governed by zeta potential and coordination state of ceramic fillers determine coating uniformity, pore connectivity and interfacial impedance. Positively charged ZrO_2 provides homogeneous fiber coatings and higher t_{Li^+}/σ (e.g., P3S7Z2), while chelated Zr precursors (under-saturated Zr^{4+}/Zr-OH) further reduce cellulose crystallinity, enhance Li-salt dissociation and enhance ionic conductivity.
- ***Active ceramic fillers (LLZO) shift inactive separators towards semi-active electrolyte function:***
  Incorporating Li-ion-conductive ceramics (LLZO) produces hybrid separators (best at ~30 wt% LLZO) that show enhancements in ionic conductivity and Li-transport

phenomena, while retaining the flexibility and inducing superior thermal safety to paper-based membranes.

- ***Composite solid polymer electrolyte with ZrO_2-reinforcement shows a pathway to develop paper-based electrolyte:***

  PLZ and their paper-cast analogues support long-term Li plating/stripping with low overpotential (Li/PLZ/Li >480 h) and reasonable room temperature conductivity ($\sigma \approx 9.26\times10^{-5}$ S·cm^{-1}, $t_{Li^+} \approx 0.55$). A clear manufacturing pathway (semi-automated roll coating) exists, yet pilot-scale uniformity, extended calendar aging, pouch-format tests and TEA/LCA are the critical next steps for commercialization.

10.3 Future Perspectives

The research presented in this thesis establishes cellulose paper as a strong candidate to replace or complement conventional polyolefin separators. At the same time, it shows the potential of paper substrates to be transformed into multifunctional solid-state electrolytes. Building on the present outcomes, several research directions emerge for the future:

- ***Wider material exploration for fillers and functionalization:*** Beyond the ceramics studied here (Al_2O_3, $BaTiO_3$, ZrO_2, LLZO), new low-cost natural materials such as layered silicates, bio-derived nanoparticles, and flame-retardant minerals could further enhance performance while reducing costs. Functional nanomaterials (e.g., MXenes, metal–organic frameworks, covalent organic frameworks) may be incorporated to tailor ionic conductivity, interfacial chemistry, and even redox activity.
- ***Designing hybrid membranes for next-generation batteries:*** Paper separators functionalized with Li-ion conducting oxides (like LLZO or LATP) can serve as hybrid separator–electrolyte systems in solid-state Li-metal batteries, improving safety without compromising energy density. Integrating polymer–ceramic composite systems directly onto paper may allow flexible, thin, yet highly conductive membranes for lithium, sodium, and potassium batteries.
- ***Scalability, manufacturability, and device prototyping:*** While this thesis demonstrated semi-automated roll-to-roll fabrication, scaling to pilot production lines remains a key next step. Future work should include inline quality control, coating uniformity optimization, and life cycle/cost analysis to evaluate commercial feasibility. Development of pouch-cell and module-level prototypes using paper-based membranes will bridge the gap between laboratory studies and real-world applications.

- ***Compatibility with advanced chemistries:*** Paper-based membranes can be tailored for metal anodes (Li, Na, K, Zn) by improving dendrite suppression and interface stability. They also hold promise in multivalent systems (Mg^{2+}, Al^{3+}) and aqueous rechargeable batteries, where their natural hydrophilicity and mechanical robustness are advantageous.
- ***Sustainability and recyclability:*** Future research should evaluate the end-of-life recyclability of paper-based separators and electrolytes, exploring recovery of cellulose and ceramic fillers from spent cells. Green solvents and bio-based binders should replace current fluorinated polymers (PVDF, PVDF-HFP) to create a fully eco-friendly battery membrane platform.
- ***Functional integration beyond energy storage:*** Paper-based membranes can also be functionalized for multi-device compatibility, serving as shared components across batteries, supercapacitors, and hybrid energy storage devices. The inherent porosity and flexibility of paper further enable applications in wearable electronics, disposable sensors, and flexible storage systems, extending the utility of this technology beyond conventional LIBs.

10.4 Technical Specifications of Paper-based Ceramic Separator

Product Name	Specifications
Paper-based Ceramic Separator	• Composition: Cellulose paper-polymer-ceramic/clay composite membrane • Fabrication Process: Industry-friendly wet-coating process • Scale of production: Large scale production up to 100 meters • Dimension: Length - as required, Width – 62 mm • Thickness: 20±2 μm • Porosity: >50% • Air permeability: Sufficient (Gurley value 5-120 seconds) • Electrolyte Wettability: Very high with 200-350% electrolyte uptake and retention • Electrolyte Soaking Time: 10-20 minutes (much less than commercial polyolefin separator) • Thermal Stability: Very high; no dimensional change up to 250°C • Flame Safety: High; no catching of fire, only char formation • Mechanical Strength: Moderate; tensile strength 45-51 MPa in machine direction and 22-28 MPa in transverse direction • Chemical Stability: No chemical degradation in presence of liquid electrolyte (as tested via aging) • Ionic Conductivity: ~10^{-4} $S.cm^{-1}$ • Electrochemical Potential Window: >5 V • Li^{+} Transference Number: 0.2-0.6 • Electrochemical Performance: Comparable to commercial separator • Cycling Stability: >500 cycles • Current Density of Operation: Highest 2.2 $mA.cm^{-2}$ • Coulombic Efficiency: >98%

APPENDIX-I

List of Publications/Conference Papers/Awards

Research Publications

1. Mir Wasim Raja, Rajendra Nath Basu, Nimai Chand Pramanik, Pradip Sekhar Das, **Mononita Das**, *Paperator: The Paper-Based Ceramic Separator for Lithium-Ion Batteries and the Process Scale-Up Strategy,* ACS Applied Energy Materials 2022, 5, 5, 5841–5854.

2. **Mononita Das**, Pradip Sekhar Das, Rajendra Nath Basu, Mir Wasim Raja, *Cellulose-ceramic composite flexible paper separator with improved wettability and flame retardant properties for lithium-ion batteries,* Cellulose 2022, 29, 9899–9917.

3. **Mononita Das**, Pradip Sekhar Das, Nimai Chand Pramanik, Rajendra Nath Basu, Mir Wasim Raja, *Advanced Sustainable Trilayer Cellulosic "Paper Separator" Functionalized with Nano-BaTiO3 for Applications in Li-Ion Batteries and Supercapacitors,* ACS Omega 2023, 8, 23, 21315–21331.

4. **Mononita Das**, Kuntal Ghosh, Mir Wasim Raja, *Flexible ceramic based 'paper separator' with enhanced safety for high performance lithium-ion batteries: Probing the effect of ceramics impregnation on electrochemical performances,* Journal of Power Sources 2024, 606, 234573.

5. Simranjot K Sapra, **Mononita Das**, M Wasim Raja, Jeng-Kuei Chang, Rajendra S Dhaka, *Flexible trilayer cellulosic paper separators engineered with the BaTiO3 ferroelectric fillers for high energy density sodium-ion batteries,* Journal of Materials Chemistry A 2025, 13, 1996-2009.

6. Kuntal Ghosh[#], **Mononita Das**[#], Mir Wasim Raja, *Role of LLZO active filler in PVDF-modified cellulosic paper matrix: A sustainable, thermally durable and high-performance separator for next generation lithium batteries,* Journal of Power Sources2025, 654, 237838. *(#equal contribution)*

7. **Mononita Das**, Kuntal Ghosh, Mir Wasim Raja, *The critical role of Al2O3, BaTiO3 and ZrO2 nanoceramic fillers in PVDF-HFP based composite polymer electrolytes for high performance lithium-metal batteries,* Solid State Ionics 2025, 430, 117008.

8. Kuntal Ghosh[#], **Mononita Das**[#], Mir Wasim Raja, *LLZO incorporated Dual Polymer-based Composite Electrolyte for Enhanced Conductivity and Long-Term Stability for Solid-State Lithium-Metal Batteries,* Journal of Solid State Electrochemistry 2025, In Press. *(#equal contribution)*

9. Kuntal Ghosh, **Mononita Das**, Alok Kumar Chaudhary, Mir Wasim Raja, *High-Performance Quasi-Solid-State Lithium Metal Batteries: Interface Engineering Using Solid-Liquid Dual Therapy by Solvated Ionic Liquid and NiO,* ACS Applied Materials & Interfaces. (Under Review)

10. Kuntal Ghosh, **Mononita Das**, Mir Wasim Raja, LiF-Rich Dual Interface Engineering in LLZO Electrolytes via NH_4F Treatment and Solvated Ionic Liquid Infusion for Solid-State Lithium Metal Batteries. (In Submission)

11. **Mononita Das**, Kuntal Ghosh, Koushik Dana, Mir Wasim Raja, Paper-Clay Separator: Montmorillonite clay impregnated paper-based sustainable advanced separator for Lithium-ion Battery application. (In Submission)

12. **Mononita Das**, Kuntal Ghosh, Srikrishna Manna, Mir Wasim Raja, Inclusion of Zr-based Organo-Inorgano hybrid materials in paper matrix: The next generation sustainable Paper Separator' for lithium-ion batteries with improved electrochemical performance and safety. (In Submission)

13. Kuntal Ghosh, **Mononita Das**, Mir Wasim Raja, Mitigating Solid-Solid Interfacial Challenges in NZSP Solid Electrolytes Using Ether-Based Liquid Therapy for High-Performance Quasi-Solid-State Sodium Metal Batteries. (In Submission)

Conferences/Seminars Attended

1. **Mononita Das**, Pradip Sekhar Das, Mir Wasim Raja
   Poster presentation titled "Paperator: A novel Cellulose based Paper Separator for Lithium-ion Batteries" in Shaping the Energy Future : Challenges and Opportunities (SEFCO), August 27, 2021, CSIR - Indian Institute of Petroleum, Dehradun, Uttarakhand, India. *(online mode)*

2. **Mononita Das**, Pradip Sekhar Das, Mir Wasim Raja
   Oral presentation titled "Paper Separator" with Improved Porosity, Thermal Stability and Electrochemical Performance for Application in Lithium-Ion Batteries" in International Virtual Conference on Advances in Ceramics and Cement Technologies: Materials and Manufacturing (IvaCCT), Indian Ceramic Society, Karnataka Chapter, December 13-14, 2021, PDA College of Engineering, Kalaburagi, Karnataka. *(online mode)*

3. **Mononita Das**, Mir Wasim Raja
   Poster presentation titled "PAPERATOR: A first-of-its-kind indigenous, sustainable and low cost separator for Lithium-ion Batteries/Supercapacitors" in International Conference on Global Trends in Traditional to Space Ceramics (GT-TSC'22), December 8-9, 2022, IIT BHU, Varanasi. *(in person)*

4. **Mononita Das,** Mir Wasim Raja
   Poster presentation titled "Paper to Paper Separator: Indigenized low cost separator for Li-ion Batteries/Supercapacitors for powering Electric Vehicles (EVs)" in MRSI Young Scientist Colloquium 2022 (YSC-2022), December 16, 2022, CSIR-CGCRI, Kolkata. *(in person)*

5. **Mononita Das**, Kausik Dana, Mir Wasim Raja
   Poster presentation titled "Indigenized Paper-Clay Separator: Low Cost, Sustainable Alternative Separator Membrane for EV Batteries" in 2nd International Meeting on Energy Storage Devices 2023 (IMESD 2023), December 7-10, 2023, IIT Roorkee, Uttarakhand. *(in person)*

6. **Mononita Das**, Kuntal Ghosh, Mir Wasim Raja
   Poster presentation titled "Interfacial Modification of NZSP Solid Electrolyte with Ionic Liquid for High Performance Quasi-Solid-State Sodium Metal Batteries" in International Conference on Advanced Energy Materials and Interfaces 2024 (AEMI-24), December 9-11, 2024, IISER Pune, Maharashtra. *(in person)*

7. **Mononita Das**, Kuntal Ghosh, Vijaya, Mir Wasim Raja
   Oral presentation titled "The Critical Role of Al_2O_3, $BaTiO_3$ and ZrO_2 Nanoceramic Fillers in PVDF-HFP based Composite Polymer Electrolytes for High Performance Lithium-Metal Batteries" in International Conference on Advances in Sustainable Solutions for Energy Transitions (ASSET 2025), January 2-4, 2025, IIT Guwahati, Assam. *(in person)*

8. **Mononita Das**, Kuntal Ghosh, Mir Wasim Raja
   Oral presentation titled "PVDF-modified Cellulosic Paper Matrix Impregnated with LLZO Active Filler: A Sustainable, Thermally Durable and High-Performance Separator for Next Generation Lithium-ion Batteries" in 2-Days International Symposium on Sustainable Technologies The Way Forward and 61st Annual Convention 2024 of Indian Photobiology Society (IPS) Organized by Centre of Excellence in Renewable Energy (CoERE) and Basic Science and Humanities Department (BSH), IEM Kolkata In Association with Indian Photobiology Society, Royal Society of Chemistry (RSC), UK and University of Engineering and Management, Kolkata, January 31-February 01, 2025, UEM Kolkata, West Bengal. *(in person)*

9. **Mononita Das**, Kuntal Ghosh, Mir Wasim Raja
   Poster presentation titled "All-Solid-State Paper Battery: A Futuristic Solution towards Sustainable Batteries" in International Conference on Sustainable Batteries (ICSB25), Organized By TCG Centres for Research and Education in Science and Technology (TCG CREST), Endorsed By Battery Research Society, Knowledge Partner Indian Energy Storage Alliance, February 24-27, 2025, Bisws Bangla Convention Center, Kolkata, West Bengal. *(in person)*

10. **Mononita Das**
    Oral presentation on "Surface Charge-Driven Performance Modulation of Nanoceramic Fillers in Paper Separators for High-Performance Lithium-ion Batteries", GLAMICS Fiesta 2025 (Research Scholars' Day), CSIR-Central Glass and Ceramic Research Institute, Kolkata, June 19-20, 2025, CSIR-CGCRI, Kolkata, West Bengal. *(in person)*

Award

2nd prize for Oral Presentation in Theme III: Energy - Materials, Storage, Transmission, Distribution & Policies, e-Mobility, International Conference on Advances in Sustainable Solutions for Energy Transitions (ASSET 2025), January 2-4, 2025, IIT Guwahati, Assam.

Reprints of the Published Works

ACS APPLIED ENERGY MATERIALS

www.acsaem.org Article

Paperator: The Paper-Based Ceramic Separator for Lithium-Ion Batteries and the Process Scale-Up Strategy

Mir Wasim Raja,*,‖ Rajendra Nath Basu,*,‖ Nimai Chand Pramanik, Pradip Sekhar Das, and Mononita Das

Cite This: *ACS Appl. Energy Mater.* 2022, 5, 5841−5854 Read Online

ACCESS | Metrics & More | Article Recommendations | Supporting Information

ABSTRACT: Due to its flexibility, cost-effectiveness, and natural abundance, paper has become a material of choice for its targeted applications in electronic and optoelectronic devices. With an aim to develop a paper-based ceramic separator (henceforth will be referred to as paperator), a low-cost paper substrate sourced from the local market has been functionalized by the wet-coating method using duo-polymer (chitosan and polyvinyl alcohol) and ceramic ($BaTiO_3$) nanopowder. The developed paperator shows excellent air permeability, improved thermal stability of up to 200 °C without dimensional shrinkage, quicker wettability to an electrolyte, and comparable electrochemical performance to that of polypropylene-based commercial separator. The modification of the paper substrate using polymer and ceramic particles has also improved the tensile strength of the paperator to a maximum value of 45.23 MPa w.r.t. 28.20 MPa for pristine paper. The electrochemical performance of the developed paperators shows satisfactory cell performance at different current densities with excellent coulombic efficiency and comparable discharge capacities with that of a commercial separator. Compared to the commercial PP-based membrane, slightly lowered discharge capacities are obtained from the cells fabricated with developed paperators, which may primarily be due to the higher thickness (60/70 μm) and cellulosic tortuosity. Electrochemical performances of the developed "paperators" were also evaluated for use in supercapacitors (SCs) by fabricating SC cells and their testing as per IEC 62391-1, which showed the cell capacitance and ESR values of 17.2 ± 0.8 F and 76 ± 3 mΩ, respectively, and the results were also compared with those of commercial cellulose-based paper separators. Based on the R&D achievements, the present study has also been extended for a scale-up strategy to produce a paper-based separator in roll form, where a "paperator" of 60 mm in width in a continuous manner has been fabricated by using in-house-designed semi-automated double-decker separator fabricator machine.

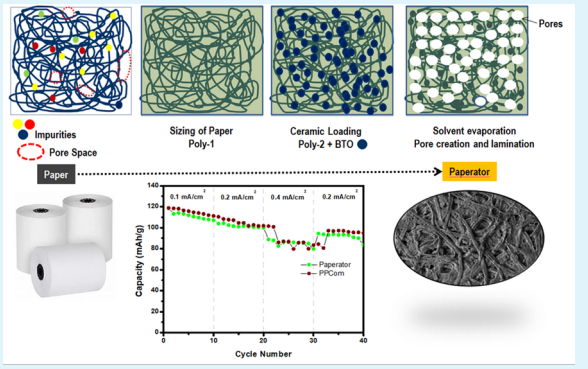

KEYWORDS: *composite separator, cellulose, paper separator, thermal shrinkage, electrolyte wettability, electrochemical performance*

INTRODUCTION

A "separator" is an essential and important component for Li-ion batteries (LiBs), supercapacitors (SCs), and similar other electrochemical energy storage devices. The major tasks of a separator in an energy storage system, LiBs and SCs in particular, are to prevent physical contact between the anode and the cathode, to avoid an electrical short circuit, and at the same time, to enable transport of ions from one electrode to another across the separator during the charge−discharge process. Today's commercial lithium-ion batteries (LiBs) use polyolefin membranes as separators, which remain inert throughout the cell performance without any participation in electrochemical reaction.[1−3] In addition to such chemical and redox inertness, a separator should also be porous (>40% porosity) and should have an intrinsic capability to absorb a sufficient amount of liquid electrolyte (high wettability) for achieving the required ionic conductivity.[4−7] A separator should also possess sufficient mechanical strength compatible with the winding tension of the battery assembly line. Apart from several positive roles in electrochemical cells, the separator's electrical resistance, dead mass, tortuosity, and thickness also have significant role in the electrochemical performance, particularly energy density, power density, cycle life, and safety.

Microporous polyolefin membranes commercially used for LiBs are generally derived either from a single polymer or from the blend of duo-polymer, namely, polyethylene (PE) and polypropylene (PP). The use of such duo-polymers in different combinations and the study of their performance in various LiBs are reported in the literature.[8,9] It would be worthy to mention

Received: January 17, 2022
Accepted: April 4, 2022
Published: April 19, 2022

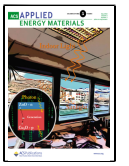

https://doi.org/10.1021/acsaem.2c00188
ACS Appl. Energy Mater. 2022, 5, 5841−5854

Cellulose (2022) 29:9899–9917
https://doi.org/10.1007/s10570-022-04873-3

ORIGINAL RESEARCH

Cellulose-ceramic composite flexible paper separator with improved wettability and flame retardant properties for lithium-ion batteries

Mononita Das · Pradip Sekhar Das · Rajendra Nath Basu · Mir Wasim Raja

Received: 20 July 2022 / Accepted: 30 September 2022 / Published online: 14 October 2022

Abstract In quest of developing sustainable separator for lithium-ion batteries (LIBs), this research focuses on functionalization of low cost cellulose based commercial paper using duo-polymer and nano-SiO_2 by designing a facile aqueous based industry friendly wet-coating process. Unlike commercial plastic based polyolefin separators (polypropylene/polyethylene), the developed paper separator shows superior thermal stability > 200 °C without dimensional shrinkage, excellent electrolyte wettability (147%) with zero contact angle, quicker electrolyte saturation and satisfactory mechanical strength (34.86–38.31 MPa). The electrochemical performance carried out in 2032 coin cells using fabricated paper separators shows comparable performance to that of commercial polypropylene (PP) based separator at different current densities of 0.05–0.4 mA/cm^2 with excellent columbic efficiency (> 96%) and good capacity retention on cycling. The developed separator is found to be compatible with most of the commercial electrodes (MCMB, $LiCoO_2$, $LiFePO_4$) used in today's LIBs. The functionalized cellulose-ceramic composite paper separator shows excellent flame retardant properties by offering an added safety features for its successful use in lithium-ion batteries.

Supplementary Information The online version contains supplementary material available at https://doi.org/10.1007/s10570-022-04873-3.

M. Das · P. S. Das · M. W. Raja (✉)
Energy Materials and Devices Division (Former Fuel Cell and Battery Division), CSIR-Central Glass and Ceramic Research Institute, Kolkata 700032, India
e-mail: mwraja@cgcri.res.in

R. N. Basu (✉)
School of Advanced Materials, Green Energy and Sensor Systems, Indian Institute of Engineering Science and Technology, Howrah 711103, India
e-mail: rajenbasu54@gmail.com

ACS OMEGA

http://pubs.acs.org/journal/acsodf

Article

Advanced Sustainable Trilayer Cellulosic "Paper Separator" Functionalized with Nano-$BaTiO_3$ for Applications in Li-Ion Batteries and Supercapacitors

Mononita Das, Pradip Sekhar Das, Nimai Chand Pramanik, Rajendra Nath Basu, and Mir Wasim Raja*

Cite This: *ACS Omega* 2023, 8, 21315−21331

Read Online

ACCESS | Metrics & More | Article Recommendations | Supporting Information

ABSTRACT: In the quest of developing a sustainable, low-cost and improved separator membrane for application in energy storage devices like lithium-ion batteries (LIBs) and supercapacitors (SCs), here we fabricated a trilayer cellulose-based paper separator engineered with nano-$BaTiO_3$ powder. A scalable fabrication process of the paper separator was designed step-by-step by sizing with poly(vinylidene fluoride) (PVDF), thereafter impregnating nano-$BaTiO_3$ in the interlayer using water-soluble styrene butadiene rubber (SBR) as the binder and finally laminating the ceramic layer with a low-concentration SBR solution. The fabricated separators showed excellent electrolyte wettability (216−270%), quicker electrolyte saturation, increased mechanical strength (43.96−50.15 MPa), and zero-dimensional shrinkage up to 200 °C. The electrochemical cell comprising graphite|paper separator|$LiFePO_4$ showed comparable electrochemical performances in terms of capacity retention at different current densities (0.05−0.8 mA/cm^2) and long-term cycleability (300 cycles) with coulombic efficiency >96%. The in-cell chemical stability as tested for 8 weeks revealed a nominal change in bulk resistivity with no significant morphological changes. The vertical burning test as performed on a paper separator showed excellent flame-retardant property, a required safety feature for separator materials. To examine the multidevice compatibility, the paper separator was tested in supercapacitors, delivering a comparable performance to that of a commercial separator. The developed paper separator was also found to be compatible with most of the commercial cathode materials such as $LiFePO_4$, $LiMn_2O_4$, and NCM111.

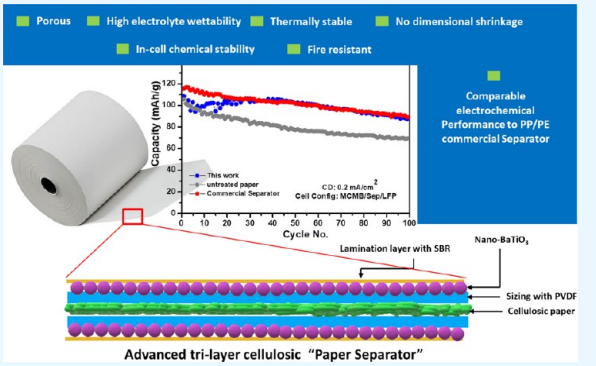

1. INTRODUCTION

A separator in batteries is primarily used to isolate the anode and cathode to prevent electrical short circuit; simultaneously, it should also possess the ability of facile ionic transaction, high porosity and electrolyte wettability, lowered thickness, good mechanical strength, thermal stability, and intrinsic safety in abused conditions.[1,2] Moreover, sustainability and cost are other two important techno-economic parameters that need to be addressed while developing separator materials. Achieving all these properties in a single material is indeed a challenging task.

Conventionally used microporous polyolefin (polypropylene/polyethylene)-based plastic separators have no doubt been a great commercial success in Li-ion batteries till date, but their low wettability towards commercial electrolytes, dimensional instability at elevated temperature, and environmental challenges due to plastic toxicity trigger the need for more advanced sustainable separators for lithium-ion batteries (LIBs).[3] To mitigate these problems, two major approaches were undertaken: either surface modification of existing polyethylene (PE)/polypropylene (PP)-based separators[4] or employment of other synthetic polymers, which include poly(ethylene terephthalate) (PET) nonwovens,[5] polyacrylonitrile (PAN),[6] poly(vinylidene fluoride) (PVDF), etc.[7]

Besides these synthetic polymers, cellulose and/or its derivatives, e.g., bacterial cellulose,[8,9] cellulose acetates,[10] carboxymethyl cellulose,[11] cellulose nanofibers or nanocrystals,[12,13] lignocellulose[14] etc., have also been investigated widely as separator membranes. The obvious reasons for choosing cellulose as the separator material is definitely due to its sustainability, natural abundance, lower cost, and ease to compositionally modify or functionalize to achieve the desired properties as separator membranes in batteries. Moreover, unlike polyolefin, the cellulosic skeleton comprises hydroxyl and carbonyl groups, which can facilitate good interaction with carbonate electrolytes, enhancing its ability to soak a large amount of the electrolyte. Cellulose, having a higher initial

Received: April 26, 2023
Accepted: May 10, 2023
Published: May 29, 2023

Journal of Power Sources 606 (2024) 234573

Contents lists available at ScienceDirect

Journal of Power Sources

journal homepage: www.elsevier.com/locate/jpowsour

Flexible ceramic based 'paper separator' with enhanced safety for high performance lithium-ion batteries: Probing the effect of ceramics impregnation on electrochemical performances

Mononita Das, Kuntal Ghosh, Mir Wasim Raja *

Energy Materials & Devices Division, CSIR-Central Glass & Ceramic Research Institute, Kolkata, West Bengal, 700032, India

HIGHLIGHTS

- Sustainable, flexible and high safety ceramic based paper separators for LIBs.
- Separators were developed using easy to scale up wet-coating process.
- Ceramic impregnation affects physical and electrochemical properties of the separators.
- Paper separators show superior electrolyte wettability and high thermal stability.
- Better electrochemical performances and flame safety are other important advantages.

GRAPHICAL ABSTRACT

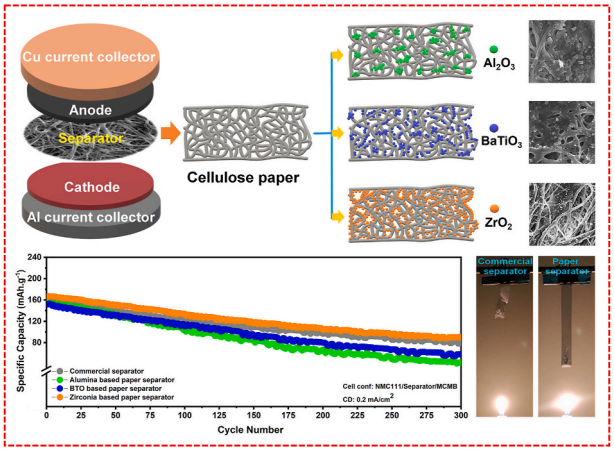

ARTICLE INFO

Keywords:
Cellulose
Ceramics
Paper separator
Lithium-ion battery
Flame resistance

ABSTRACT

Cellulose is now considered as an appealing environment friendly material for the development of sustainable separators for rechargeable batteries. This study thus aims to develop high performance paper based ceramic separators with superior electrolyte wettability (>170 %), high thermal stability (>200 °C) and excellent flame safety. While developing paper based ceramic separator, extensive studies are carried out to understand the-nature and functionality of different nano-structured ceramic materials (Al_2O_3, $BaTiO_3$ and ZrO_2) impregnated in paper matrix. Nano-ZrO_2 facilitates an effective pathway for Li^+-ion transport ($t_{Li}^+ = 0.51$), whereas $BaTiO_3$ and Al_2O_3 ceramics show moderate Li^+-ion transport properties (t_{Li+} of 0.29 and 0.30 respectively). Electrochemical Impedance Spectroscopy (EIS) measurement clearly reveals that ZrO_2 exhibits more interfacial compatibility with the electrodes (MCMB and $LiNi_{1/3}Mn_{1/3}Co_{1/3}O_2$) compared to the other two ceramic separators during full cell operation. The developed paper separators show excellent electrochemical properties in terms of cycling (tested 300 cycles), multi-electrode compatibility and rate capabilities at different current densities of 0.1–1.2 $mAcm^{-2}$. The pre- and post-electrochemical EIS data reveal that ZrO_2 based impregnation offers significantly

* Corresponding author.
E-mail addresses: das.mononita17@gmail.com (M. Das), kuntalghosh1004@gmail.com (K. Ghosh), mwraja@cgcri.res.in (M.W. Raja).

https://doi.org/10.1016/j.jpowsour.2024.234573
Received 5 February 2024; Received in revised form 4 April 2024; Accepted 16 April 2024

Journal of Materials Chemistry A

ROYAL SOCIETY OF CHEMISTRY

PAPER

View Article Online
View Journal | View Issue

Cite this: J. Mater. Chem. A, 2025, 13, 1996

Flexible trilayer cellulosic paper separators engineered with the $BaTiO_3$ ferroelectric fillers for high energy density sodium-ion batteries†

Simranjot K. Sapra,[abc] Mononita Das,[d] M. Wasim Raja,[d] Jeng-Kuei Chang[bce] and Rajendra S. Dhaka *[a]

Cellulose-based paper separators are employed in sodium-ion batteries (SIBs) as a viable and economical substitute of conventional separators, owing to their sustainability, scalability, safety and cost-effectiveness. We design a full cell configuration having $Na_3V_2(PO_4)_3$ as the cathode and pre-sodiated hard carbon as the anode with different separators and compare the electrochemical performance of these ceramic-impregnated polymer-coated cellulose paper separators with that of commercial glass fiber separators. Notably, the paper-based multilayer separators provide desirable characteristics such as excellent electrolyte wettability, thermal stability up to 200 °C, and ionic conductivity, which are essential for the efficient operation of SIBs. The cellulose separator is coated with a layer of polyvinylidene fluoride polymer, followed by a second layer of styrene butadiene rubber (SBR) polymer in which ferroelectric filler $BaTiO_3$ is integrated, which interacts with the polymer hosts through Lewis acid–base interactions and improves the conduction mechanism for the Na^+ ions. The final lamination is performed by varying the SBR concentrations (0.5, 0.75, and 1.0 w/v%). The incorporated polymer matrices improve the flexibility, adhesion and dispersion of the nanoparticles and affinity of the electrolyte to the electrode. The morphology of the paper separators shows uniform interconnected fibers with a porous structure. Interestingly, we find that the paper separator with 0.75 w/v% content of SBR exhibits decreased interfacial resistance and improved electrochemical performance, having retention of 62% and nearly 100% coulombic efficiency up to 240 cycles, as compared to other concentrations. Moreover, we observe the energy density to be around 376 W h kg^{-1} (considering the cathode weight), which was found to be comparable to that of the commercially available glass fiber separator. Our results demonstrate the potential of these multilayer paper separators towards achieving sustainability and safety in energy storage systems.

Received 26th September 2024
Accepted 28th November 2024

DOI: 10.1039/d4ta06863g

rsc.li/materials-a

1. Introduction

The abundance of sodium resources on Earth has been the driving force behind the emergence of sodium-ion batteries (SIBs) as efficient and ecologically friendly energy storage technologies, with the objective of achieving a sustainable and green power storage system.[1–6] In the interim, SIBs continue to captivate researchers as potential replacements for lithium-ion batteries (LIBs) due to their cost-effectiveness and comparable intercalation mechanism.[7–11] Among the primary components of a battery, the function of a separator is to prevent a short circuit by creating a physical barrier between the electrodes and ensuring that the battery's functionality is improved by the presence of sufficient pores that facilitate the passage of ions during the charge–discharge process.[12,13] The shutoff mechanism of the separator is essential for maintaining the thermal stability, *i.e.*, in the event of battery overheating, it melts and halts the flow of ions, thereby averting thermal runaway.[14,15] The separators also demonstrate great electrolyte wettability, which is a critical factor in enhancing ionic conductivity and further optimizing the battery performance.[16] The introduction of electric vehicles has significantly altered the performance requirements of separators, despite their long-standing use in the industry.[17] Consequently, it is imperative to create separators that can withstand the difficult operational conditions by exhibiting remarkable thermal and mechanical stability.

[a]Department of Physics, Indian Institute of Technology Delhi, Hauz Khas, New Delhi 110016, India. E-mail: rsdhaka@physics.iitd.ac.in

[b]International College of Semiconductor Technology, National Yang Ming Chiao Tung University, 1001 University Road, Hsinchu 30010, Taiwan

[c]Department of Materials Science and Engineering, National Yang Ming Chiao Tung University, 1001 University Road, Hsinchu 30010, Taiwan

[d]Energy Materials and Devices Division, CSIR-Central Glass and Ceramic Research Institute, Kolkata 700032, India

[e]Department of Chemical Engineering, Chung Yuan Christian University, 200 Chung Pei Road, Taoyuan, 32023, Taiwan

† Electronic supplementary information (ESI) available. See DOI: https://doi.org/10.1039/d4ta06863g

Journal of Power Sources 654 (2025) 237838

Contents lists available at ScienceDirect

Journal of Power Sources

journal homepage: www.elsevier.com/locate/jpowsour

Role of LLZO active filler in PVDF-modified cellulosic paper matrix: A sustainable, thermally durable and high-performance separator for next generation lithium batteries

Kuntal Ghosh [1], Mononita Das [1], Mir Wasim Raja [*]

Energy Materials & Devices Division, CSIR-Central Glass & Ceramic Research Institute, Kolkata, 700032, India

HIGHLIGHTS

- Sustainable, flexible paper separator impregnated with LLZO for high performance LIBs.
- An industry-friendly wet-coating process optimized for 'roll-to-roll' fabrication.
- Paper separator with LLZO shows better Li-ion transport than Al_2O_3 loaded separator.
- Improved flame resistance and multi-electrode compatibility for LLZO-coated separator.
- Better electrochemical performance of LLZO coated separator after thermal shock.

GRAPHICAL ABSTRACT

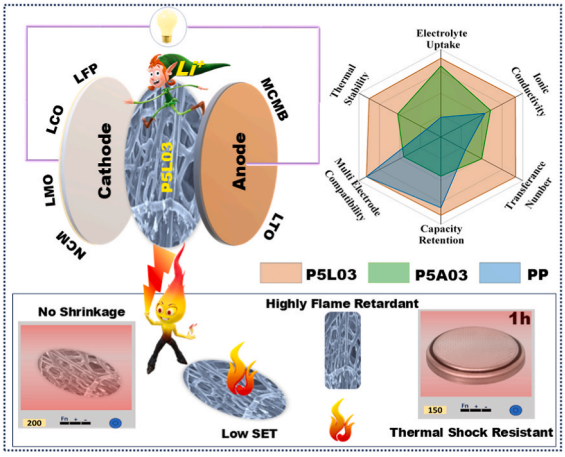

ARTICLE INFO

Keywords:
Paper separator
LLZO electrolyte
Flame retardant
High-rate capability
Multielectrode compatibility

ABSTRACT

The present study highlights the effect of active (LLZO) and inactive (Al_2O_3) ceramic impregnation in paper-based cellulosic separators developed using an industry-friendly dip-coating process. The fabricated separator with 30 wt% LLZO (P5L03) exhibits superior ionic conductivity (1.23 mS cm^{-1}), higher Li-ion transport properties (t_{Li}^{+} = 0.64), wider electrochemical window (>5.5V) as compared to Al_2O_3 (30 wt%) based (P5A03) and commercial PP based separators. The enhancement in electrical properties is likely due to the intrinsic Li-ion conductivity of LLZO and the structural modification of PVDF chain induced by the Lewis basic environment of LLZO. P5L03 shows better capacity retention after long cycling and excellent compatibility against different cathodic (LFP, LMO, LCO, NMC) and anodic (LTO, MCMB) configurations. The developed P5L03 separator exhibits excellent flame retardancy and better self-extinguishing properties with lowest self-extinguishing time of 5.55s, as compared to P5A03 (8.76s) and PP (11.10s). It also shows outstanding electrochemical performance even after self-extinguishing test and thermal shock treatment at 120 °C and 150 °C for 1 h. In summary, paper

* Corresponding author.
E-mail addresses: kuntalghosh1004@gmail.com (K. Ghosh), das.mononita17@gmail.com (M. Das), mwraja@cgcri.res.in (M.W. Raja).
[1] These two authors contributed equally to this work.

https://doi.org/10.1016/j.jpowsour.2025.237838
Received 9 January 2025; Received in revised form 24 June 2025; Accepted 4 July 2025
Available online 11 July 2025

Solid State Ionics 430 (2025) 117008

Contents lists available at ScienceDirect

Solid State Ionics

journal homepage: www.elsevier.com/locate/ssi

The critical role of Al_2O_3, $BaTiO_3$ and ZrO_2 nanoceramic fillers in PVDF-HFP based composite polymer electrolytes for high performance lithium-metal batteries

Mononita Das [a], Kuntal Ghosh [a], Vijaya [b], Mir Wasim Raja [a,*]

[a] Energy Materials & Devices Division, CSIR-Central Glass & Ceramic Research Institute, India
[b] School of Energy Science and Engineering, Indian Institute of Technology Guwahati, India

ARTICLE INFO

Keywords:
Composite solid polymer electrolytes
Lithium-metal batteries
Inorganic fillers
Li dendritic growth
Ionic conductivity

ABSTRACT

Lithium metal batteries (LMBs) can be the ultimate choice for future battery technologies since they use Lithium metal as anode, which offers high theoretical capacity (3860 $mAh.g^{-1}$) and lowest electrochemical potential (−3.04 V vs. SHE). However, their commercialization is limited by dendritic growth, interfacial instability, and safety risks associated with liquid electrolytes. In this work, composite solid polymer electrolytes (CSPEs) are developed by incorporating various (Al_2O_3, $BaTiO_3$, and ZrO_2) ceramic fillers into a PVDF-HFP/LiTFSI matrix via a scalable solution casting method. Among these, optimized 10 wt% ZrO_2-based CSPE (PLZ) delivers the highest room-temperature ionic conductivity (9.26×10^{-5} S cm^{-1}), excellent Li^+ transference number (0.55), superior tensile strength (3.23 MPa), wide potential window (5.33 V), and good flame retardancy. Li/Li symmetric cells using PLZ showed stable lithium plating/stripping for more than 480 h at 0.10 $mA.cm^{-2}$ with a low overpotential of ~7 mV. Electrochemical impedance spectroscopy and equivalent circuit fitting confirmed the lowest increase in interfacial resistance after cycling. Time-resolved distribution of relaxation time (DRT) and 2D contour analysis revealed that PLZ maintained stable SEI and charge-transfer resistances, while bare CSPEs showed growing interfacial instability during cycling. These improvements are attributed to Lewis acid-base interactions and surface charge effects that reduce crystallinity and promote Li^+ mobility. Full-cell evaluations with $LiFePO_4$ and NMC111 cathodes demonstrated high discharge capacities and good cycling stability. Thus, this study offers a promising pathway for developing robust and safe CSPEs for next-generation solid-state LMBs.

1. Introduction

In the ongoing digital era, Lithium-ion batteries (LIBs) are an integral part of daily life. They are essential in powering almost every needful device, ranging from household to sustainable transportation and e-mobility, due to their high theoretical capacity and impressive energy and power density. Conventional LIBs consist of Graphite-based anodes and Nickel or Cobalt-rich cathodes, along with carbonate-based liquid electrolytes containing $LiPF_6$ and polyolefin-based separator membranes [1]. While the carbonate-based liquid electrolytes are efficient to use due to their high ionic conductivity (~10^{-3} S.cm^{-1}), they impose several challenges like leakage, flammability, narrow electrochemical stability window, and untimely decomposition inside the battery [2,3]. Additionally, the plastic-based separators are also prone to dimensional instability and combustion at high temperatures [4,5]. Together, these components can cause serious safety concerns, which mandates the exploration of more efficient, sustainable, thermally stable, and flame-retardant alternatives with similar or better performance.

Here, solid electrolytes could be an effective alternative as they do not present any risk of leakage and flammability, and can additionally provide a wider electrochemical stability window, high performance, and good compatibility with Lithium metal anodes [6]. In view of this, the replacement of both liquid electrolyte and polymeric separator with solid electrolyte can be a promising approach to overcome the challenges of short-circuit and thermal runaway [7]. Solid electrolytes can be of three major types: (a) inorganic solid electrolytes (ISEs), (b) solid polymer electrolytes (SPEs), and (c) composite solid polymer electrolytes (CSPEs) [8,9]. The inorganic solid electrolytes like oxides (LLZO,

* Corresponding author.
E-mail addresses: das.mononita17@gmail.com (M. Das), kuntalghosh1004@gmail.com (K. Ghosh), vijaya19@iitg.ac.in (Vijaya), mwraja@cgcri.res.in, mwraja.cgcri@csir.res.in (M.W. Raja).

https://doi.org/10.1016/j.ssi.2025.117008
Received 20 June 2025; Received in revised form 14 August 2025; Accepted 24 August 2025